Synthesis, characterization and applications of highly stable pyrazolate-based metal-organic frameworks

By
Valentina Colombo

A dissertation submitted in partial satisfaction
of the requirements for the
Degree of Doctor of Philosophy
In Chemistry

Università degli Studi dell'Insubria
Facoltà di Scienze MM. FF. NN. - Como

XXIV Ciclo di dottorato in scienze Chimiche
Supervisors: Dott. Angelo Maspero, Prof. Norberto Masciocchi

Graphics provided by Dr. Paola Colombo

“Experiments are the only means
of knowledge at our disposal;
the rest is poetry, imagination”
Max Planck

To my husband
and my family

Contents

Chapter 1
The Fascinating Chemistry of Metal-Organic Frameworks

Introduction

Fifteen years have passed since the term "metal-organic frameworks" (MOFs) first appeared in the literature:[1] MOFs, also known as coordination polymers, are a recent class of new hybrid porous solids materials that now represents one of the most rapidly developing areas of chemical science. At the beginning, this class of hybrid porous solids was considered more or less as a curiosity but later on, has been transformed into a fully qualified field of research with an explosion of papers into the literature.[2] Moreover, a small number of MOFs, such as zeolitic imidazolate frameworks (ZIFs), are nowadays industrially prepared, for example, by BASF (marked under the trademark BASOLITE™) and commercially available through Aldrich.[3]

MOFs posses unique properties among the various classes of microporous and mesoporous materials that generates interest for an unprecedented range of applications. The richness of this research field could be justified by looking closer to the features of these porous materials: MOFs are crystalline materials resulting from the reaction between an organic linker and inorganic species, such as clusters or metal ions (often called as SBUs, secondary building units).

The linkage between these two partners generates a three dimensional framework whose skeleton contains both organic and inorganic units linked by classical coordination bonds (Scheme 1.1). By exploiting the features of this two moieties within a single material, the scientist has the ability to predict and tune the chemical and physical properties of the framework by judicious selection of these two components. This offers a wide range of tunable properties that depend both from the inorganic joints and the organic linkers. By looking closer at the organic linker, it is possible to imagine a tuning of the shape (e.g. ligand coordination angles), size (e.g. dimension of the ligand as expansion or shrinkage) but also, functionality (e.g. decoration of the pores depending on the substituent of the organic unit) of the MOF.[4] Again, inorganic joints as metal ions or inorganic clusters (also called as secondary building units, SBUs), provides the potential of having similarity in properties to traditional zeolites that could include thermal stability, the presence of active catalytic sites and a good mechanical robustness.[5] The self assembly of these components, typically done in solution, generate a linkage extended in a 3D crystalline framework that is characterized by large pores filled of solvent. Interesting, this rigid structure can stand vacuum, indeed, after removal of the solvent molecules, the structure remains intact. Intriguingly, this process leaves behind an impressive surface area. Landmarks in this respect are MOF-177 with a high surface area of 5640 m^2/g,[6] followed by MIL-101 having an even higher surface area of 5900 m^2/g,[7] and the current record is held by UMCM-2 which possesses an exceptional surface area of over 6000 m^2/g.[8] These unique characteristics of MOFs set them apart from other traditional porous materials. Zeolites and mesoporous silica are usually crystalline but fully inorganic, thus lack synthetic flexibility and structural diversity/tailorability. The high surface area of porous MOFs is the reason why the early excitement for MOFs was widely focused on their use for gas storage and gas separation applications (e.g. hydrogen storage and CO_2 sequestration). This

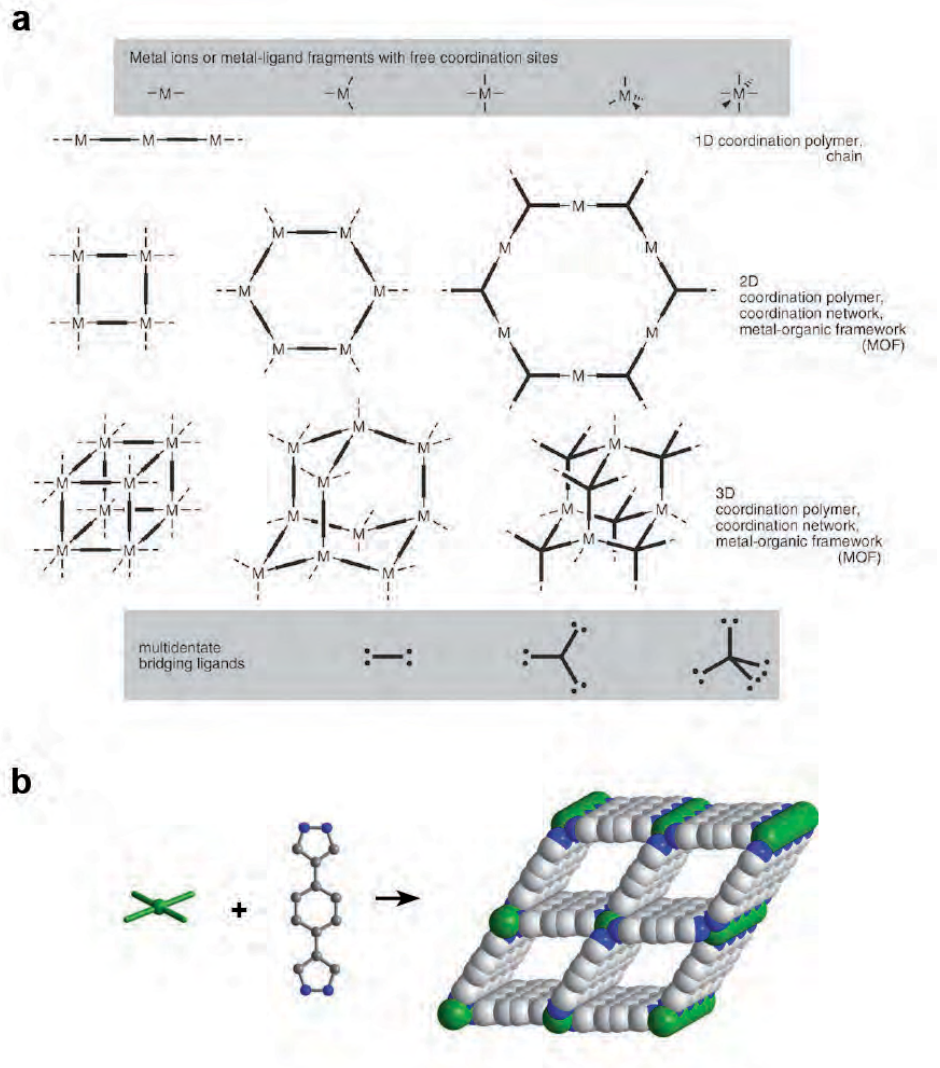

Scheme 1.1. a) Schematic representation of the construction of typical coordination polymers/MOFs from metal ions or inorganic clusters and multidentate bridging ligands. b) Depiction of the construction of a MOF starting from Ni(II) ions in a square planar geometry and a polytopic pyrazolate ligand.

is due to the fact that the high surface area of these porous materials increases van der Waals interactions needed for uptake of weakly interacting gases, and MOFs pore dimension and shape can be exploit to tune relative adsorption rates and transport of gases through the pores.[9]

Notwithstanding the importance and the worldwide interest in such kind of applications, due to a reasonably needed of new energy sources and new strategies for CO_2 capture,[10] metal-organic frameworks posses other properties that can expand their applications in different fields. These include: electronic and conductive properties,[11] luminosity resulting from a conjugated organic linkers,[12] drug delivery,[13] heterogeneous catalysis by exploiting the presence of open metal sites[14] and linkers properties,[15], magnetic properties[16] and application in sensor technologies.[17] The fact that metal-organic frameworks have such a large possibility in applications of high interest is due, of course, to their hybrid porous nature, but also to the emerging ability to tune the pore size and pore wall functionality of their structures. This has allows the researchers to focus on those factors which hold the most promise, increasing both the volume available for storage and the affinity of the network for the stored gas molecules. Particularly, as alternative clean fuels such as hydrogen and methane continue to be developed in automotive and other applications and as the emission of carbon dioxide won't be reduced significantly in the short term, the need for effective storage technologies will continue to increase, and porous MOFs are well-positioned to play an important role at the forefront of this research. Therefore, in a moment in which our civilization has crucial energy problems and the sustainable development is the way for surviving, MOFs can provide many solutions in different areas owing to the already mentioned infinity of possibilities in their design for dedicated applications.

The mainstream of this thesis is focused on the investigation of a new class of metal-organic frameworks constructed by polytopic pyrazolate-bridging ligands.

This class of linkers has been designed in order to obtain highly stable porous materials and investigate the ability of the pyrazole ring in the construction of extended 3-dimentional frameworks with porous features. Worthy of note, the investigation of porous metal-organic frameworks by exploiting the chemistry of pyrazoles, has not been deeply explored prior to this thesis project, since only few examples were found in the literature.[18] This could be ascribed to a more difficulty in obtaining polytopic pyrazole-based ligands compared to polytopic carboxylic acids that are, in most cases, directly available though the mayor chemical companies or easily obtainable by simple one-step reactions. Moreover, pyrazolate-based metal-organic frameworks generally precipitates in the form of highly insoluble and crystalline powders, the structure of which cannot be retrieved by conventional single-crystal X-Ray diffraction. However, *ab-initio* X-Ray Powder Diffraction (XRPD) methods come to our aid for the comprehension of their structural features.

Accordingly, in the next chapters are reviewed in details the results obtained on the synthesis of a new series of pyrazole-based ligands (Chapter 3) and on the discovery of a number of MOFs based on the linkage between such polytopic pyrazolate ligands and transition metal ions (Chapters 4-8). Once characterized, the new porous frameworks have been studied for targeted applications depending on their structural features (metal ion, structure type, porosity etc.), showing either outstanding thermal and chemical stability but also interesting properties in gas adsorption/purification and in harmful organic vapor separation.

On the design and synthesis of MOFs

Due to the close correlation between MOF structures and their potential properties, the 'design' of desiderable structures with expected properties becomes very important and attractive, although is still a very challenging issue.

Michel O'Keefee reported, in his personal view: '*The Shorter Oxford Dictionary on my desk gives six meanings for the noun 'design'. The first of which is "a plan or scheme conceived in the mind...". Merriam Webster's Collegiate Dictionary (also highly regarded as authoritative) gives eight meanings, of which the first is "deliberate purposive planning...", and another is (I quote exactly) "a plan or protocol for carrying out or accomplishing something (such as a scientific experiment)". This sounds to me very much like what goes on in the Yaghi laboratory and elsewhere*'.[19] The knowledge of possible topologies as well as the understanding of typical metal coordination geometries or the formation conditions related to the existence of a known inorganic secondary building unit (SBU), helps in understanding and direct the synthesis efforts in the view of predetermined structures. This is what we mean with the use of the expression "design" related to the construction of a metal-organic framework structure.

One of the main goals in MOF synthesis is to establish the synthetic conditions that lead to defined inorganic building blocks without decomposition of the organic linker. At the same time, the kinetics of crystallization must be appropriate to allow nucleation and growth of the desired phase to take place. Sometimes, as will be highlighted in this thesis, growing single crystals is also a very difficult and challenging issue. However, when crystalline powders are available, state-of-the-art structure solution from powder diffraction data (XRPD) can help the scientist in retrieve structural information otherwise inaccessible with other solid state techniques.

The variety of synthetic methodologies and strategies adopted in the field of MOF synthesis is incredibly large. These techniques range from classical room temperature synthesis, hydrothermal and solvothermal reactions, electrochemical and mechanochemical syntheses, to the use of structure-directing agents and, during the last decade, even to the introduction of microwave-assisted synthesis and post-synthetic modifications.[20]

Delicacy in the selection of the synthetic method when we design a new MOF is required to obtain pure and crystalline phases. As a matter of fact, from the same reaction mixture it is possible to obtain different MOFs. Moreover, the reaction conditions may have a strong impact on yields, particle size, morphology, etc. and may be differently well suited for the implementation in large-scale processes. In the last years, high-throughput method to speed up the discovery of MOFs and in order to find the best reaction conditions (time, temperature program, solvent or mixture of solvents, etc.) for the synthesis of a targeted structure, have been developed.[21]

In this thesis, pyrazolate-based metal-organic frameworks have been synthesized with a classical solvothermal method. Indeed, the syntheses have been performed in a closed vessel under autogenous pressure above the boiling point of the solvent (in most cases, *N, N*-dymethylformamide, DMF) leading to crystalline and pure powders of porous pyrazolate-based frameworks, later on structurally characterized, in most cases, by X-Ray powder diffraction analysis.

Background on MOFs structures

Metal-organic frameworks have a rich history were numerous efforts have been done to design and synthesize functional porous structures. Prior to the late 1980s, a variety of metalorganic coordination compounds were discovered (e.g., Werner complexes,[22] Hofmann clathrates,[23] Prussian blue[24]) and studied for their interesting properties. However, no systematic approach to the construction of this class of solid-state materials had been introduced until Hoskins and Robson, in 1989, proposed the design of open frameworks based on a node-and-spacer approach where tetrahedral nodes (e.g. Zn^{2+}) were linked by linear molecular spacers (*e.g.* cyanide anion) to construct an open structure based on the extension of cubic diamond (*i.e.*, $Zn(CN)_2$, Cu[4,4',4'',4'''-tetracyanotetraphe nylmethane]$\cdot BF_4 \cdot x C_6H_5NO_2$).[25]

Later on, Hoskin's and Robson's design principles were exploited with the introduction of polytopic monodentate *N*-donor ligands, such as 4,4'-bipyridine (4,4'-Bipy), that coordinate in a similar linear ditopic manner of the shorter cyanide anion, but with extending the length of connections between the inorganic nodes. This has resulted in enlarged cavities and more open structures compared to zeolites and analogous metal cyanides.[26] However, since 4,4'-Bipy is a simple linear linker, the determination of each structure's network topology is directly governed by the coordination environment and geometry of the metal ion. The control of the metal ion geometry has been done with rather success by Fujita and coworkers with their "capping method", were a terminal chelating ligand (e.g. ethylendiamine) is used to cap the metal ions to give a specific geometry (Figure 1.1).[27] Therefore, 4,4'-Bipy is a prominent example for a prototypical bridging ligand and an attractive molecular building block for diverse architectures of metal-organic coordination networks such as one dimensional (1D) chains[28] or ladders,[29] two-dimensional (2D) grids[30] and three-dimensional frameworks.[31] It is worthy of note that, in the case of 4,4'Bipy-like neutral bridging ligands (Scheme 1.2), charge balance is achieved by anions from the original metal salt, for example, Cl^-, NO_3^-, SO_4^{2-} and BF_4^-.

Although the first porous 4,4'Bipy-based material was reported by Kitagawa and coworkers in 1997,[32] permanently porous monodentate (4,4'Bipy-like)-based frameworks are still scarce as these materials are typically unstable and irreversibly lose crystallinity, undergo to a phase change, or alter their morphology upon exchange or removal of guests.[33]

In the mid-1990s, the potential of polytopic carboxylate-based bridging ligands began to be explored, since carboxylic acids can be deprotonated for charge balance, precluding the need for extra-framework counterions, and can bind metals in a variety of ways, including monodentate fashion like the N-donor ligands (Scheme 1.3).[34] Within these ligands, benzene-1,4-dicarboxylate

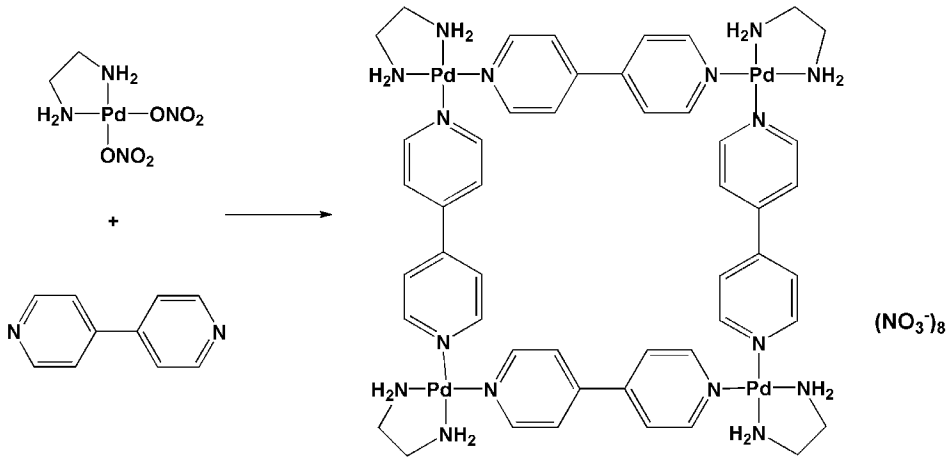

Figure 1.1. The construction of molecular squares achieved by using diethylamine as a capping agent in a Pd(II) complex.

(BDC^{2-}, Scheme 1.4), with a 180° angle between the two carboxylic groups, can form short bridges via one carboxylato end, thereby simultaneously linking up to four metal ions, or it forms long bridges via the benzene ring, leading to a great variety of structures. Therefore, these structures are often formed by in-situ generated inorganic clusters, SBUs, connected through long, aromatic bridges. These SBUs were and still are of particular interest in the MOF community, since they often possess multiple metal-oxygen coordination bonds that result in the generation of rigid nodes with fixed geometry and facilitate the formation of robust (and likely, permanently porous) 3D frameworks, as well as hold potential for open (or coordinatively unsaturated) metal sites that are of interest for various applications (i.e., gas storage and catalysis).[35]

Indeed, in 1999, two key microporous 3D MOFs were reported based on the assembly of polytopic carboxylates and metal-carboxylate clusters. The first of these MOFs, $[Cu_3(BTC)_2(H_2O)_3]$ (also called HKUST-1 or CuBTC)[36] contains Cu_2

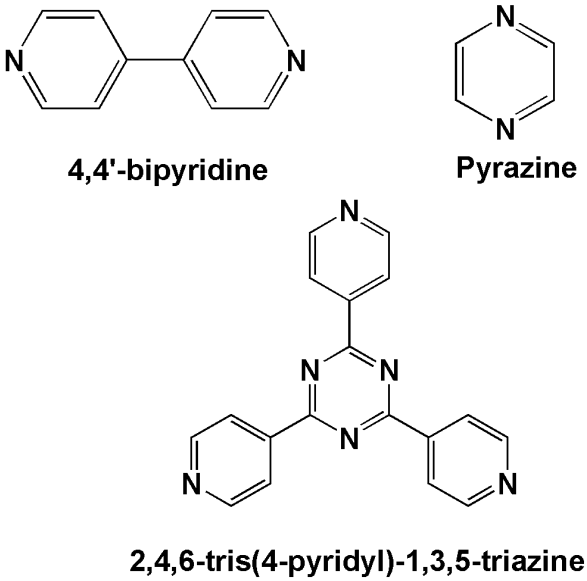

Scheme 1.2. Examples of neutral nitrogen-heterocycle bridging ligands for MOFs.

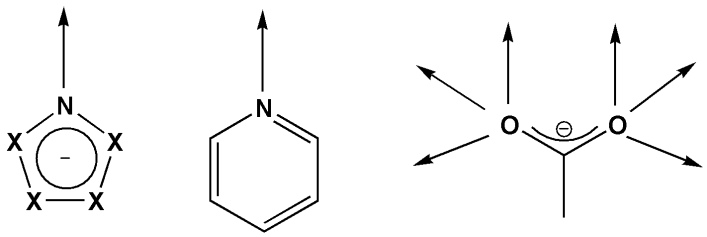

Scheme1.3. Comparison of the typical coordination modes of azolates, pyridine, and carboxylate (X = C_H or N).

units coordinated by four carboxylate groups in the paddle-wheel structure of copper acetate (Figure 1.2) and the tritopic ligand, 1,3,5-benzenetricarboxylic acid (BTC), that possesses three-fold symmetry (trigonal).[37] The overall framework is neutral and possesses large openings and cavities. As in other MOFs, the aqua ligands bound to the axial sites on the paddlewheel cluster can be removed upon heating to provide open-metal sites or replaced by other terminal ligands (namely pyridine), while maintaining framework stability (*in air* up to 240 °C).

The second of these MOFs, $Zn_4O(BDC)_3(DMF)_8$ or MOF-5,[38] was constructed from basic zinc acetate clusters of general formula $Zn_4O(O_2CR)_6$ and octahedral symmetry, that were generated in situ, and linear BDC^{2-} to give a neutral 3D MOF that has now become the prototypical MOF with an open cubic-like network topology (Figure 1.3). The apparent Langmuir surface area was estimated at $2900 m^2/g$, which was higher than that of most zeolites and the density (0.59 g/cm^3) was among the lowest recorded for any crystalline material.

Based on the $\{Zn_4O\}$ building units of MOF-5, a series of cubic iso-reticular MOF structures, IR-MOF-*n* (*n* = 1-16), with larger tunable pore sizes ranging from 3.8 to 29 Å, specific pore volumes up to 1 $cm^3 g^{-1}$ and, thus, very high porosity, has been synthesized by Yaghi et al.[39] These materials were obtained using the geometric concept of *isoreticular synthesis* with coordinated metal ions in the so-called secondary building units (SBUs) $\{Zn_4O\}$ and the organic carboxylate linkers shown in Scheme 1.5. Another exceptional example from Yaghi and coworkers is MOF-177. This porous framework has been reported in 2004 from the assembly of the tetranuclear basic zinc acetate cluster and 1,3,5-benzenetribenzoate (BTB, Scheme 1.4) and had the highest observed surface area (i.e., $4500 m^2/g$ using the Langmuir model) of any porous material at the time, up to ~5 times higher than the most open inorganic zeolite (Figure 1.4).[40]

In addition to the tetranuclear basic zinc acetate cluster $\{Zn_4O\}$ and the previously mentioned dinuclear paddlewheel cluster, there are a variety of

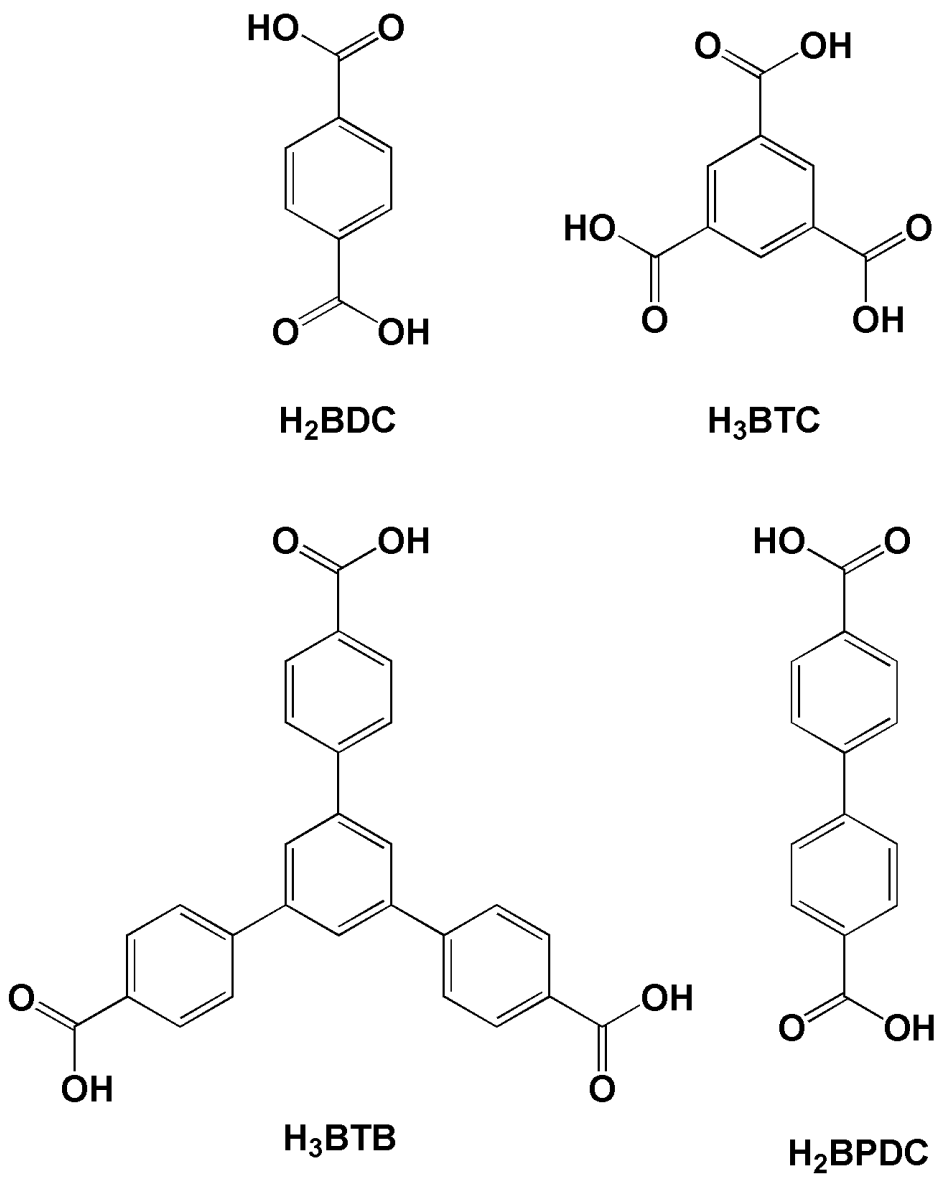

Scheme 1.4. Examples of carboxylate-based organic ligands. H_2BDC: benzene-1,4-dicarboxylic acid; H_3BTC: benzene-1,3,5-tricaboxylic acid; H_3BTB: 1,3,5-Tri(4-carboxyphenyl) benzene; H_2BPDC: 4,4'-biphenyldicarboxylic acid.

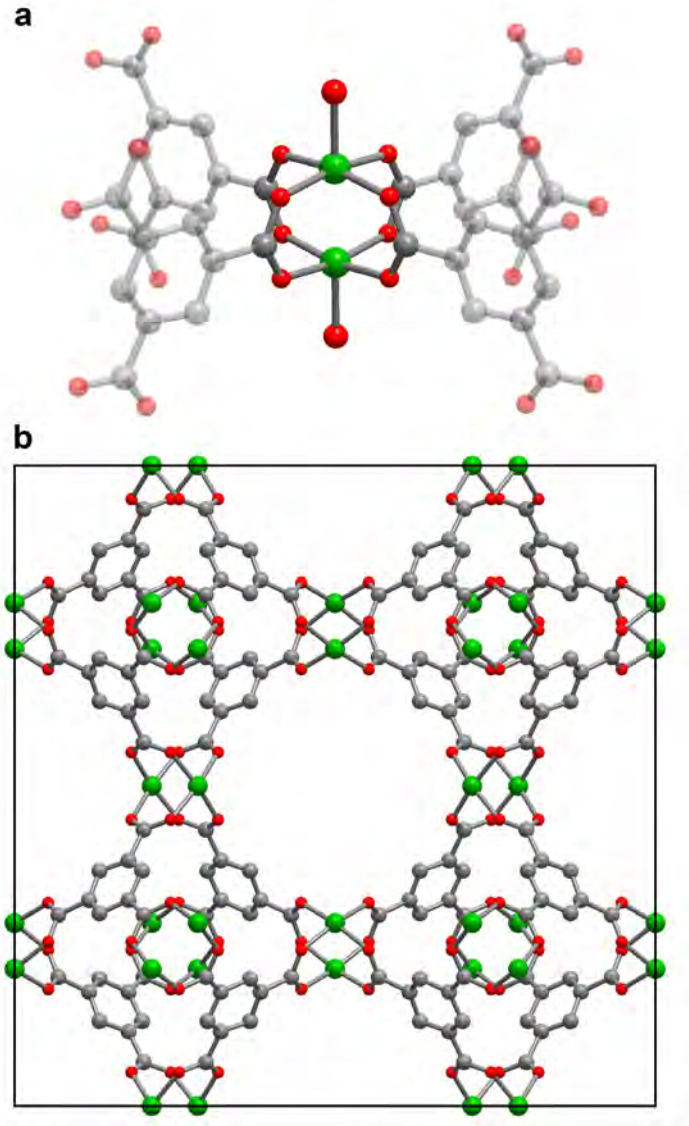

Figure 1.2. a) $\{Cu_2(BTC)_4\}$ paddlewheel building unit and b) packing diagram with the cubic unit cell of 3D-$[Cu_3(BTC)_2(H_2O)_3]$ (HKUST-1, a = 26.34 Å, from Ref. 36). The disordered water molecules in the pores are not shown, nor are the H atoms in the packing diagrams. Copper, green; oxygen, red; carbon, gray.

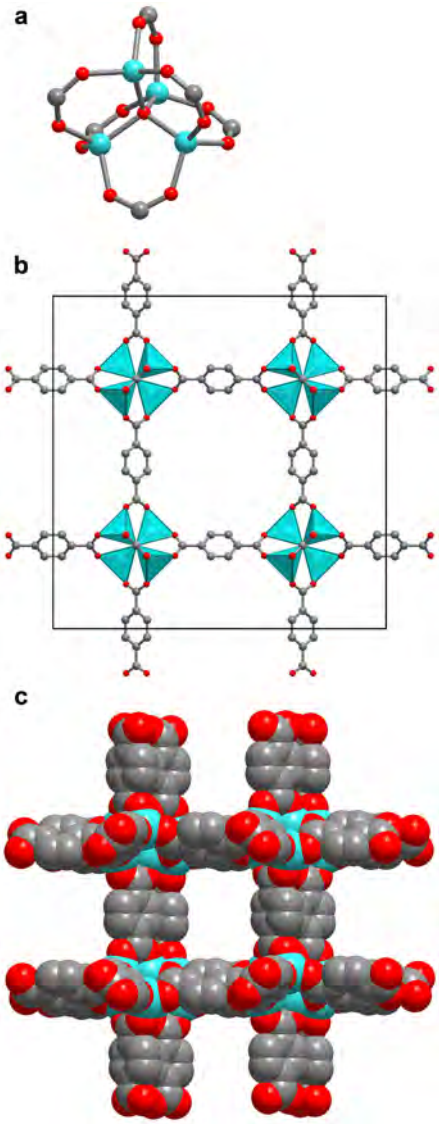

Figure 1.3. a) Ball-and-stick presentation of the tetrahedral $\{Zn_4O\}$ secondary building unit with the carboxylate groups which span the edges of the $\{Zn_4O\}$ tetrahedron in an octahedral fashion; b) the crystal structure packing diagram as ball-and-stick, with polyhedral $\{Zn_4O\}$ and c) space-filling representation for MOF-5 (IRMOF-1), 3D-$[Zn_4O(BDC)_3]$, from Ref. 38. Zinc, light blue; oxygen, red; carbon, gray.

metalcarboxylate clusters that have been and can be targeted successfully as SBUs in MOFs, including trinuclear clusters (e.g., $M_3O(O_2CR)_6L_3$, e.g. basic chromium acetate, where L are ancillary terminal ligands).[41] These SBUs offer building blocks of various geometries and, thus, shapes to utilize in the construction of MOFs based on nets comprised of nodes of a particular geometry corresponding to the SBU (Figure 1.5). This strategy has permitted the construction of robust, very open MOFs: a good examples are the MIL-n type (for Materials Institute Lavoisier) materials by Férey et al. These frameworks were derived using trivalent cations, such as vanadium(III), chromium(III) and iron(III), extended with the use of the p-elements such as aluminium(III), gallium(III) or indium(III). Important MIL-type structures like 3D-[M(μ_4-BDC)(μ-OH)], MIL-53 (Figure 1.6), consist of M = Al-, Cr- or Fe-terephthalate.[42] The framework of MIL-53 is highly flexible and it can assume different shapes depending on the strong host–guest interaction. Moreover, MIL-100 and MIL-101, with unusually large pore volumes were reported in 2004 and 2005 from the assembly of trinuclear $Cr_3O(O_2CR)_6L_3$ clusters (Figure 1.7) were L is BDC^{2-} or BTC^{3-} ligands, respectively, with the latter having a very high Langmuir surface area of 5900 ± 300m^2/g.[43]

Recently, metal-azolate frameworks (MAF), have emerged as a new class of coordination polymers promising for crystal engineering an materials science, because azolate ligands have the advantage of strong and directional coordination ability in bridging metal ions. Within metal-azolate frameworks, two type of very interesting class of materials have been (and are) widely studied. The zeolitic-imidazolate series of MOFs, called as ZIFs, has been synthesized by Yaghi and coworkers in 2006, Figure 1.8.[44] The similarity of coordination geometries between tetrahedral metal imidazolate and aluminosilicates has been recognized for long time. Indeed, zeolitic imidazolate frameworks (ZIFs; termed ZIF-1 to -12) have been synthesized as single crystals by copolymerization of either

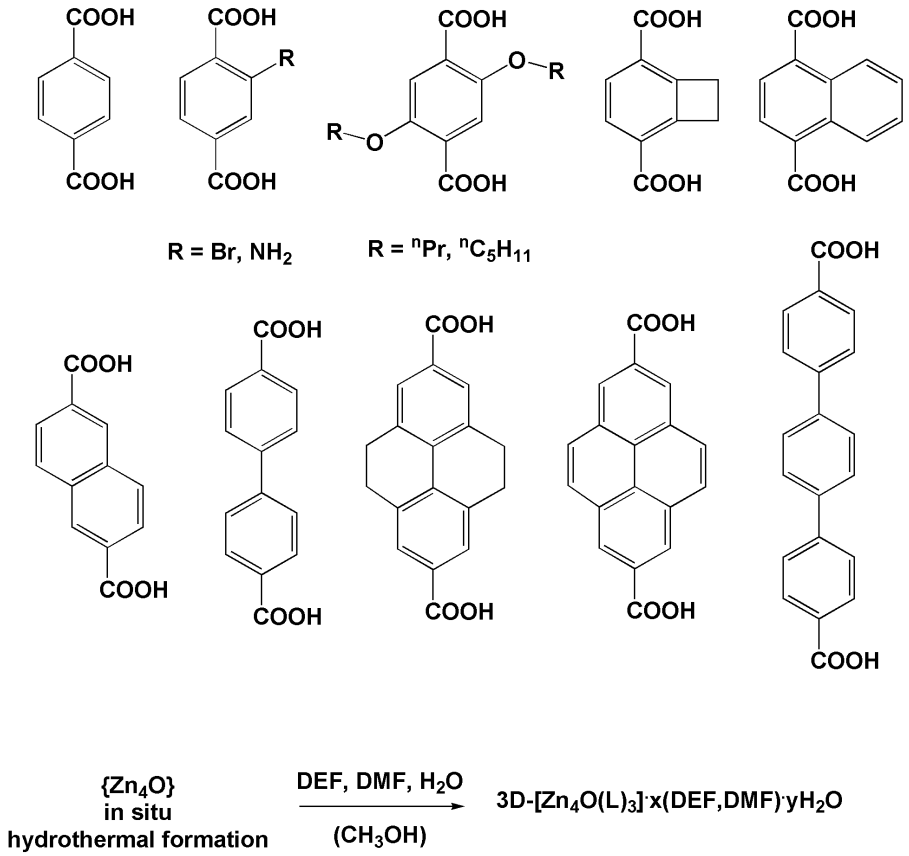

Scheme 1.5. Terephthalate-type linkers (L) used for the construction of the IR-MOF-n (n = 1–16) series, that is 3D-$[Zn_4O(L)_3]\cdot x$(def, dmf)$\cdot yH_2O$ (def = diethylformamide and dmf = dimethylformamide).

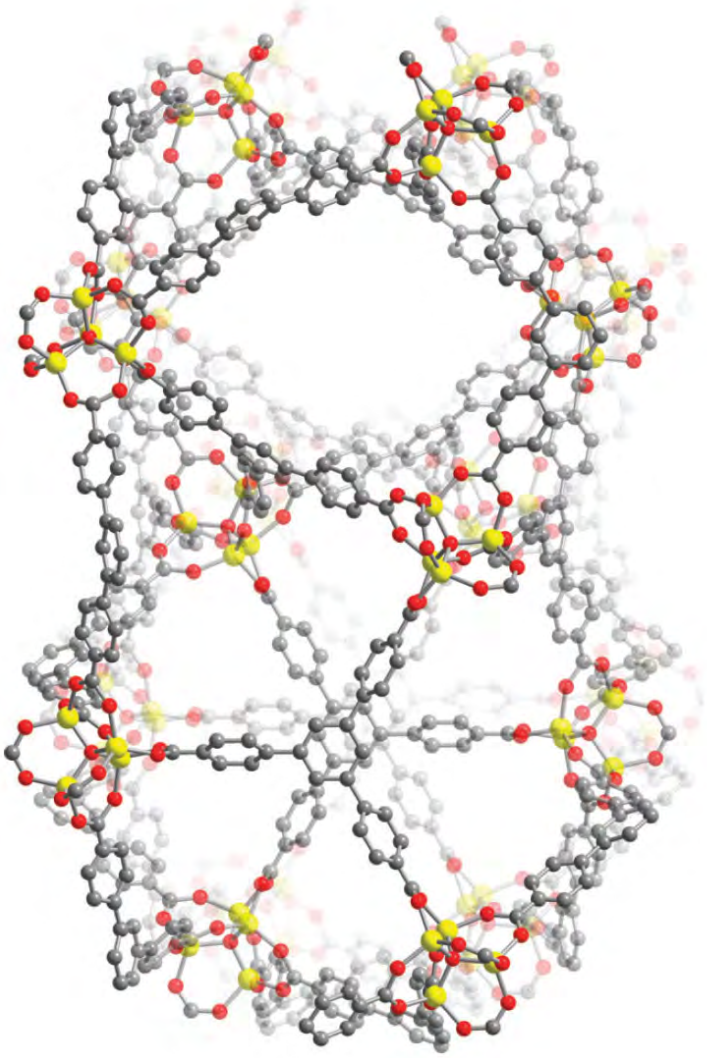

Figure 1.4. A portion of the crystal structure of $Zn_4O(BTB)_3$ (MOF-177). Yellow, gray, and red spheres represent Zn, C, and O atoms, respectively; H atoms are omitted for clarity. The structure consists of six diamond-shaped channels (upper), with a diameter of 10.8 Å, surrounding a pore containing eclipsed BTB^{3-} moieties (lower). For the latter, the separation between the central benzene rings of BTB^{3-} can accommodate a sphere with a diameter of 11.8 Å.

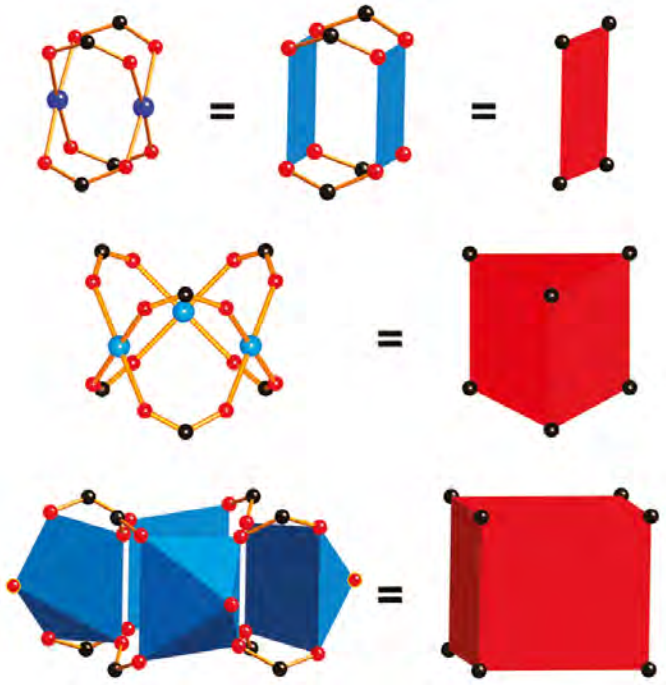

Figure 1.5. SBUs with two, three, or four square planar or square pyramidal units.

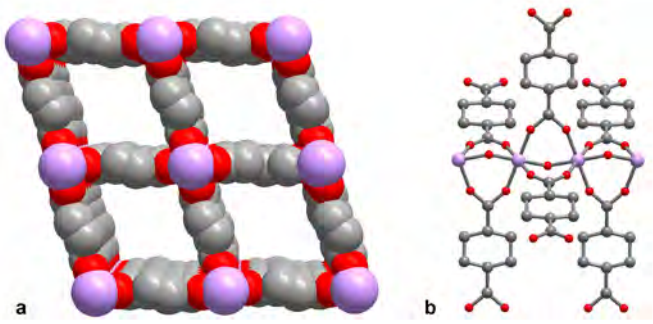

Figure 1.6. a) Packing diagram of 3D-[M(μ_4-bdc)(μ-OH)] (M = Cr, Fe, and Al), MIL-53 and b) terephthalato- and hydroxo-bridged metal strand as a subunit, from Ref. 42f. Chromium, pink; oxygen, red; carbon, gray.

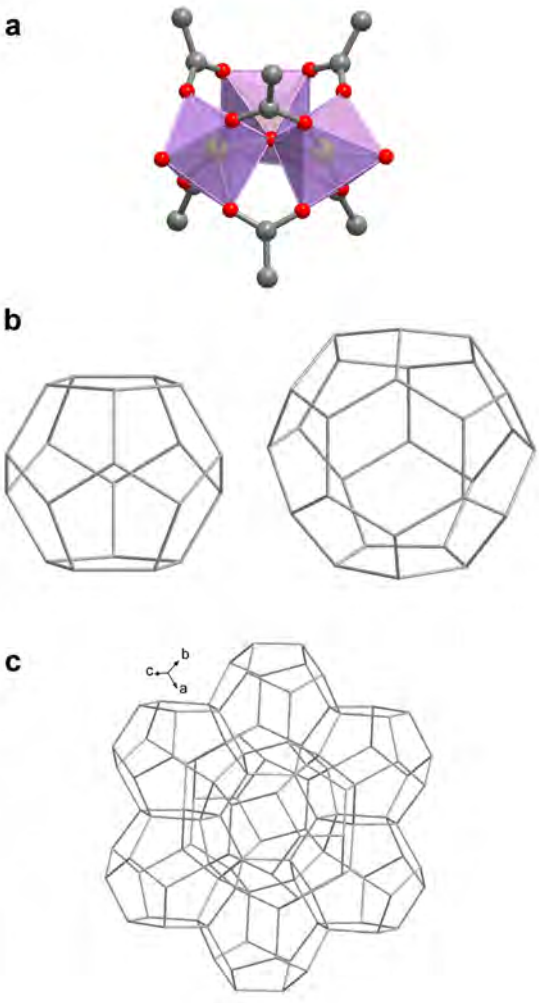

Figure 1.7. a) ball-and-stick rapresentation of the trigonalprismatic $\{Cr_3(O)(H_2O)_2\}$ secondary building unit in MIL-101 with the carboxylate groups that bridge between the Cr octahedra, from Ref. 43b. Chromium, pink; oxygen, red; carbon, gray. b) Cages in MIL-100 and MIL-101, Left, pentagon dodecahedron (Internal diameter: MIL-100, 25 Å; MIL-101, 29 Å); Right, polyhedron (Internal diameter: MIL-100, 29 Å, MIL-101, 34 Å). c) Structure of MIL-100 and MIL-101 represented with the centres of the trigonalprismatic SBUs as the vertices and connections between the SBUs as straight lines. Connectivity between the two different types of cages illustrated.

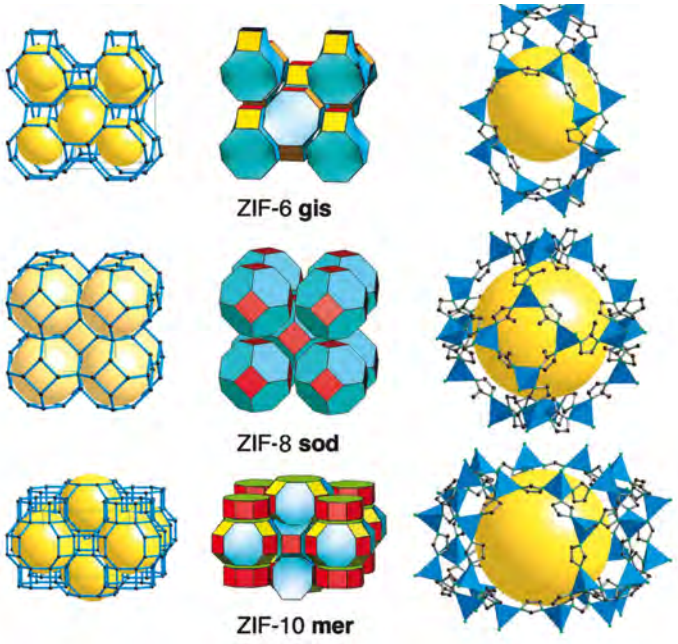

Figure 1.8. Three of the 12 ZIFs structures. In each row, the net is shown as a stick diagram (*Left*) and as a tiling (*Center*). The largest cage in each ZIF is shown with ZnN_4 tetrahedra in blue (*Right*), from Ref. 44. H atoms are omitted for clarity.

Zn(II) (ZIF-1 to -4, -6 to -8, and -10 to -11) or Co(II) (ZIF-9 and -12) with imidazolate-type links. The ZIF crystal structures are based on the nets of seven distinct aluminosilicate zeolites: tetrahedral Si(Al) and the bridging O are replaced with transition metal ion and imidazolate link, respectively. One exceptional example of the ZIFs series is the sodalite-type $Zn(mim)_2$ [ZIF-8, H_2mim = 2-methylimidazole, Figure 1.8]. This material has been exceptionally studied due to its high stability (T_d = 420 °C in air and stable up to 1 day in boiling water) and porosity and is also one of the few commercialized metal-organic frameworks by Sigma-Aldrich. ZIF-8 contains a large 3D intersecting channel

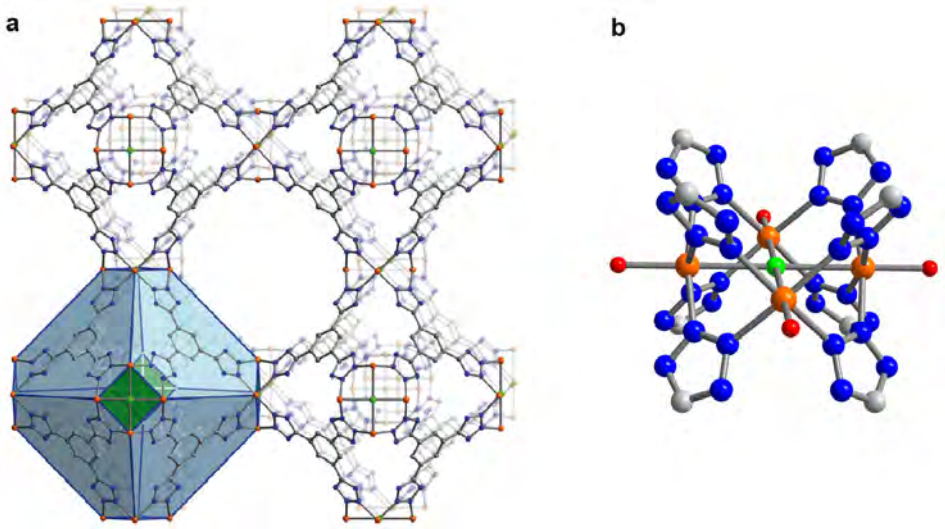

Figure 1.9. a) Cube of eight sodalite cage-like unit encasing a $[Mn(DMF)_6]^{2+}$ complex sharing square Mn_4Cl faces. And square-planar Mn_4Cl cluster surrounded by eight tetrazolate rings, from Ref. 45. Hydrogen atoms and solvent molecules are omitted for clarity. Manganese, orange; chlorine, green; oxygen, red; carbon, gray; nitrogen, blue.

system composed of large cavities (d = 11.4 Å) and small apertures (d = 3.2 Å). As completely lined with methyl groups and aromatic rings, its pore surface is highly hydrophobic and inert.

The second, important, series of azolate-based frameworks has been proposed by Long et al. This group have constructed a series of highly porous frameworks in which cubic clusters of general formula $[M_4Cl(ttz)_8(Solv)_4]$, [M = Mn^{2+}, Cu^{2+}, Fe^{2+}, Ni^{2+}; ttz = tetrazole] are connected through different triangular polytetrazolate ligands.[45] Among the azolate-based metal-organic frameworks of this type, $Mn_3[(Mn_4Cl)_3(BTT)_8]_2 \cdot 20MeOH$, [Mn-BTT, H_3BTT

= 1,3,5-tris(2H-tetrazol-5-yl)benzene], Figure 1.9, a rigid high-surface area framework with an expanded sodalite-like structure and exposed Mn^{2+} sites, exhibited a high H_2 binding affinity, and Lewis acid catalytic activity. Unfortunately, the low thermal stability characteristic of tetrazoles results in a framework with a very low decomposition temperature (T_{dec} < 200 °C). The water-sensitivity of this framework limits its utility in practical applications. In the quest for analogous structures with increased stability, a isolelectronic and isosteric triangular polytriazolate ligand of formula $H_3[(Cu_4Cl)_3(BTTri)_8]$ (Cu-BTTri, H_3BTTri = 1,3,5-tris(1*H*-1,2,3-triazol-5-yl)benzene), has been synthesized. With improved thermal stability (T_{dec} = 270 °C), this compound exhibits substantial chemical resistance, retaining its porous structure in a diluted HCl solution (pH 3) at room temperature or in boiling water for 3 days. Moreover, its stability in basic media enabled grafting of ethylenediamine on the open Cu^{2+} sites, leading to a record heat of CO_2 adsorption for a metal-organic framework.[46] In Chapter 6, a new framework of the same series, in which the cubic clusters are connected through triangular pyrazolate-based linkers, showing an even higher chemical and thermal stability, is presented.

Conclusions

Regarding the chemistry of hybrid porous materials, Gerard Férey said, in one of his review,[5] "In my opinion, the only limitation is the imagination of researchers". This is particularly true if we look at the incredibly high pace with which this class of materials is growing with application in many, diverse, fields that also reach domains usually reserved to other disciplines like solid state chemistry, physics, life sciences, etc.

This introduction has been written just to give a general overview on the chemistry and on the most important structures of metal-organic frameworks, indeed, no detailed description of the numerous applications in which these

materials are involved has been provided. However, in the next Chapters, the current trends and status of MOFs applications are discussed, in order to help the reader at looking at the presented results in a global view of the recent literature.

The work presented in this thesis has been also possible thanks to many people involved in: first of all, the Inorganic Chemistry Groups of Doctor Angelo Maspero and Professor Norberto Masciocchi at the Università degli Studi dell'Insubria in Como (Italy). Other partners of this project are international universities were I personally developed my work during a stay in different research groups. Indeed, a large part of this work was done at the University of Granada (Spain), under the supervision of Professor Jorge A. R. Navarro and at the University of California, Berkeley, working in the inorganic chemistry laboratory of Professor Jeffrey R. Long (USA). Moreover, fruitful collaborations with the groups of Professors Silvia Bordiga and Carlo Lamberti of the University of Torino (Italy) allow us to increase either the number of different techniques used for the investigation of these porous materials and the knowledge on the features of this new class of MOFs.

References and Notes

1 Yaghi, O. M.; Li, H. L. *J. Am. Chem. Soc.* **1995**, *117*, 10401.

2 Long, J. R.; Yaghi, O. M. *Chem. Soc. Rev.* **2009**, *38*, 1213. Editorial to the 2009 Metal–organic framework issue.

3 BASOLITE MOF at *www.sigma-aldrich.com* or at *www.mof.basf.com*.

4 (a) Eddaoudi, M.; Kim, J.; Rosi, N.; Vodak, D.; Wachter, J.; O'Keeffe, M.; Yaghi, O. M. *Science* **2002**, *295*, 469. (b) Zhao, D; Timmons, D. J.; Yuan, D.; Zhou, H.-C. *Acc. Chem. Res.* **2011**, *44*, 123.

5 Férey, G. *Chem. Soc. Rev.* **2008**, *37*, 191.

6 Chae, H. K.; Siberio-Perez, D. Y.; Kim, J.; Go, Y.; Eddaoudi, M.; Matzger, A. J.; O'Keeffe, M.; Yaghi, O. M. *Nature* **2004**, *427*, 523.

7 Férey, G.; Mellot-Draznieks, C.; Serre, C.; Millange, F.; Dutour, J.; Surble, S.; Margiolaki, I. *Science* **2005**, *309*, 2040.

8 Koh, K.; Wong-Foy, A. G.; Matzger, A. J. *J. Am. Chem. Soc.* **2009**, *131*, 4184.

9 Ma, S.; Zhou, H.-C. *Chem. Commun.* **2010**, *46*, 44.

10 D'Alessandro, D. M.; Smit, B.; Long, J. R. *Angew. Chem., Int. Ed.* **2010**, *49*, 6058.

11 (a) Zhang, W.; Xiong, R.-G. *Chem. Rev.* **2012**, DOI: 10.1021/cr200174w. (b) Kobayashi, Y.; Jacobs, B.; Allendorf, M. D.; Long, J. R. *Chem. Mater.* **2010**, *22*, 4120.

12 Cui, Y.; Yue, Y.; Qian, G.; Chen, B. *Chem. Rev.* **2012**, DOI: 10.1021/cr200101d.

13 (a) Horcajada, P.; Gref, R.; Baati, T.; Allan, P. K.; Maurin, G.; Couvreur, P.; Férey, G.; Morris, R. E.; Serre, C. *Chem. Rev.* **2012**, DOI: 10.1021/cr200256v. (b) Della Rocca, J.; Liu, D.; Lin, A. W. *Acc. Chem. Res.* **2011**, *44*, 957.

14 Farrusseng, D.; Aguado, S.; Pinel, C. *Angew. Chem., Int. Ed.* **2009**, *48*, 7502.

15 Yoon, M.; Srirambalaji, R.; Kim, K. *Chem. Rev.* **2012**, DOI: 10.1021/cr2003147.

16 (a) Kurmoo, M. *Chem. Soc. Rev.* **2009**, *38*, 1353. (b) Dechambenoit, P.; Long, J. R. *Chem. Soc. Rev*. **2011**, *40*, 3249.

17 (a) Kreno, L. E.; Leong, K.; Farha, O. K.; Allendorf, M.; Van Duyne, R. P.; Hupp, J. T. *Chem. Rev.* **2012**, DOI: 10.1021/cr200324t. (b) Wang, C.; Zhang, T.; Lin, W. *Chem. Rev*. **2012**, DOI: 10.1021/cr200252n.

18 (a) He, J.; Yin, Y. G.; Wu, T.; Li, D.; Huang, X. C. *Chem. Commun.* **2006**, 2845. (b) Zhang, J. P.; Horike, S.; Kitagawa, S.; *Angew. Chem., Int. Ed.* **2007**, *46*, 889. (c) Zhang, J. P.; Kitagawa, S. *J. Am. Chem. Soc.* **2008**, *130*, 907. (d) Choi, H. J.; Dincă, M.; Dailly, A.; Long, J. R. *J. Am. Chem. Soc.* **2008**, *130*, 7848.

19 O'Keeffe, M. *Chem. Soc. Rev.* **2009**, *38*, 1215.

20 (a) Stock, N.; Biswas, S. *Chem. Rev.* **2012**, DOI: 10.1021/cr200304e. (b) Meek, S. T.; Greathouse, J. A.; Allendorf, M. D. *Adv. Mater.* **2011**, *23*, 249. (c) Walton, R. I. *Chem. Soc. Rev.* **2002**, *31*, 230. (d) Klinowski, J.; Almeida Paz, F. A.; Silva, P.; Rocha, J. *Dalton Trans.* **2011**, *40*, 321. (e) Cohen, S. M. *Chem. Rev.* **2012**, DOI: 10.1021/cr200179u.

21 Sumida, K.; Horike, S.; Kaye, S. S.; Herm, Z. R.; Queen, W. L; Brown, C. M.; Grandjean, F.; Long, G. J.; Dailly, A.; Long, J. R. *Chem. Sci.* **2010**, *1*, 184.

22 Lipowski, J. *Inclusion Compounds: Structural Aspects of Inclusion Compounds Formed by Inorganic and Organometallic Host Lattices*; In Atwood, J. L.; Davies, J. E. D.; MacNicol, D. D., Eds., Academic Press: London, **1984**, pp. 59–103 and references therein.

23 Iwamoto, T.; Nakano, T.; Morita, M.; Miyoshi, T.; Miyamoto, T.; Sasaki, Y. *Inorg. Chim. Acta* **1968**, *2*, 313.

24 Dunbar, K. R.; Heintz, R. A. *Prog. Inorg. Chem.* **1997**, *45*, 283.

25 (a) Hoskins, B. F.; Robson, R. *J. Am. Chem. Soc.* **1989**, *111*, 5962. (b) Hoskins, B. F.; Robson, R. *J. Am. Chem. Soc.* **1990**, *112*, 1546. (c) Gable, R. W.; Hoskins, B. F.; Robson, R. *J. Chem. Soc. Chem. Commun.* **1990**, 1677.

26 (a) Fujita, M.; Kwon, Y. J.; Washizu, S.; Ogura, K. *J. Am. Chem. Soc.* **1994**, *116*, 1151. (b) Lu, J.; Paliwala, T.; Lim, S. C.; Yu, C.; Niu, T.; Jacobson, A. J. *Inorg. Chem.* **1997**, *36*, 923. (c) Subramanian, S.; Zaworotko, M. J. *Angew. Chem. Int. Ed. Engl.* **1995**, *34*, 2127. (d) Carlucci, L.; Ciani, G.; Prosperio, D. M.; Sironi, A. *J. Chem. Soc. Chem.*

Commun. **1994**, 2755. (e) Yaghi, O. M.; Richardson, D. A.; Li, G.; Davis, C. E.; Groy, T. L. *Mater. Res. Soc. Symp. Proc.* **1995**, *371*, 15.

27 See, e.g.: Fujita, M.; Tominaga, M.; Hori, A.; Therrien, B. *Acc. Chem. Res.* **2005**, *38*, 369.

28 Kondo, M.; Shimamura, M.; Noro, S.-I.; Yoshitomi, T.; Minakoshi, S.; Kitagawa, S. *Chem. Lett.* **1999**, 285.

29 Cussen, E. J.; Claridge, J. B.; Rosseinsky, M. J.; Kepert, C. J. *J. Am. Chem. Soc.* **2002**, *124*, 9575.

30 (a) Zheng, L.-M.; Yin, P.; Xin, X.-Q. *Inorg. Chem.* **2002**, *41*, 4084. (b) Li, J.-M.; Zhang, Y.-G.; Chen, J.-H.; Rui, L.; Wang, Q.-M.; Wu, X.-T. *Polyhedron* **2000**, *19*, 1117. (c) Li, J.-M.; Zhang, Y.-G.; Chen, J.-H.; Wang, Q.-M.; Wu, X.-T. *Chem. Commun.* **1997**, 1213. (d) Lu, J. Y.; Cabrera, B. R.; Wang, R.-J.; Li, J. *Inorg. Chem.* **1999**, *38*, 4608. (e) Tong, M.-L.; Chen, X.-M.; Yu, X.-L.; Mak, T. C. W. *J. Chem. Soc., Dalton Trans.* **1998**, 5.

31 (a) Inman, C.; Knaust, J. M.; Keller, S. W. *Chem. Commun.* **2002**, 156. (b) Subramanian, S.; Zawarotko, M. *Angew. Chem., Int. Ed. Engl.* **1995**, *34*, 2127. (c) Lightfoot, P.; Snedden, A. *J. Chem. Soc., Dalton Trans.* **1999**, 3549.

32 Kondo, M.; Yoshitomi, T.; Seki, K.; Matsuzaka, H.; Kitagawa, S. *Angew. Chem., Int. Ed. Engl.* **1997**, *36*, 1725.

33 Kitagawa, S.; Kondo, M. *Bull. Chem. Soc. Jpn* **1998**, *71*, 1739.

34 Eddaoudi, M.; Li, H.; Reineke, T. M.; Fehr, M.; Kelley, D. G.; Groy, T. L.; Yaghi, O. M. *Top Catal.* **1999**, *9*, 105.

35 (a) Vitillo, J. J.; Regli, L.; Chavan, S.; Ricchiardi, G.; Spoto, G.; Dietzel, P. D. C.; Bordiga, S.; Zecchina, A. *J. Am. Chem. Soc.* **2008**, *130*, 8386. (b) Llabrés i Xamena, F. X.; Abad, A.; Corma, A.; Garcia, H. *J. of Catal.* **2007**, *250*, 294.

36 Chui, S. S. -Y.; Lo, S. M. -F.; Charmant, J. P. H.; Orpen, A. G.;Williams, I. D. *Science* **1999**, *283*, 1148.

37 Other syntheses of CuBTC: (a) Wang, Q. M.; Shen, D.; Bulow, M.; Lau, M. L.; Deng, S.; Fitch, F. R.; Lemcoff, N. O.; Semanscin, J. *Microporous Mesoporous Mater.* **2002**,

55, 217. (b) Schlichte, K.; Kratzke, T.; Kaskel, S. *Microporous Mesoporous Mater.* **2004**, *73*, 81.

38 Li, H.; Eddaoudi, M.; O'Keeffe, M.;Yaghi, O. M. *Nature* **1999**, *402*, 276.

39 (a) Eddaoudi, M.; Kim, J.; Rosi, N.; Vodak, D.; Wachter, J.; O'Keeffe, M.; Yaghi, O. M. *Science* **2002**, *295*, 469. (b) Tranchemontagne, D. J.; Mendoza-Cortés, J. L.; O'Keefe, M.; Yaghi, O. M. *Chem. Soc. Rev.* **2009**, *38*, 1257.

40 Chae, H. K.; Siberio-Perez, D. Y.; Kim, J.; Go, Y. B.; Eddaoudi, M.; Matzger, A. J.; O'Keeffe, M.; Yaghi, O. M. *Nature* **2004**, *427*, 523.

41 (a) Li, H.; Davis, C. E.; Groy, T. L.; Kelley, D. G.; Yaghi, O. M. *J. Am. Chem. Soc.* **1998**, *120*, 2186. (b) Seo, J. S.; Whang, D.; Lee, H.; Jun, S. I.; Oh, J.; Jeon, Y. J.; Kim, K. *Nature* **2000**, *404*, 982. (c) Sudik, A. C.; Cote, A. P.; Yaghi, O. M. *Inorg. Chem.* **2005**, *44*, 2998. (d) Ma, S.;Wang, X.; Manis, E. S.; Collier, C. D.; Zhou, H. *Inorg. Chem.* **2007**, *46*, 3432. (e) Liu, Y.; Eubank, J. F.; Cairns, A. J.; Eckert, J.; Kravtsov V.Ch.; Luebke R.; Eddaoudi, M. *Angew. Chem. Int. Ed.* **2007**, *46*, 3278.

42 (a) Barthelet, K.; Riou, D.; Férey, G. *Chem. Commun.* **2002**, 1492. (b) Serre, C.; Millange, F.; Surblé, S.; Férey, G. *Angew. Chem. Int. Ed.* **2004**, *43*, 6285. (c) Volkringer, C.; Loiseau, T. *Mater. Res. Bull.* **2006**, *41*, 948. (d) Serre, C.; Millange, F.; Thouvenot, C.; Nogues, M.; Marsolier, G.; Louer, D.; Férey, G. *J. Am. Chem. Soc.* **2002**, *124*, 13519. (e) Millange, F.; Guillou, N.; Walton, R. I.; Greneche, J.-M.; Margiolaki, I.; Férey, G. *Chem. Commun.* **2008**, 4732. (f) Millange, F.; Serre, C.; Férey, G. *Chem. Commun.* **2002**, 822.

43 (a) Férey, G.; Serre, C.; Mellot-Draznieks, C.; Millange, F.; Surble, S.; Dutour, J.; Margiolaki, I. *Angew. Chem. Int. Ed.* **2004**, *43*, 6296. (b) Férey, G.; Mellot-Draznieks, C.; Serre, C.; Millange, F.; Dutour, J.; Surble, S.; Margiolaki, I. *Science* **2005**, *309*, 2040.

44 (a) Huang, X. C.; Zhang, J. P.; Chen, X. M. Chin. Sci. Bull. 2003, 48, 1531. (b) Park, K. S.; Ni, Z.; Côté, A. P.; Choi, J. Y.; Huang, R.; Uribe-Romo, F. J.; Chae, H. K.; O'Keeffe, M.; Yaghi, O. M. *Proc. Natl. Acad. Sci. USA* **2006**, *103*, 10186.

45 Dincă, M.; Dailly, A.; Liu, Y.; Brown, C. M.; Neumann, D. A.; Long, J. R. *J. Am. Chem. Soc.* **2006**, *128*, 16876. (c) Dincă, M.; Han, W. S.; Liu, Y.; Dailly, A.; Brown, C. M.; Long,

J. R. *Angew. Chem. Int. Ed.* **2007**, *46*, 1419. (d) Dincă, M.; Long, J. R. *J. Am. Chem. Soc.* **2007**, *129*, 11172. (e) Dincă, M.; Dailly, A.; Tsay, C.; Long, J. R. *Inorg. Chem.* **2008**, *47*, 11. (f) Sumida, K.; Horike, S.; Kaye, S. S.; Herm, Z. R.; Queen, W. L.; Brown, C. M.; Grandjean, F.; Long, G. J.; Dailly, A.; Long, J. R. *Chem. Sci.* **2010**, *1*, 184. (g) Sumida, K.; Horike, S.; Bloch, E. D.; Foo, M. L.; Murray, L. J.; Long, J. R. *unpublished results*.

46 Demessence, A.; D'Alessandro, D. M.; Foo, M. L.; Long, J. R. *J. Am. Chem. Soc.* **2009**, *131*, 8784.

Chapter 2
On the nature of the pyrazole ring

Introduction

Of the more than 20 million chemical compounds currently registered, about one half contain heterocyclic systems.[1] Heterocycles are important for many reasons: because of their abundance, of course, but above all because of their chemical, biological and technological significance. Within heterocycles, azoles owe their importance to their occurrence in natural and synthetic molecules with biological activity but also to their fascinating coordination chemistry that has allowed their use in a wide range of applications.[2]

Although azoles are mostly known as bases (the protonated form is azolium cation), as pyridines, the five-membered azoles, including imidazole, pyrazole, triazole, and tetrazole (Figure 2.1) can also be deprotonated by using a base such as triethylamine, LDA or NaH, to form the corresponding azolate (or azolide) anion. The possibility of generating this azolate anions underlies the broad research activity in coordination chemistry, because not only it allows all N atoms to coordinate with metal ions in many different coordination modes, but also further increases the basicity of these donor sites. Consequently, azolate ligands can generate coordination compounds with a particularly high thermal

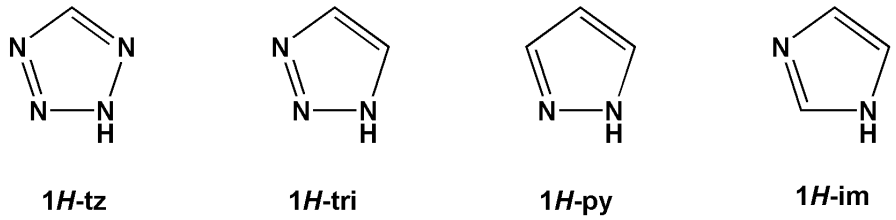

Figure 2.1. Azoles heterocycles rings: 1*H*-tetrazole (1*H*-tz); 1*H*-triazole (1*H*-tri); 1*H*-pyrazole (1*H*-pz) and 1*H*-imidazole (1*H*-im). Note that for triazole two isomers are possible, the 1,2,3-triazole and 1,2,4-triazole.

and chemical stability, which is one of the most important issues for practical applications of coordination polymers. Nevertheless, azolates have not been widely used as bridging ligands for coordination polymers before the beginning of the past decade. Possible reasons include the very short bridging length and difficulty of deprotonation of the ligand, as well as the ease of forming highly insoluble and intractable products. As a matter of fact, many coordination polymers containing pyrazoles precipitate in the form of highly insoluble crystalline powders, preventing to grow single crystals for their XRD structural investigation. In this field, state-of-the-art powder diffraction methods allow to unravel otherwise not accessible key structural aspects on simple crystalline powders.[3]

This chapter is focused mainly on the chemistry of pyrazoles, with an initial description of their nature, followed by a quick overview on the synthetic procedures for preparing 1H-pyrazoles. Finally, a description of some of the most common geometries adopted by the pyrazolate anions towards late transition metal ions will be reported.

The Pyrazole ring

Simple 1*H*-pyrazoles have a Lewis acid pyrrolic N-H group at *N*1, and a Lewis basic pyridine N-donor *N*2, directly adiacent to each other (Figure 2.1).

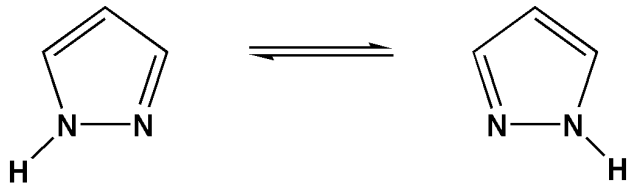

Figure 2.2. Prototropy in unsubstituted or symmetrical substituted 1*H*-pyrazoles.

Therefore, electronically, these heterocycles are both σ-donor and π-acceptor ligands and, as per their steric and electronic features, they are planar and non-bulky ligands.[4] Tautomeric prototropy (Figure 2.2) exists in the case of symmetrical substitution (including non-substitution) of the ring, unless the substituent is in position 1. For many pyrazoles, this has been found to be a fast process in solution at room temperature. However, with a combination of low temperature and polar aprotic solvents, it can be slowed down to the point that signals for the two tautomers can be separated and observed by NMR spectroscopy.

The pyrazole ring is one of the easiest and most flexible N-donor heterocycles to incorporate into larger polydentate ligand structures.[5-7] As brilliantly discussed in Trofimenko's numerous reviews,[6] tripodal "scorpionate" ligands with two or three pyrazol-1-yl groups linked by BH^-,[7] CH,[8] or another monoatomic bridge are particularly important as flexible protecting ligands that allow the steric environment of a metal ion to be controlled at will.

Also 1*H*-pyrazoles as isolated rings are remarkably flexible ligands in coordination chemistry.[9] Pyrazole itself and only a handful of its derivatives are commercially available, however, using different synthetic approaches, substituted pyrazole rings can be created with a variety of substituents at its carbon atoms

(alkyl, aryl, etc.). The preparations commonly used for the synthesis of substituted pyrazoles are thus described in the next section.

General methods for the preparation of pyrazoles

Pyrazoles, which can be used as ligands or as precursors of pyrazolate-based ligands, are, in general, accessible by well-established synthetic methods. These methods are quite general and allow the preparation of a variety of pyrazoles with different functionalities as substituents of the pyrazole ring. In the following some of the most common preparations are reported.

In 1898, H. Pechmann (1850-1902), a German chemist, after the discovery of diazomethane in 1894, developed the synthesis of pyrazole from acetylene and diazomethane.[10] In this process, diazomethane reacts with acetylene in a concerted [3+2] cycloaddition to give 3*H*-pyrazole which rapidly isomerizes to 1*H*-pyrazole (Scheme 2.1). Substitution at *C*3 and/or *C*5 adjacent to the nitrogen atoms is particularly straightforward to achieve, and can strongly affect the steric environment around the N-donors and any metal ion coordinated to them, thus inducing different crystal structures. Hydrazinolysis, an alternative strategy for the synthesis of pyrazoles, can be another way to control the substituents in this two positions. This preparation is a cyclocondensation of hydrazine and alkyl- or arylhydrazines with 1,3-dicarbonyl compounds (Scheme 2.2). Unsymmetrical 1,3-diketones give mixtures of structural isomers. The mechanism of this reaction will not be discussed here, but depends strongly on the nature of the substituent R as well as on the pH. Several simple 1,3-diketones, that can be converted to pyrazoles with the latter procedure, are commercially available. Many other 3{5}-alkyl or aryl pyrazole derivatives can be prepared in good yields on a multi-gram scale in two steps from an acyl precursor.[11] Yields are usually higher than 50% over the two steps, although the hydrazinolysis step sometimes has to be performed twice to go to completion.[12]

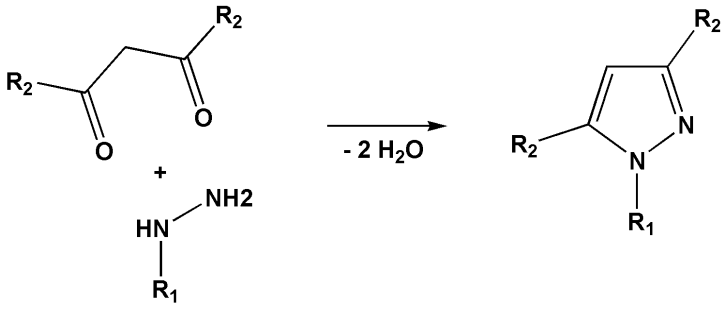

Scheme 2.1. Pechmann's reaction: concerted [3+2] cycloaddition between diazomethane and acetylene.

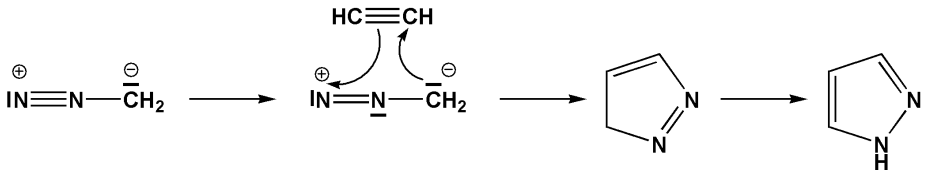

Scheme 2.2. Cyclocondensation reaction of hydrazine and alkyl- or arylhydrazines with 1,3-dicarbonyl compounds

Substitution of the pyrazole ring at position *C*4 can be achieved by cyclocondensation of hydrazine with a 2-substituted 1,3-diketone, previously obtained by following the Vilsmeier-Haack protocol (Scheme 2.3).[13] Worthy of note, the route to *C*4-substituted pyrazoles can be exploited for the synthesis of polytopic pyrazoles suitably designed for the construction of porous metal-organic frameworks.

N–H pyrazoles, once prepared, can also be halogenated at the *C*4-position, but other electrophiles may add to a nitrogen atom rather than, or as well as, to *C*4.[10]

To obtain quantitatively halogenations at the *C*4-position, the *N*-H of the pyrazole should be suitably protected in advance. Then, protected 4-iodopyrazoles can be good reagents for palladium-catalyzed cross-coupling reactions through a number of different pyrazolate-based ligands.[14]

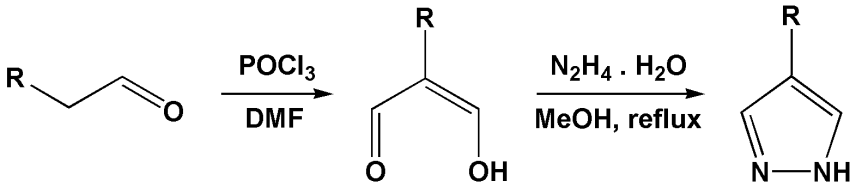

Scheme 2.3. Route for *C*4-substituted pyrazoles: the Vilsmeier-Haak reaction ($POCl_3$ in DMF) followed by hydrazinolysis.

1*H*-pyrazoles as ligands in coordination chemistry

Pyrazoles have attracted considerable interest mainly because their conjugate bases, pyrazolates (obtained by deprotonation of the N(1)-H bond with a base), have been found to bind metals in a variety of coordination modes and are also robust bridging ligands.[4-8,15] After deprotonation of the *N*-H pyrazole, the obtained pyrazolate anion can be classified to act mainly in three different coordination modes: the *mono*-dentate mode; the *exo*-bidentate (η^1-η^1) and the *endo*-bidentate (η^2) ones (Figure 2.3). This coordination ability or nucleophilicity is controlled by the nature of the metal ion and the substituents on the pyrazole ring. Substituents at the 3- and 5-positions can modify the steric properties, whereas substituents at the 4-position can mainly change the electronic properties.

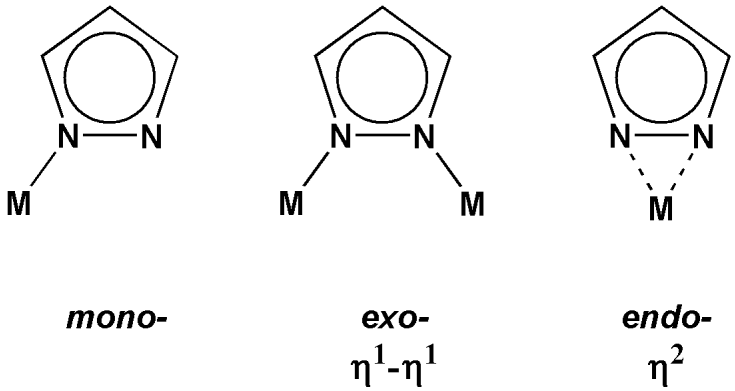

Figure 2.3. Common coordination modes for the pyrazolate anion.

Hereafter, the chemistry of the pyrazolate anion (pz^-) will be described with particular emphasis on its ability to act as a prototypical N,N-*exo*-bidentate ligand, thus favoring the construction of polynuclear metal complexes. However, monodentate, *endo*-bidentate and even more exotic coordination modes have been recently observed for substituted pyrazolate species, particularly when bulky substituents are present in the 3,5-positions,[16] or when lanthanides are employed.[17] Therefore, the ditopic nature and coordinative flexibility of the pyrazolate anion means that the pyrazole ring can be considered one of the most flexible ligand in coordination chemistry. With their exo-bidentate coordination mode, pyrazolate ligands have a strong tendency to act as bridges between two metal centers, with a rather small bridging angle (ca. 72°), which results in a metal-metal distance of 3.5-4.5 Å (depending on the ion radius).[14] Changes in the substituents of the pyrazole ring can induce changes in the intermetallic distances, hence controlling the functional properties of these coordination compounds. As a matter of fact, these materials generally posses interesting chemical and physical

properties for a wide range of applications, *e.g.* in medicine,[18] catalysis,[19] as liquid crystals and ionic liquids,[20] or as luminescent materials.[21] Moreover, modification of the distance between the metal ions can modify the ability of pyrazole in providing a pathway for magnetic exchange interactions.[4c,22]

Actually, pyrazolate derivatives are well explored as ligands for the construction of discrete, polynuclear complexes rather than coordination polymers. The variety of geometry is rather complex for coordination compounds containing the pyrazolate anion, whose coordination chemistry has greatly expanded over the past ten years. Therefore, this chapter does not intend to provide a comprehensive collection of the available literature on the subject, but will instead focus only on the description of different pyrazolate coordination complexes assuming distinguished geometries towards late transition metal ions. It should be anticipated that many of the geometries discussed hereafter have been chosen since they are comparable to the SBUs found in the porous polymers synthesized in this project, as it will be described in the next chapters.

Structural diversity of the pyrazolate anion complexes

The first report on the chemistry of a polymeric complex containing the exobidentate (1,2-dihapto)pyrazolate ligand has been known since 1889, when Buchner, in his paper,[23] reported the formation of a silver(I) complex, $[Ag(pz)]_n$, which he simply denoted as "silber salz". Due to its pronounced insolubility in the common organic solvents, and consequently, to the difficulty in growing suitable single crystals for XRD studies, the oligomeric or polymeric nature of Buchner's silver(I) complex was not clarified until the late '90s, when the possibility of solving simple structures of crystalline powdered samples from powder diffraction data became possible. At that time, a similar structure for $[Cu(pz)]_n$ was claimed on the basis of IR evidences,[24] and in 1994 the structures of $[Ag(pz)]_n$ and $[Cu(pz)]_n$ from ab initio powder diffraction analysis were reported.[25] In those

studies it has been established that both copper(I) and silver(I) pyrazolates, depending on the synthetic method used, could be isolated in two phases. The copper species with α-$[Cu(pz)]_n$ and β-$[Cu(pz)]_n$ formulations, contain infinite 1D chains of linearly coordinated copper atoms, bridged by exo-bidentate pyrazolate anions (Figure 2.4). The difference between these two structures was found to be the interchain Cu···Cu contacts which are 3.34 Å in α-$[Cu(pz)]_n$ and 2.97 Å in β-$[Cu(pz)]_n$, where 'dimeric' units were envisaged. At variance, the two $[Ag(pz)]_n$ phases contain 1D polymer and trimeric (cyclic) species, respectively.

Homoleptic pyrazolate comples of divalent and trivalent ions of the late transition with sterically unhindered pyrazoles also adopt 1D polymeric structures

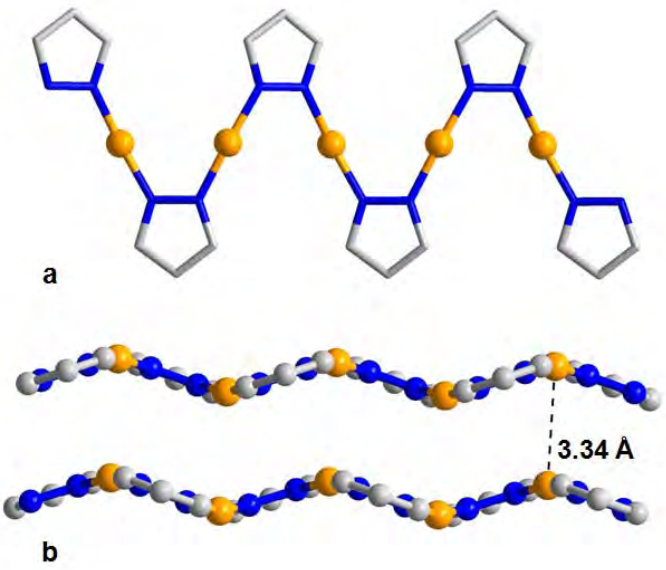

Figure 2.4. (a) Crystal structure of the infinite 1D chain of linear coordinate Cu(I) ions in α-$[Cu(pz)]_n$ and (b) the interchain Cu···Cu contacts found in its structural packing. Copper, orange; nitrogen, blue; carbon, light grey.

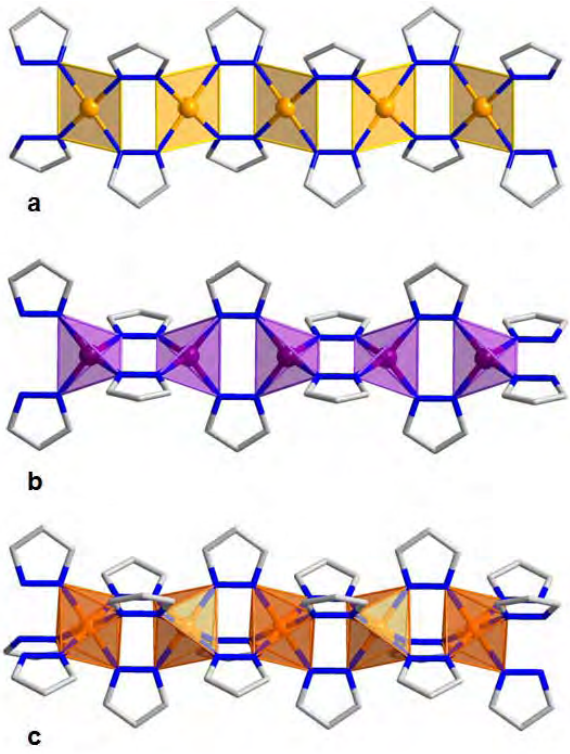

Figure 2.5. (a) Double zig-zag chain in $[Cu(\mu\text{-}pz)_2]$ highlighting the square planar geometry of Cu(II) ions. (b) Triple zig-zag chain of $[Co(\mu\text{-}pz)_2]$ with tetrahedral Co(II) ions and (c) Triple zig-zag chain of $[Fe(\mu\text{-}pz)_3]$ evidencing the octahedral geometry of Fe(III) ions. Copper, orange; Cobalt, purple; Iron, dark orange; nitrogen, blue; carbon, light grey.

as in $[M(\mu\text{-}pz)_2]$ (M^{2+} = Co^{2+}, Ni^{2+}, Cu^{2+}, Zn^{2+}, Cd^{2+}, Hg^{2+} and Fe^{2+}) and in $[M(\mu\text{-}pz)_3]$ (M^{3+} = Co^{3+} and Fe^{3+}).[26] Depending on the nature of the metal ion, *i.e.* on its coordination ability and charge, it is possible to observe double zig-zag chains formed by vertex-sharing $M_2(pz)_2$ units with square-planar or tetrahedral metal ions (FIGURE 2.5a-b). Even triple zig-zag chains with octahedral metal ions were observed (FIGURE 2.5c).

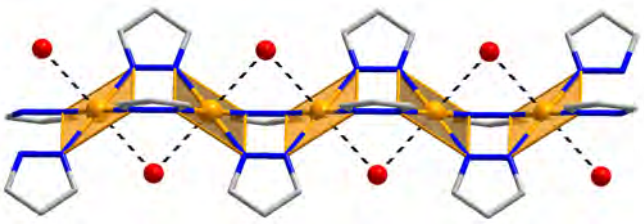

Figure 2.6. Crystal structure of [Cu(μ-pz)$_2$(μ-OH$_2$)] evidencing the weak contacts between guest water molecules and Cu(II) ions. Oxygen, red; copper, orange; nitrogen, blue; carbon, light grey, from ref. 25h.

The example of Cu(II) ions is interesting since it can adopt both square planar and tetrahedral geometries to form the two types of [Cu(μ-pz)$_2$] chains.[26h,f] It was recently demonstrated that one of these two polymorphs readily absorbs gaseous water, ammonia and organic solvent vapors to yield polycrystalline clathrates. The hydrate, *catena*-[Cu(μ-pz)$_2$(μ-OH$_2$)], was indeed structurally characterized and has been found to have weakly bound water molecules bridging the copper ions (Figure 2.6). An isostructural [Ni(μ-pz)$_2$] polymer was also isolated, but no adsorption activity was found, probably due to the lower Lewis acidity of the Ni(II) ion.[26h,f]

The small bridging angle of pyrazolates makes them suitable also for the construction of low-dimensional structures. Indeed, linear 2-coordinate univalent coinage-metal ions can form, other than 1D chains, trinuclear complexes. [M(R-pz)]$_3$ clusters [M = Cu(I), Ag(I), Au(I)] have been made with pyrazolate derivatives bearing many different substituent groups (Figure 2.7a).[27]

In cyclic trimers, the metal ions are 3.1-3.3 Å apart, which is consistent with intramolecular metallophilic interactions. In some cases, the distances between two trimeric units in a crystal structure are small, thus allowing the formation of

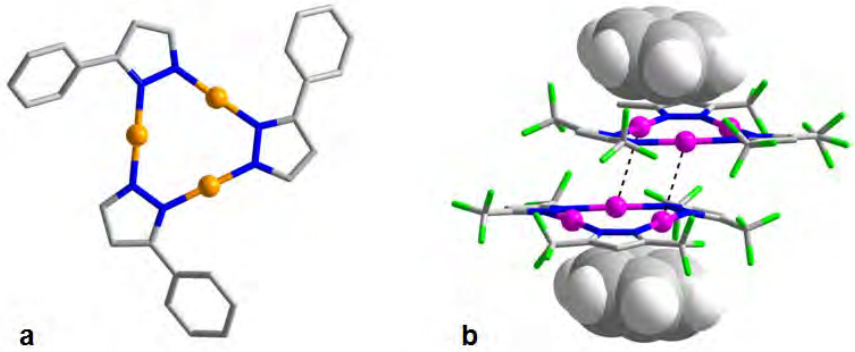

Figure 2.7. (a) Crystal structure of the trimer $[Cu(3\text{-}Phpz)]_3$ taken from ref. 28 and (b) Crystal structure of $\{Au[3,5\text{-}(CF_3)_2pz]\}_3$ showing dimerization of trimers with argentophilic interactions and formation of a of π-acid/base sandwich with benzene solvent from ref. 27k. Copper, orange; silver, purple; fluorine, green; nitrogen, blue; carbon, light grey, hydrogen, white.

dimers of trinuclear units.[27 e,g,i,28,29] Several $[M_3(\mu\text{-}pz)_3]$ trimers have a strong photoluminescence as single crystals or thin films, upon irradiation of UV light.[28e,f, 27i, 21a] As shown for different copper(I) compounds, the emission spectra vary substantially with emission of red, yellow, green or blue light depending on the use of different ligands.[21a] It was also demonstrated that these complexes possess interesting host-guest properties due to the close arrangement of three coordinatively unsaturated coinage-metal ions, which may interact, as well as through metallophilicity within each others, even with other molecules via π coordination or Lewis acid-base pairing (Figure 2.7b).[27m]

Copper(I) ions with pyrazolate ligands bearing two bulky substituents in positions 3- and 5- can afford cyclic trimers; although less common, tetramers have also been found.[30]

Pyrazolate complexes of platinum(II) and palladium(II) show a different behavior in their aggregation because these complexes are generally isolated only as cyclic trimers: no 1D polymeric structures of this metal ions are known (Figure 2.8).[31] These complexes are described with a general formula $[M_3(R\text{-}pz)_6]$, where the metal ions are coordinated in a square planar geometry. Even a mixed-valent $Pt^{III}_2Pt^{II}$ product can be formed by oxidation of the $[Pt_3(\mu\text{-}pz)_6]$ in the presence of $[NH_4]_2[Ce(NO_3)_6]$/KBr.[32]

It is noteworthy that, by introduction of some simple anions, also many high-symmetry polynuclear clusters can be produced with divalent Cu(II), Ni(II) and Co(II) ions. The tetranuclear cluster $[Co_4(\mu_4\text{-}O)\text{-}(\mu\text{-}dmpz)_6]$ is an example of heteroleptic cluster in which a μ_4-oxo unit is found at the center of an octahedron (Figure 2.9).[33] This molecular compound is structurally similar to those observed in the chemistry of carboxylate clusters. At variance, many pyrazolate-bridged clusters have never been observed with different

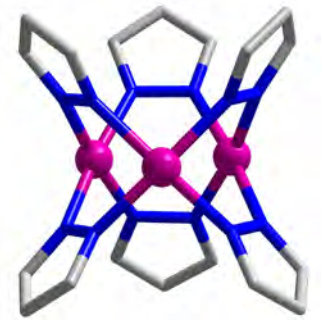

Figure 2.8. Crystal structure of the cyclic trimer $[Pd_3(\mu\text{-}pz)_6]$, with square planar Pd(II) ions, from ref. 31c. Palladium, purple; nitrogen, blue; carbon, light grey.

Figure 2.9. Crystal Structure of the heteroleptic cluster $[Co_4(\mu_4\text{-}O)\text{-}(\mu\text{-}dmpz)_6]$, dmpz = dimethyl pyrazole, from ref. 33. A tetranuclear core of tetrahedral Co(II) ions generates an octahedron in which a μ4-oxo unit is found in its center. Cobalt, purple; oxygen, red; nitrogen, blue; carbon, gray.

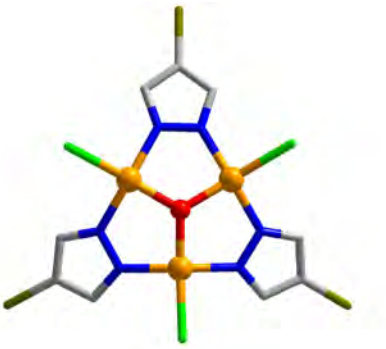

Figure 2.10. Structure of a selected trinuclear cluster of Cu(II) from ref. 34 of formula $[Cu_3(\mu_3\text{-}O)(4\text{-}Br\text{-}pz)_3Cl_3]^-$. Copper, orange; oxygen, red; chlorine, bright green; bromine, olive green; nitrogen, blue; carbon, gray.

O-based ligand systems. This is the case of triangular copper(II) complexes of general formula $[Cu_3(\mu_3\text{-}X)(R\text{-}pz)_3L_3]^{m+}$, where X^{n-} in most cases is OH (but can also be OMe,[33e,j] or O^{2-},[33c,d,m]), while L can be a halide, nitrate or carboxylate anion, a neutral ligand (*e.g.* pyridine, R-pzH, water or solvents) or a mixture of both (Figure 2.10).[34] These trinuclear complexes were synthesized mostly starting from copper(II) salts and pyrazole ligands in the presence of a base, taking into account the use of different counterions. The control of the pH is also very important in the formation of these clusters and substitution of the pyrazolate ligand in *C*4-position does not affect the formation of trinuclear Cu(II) complexes. On the contrary, it has been shown that 3,5-substituted pyrazoles preclude the formation of cyclic trimers because of steric effects of the side groups of the ligands.

A homoleptic tetranuclear cluster of divalent Cu(II) ions was also isolated with bulky substituents on the pyrazole ring which formula is $[Cu_4(\mu\text{-}pz^{Ph})_8]$. In this cluster, four tetra-coordinated Cu(II) ions are each linked to their neighbors by two pyrazolate-bridges with an approximate idealized S_4 symmetry (actually, there are some distortions from this symmetry due to the presence of the phenyl group on the pyrazolate ligand).[35]

Species of even higher nuclearity have been also observed: within the numerous examples reported in the literature, hexanuclear,[26b] and heptanuclear,[21d] compounds, although less common, are known and were obtained by using bulky pyrazolate ligands. As an example, even an octanuclear copper(II) wheel,

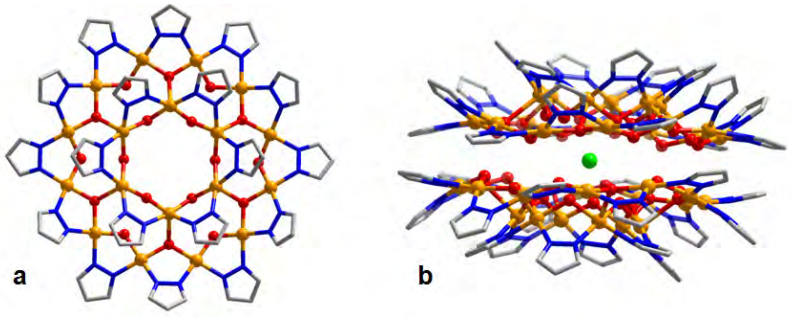

Figure 2.11. (a) Crystal Structure of $[Cu_6(\mu\text{-}OH)_6(\mu\text{-}pz)_6]$-$[Cu_{12}(\mu\text{-}OH)_{12}(\mu\text{-}pz)_{12}]$ formed by two concentric metallocycles. (b) Sandwich of two assemblies with a chloride anion in the middle. Copper, orange; oxygen, red; chlorine, bright green; nitrogen, blue; carbon, light gray.

$[Cu(\mu\text{-}dmpz)(\mu\text{-}OH)]_8$ (Hdmpz = 3,5-dimethylpyrazole), was formed by oxidation of $[Cu(dmpz)]_n$, which was found to be catalytically active in some oxidation reactions.[36] A series of cyclic crown ether analogues, $[Cu_n(\mu\text{-}OH)_n(\mu\text{-}pz)_n]$ (n = 6, 8, 9, 12 and 14), have also been isolated (Figure 2.11a),[37] in which the distorted square-planar copper(II) ions are connected by μ-pz ligands on the ring periphery, with μ-OH ligands pointing inwards. Moreover, some of these metallocycles can encapsulate anions (chloride, carbonate and sulfate) in their inner cavities, stabilized by numerous weak hydrogen bonds (Figure 2.11b).

Finally, Xu reported an octanuclear cluster formulated $[Ni(bma)(H_2O)_3][Ni_8(OH)_6(pz)_{12}]\cdot 6DMSO$, bma = bis(2-benzinidazolylmethyl)amine, showing interesting magnetic properties.[38] This octanuclear cluster consists of an anionic structure composed by an anionic octanuclear nickel(II) unit, $[Ni_8(OH)_6(pz)_{12}]^{2-}$, and a cation formed by a mononuclear nickel(II) entity, $[Ni(bma)(H_2O)_3]^{2+}$. In the octanuclear cluster, the eight nickel(II) ions form a cube and the Ni···Ni···Ni angles are around 90° (Figure 2.12).

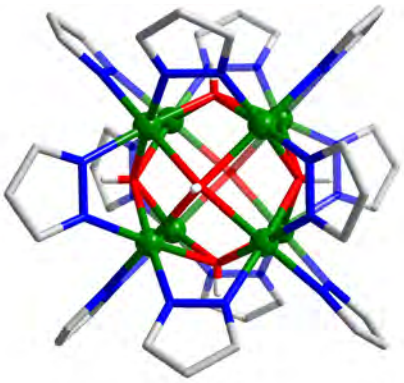

Figure 2.12. Structural depiction of the octanuclear cluster $[Ni_8(OH)_6(pz)_{12}]^{2-}$, in $[Ni(bma)(H_2O)_3][Ni_8(OH)_6(pz)_{12}]\cdot 6DMSO$, bma = bis(2-benzinidazolylmethyl)amine in which is possible to appreciate the octahedral coordinated Ni(II) ions arranged in a cubic fashion. Nickel, green; oxygen, red; nitrogen, blue; carbon, light gray; hydrogen, white.

Conclusions

In this chapter, it has been shown that pyrazoles are very versatile ligands, as they are able, once deprotonated, to form metal complexes with a variety of architectures, ranging from polynuclear clusters to metallocycles or even polymeric 1D chains. Worthy of note, when polymeric metal pyrazolates are isolated (generally as insoluble powders) the complete retrieval of their structures can be done by exploiting ab-initio X-ray powder diffraction methods. As for the nature of this project, this point is extremely important, since the majority of the pyrazolate-based metal-organic frameworks, presented in this thesis and even in earlier works, have been isolated only as crystalline powders.

Similar to the relation between traditional coordination compounds and coordination polymers, the collection of clusters and chains discussed in this chapter may serve as secondary-building units, SBUs, which can be connected into higher dimensional networks using polytopic pyrazolate-based ligands. This is the underlying idea of this research project, in which a new set of polytopic pyr-

azolate-based ligands is designed and coupled to late transition metal ions (M^{2+} = Co, Ni, Cu, Zn) with the aim of generating porous metal-organic frameworks. The design of many organic linkers with different aromatic spacers, or bearing various donor sites, epitomizes the conceptual approach, called 'reticular approach', that requires the use of small building units to direct the assembly of ordered networks. Moreover, it has been demonstrated that this chemistry can yield materials with predetermined structures, compositions and properties. Finally, as in our case, it can generate structures with the high chemical inertness and thermal stability characteristic of pyrazolate-based polymers.

References and Notes

1 *'Heterocycles'* Guest Editor A. R. Katritzky.Chem. Rev. **2004**, *104*, issue 5.

2 Eicher, T.; Hauptmann, S. (2nd ed. **2003**). *The Chemistry of Heterocycles: Structure, Reactions, Syntheses, and Applications.* Wiley-VCH. ISBN 3527307206.

3 (a) Masciocchi, N.; Galli, S.; Sironi, A. *Comments Inorg. Chem.* **2005**, *26*,1. (b) Fackler, J. P.; Falvello, L. *Techniques in Inorganic Chemistry*, CRC Press Taylor and Francis: Boca Raton, **2010**, Florida.

4 Reedijk, J. *Heterocyclic Nitrogen-Donor Ligands. Vol. II* (Eds. Wilkinson, G., Gillard, R. D., McCleverty, J. A.). Pergamon, Oxford, **1987**, 73-98.

5 (a) Pérez, J.; Riera, L. *Eur. J. Inorg. Chem.* **2009**, 4913. (b) Klingele J., Dechert, S.; Meyer, F. *Coordination Chemistry Reviews* **2009**, *253*, 2698. (c) Viciano-Chumillas, M.; Tanase, S.; Jos de Jongh, L.; Reedijk, J. *Eur. J. Inorg. Chem.* **2010**, 3403.

6 (a) Trofimenko, S. *Chem. Rev.* **1972**, *72*, 497. (b) Trofimenko, S. *Adv. Chem.* **1976**, 289. (c) Trofimenko, S. *Prog. Inorg. Chem.* **1986**, *34*, 115. (d) Trofimenko, S. *Chem. Rev.* **1993**, *93*, 943.

7 (a) Trofimenko, S. *Scorpionates – The coordination Chemistry of Polypyrazolylborate Ligands*, Imperial College Press, London, **1999** p. 282. (b) Pettinari, C. and Santini, C. *Comprehensive Coordination Chemistry II* (Eds. McCleverty, J. A., Meyer, T. J.), Elsevier, Amsterdam, **2004**, *1*, pp. 159-210. (c) Ward, M. D.; McCleverty, J. A. and Jeffery, J. C. *Coord. Chem. Rev.* **2001**, *222*, 251.

8 Pettinari, C. and Pettinari, R. *Coord. Chem. Rev.* **2005**, *249*, 525; C. Pettinari and R. Pettinari, *Coord. Chem. Rev.*, **2005**, *249*, 663.

9 (a) LaMonica, G. and Ardizzoia, G. A. *Prog. Inorg. Chem.* **1997**, *46*, 151. (b) Halcrow, M. A. *Dalton Trans.* **2009**, 2059.

10 Pechmann, H. v. *Berichte der deutschen chemischen Gesellschaft* **1898**, *31*, 3, 2950.

11 (a) Fusco, R. *Chemistry of Heterocyclic Compounds: Pyrazoles, Pyrazolines, Indazoles and Condensed Rings. Vol. 22* (Eds. Wiley, R. H. B.; Fusco, R.; Jarboe, C. H.). John Wiley & Sons, Ltd., New York, **1967**, 1-174. (b) Grimmett, M. R. *Adv. Heterocycl. Chem.* **1993**, *57*, 291. (c) Elguero, J. *Comprehensive Heterocyclic Chemistry II*, vol. 3, (Eds. Shinkai, I.) Elsevier, Oxford, UK, **1996**, 1–75.

12 See e.g.: Calabrese, J. C. and Trofimenko, S. *Inorg. Chem.* **1992**, *31*, 4810; Rheingold, A. L.; Ostrander, R. L.; Haggerty, B. S. and Trofimenko, S. *Inorg. Chem.*, **1994**, *33*, 3666.

13 (a) Marson, C. M. *Tetrahedron* **1992**, *48*, 3659. (b) Jutz, C. *Advances in Organic Chemistry* (Eds. Taylor, E. C.). John Wiley & Sons, New York, **1976**, Vol. 9, 252. (c) Reichardt, C. *J. Prakt. Chem.* **1999**, *341*, 609.

14 See e.g.: (a) Schnürch, M.; Flasik, R.; Khan, A. F.; Spina, M.; Mihovilovic, M. D. and Stanetty, P. *Eur. J. Org. Chem.* **2006**, 3283. (b) S. Guillou et al. Tetrahedron 65 (2009) 3529–3535

15 See, e.g. (a) Sadimenko, A. P., Basson, S. S. *Coord. Chem. Rev.* **1996**, *147*, 247. (b) Halcrow, M. A. *Coord. Chem. Rev.* **2005**, *249*, 2880. (c) Mukherjee, R. *Coord. Chem. Rev.* **2000**, *203*, 151. (d) Burini, A.; Mohamed, A. A. and Fackler, J. P. *Comments Inorg. Chem.*, **2003**, *24*, 253. (e) Olguin, J.; Brooker, S. *Coord. Chem. Rev.* **2011**, *255*, 203.

16 See, *e.g.*: (a) Perera, J. R., Neeg, M. J.; Schlegel, H. B.; Winter; C. H. J. Amer. Chem. Soc. **1999**, *121*, 4536; (b) Gust, K. R., Knox, J. E.; Heeg, M. J.; Schlegel, H. B.; Winter, C. H. Eur. J. Inorg. Chem. **2002**, *9*, 2327. (c) Beaini, S.; Deacon, G. B.; Erven, A. P.; Junk, P. C. and Turner, D. R. *Chem. Asian J.* **2007**, *2*, 539.

17 See, *e.g.*: (a) Deacon, G. B., Gitlits, A.; Roesky, P. W.; Bürgstein, M. R.; Lim, K. C.; Skelton, B.W.; White, A. H. *Chem. Eur. J.* **2001**, *7*, 127. (b) Deacon, G. B.; Delbridge, E. E. and Forsyth, C. M. *Angew. Chem., Int. Ed.* **1999**, *38*, 1766. (c) Deacon, G. B.; Forsyth, C. M.; Gitlits, A.; Harika, R.; Junk, P. C.; Skelton, B. W. and White, A. H. *Angew. Chem., Int. Ed.* **2002**, *41*, 3249.

18 Keter, F. K.; Darkwa, J. *Biometals* **2011**. DOI: 10.1007/s10534-011-9496-4, and references therein.

19 (a) Sachse, A.; Demeshko, S.; Dechert, S.; Daebel, V.; Lange A. and Meyer, F. *Dalton Trans.* **2010**, *39*, 3903. (b) Noël, G.; Röder, J. C.; Dechert, S.; Pritzkow, H.; Bolk, L.; Mecking, S.; Meyer, F. *Adv. Synth. Catal.* **2006**, *348*, 887. (c) Maspero, A; Brenna, S; Galli, S; Penoni, A *J. Org. Chem.* **2003**, 672, 123. (d) Diaz-Requejo, M. M.; Caballero, A.; Belderrain, T. R.; Nicasio, M.C.; Trofimenko, S.; Perez, P. J. *J. Am. Chem. Soc.* **2002**, *124*, 978.

20 See, *e.g.*: (a) Mayoral, M. J.; Ovejero, P.; Campo, J. A.; Heras, J. V.; Torres, M. R.; Lodeiro, C. and Cano, M. New J. Chem. 2010, 34, 2766. (b) Barberá, J.; Elduque, A.; Giménez, R.; Oro, L. A.; Serano, J. L. *Angew. Chem., Int. Ed.***1996**, *35*, 2832. (c) Porta, B.; Khamsi, J.; Noveron, J. C. *Curr. Org. Chem.* **2008**, *12*, 1298. (d) Torralba, M. C.; Cano, M.; Campo, J. A.; Heras, J. V.; Pinilla, E.; Torres, M. R. *J. Organomet. Chem.* **2002**, *654*, 150. (e) Nieto, S.; Pérez, J.; Riera, L.; Riera, V.; Miguel, D.; Golen, J. A.; Rheingold, A. L. *Inorg. Chem.* **2007**, *46*, 33407.

21 See, *e.g.*: (a) Dias, H. V. R.; Diyabalanage, H. V. K.; Eldabaja, M. G.; Elbjeirami, O.; Rawashdeh-Omary, M. A.; Omary, M. A. *J. Am. Chem. Soc.* **2005**, *127*, 7489. (b) Enomoto, M.; Kishimura, A.; Aida, T. *J. Am. Chem. Soc.* **2001**, *123*, 5608. (c) Chen, K.; Yang, C.-H.; Chi, Y.; Liu, C.-S.; Chang, C.-H.; Chen, C.-C.; Wu, C.-C.; Chung, M.-W.; Cheng,

Y.-M.; Lee, G.-H. and Chou, P.-T. *Chem. Eur. J.* **2010**, *16*, 4315. (d) Rawashdeh-Omary, M. A.; Rashdan, M. D.; Dharanipathi, S.; Elbjeirami, O.; Rameshb, P. and Dias H. V. R. *Chem. Commun.* **2011**, *47*, 1160.

22 See, *e.g.*; (a) Angaroni, M.; Ardizzoia, G. A.; Beringhelli, T.; La Monica, G.; Gatteschi, G.; Masciocchi, N.; Moret, M. *J. Chem. Soc. dalton. Trans*. **1990**, 3305. (b) Rinehart, J. D.; Kozimor, S. A.; Long, J. R. *Angew. Chem. Int. Ed.* **2010**, *49*, 2560. (c) Noble, A.; Olguín, J.; Clérac, R. and Brooker, S. *Inorg. Chem.* **2010**, *49*, 4560. (d) Liu, X. M.; McAllister, J. A.; de Miranda, M. P.; Whitaker, B. J.; Kilner, C. A.; Thornton-Pett, M.; Halcr ow, M. A. *Angew. Chem. Int. Ed.* **2002**, *41*, 756.

23 Büchner, E. *Ber. Dtsch. Chem. Ges.* **1889**, *22*, 842.

24 Okkersen, H; Groeneveld, W. L.; Reedijk, *J. Recl. Trav. Chim. Pays-Bas* **1973**, *92*, 945.

25 Masciocchi, N.; Moret, M.; Cairati, P.; Sironi, A.; Ardizzoia, G. A. and La Monica, G. *J. Am. Chem. Soc.* **1994**, *116*, 7668.

26 (a) Ehlert, M. K.; Storr, A.; Thompson, R. C. *Can. J. Chem.* **1993**, *71*, 1412. (b) Masciocchi, N.; Ardizzoia, G. A.; Brenna, S.; La Monica, G.; Maspero, A.; Galli, S.; Sironi, A. *Inorg. Chem.* **2002**, *41*, 6080. (c) Storr, A.; Summers, D. A.; Thompson, R. C. *Can. J. Chem.* **1998**, *76*, 1130. (d) Ehlert, M. K.; Rettig, S. J.; Storr, A.; Thompson R. C.; Trotter, J. *Can. J. Chem.*, **1989**, *67*, 1970. (e) Ehlert, M.K.; Storr, A.; Thompson, R.C.; Einstein, F. W. B.; Batchelor, R. J. *Can. J. Chem.* **1993**, *71*, 331. (f) Ehlert, M. K.; Rettig, S. J.; Storr, A.; Thompson R. C.; Trotter, J. *Can. J. Chem.* **1991**, *69*, 432; (g) Ehlert, M. K.; Storr A.; Thompson, R. C. *Can. J. Chem.* **1992**, *70*, 1121. (h) Cingolani, A.; Galli, S.; Masciocchi, N.; Pandolfo, L.; Pettinari, C.; Sironi, A. *J. Am. Chem. Soc.* **2005**, *127*, 6144. (i) Masciocchi, N.; Ardizzoia, G. A.; Maspero, A.; LaMonica, G.; Sironi, A. *Inorg. Chem.* **1999**, *38*, 3657; (j) Hu, T.-L.; Wang, J.-J.; Li J.-R.; Bu, X.-H. *J. Mol. Struct.* **2006**, *796*, 18. (k) Quitmann, C. C.; Müller-Buschbaum, K. Z. *Anorg. Allg. Chem.* **2005**, *631*, 1191.

27 See, *e.g.*: (a) Bovio, B.; Bonati, F.; Banditelli, G. Inorg. Chim. Acta **1984**, *87*, 25. (b) Murray, H. H.; Raptis, R. G.; Fackler, J. P. *Inorg. Chem.* **1988**, *27*, 26. (c) Ehlert, M. K.; Rettig, S. J.; Storr, A.; Thompson, R. C.; Trotter, *J. Can. J. Chem.* **1990**, *68*, 1444. (d) Ardizzoia, G.

A.; Cenini, S.; La Monica, G.; Masciocchi, N.; Maspero, A.; Moret, M. *Inorg. Chem.* **1998**, *37*, 4284. (e) Kim, S. J.; Kang, S. H.; Park, K.-M.; Kim, H.; Zin, W.-C.; Choi, M.-G.; Kim, K. *Chem. Mater.* **1998**, *10*, 1889. (f) Yang, G.; Raptis, R. G. *Inorg. Chem.* **2003**, *42*, 261. (g) Fujisawa, K.; Ishikawa, Y.; Miyashita, Y.; Okamoto, K.-i. *Chem. Lett.* **2004**, *33*, 66. (h) Torralba, M. C.; Ovejero, P.; Mayoral, M. J.; Cano, M.; Campo, J. A.; Heras, J. V.; Pinilla, E.; Torres, M. R. *Helv. Chim. Acta* **2004**, *87*, 250. (i) Omary, M. A.; Rawashdeh-Omary, M. A.; Gonser, M. W. A.; Elbjeirami, O.; Grimes, T.; Cundari, T. R. *Inorg. Chem.* **2005**, *44*, 8200. (j) Dodge, M. W.; Wacholtz, W. F.; Mague, J. T. *J. Chem. Crystallogr*. **2005**, *35*, 5. (k) Dias, H. V. R.; Gamage, C. S. P. *Angew. Chem., Int. Ed.* **2007**, *46*, 2192. (l) Dias, H. V. R.; Gamage, C. S. P.; Keltner, J.; Diyabalanage, H. V. K.; Omari, I.; Eyobo, Y.; Dias, N. R.; Roehr, N.; McKinney, L.; Poth, T. *Inorg. Chem.* **2007**, *46*, 2979. (m) Omary, M. A.; Elbjeirami, O.; Gamage, C. S. P.; Sherman, K. M.; Dias, H. V. R. *Inorg. Chem.* **2009**, *48*, 1784.

28 (a) Meyer, F.; Jacobi, A.; Zsolnai, L. *Chem. Ber./Recl.* **1997**, *130*, 1441. (b) Singh, K.; Long, J. R.; Stavropoulos, P. *J. Am. Chem. Soc.* **1997**, *119*, 2942 (c) Mohamed, A. A.; Perez, L. M.; Fackler, J. P. *Inorg. Chim. Acta* **2005**, *358*, 1657. (d) Dias, H. V. R.; Diyabalanage, H. V. K. *Polyhedron* **2006**, *25*, 1655. (e) He, J.; Yin, Y.-G.; Wu, T.; Li, D.; Huang, X.-C. *Chem. Commun.* **2006**, 2845. (f) Zhang, J.-X.; He, J.; Yin, Y.-G.; Hu, M.-H.; Li, D.; Huang, X.-C. *Inorg. Chem.* **2008**, *47*, 3471.

29 Morawitz, T.; Lerner, H.-W.; Bolte, M. *Acta Crystallogr., Sect. E: Struct. Rep. Online* **2006**, *62*, 1474.

30 Ardizzoia, G. A.; Cenini, S.; La Monica, G.; Masciocchi, N.; Moret, M. *Inorg. Chem.* **1994**, *33*, 1458.

31 (a) Burger, W.; Strähle, J. Z. *Anorg. Allg. Chem.* **1985**, *529*, 111. (b) Baran, P., Marrero, C. M.; Perez, S.; Raptis, R. G. *Chem. Commun.* **2002**, 1012. (c) Umakoshi, K.; Yamauchi, Y.; Nakamiya, K.; Kojima, T.; Yamasaki, M.; Kawano, H.; Onishi, M. *Inorg. Chem.* **2003**, *42*, 3907.

32 Umakoshi, K.; Kojima, T.; Kim, Y. H.; Onishi, M.; Nakao, Y.; Sakaki, S. *Chem.–Eur. J.* **2006**, *12*, 6521.

33 Ehlert, M. K.; Rettig, S. J.; Storr, A.; Thompson, R. C.; Trotter, *J. Acta Crystallogr. ,Sect. C* **1994**, *50*, 1023.

34 (a) Hulsbergen, F. B.; ten Hoedt, R.W. M.; Verschoor, G. C.; Reedijk, J.; Spek, A. L. *J. Chem. Soc., Dalton Trans.* **1983**, 539. (b) Sakai, K.; Yamada, Y.; Tsubomura, T.; Yabuki M.; Yamaguchi, M. *Inorg. Chem.* **1996**, *35*, 542. (c) Angaridis, P. A.; Baran, P.; Boča, R.; Cervantes-Lee, F.; Haase, W.; Mezei, G.; Raptis, R. G.; Werner, R. *Inorg. Chem.* **2002**, *41*, 2219. (d) Shen, W.-Z.; Yi, L.; Cheng, P.; Yan, S.-P.; Liao, D.-Z.; Jiang, Z.-H. *Inorg. Chem. Commun.* **2004**, *7*, 819. (e) Liu, X.; de Miranda, M. P.; McInnes, E. J. L.; Kilner, C. A.; Halcrow, M. A. *Dalton Trans.* **2004**, 59. (f) Mezei, G.; Rivera-Carrillo, M.; Raptis, R. G. *Inorg. Chim. Acta* **2004**, *357*, 3721. (g) Casarin, M.; Corvaja, C.; di Nicola, C.; Falcomer, D.; Franco, L.; Monari, M.; Pandolfo, L.; Pettinari, C.; Piccinelli, F.; Tagliatesta, P. *Inorg. Chem.* **2004**, *43*, 5865. (h) Casarin, M.; Corvaja, C.; Di Nicola, C.; Falcomer, D.; Franco, L.; Monari, M.; Pandolfo, L.; Pettinari, C.; Piccinelli, F. *Inorg. Chem.* **2005**, *44*, 6265. (i) Zhou, J.-H.; Liu, Z.; Li, Y.-Z.; Song, Y.; Chen, X.-T.; You, X.-Z. *J. Coord. Chem.* **2006**, *59*, 147. (j) Mezei, G.; Raptis, R. G.; Telser, J. *Inorg. Chem.* **2006**, *45*, 8841. (k) Di Nicola, C.; Karabach, Y.Y.; Kirillov, A. M.; Monari, M.; Pandolfo, L.; Pettinari, C.; Pombeiro, A. J. L. *Inorg. Chem.* **2007**, *46*, 221. (l) Casarin, M.; Cingolani, A.; Di Nicola, C.; Falcomer, D.; Monari, M.; Pandolfo, L.; Pettinari, C. *Cryst. Growth Des.* **2007**, *7*, 676. (m) Rivera-Carrillo, M.; Chakraborty, I.; Mezei, G.; Webster, R. D.; Raptis, R. G. *Inorg. Chem.* **2008**, *47*, 7644. (n) Pettinari, C.; Masciocchi, N.; Pandolfo, L.; Pucci, D. *Chem.—Eur. J.* **2010**, *16*, 1106.

35 Mokuolu, Q. F.; Foguet-Albiol, D.; Jones, L. F.; Wolowska, J.; Kowalczyk, R. M.; Kilner, C. A.; Christou, G.; McGowan, P. C.; Halcrow, M. A. *Dalton Trans.* **2007**, 1392.

36 Ardizzoia, G. A.; Angaroni, M. A.; La Monica, G.; Cariati, F.; Moret, M.; Masciocchi, N. *Chem. Commun.* **1990**, 1021.

37 Mezei, G.; Baran, P.; Raptis, R. G. *Angew. Chem., Int. Ed.* **2004**, *43*, 574.

38 Xu, J. Y.; Qiao, X.; Song, H. B.; Yan, S. P.; Liao, D. Z.; Gao, S.; Journaux, Y.; Cano, J. *Chem. Commun.* **2008**, 6414.

Chapter 3
Design and Synthesis of substituted Pyrazolate-based Ligands

Introduction

In the field of coordination polymers, researchers are continually investigating for new ideas and strategies to design and synthesize functional materials that could show different of even better properties than the already existing ones. A widespread interest on the aforementioned aim has resulted in a rational, designed approach where judicious selection of the metal ions and of the organic ligands are performed for the preparations of porous metal-organic frameworks possessing physical and chemical properties that are finely tuned for specific applications.[1] The ability of rationalizing the topologies in metal-organic frameworks is generally based on the study of the metal clusters or secondary building units (SBUs) which are always generated *in-situ*, thus suffering anyway of an arbitrariness that could limit their utility in topological predictions. On the contrary, most of the organic ligands used in MOFs synthesis are robust moieties during the assembly procedure, inducing a control on the structure and properties arising from the nature of the ligand. Whatever synthetic strategies are implemented, these organic bridges are part of the basic components of coordination polymers and a careful selection of the molecular spacers is an important step towards desired

structures and functions. Indeed, ligand design could be used not only to enrich diversity in MOFs structures, but also to modify their functionality for specific applications, always remembering that it is the combination of both organic units and inorganic SBUs that determines the final framework topologies.

In the past two decades, many types of polytopic organic ligands with different donor groups, such as carboxylate, pyridyl, amine, sulfonate, phosphonate, etc., have been used in the generation of coordination polymers.[2] Carboxylate-based ligands are actually ubiquitous in this field. This could be ascribed to the versatility of these ligands in coordination chemistry because each O-donor atom can bind one, two, and even three metal ions, which induces significant variability in structures formations and properties. Moreover, these ligands have the advantage of a good commercial availability and of the easiness of the synthetic processes, since their preparations are usually cheap and facile.

Another class of ligands that only recently has been used in MOFs is based on the azole functional group. This functional group is appealing in coordination chemistry, for crystal engineering and material science, because it has the advantage of strong and directional coordination modes in bridging metal ions and the ability to generate many different metal-containing SBUs.

In metal-organic frameworks chemistry, the first most prominent examples of metal-azolate frameworks are probably the ones published by Long and coworkers.[3] In their first publications in this field, they have shown the construction of a series of porous materials by connecting rigid polytetrazolates with late transition metal ions.[3a] The mainstay of their work is based on a series of highly porous 3,8-connected frameworks in which cubic clusters of general formula $[M_4Cl(ttz)_8(Solv)_4]$, [M = Mn^{2+}, Cu^{2+}, Fe^{2+}, Ni^{2+}; ttz = tetrazole] are connected through different triangular polytetrazolate ligands.[3b-g] Among the azolate-based metal-organic frameworks of this type, $Mn_3[(Mn_4Cl)_3(BTT)_8]_2 \cdot 20MeOH$, [Mn-BTT, H_3BTT = 1,3,5-tris(2H-tetrazol-5-yl)benzene], a rigid high-surface area frame-

work with an expanded sodalite-like structure and exposed Mn^{2+} sites, exhibited a high H_2 binding affinity,[3b] and Lewis acid catalytic activity.[3h] Unfortunately, the low thermal stability characteristic of tetrazoles results in a framework with a very low decomposition temperature (T_{dec} < 200 °C). Moreover, the water-sensitivity of this framework limits its utility in practical applications. In the quest for analogous structures with increased stability, a isolelectronic and isosteric triangular polytriazolate ligand was used with success by this group.[3i]

Interestingly, in the coordination chemistry of azoles, a basicity concept can be applied to estimate the strength of the resulting M–N bonds, thus allowing the chemist to control the robustness of the obtained material. This prediction can be done on the basis of the strength of the M–N bonds that is closely related to the pKa values for the deprotonation of the N–H bonds. Indeed, it has been demonstrated that azolate-based ligands afford robust coordination polymers compared to the O-based ones.[4] Within azolates, increased stability has been observed for pyrazolate- and imidazolate- derivatives rather than triazolate- and tetrazolate-based ones, accordingly with their pKa values.[3-5]

In terms of stability, Yaghi et al. have done a rather extensive work for a new type of porous materials termed zeolitic imidazolate frameworks (ZIFs).[6] ZIFs are a new class of porous crystals with extended three-dimensional structures constructed from tetrahedral metal ions (*e.g.*, Zn^{2+}, Co^{2+}) bridged by substituted simple 1*H*-imidazolate ligands. The fact that the M-Im-M angle is similar to the Si-O-Si angle preferred in zeolites (145°) has led to the synthesis of a large number of ZIFs with zeolite-type tetrahedral topologies. In a recent review, this group summarized comprehensively the zeolitic frameworks that have been accessible from different azolate ligands and they also demonstrated that ZIF-8 shows a higher chemical stability compared to that of tetrazolate- and carboxylate-based metal-organic frameworks, which makes them attractive candidates for many applications such as separation and storage of gases.[7]

Through these notable examples, it is evident that an important key feature of porous materials is their chemical and thermal stability, toward which researchers are continuously striving. In this regard, it is clearly beneficial to discover new porous metal–organic frameworks that are stable towards diverse environments such as air, water, acidic and basic media, and even extreme temperatures and pressures, to extend their utility toward a variety of applications where other porous materials, such as zeolites, have been playing a major role.

In order to find a suitable N-donor substitute for linear and branched O-donor ligands, we designed a series of linear and triangular pyrazolate-based ligands, aiming at the construction of progressively more stable porous materials. Although many pyrazolate-based coordination compounds have already been reported, the coordination chemistry of polytopic pyrazolate-based ligands remains largely unexplored. The organic ligands presented in this thesis are constructed by 1*H*-pyrazoles connected each other through spacers of different nature by substitution at their *C*4 position. Moreover, in some cases, they are decorated with a number of functional groups. A synoptic collection these ligands is reported in Figure 3.1.

Unfortunately, polytopic pyrazolate ligands are not readily available, nor have their synthetic procedures been deeply explored. Therefore, the quest for novel and accessible routes for their synthesis, employing cheap reactants in mild and environmentally friendly conditions, has been here pursued in order to make these species readily, and widely, available.

This chapter describes in detail the synthesis and characterization of this new series of polytopic pyrazolate-based ligands and, for the ease of reading, it is subdivided in four different sections: i) ligands with an aromatic core; ii) ligands bearing functional groups on the aromatic core; iii) ligands with an aromatic bisimide core and, finally, iv) hetero-functional ligands.

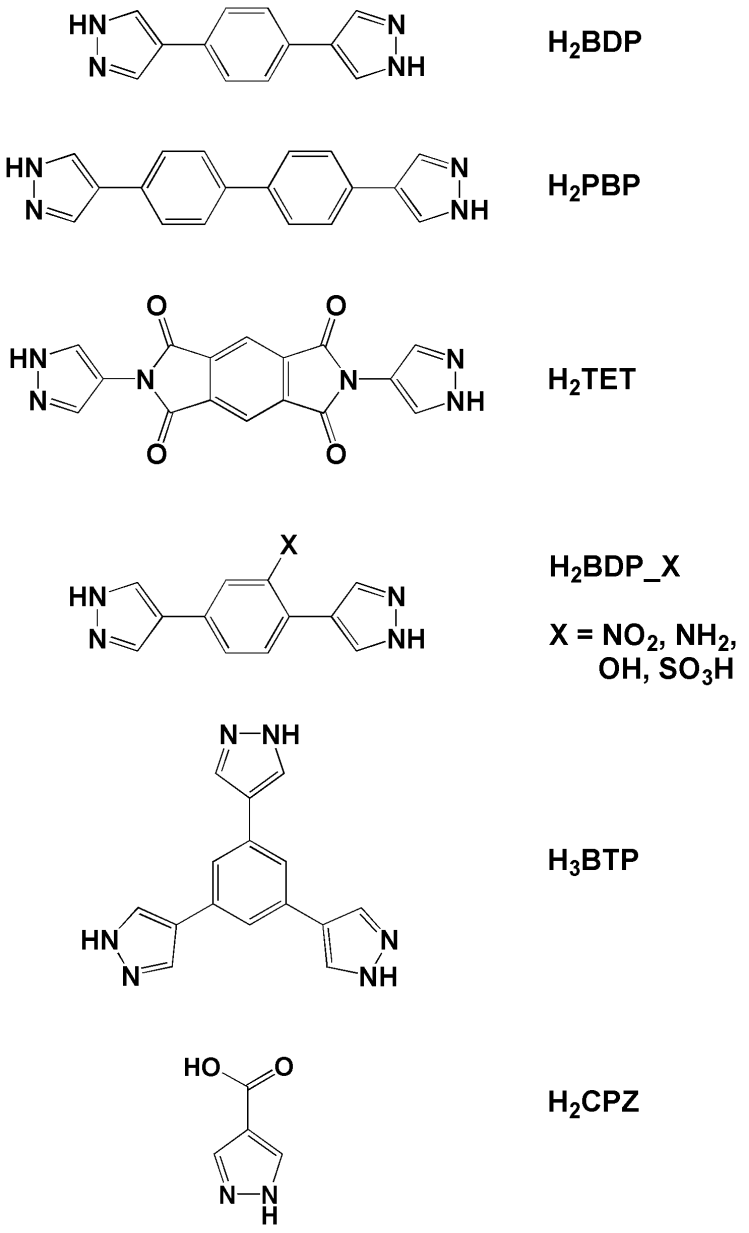

Figure 3.1. Polytopic pyrazole-based ligands synthesized in this project.

Experimental Details

1,4-Bis(pyrazol-4-yl)benzene (H_2BDP). The first intermediate, 1,4-bis(1-dimethylamino-3-dimethylimonio-prop-1-en-2-yl)benzene bis(perchlorate), was prepared as previously reported by Arnold et al.[8] M.p. 300 °C. IR (KBr) 2936(w), 1582(vs), 1489(w), 1452(w), 1393(m), 1287(m), 1211(m), 1078(vs), 975(m), 761(w), 622(m), 586(w) cm^{-1}. ^{1}H NMR δ 2.45 (s, 3H), 3.36 (s, 3H), 7.39 (s, 2H), 7.73 (s, 2H). ^{13}C NMR δ 40.4 (Me), 49.5 (Me), 105.1 (C), 133.1 (C), 134.3 (C), 163.9 (CH). Anal. Calcd. for $C_{20}H_{32}Cl_2N_4O_8$ (Mw = 527.40 g/mol): C, 45.55; H, 6.12, N, 10.62. Found: C, 44.95; H 6.10, N,10.48.

The bis(perchlorate) intermediate (470 mg, 0.89 mmol) in EtOH (60 mL) was placed in a 100-mL round-bottomed flask under vigorous stirring, while 98% hydrazine monohydrate (95 μL,1.96 mmol) was added dropwise over 2 min. After being refluxed for 2 h, the pale-yellow solid was filtered off, washed with methanol (2 x 10 mL) and dried in vacuum at room temperature to afford pure **H_2BDP** in the form of polycrystalline powders (172 mg, yield 92 %). Sublimation above 360 °C. IR (KBr) 3144(br), 1583(w), 1527(w), 1263(w), 1236(w), 1159(s), 1037(w), 965(w), 951(s), 866(s), 824(s), 719(w), 657(w), 627(w) cm^{-1}. ^{1}H NMR δ 7.58 (s, 2H), 8.05 (s, 2H), 12.5 (br s, 1H). ^{13}C NMR δ 121.9 (C), 126.3 (HC-Ph), 131.3 (C), 137.0 (HC-pz). Anal. Calcd. for $C_{12}H_{10}N_4$ (Mw = 210.24 g/mol): C, 68.56; H, 4.79; N, 26.65. Found: C, 67.98 H, 4.83, N, 26.26.

4,4'-bis(1*H*-pyrazol-4-yl)biphenyl (H_2PBP). 4,4'-Bis(chloromethyl)-1,1'-biphenyl (6.5 g, 0.026 mol), was added in small portions to a suspension of NaCN (2.664 g, 0.054 mol) in DMSO (14 mL) in a 50-mL one-necked round-bottomed flask equipped with a magnetic stirrer bar. After being heated at 40 °C for 8 h and left at room temperature overnight, the reaction mixture was poured into ice-water (20 mL). The pale-yellow solid was filtered off, washed with cold water (10 mL) and dried under vacuum at room temperature to afford the first intermediate, 4,4'-bis(cyanomethyl)-1,1'-biphenyl (4.5 g, 75%). M.p. 183-184 °C (MeOH).[9]

^{1}H NMR δ 4.07 (s, 2H), 7.44 & 7.69 (dd, 4H). ^{13}C NMR δ 22.5 (CH_2), 119.65 (C), 127.6 (CH), 129.2 (CH), 131.1 (C), 139.3 (C). IR (nujol) 2247(s), 1111(vs), 1006(vs), 913(vs), 793(s), 720(w) cm^{-1}. Anal. Calcd. for $C_{16}H_{12}N_2$ (Mw = 232.27 g/mol): C, 82.73; H,5.21; N, 12.06. Found: C, 82.68; H, 5.31; N, 12.18.

The cyanomethyl derivative (4.5 g, 0.019 mol) in EtOH (80 mL) was then placed in a 250 mL one-necked round-bottomed flask equipped with a magnetic stirrer bar and a condenser. Aqueous 2 M KOH (20 mL) was added and the flask was heated at reflux for 24 h. After cooling to room temperature, conc. HCl was added dropwise until pH 1. The solid was filtered off, washed with cold water (50 mL) and dried under vacuum at room temperature to afford 1,1'-biphenyl-4,4'-di(acetic acid) (3.81 g, 73%), which, upon crystallization from AcOH, yielded pale yellow crystals. M.p. 280-282 °C.[10] ^{1}H NMR δ 3.44 (s, 2H), 7.33 & 7.58 (dd, 4H), 12.35 (br s, OH). ^{13}C NMR δ 40.7 (CH_2), 126.9 (CH), 130.4 (CH), 134.4 (C), 138.7 (C), 173.1 (C). IR (nujol) 1718(s) 1693(vs), 1253(s), 929(w), 799(s), 725(w), 679(w) cm^{-1}. Anal. Calcd. for $C_{16}H_{14}O_4$ (Mw = 270.28 g/mol): C, 71.10; H, 5.22. Found: C, 71.35; H, 5.02.

Under argon atmosphere, $POCl_3$ (2.0 mL, 0,021 mol) was added to anhydrous DMF (23 mL, 0,297 mol) in a 100-mL two-necked round-bottomed flask equipped with a magnetic stirrer bar, argon inlet and condenser. Then, 1,1'-biphenyl-4,4'-di(acetic acid) (3 g, 0,011 mol) was added, the mixture becoming dark orange. After being heated at 90 °C for 8 h and at room temperature overnight, the reaction mixture was poured in an ice bath; a saturated $NaClO_4$ aqueous solution (20 mL) was added to yield a yellow precipitate. The solid was collected by filtration, washed with cold water (5 mL) to afford the 4,4'-bis-(1-dimethylamino-3-dimethylimonio-prop-1-en-2-yl) biphenyl bis(perchlorate) (4.7g, 70%). ^{1}H NMR δ 2.49 (s, 6H), 3.25 (s, 6H), 7.40 & 7.85 (dd, 4H), 7.75 (s, 2H). ^{13}C NMR δ 39.8 (CH_3), 49.0 (CH_3), 104.9 (C), 126.8 (CH), 131.4 (C), 133.3 (CH), 139.2 (C), 163.5 (CH). IR (nujol) 1588(vs), 1403(s), 1289(s), 1208(w), 1090(vs), 810(w), 624(s), cm^{-1}. Anal. Calcd.

for $C_{26}H_{36}Cl_2N_4O_8$ (Mw = 603 g/mol): C, 51.74; H, 6.12; N, 10.62. Found: C, 50.98; H, 6.09; N, 10.48.

To a well stirred suspension of bis(perchlorate) intermediate (4,7 g, 0,0078 mol) in 2-methoxyethanol (100 mL) 98% hydrazine monohydrate (0.5 mL, 0,0162 mol) in EtOH (5 mL) was added dropwise over 5 min. After being refluxed for 2 h, the mixture was filtered and the residue was washed with MeOH (30 mL) and dried under vacuum to afford **H_2PBP** (1.50 g, 68%) as a light yellow crystalline solid. ^{1}H NMR (TFA-d) δ 8.12 & 8.21 (dd syst, 4H), 8.87 (s, 2H). ^{13}C NMR δ 126.7 (CH), 127.9 (CH), 130.5 (CH), 141.5 (C). IR (nujol) 3166(br), 1157(s), 1091(br), 1037(s), 965(s), 872(w), 817(vs), 730(w) cm^{-1}. Anal. Calcd. for $C_{18}H_{14}N_4$ (Mw = 286.33 g/mol): C, 75.50; H, 4.93; N, 19.57. Found: C, 75.68; H, 5.01; N, 19.78. Sublimation under nitrogen atmosphere (1 bar) observed near 400 °C (TGA/DSC evidence).

1,3,5-tris(1*H*-pyrazol-4-yl)benzene (H_3BTP). The first intermediate, 1,3,5-benzenetriacetic acid, was prepared from 1,3,5-triacetyl benzene following a procedure described previously.[11] When necessary, recrystallization of the sample was carried out in acetic acid (65% isolated yield). ^{1}H NMR δ 3.52 (s, 2H), 7.03 (s, 1H), 12.32 (br s, 1H). Anal. Calcd. for $C_{12}H_{12}O_6$ (Mw = 252.20 g/mol): C, 57.14; H, 4.80. Found: C, 56.92; H, 4.82.

Under a nitrogen atmosphere, $POCl_3$ (10 mL, 0.11 mol) was added dropwise to anhydrous DMF (40 mL, 0.52 mol) cooled in an ice bath. Then, 1,3,5-benzenetriacetic acid (3 g, 0.0119 mol) was added and the mixture was heated at 90 °C for 18 h. The reaction mixture was then quenched by pouring it into ice water (50 mL) and a saturated aqueous solution of $NaClO_4$ (13.4 g) was added. The yellowish solid was collected by filtration and washed with cold water to afford 6.98 g (78%) of 1,3,5-tris(1-dimethylamino-3-dimethylimonio-prop-1-en-2-yl) benzene tris(perchlorate). ^{1}H NMR δ 2.60 (br s, 6H), 3.28 (br s, 6H); 7.28 (s, 1H); 7.76 (s, 2H). Anal. Calcd. for $C_{27}H_{45}Cl_3N_6O_{12}$ (Mw = 752.04 g/mol): C, 43.12; H, 6.03; N, 11.17. Found: C, 43.92; H, 5.59; N, 11.65.

The tris(perchlorate) salt (6.98 g, 0.0093 mol) was suspended in a mixed solution of ethanol (100 mL) and water (30 mL) and hydrazine monohydrate (1.44 mL, 0.0297 mol) was added to the mixture. After heating at reflux for 2 h, the mixture was filtered and the residue was washed with methanol (3 x 10 mL) and dried under vacuum to afford 1.74 g (68%) of 1,3,5-tris(1*H*-pyrazol-4-yl)benzene, **H_3BTP**, as a light yellow solid. ^{1}H NMR δ 7.68 (s, 1H), 8.26 (br s, 2H), 12.94 (br s, 1H). IR (neat) 3164(br), 2941(br), 1605 (vs), 1371(w), 1348(w), 1232(w), 1158(s), 1044(s), 994(vs), 947(s), 847(s), 792(s), 747(vs), 690(w), 656(s), 619(vs) cm^{-1}. Anal. Calcd. for $C_{15}H_{12}N_6$ (Mw = 276.30 g/mol): C, 65.21; H, 4.38; N, 30.42. Found: C, 64.55; H, 4.50; N, 29.97.

2-nitro[1,4-bis(1H-pyrazol-4-yl)benzene] (H_2BDP_NO_2). 1,4-bis(1*H*-pyrazol-4-yl)benzene (1 g, 4.76 mmol) was added in portions to concentrated sulfuric acid (10 mL) while keeping the reaction cold with an ice bath. To the solution 70% nitric acid (0.255 mL, 5.71 mmol) was then added dropwise while maintaining the reaction mixture cold. The ice bath was then removed, and the solution was left at room temperature under stirring for 1 h. Then, 5 g of ice were added and the precipitate was filtered off and washed with 10 mL (2 x 5 mL) of water. The precipitate was neutralized with aqueous $NaHCO_3$ and the resulting precipitate was collected by filtration and washed with 10 mL of water (2 x 5 mL) affording the pure product as a yellow solid (1.03 g, yield 85%). ^{1}H NMR (DMSO-*d6*) δ 7.63 (d, *J* = 8.2 Hz, 1H), 7.79 (s, 2H), 7.89 (dd, *J* = 8.2, 1.8 Hz, 1H), 8.08 (d, *J* = 1.8 Hz, 1H); 8.23 (s, 2H). IR (nujol): 3164(br), 1580(s), 1522(vs), 1350(vs), 1256(w), 1175(w), 1151(w), 1041(s), 976(w), 947(s), 894(w), 865(w), 815(s), 741(w), 664(w) cm^{-1}. Anal. Calcd. for $C_{12}H_9N_5O_2$ (Mw = 255.2 g/mol): C, 56.47; H, 3.55; N, 27.44. Found: C, 55.7; H, 3.26; N, 26.37.

2-amino[1,4-bis(1H-pyrazol-4-yl)benzene] (H_2BDP_NH_2). To a suspension of H_2BDP_NO_2 (0.300 g, 1.176 mmol) in DMF (5 mL), ammonium formate (0.370 mg, 5.873 mmol) was added at room temperature. The reaction mixture was

then heated to 120 °C and Pd/C (5%, 30 mg) was added in small portions. The final mixture was then kept under stirring at 100 °C for 2 h. After the reaction mixture became clear, it was filtered through the pad of celite. The celite was then washed with a small amount of DMF and the filtrate was diluted with crushed ice (5 g). The obtained precipitate was then filtered off and washed with water (2 x 5 mL) affording a white powder of pure **H_2BDP_NH_2** product (250 mg, yield 94%). ^{1}H NMR (DMSO-*d6*) δ 4.77 (s, 2H), 6.84 (dd, *J* = 7.8, 1.7 Hz, 1H), 6.97 (d, *J* = 1.7 Hz, 1H), 7.15 (d, *J* = 7.8 Hz, 1H), 7.86 (br s, 4H), 12.88 (br s, 2H). IR (nujol): 3420(s), 3338(s), 3111(br), 1621(s), 1575(s), 1522(w), 1334(w), 1290(w), 1169(vs), 1042(s), 988(w), 961(s), 946(w), 880(w), 864(s), 805(vs), 721(w), 660(w), 627(w) cm^{-1}. Anal. Calcd. for $C_{12}H_{11}N_5$ (Mw = 225.2 g/mol): C, 63.99; H, 4.92; N, 31.09. Found: C, 63.31; H, 5.42; N, 31.30.

2-hydroxo[1,4-bis(1H-pyrazol-4-yl)benzene] (H_2BDP_OH). 1 g (4.444 mmol) of H_2BDP_NH_2 was dissolved in 5 mL of sulfuric acid. The mixture was stirred till a thick paste was formed. To this, about 3 g of crushed ice were added and the mixture was then kept in an ice bath. In a separate beaker, $NaNO_2$ (0.440 g, 5.176 mmol) was dissolved in 4 mL of water. This solution was cooled and added dropwise, with constant stirring, to the acid amine solution. In a separate flask, a solution of H_2SO_4 (3 mL) and water (3 mL) was heated to 110 °C and the entire diazonium salt solution was added dropwise. After the addition was over, the solution was allowed to boil for another 30 min. It was then cooled with an ice bath and the precipitate was filtered off and suspended in a solution of $NaHCO_3$ in water and stirred for 2 h at 80 °C. The yellowish precipitate was then filtered off, washed with water (2 x 5 mL) and dried under vacuum (0.763 g, yield 76%). ^{1}H NMR (DMSO-*d6*) δ 7.04 (m, 2H), 7.51 (d, *J* = 7.8 Hz, 1H), 8.04 (br s, 4H), 9.67 (s, 1H), 12.83 (br s, 2H). IR (nujol): 3525(s), 3387(br), 3182(br), 1621(w), 1588(s), 1563(w), 1534(w), 1440(s), 1346(w), 1274(w), 1254(w), 1216(w), 1160(vs), 1106(w), 1036(s), 959(s), 948(s), 888(w), 865(w), 834(w), 817(s), 736(w), 670(w)

cm^{-1}. Anal. Calcd. for $C_{12}H_{10}N_4O$ (Mw = 226.2 g/mol): C, 63.71; H, 4.46; N, 24.76. Found: C, 62.41; H, 5.11; N, 24.50.

2,5-di(1*H*-pyrazol-4-yl)benzenesulfonic acid (H_2BDP_SO_3H). 1,4-bis(1*H*-pyrazol-4-yl)benzene (1 g, 4.76 mmol) was added in portions to fuming sulfuric acid (10 mL) and was stirred for 1 h at room temperature. To the resulting solution, crushed ice was added slowly to give a white precipitate that was filtered off, washed thoroughly with water (2 x 10 mL) and dried under vacuum to give pure **H_2BDP_SO_3H** (0.953 g, yield 69%). ^{1}H NMR (DMSO-*d6*) δ 3.16 (s, 1H), 7.48 (d, *J* = 8 Hz, 1H), 7.61 (dd, *J* = 8, 1.9 Hz, 1H), 8.11 (s, 2H), 8.15 (d, *J* = 1.9 Hz, 1H), 8.58 (s, 2H). IR (nujol): 3415(br), 3174(br), 1580(w), 1564(w), 1511(w), 1346(w), 1311(w), 1256(w), 1215(vs), 1176(vs), 1113(s), 1084(s), 1047(s), 1026(s), 969(w), 943(w), 886(w), 831(s), 737(w), 682(w), 656(w) cm^{-1}. Anal. Calcd. for $C_{12}H_{10}N_4O_3S$ (Mw = 290.3 g/mol): C, 49.65; H, 3.47; N, 19.30. Found: C, 49.84; H, 3.97; N, 18.64.

2,6-bis(1*H*-pyrazol-4-yl)pyrrolo[3,4-*f*]isoindole-1,3,5,7(2*H*,6*H*)-tetrone (H_2TET). A suspension of pyromellitic dianhydride (0.500 g, 2.290 mmol) in *N*, *N*-dimethylacetamide (20 mL) was refluxed under nitrogen for 5 min. 4-Amino-1*H*-pyrazole**,** (0.380 g, 4.580 mmol) in *N*, *N*-dimethylacetamide (5 mL) was added to this solution by means of a syringe and the resulting dark mixture was stirred at reflux for 4 h. After being cooled, the suspension was filtered and the straw yellow solid was washed with successive aliquots of dichloromethane (2 × 5 mL) and dried under vacuum at 130 °C to afford **H_2TET** (0,733 g, 92%). M.p. 490 °C (DSC/TG evidence). ^{1}H NMR (TFA-d) δ 9.09 (s, 2H), 9.45 (s, 4H). ^{13}C NMR δ 117.7 (C), 120.5 (CH), 126.9 (CH), 137.4 (C), 163 (C). IR (nujol) 3114(w), 3102(w), 1707(vs), 1526(w), 1217(w), 1094(vs), 1049(w), 947(w), 928(w), 834(s), 720(s) cm^{-1}. Anal. Calcd. for $C_{16}H_8N_6O_4$ (Mw = 348,06 g/mol): C, 55.18; H, 2.32; N, 24.13. Found: C, 55.28; H, 2.18; N, 24.52.

X-Ray Powder Diffraction Structure Analysis. Powdered, microcrystalline samples were gently ground in an agate mortar, then deposited in the hollow of an

aluminum sample holder equipped with a zero-background plate. Diffraction data were collected with overnight scans, typically in the 5-105° 2θ range, on a Bruker AXS D8 Advance diffractometer, equipped with a linear position-sensitive Lynxeye detector, primary beam Soller slits, and Ni-filtered Cu-Kα radiation (λ = 1.5418 Å). The generator was set at 40 kV, 40 mA. Standard peak search, followed by indexing with TOPAS,[12] allowed the detection of the approximate unit cell parameters. The space groups were assigned on the basis of the systematic absences, checked by Le Bail refinements and later confirmed by successful structure solutions and refinements. Structure solutions were performed by the simulated annealing technique, as implemented in TOPAS, using for the ligands a rigid, idealized model, flexible, when necessary, at the arene-pyrazole torsion. The final refinements were carried out by the Rietveld method, maintaining the rigid bodies introduced at the structure solution stage. In all cases, the background was modeled by a polynomial function. Peak shapes were determined by the Fundamental Parameters Approach.

Crystal data for H_2BDP. $C_{12}H_{10}N_4$, *fw* = 210.24 g mol^{-1}, *a* = 11.888(1), *b* = 5.5014(5), *c* = 7.7446(7) Å, β = 90.772(5)°, *V* = 506.44(8) Å^3, *Z* = 2; R_{Bragg} = 0.075; R_{wp} = 0.111 for 5001 data collected in the 5.0-105.0° 2θ range.

Crystal data for H_2PBP. $C_{18}H_{14}N_4$, *fw* = 286.34 g mol^{-1}, monoclinic, $P2_1/c$, *a* = 16.042(2), *b* = 5.5181(6), *c* = 7.8621(7) Å, β = 93.96(1)°, *V* = 694.3(1) Å^3, *Z* = 2, *ρ* = 1.370 g cm^{-3}, R_p, R_{wp} and R_{Bragg} = 0.035, 0.048, 0.015, respectively, for 3501 data collected in the 5.0-75.0° 2*ϑ* range.

Crystal data for H_2TET. $C_{16}H_8N_6O_4$, *fw* 348.28 g mol^{-1}, monoclinic, $P2_1/c$, *a* = 5.2503(4), *b* = 5.3608(3), *c* = 24.376(2) Å, *β* = 90.480(4)°, *V* = 686.0(1) Å^3, *Z* = 2, *ρ* = 1.686 g cm^{-3}, R_p, R_{wp} and R_{Bragg} = 0.075, 0.104, 0.058, respectively, for 5001 data collected in the 5.0-105.0° 2θ range.

Crystal data for H_3BTP. $C_{15}H_{12}N_6$, *fw* 276.3 g mol^{-1}, orthorhombic, *P c a b*, *a* = 19.71(2), *b* = 12.21(3), *c* = 11.05(1), *V* = 2660.3(2) A^3, Z = 4, R_{Bragg} = 0.075; R_{wp} = 0.101 for 5001 data collected in the 5.0-105.0° 2θ range.

Other Physical Measurements. Elemental analyses were carried out on a Shimadzu CHNS elemental analyzer. IR spectra (nujol mull) were recorded on a Shimadzu IRPrestige-21. Simultaneous DSC/TG analyses were obtained on a Netzsch STA 409 PC under a nitrogen purge at 10 °C min^{-1}. NMR spectra (in DMSO-d_6, unless stated otherwise) were recorded at 298 K on a Bruker Avance 400 instrument (400 MHz for ^1H; 100 MHz for ^{13}C) internally referenced to the $SiMe_4$ signal. For **H_3BTP** ligand ^1H-NMR spectra (in DMSO-d_6) were recorded at 298 K on a Bruker Avance 400 instrument (400 MHz) in the NMR Facility of the University of California, Berkeley. Elemental analyses were obtained from the Microanalytical Laboratory of the University of California, Berkeley. Infrared spectra (neat) were recorded on a Perkin Elmer Spectrum 100 Optica FTIR spectrometer.

Results and Discussion

Pyrazolate Ligands with an Aromatic Core. When the skeleton of the ligand is based on a combination of arenes (benzene, biphenyl, *etc.*) and the 1*H*-pyrazoles are linked to this inner aromatic core through their *C*4 position, a common synthetic procedure can be envisaged. Indeed, the preparation of this first class of ligands exploits the reactivity of phenylen acetic acids (*e.g. p*-phenylenediacetic acid) that can be easily transformed into pyrazoles derivatives through a simple series of reactions. In this context, vinamidinium salts,[14] have been successfully utilized as part of the synthetic strategy for the construction of substituted pyrazoles and are readily accessible through a Vilsmeier–Haack–Arnold (VHA) formylation reaction.[15] When a phenylen acetic acid derivative is not commercially available, a series of simple reactions on purchasable starting materials can be designed and performed to obtain the acetic acid functionality on the arene core (see below).

The cornerstone of this ligands series is 1,4-bis(pyrazol-4-yl)benzene, **H_2BDP**, that could be derived by heterocyclization of *p*-phenylenebis(malondialdehyde)[8]

(or its synthetic equivalents) with hydrazine. Thus, **H_2BDP** was best prepared from commercially available *p*-phenylenediacetic acid (Scheme 3.1) by a sequence of reactions starting with the VHA reaction ($POCl_3$, DMF, 90 °C, 11 h) followed by quenching in water and metathesis with $NaClO_4$. Overcoming the necessity of isolating the rather unstable tetraldehyde, as done by other research groups,[16] the resulting bis(perchlorate) vinamidinium salt was directly reacted with hydrazine monohydrate (refluxing EtOH, 1 h) to provide the required ligand in good yields (76% over two steps).[17]

The **H_2BDP** ligand was fully characterized with different techniques and, due to its highly insoluble nature, the structural investigation was done by means of XRPD experiments on a recrystallized sample from EtOH at reflux. **H_2BDP** crystallizes in the monoclinic $P2_1/c$ space group. The molecules, lying on crystallographic inversion centers, generate 2-D sheets through NH···N hydrogen-bond interactions (Figure 3.2) which develop through relatively weak contacts (N···N 3.05 Å), with the molecules windy up the crystallographic 2_1 screw axis aligned with the b cell axis. Notably, the extended net of hydrogen-bond interactions can be considered responsible for the very high thermal and chemical inertness and the limited solubility of this compound. Finally, the torsion angle about the (formally) single CC bond is very small [9.2(3)°], thus maintaining a largely delocalized ring system. Simultaneous TG and DSC thermal analyses indicated that this ligand is thermally stable up to ca. 360 °C, where sublimation, in air and at ambient pressure, occurs (apparently without chemical decomposition).

With the aim of obtaining metal-organic frameworks possessing pores of higher dimensions, that are usually dependent on the length of the organic bridge, a longer pyrazolate-based ligand has been designed, 4,4'-bis(1*H*-pyrazol-4-yl)biphenyl, **H_2PBP** (Figure 3.1). Unfortunately, the 1,1'-biphenyl-4,4'-di(acetic acid) derivative is not commercially available but can be easily prepared with a two-step conversion of the cheap and commercially available

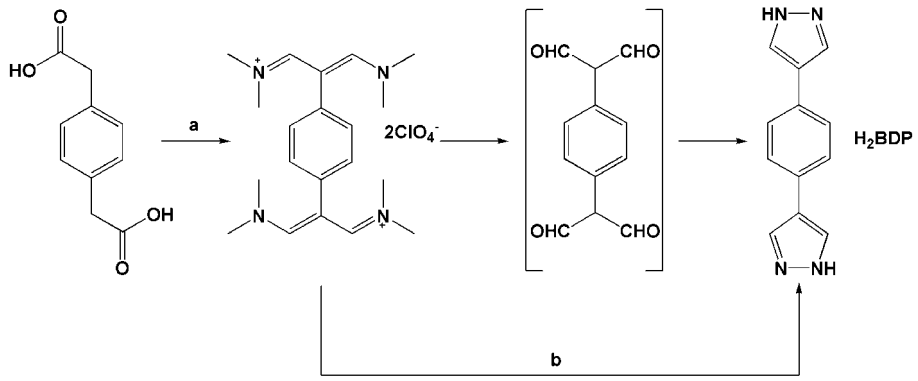

Scheme 3.1. Synthesis of the **1,4-bis(pyrazol-4-yl)benzene (H_2BDP)** ligand. (a) $POCl_3$, N,N-dimethylformamide, 90 °C, 11 h; Then, ice/water and $NaClO_{4(aq)}$. (b) $N_2H_4 \cdot H_2O$, ethanol, reflux, 2h.

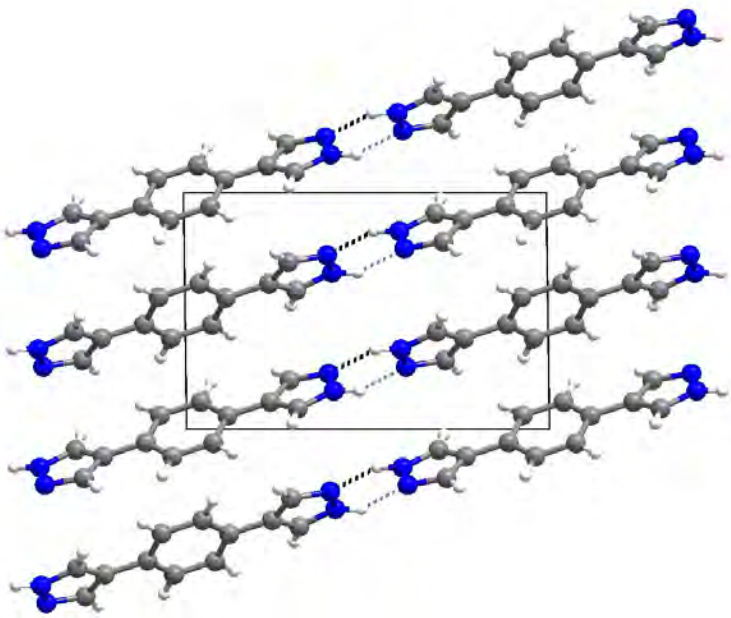

Figure 3.2. Crystal packing of **H_2BDP** viewed down [010]. The NH···N interactions are highlighted as dashed lines. Nitrogen, blue; carbon, gray; hydrogen, white.

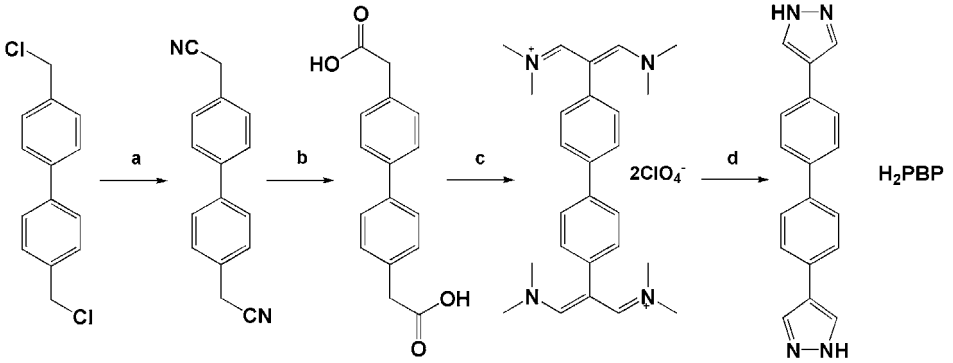

Scheme 3.2. Synthesis of the **4,4'-bis(1*H*-pyrazol-4-yl)biphenyl (H_2PBP)** ligand. (a) NaCN, dimethyl sulfoxide, 40° C, 8 h. Then, ice/water. (b) KOH (2 M), ethanol, reflux, 24 h. Then, $HCl_{(conc)}$. (c) $POCl_3$, N,N-dimethylformamide, 90 °C, 11 h; Then, water/ice and $NaClO_{4(aq)}$. (d) $N_2H_4 \cdot H_2O$, 2-methoxyethanol, reflux, 2 h.

4,4'-bis(chloromethyl)-1,1'-biphenyl (Scheme 3.2). Thus, a nucleophilic substitution of the chloride by the cyanide anion was performed and the dinitrile specie was then hydrolyzed to the desired 1,1'-biphenyl-4,4'-di(acetic acid) intermediate in basic media. At this point, the VHA formylation was successfully adopted, later followed by heterocyclization with hydrazine until formation of a pale yellow, highly insoluble precipitate of **H_2PBP**.[18] This ligand was recovered from solution as polycrystalline material, whose structure was retrieved by XRPD data. This rod-like molecule crystallizes in the *$P2_1/c$* space group, within a rather elongated cell, in which evident N-H···N interactions among neighboring molecules generate corrugated two-dimensional sheets of fishbone aspect, well separated from adjacent ones (Figure 3.3). Simultaneous TG and DSC analyses showed that the **H_2PBP** ligand undergoes sublimation under nitrogen atmosphere at about 400 °C.

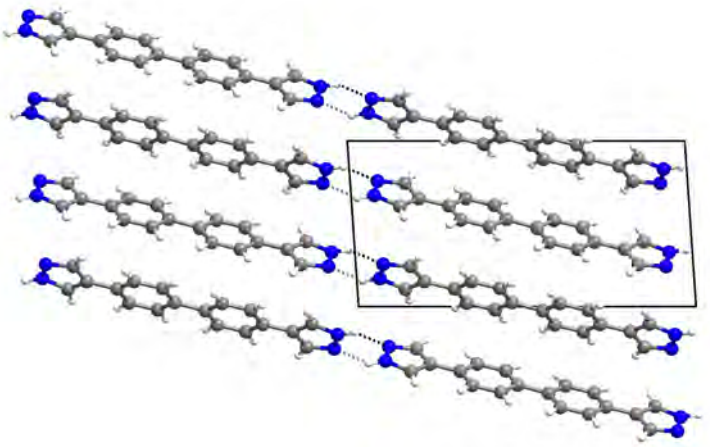

Figure 3.3. Crystal packing of **H_2PBP**, viewed down [010]. Nitrogen, blue; carbon, gray; hydrogen, white. Hydrogen bonds, depicted as fragmented lines, generate chains elongating along the [-201] direction; further hydrogen bond interactions along **b** connect the chains into corrugated 2D layers.

Similarly to what performed for these two linear bis-pyrazolate ligands, a triangular pyrazolate-based spacer, 1,3,5-tris(1*H*-pyrazol-4-yl)benzene, **H_3BTP**, could be synthesized following the same synthetic idea. Indeed, its synthesis was tailored on the basis of the available starting material: the 1,3,5-triacetyl benzene derivative was reacted following the triple-Willgerodt protocol for the preparation of the 1,3,5-benzenetriacetic acid intermediate (Scheme 3.3).[19] The corresponding tritopic **H_3BTP** was then obtained with the same sequence of reactions reported for the linear pyrazolate-based ligands.[20]

The 1,3,5-tris(1*H*-pyrazol-4-yl)benzene species, **H_3BTP**, despite its rather higher solubility, was recovered as a microcrystalline powder and structurally characterized by XRPD methods. This ligand crystallizes in the orthorhombic P*cab* space group. In its crystal structure, only one of the three pyrazole rings is found to be coplanar with the inner benzene ring, while the other two (in position 3 and 5) are

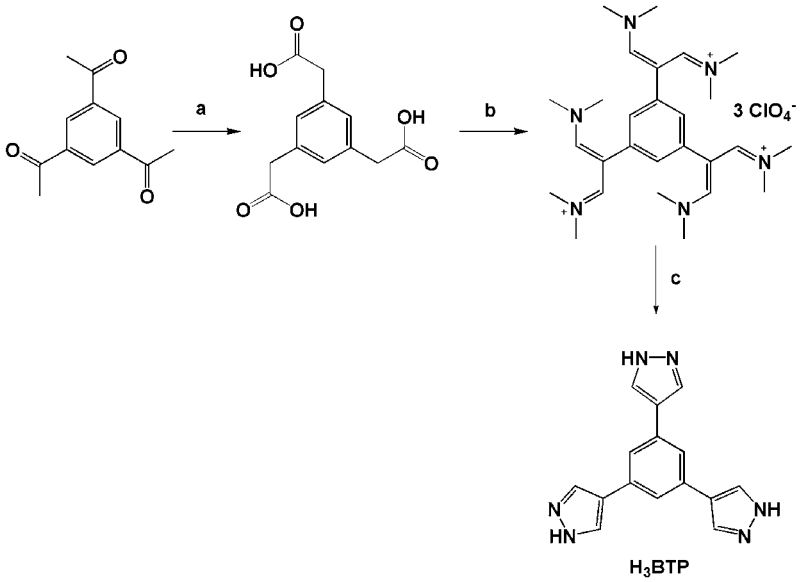

Scheme 3.3. Synthesis of the **1,3,5-tris(1*H*-pyrazol-4-yl)benzene (H_3BTP)** ligand. (a) S_8, morpholine, 120 °C, 20 h. Then, water; (b) $H_2SO_{4(conc.)}$, CH_3COOH, water, 100 °C, 15 h; (c) $POCl_3$, *N, N*-dimethylformamide, 90 °C, 15 h. Then, ice/H_2O, $NaClO_4$; (d) $N_2H_4 \cdot H_2O$, ethanol, reflux, 3 h.

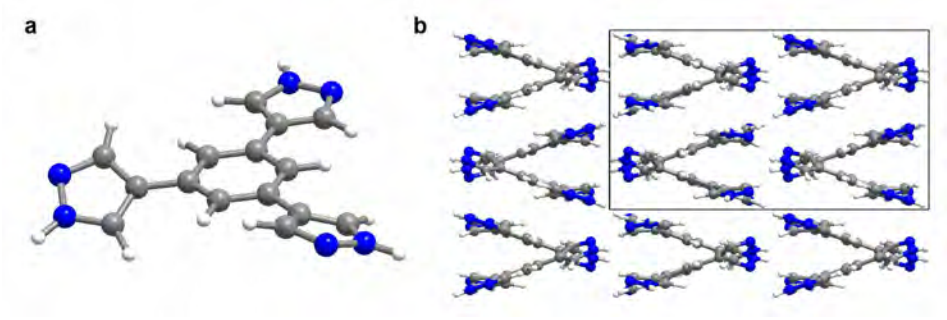

Figure 3.4. Crystal structure of **H_3BTP** in which are highlighted (a) the conformation of the molecules and (b) the interpenetrated crystal packing viewed down [010]. Nitrogen, blue; carbon, gray; hydrogen, white.

rotated with torsion angles that account for 20.2° and 28.2° respectively (Figure 3.4a). Moreover, in its crystal packing, the molecules are connected though several N-H···N interactions, generating an interpenetrated structure of wavy 2D sheets (Figure 3.4b).

Ligands bearing functional groups on the aromatic core. One of the current challenges is the development of stable MOFs including functional organic sites. The incorporation of ligands including additional functional moieties is not trivial, since such groups may directly coordinate to the metal ions mostly depending upon the chosen reaction conditions. For instance, only a few amine-functionalized frameworks are known out of the more than 10000 MOF structures reported in the literature.[21] Moreover, functional groups on the organic linkers, oriented to the inner of the pores, may influence the application properties of the material indipendently from its overall structure. Indeed, we concentrated our efforts on the synthesis of new otherwise functionalized pyrazolate-based ligands starting from the 1,4-bis(pyrazol-4-yl)benzene, **H_2BDP**, moiety (Figure 3.1). The choice of the parent ligand for the introduction of new functional groups on its aromatic core was done on the basis of the availability of the starting materials and the easiness of its synthesis.

The first functional group introduced on the aromatic spacer was a nitro group: 2-nitro[1,4-bis(1H-pyrazol-4-yl)benzene], H_2BDP_NO_2, was thus prepared by a simple nitration in sulfuric and nitric acid mixtures (Scheme 3.4).[22] Then, reduction of the nitro group was performed to obtain the 2-amino[1,4-bis(1H-pyrazol-4-yl)benzene] derivative, H_2BDP_NH_2.[23] The crucial point of this reaction was that, due to the high insolubility of the H_2BDP_NO_2 ligand, the reduction was carried out in N,N-dimethylformamide solution (Scheme 3.5) rather than adopting the most common strategies that involved the use of homogeneous methanolic solution.[24] Then, by exploiting the reactivity of the diazonium salts, readily available through primary aromatic amines, the amino group was con-

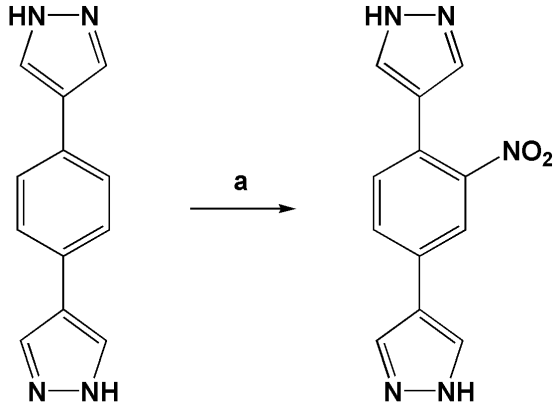

Scheme 3.4. Synthesis of the **2-nitro[1,4-bis(1H-pyrazol-4-yl)benzene] (H_2BDP_NO_2)** ligand. (a) H_2SO_4/HNO_3, 1 h, RT. Then, ice/water.

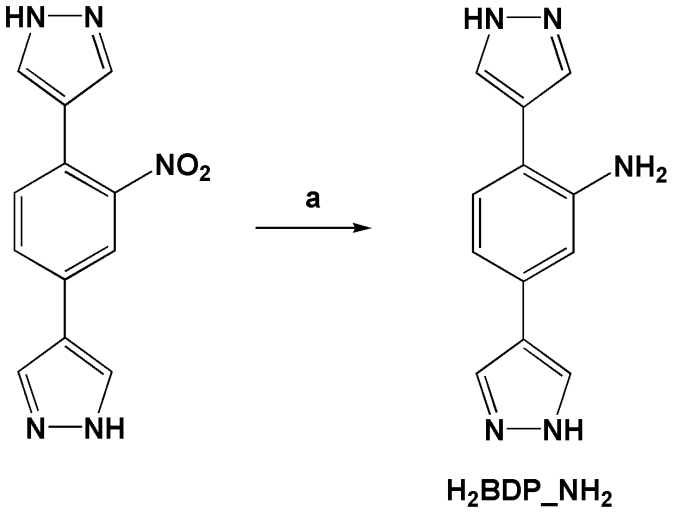

Scheme 3.5. Synthesis of the **2-amino[1,4-bis(1H-pyrazol-4-yl)benzene] (H_2BDP_NH_2)** ligand. (a) NH_4HCO_2, Pd/C, N, N-dimethylformamide, 110 °C, 2 h. Then, ice/water.

verted into an hydroxo functionality.[25] The preparation of the diazonium salt was performed by treatment of H_2BDP_NH_2 with nitrous acid, followed by hydrolysis of the diazonium salt, yielding the 2-hydroxo[1,4-bis(1H-pyrazol-4-yl)benzene] ligand, H_2BDP_OH (Scheme 3.6).

Another functionalization performed on the non-substituted **H_2BDP** ligand is the electrophilic aromatic substitution for the preparation of the benzene sulfonic acid, giving rise, according to our target, to 2,5-di(1*H*-pyrazol-4-yl)benzenesulfonic acid, **H_2BDP_SO_3H** (Scheme 3.7).

Since each functional group introduced on the organic linkers shows a characteristic signal in the IR region, the whole series of ligands was studied by means of IR spectroscopy (Figure 3.5).[26] In the IR spectra of the whole series of the ligands reported in this chapter the presence, in the region between 3000 and 3200 cm^{-1}, of the strong broad band typically found in 1*H*-pyrazoles, is attributed to the [ν(NH)] stretching mode.[27] Beside this broad band, the whole series of modified ligands, shows the typical absorption bands related to the presence of the functional group introduced on their benzene ring. Indeed, the FTIR spectrum of **H_2BDP_NO_2** shows a typical spectroscopy band at 1522 cm^{-1}, assigned to the asymmetric [$\nu(NO)_{asym}$] stretching mode. Unfortunately, the symmetric mode, [$\nu(NO)_{sym}$], is partially overshadowed by the strong band of the nujol mull and found at 1350 cm^{-1}. The presence of numerous bands in the lower frequencies region of the IR spectrum complicates the assignment of the C-N stretching vibration that should be present in the 920-850 cm^{-1} region. As well as for the latter, also the amino-tagged ligand, **H_2BDP_NH_2**, can be analyzed by IR spectroscopy: indeed, the two absorptions in the high frequency region at 3422 and 3338 cm^{-1} can be assigned to the asymmetric and symmetric N-H stretching modes, respectively. Is it also possible to distinguish another characteristic band at 1621 cm^{-1} related to the N-H bending vibration (scissoring).

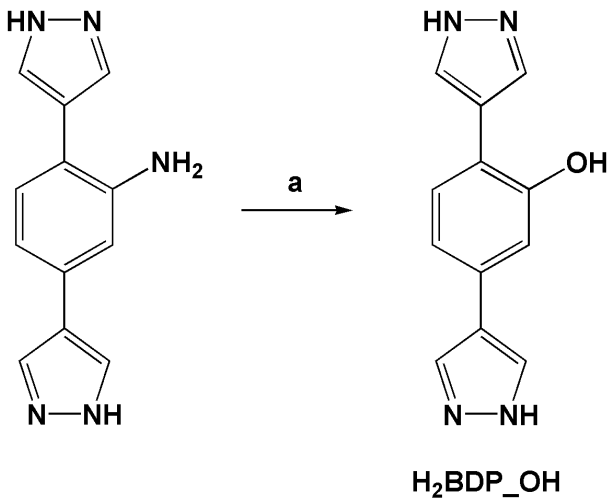

Scheme 3.6. Synthesis of the **2-hydroxo[1,4-bis(1H-pyrazol-4-yl)benzene] (H_2BDP_OH)** ligand. (a) H_2SO_4, $NaNO_2$. Then, H_2SO_4/water (1:1) 110 °C, 1 h and $NaHCO_3$, water, 80 °C, 1 h.

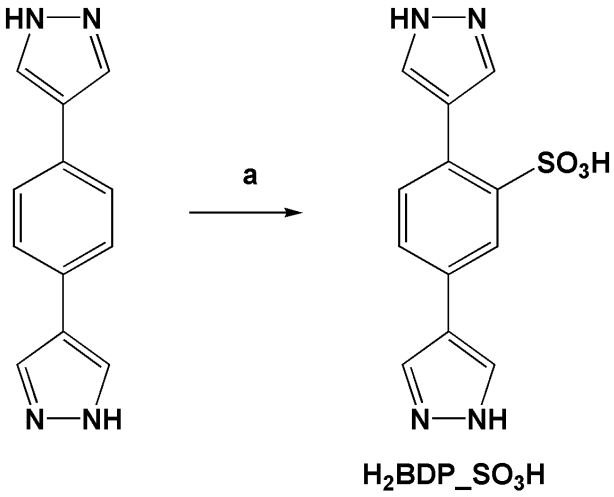

Scheme 3.7. Synthesis of the **2,5-di(1*H*-pyrazol-4-yl)benzenesulfonic acid (H_2BDP_SO_3H)** ligand. (a) $H_2SO_{4(conc.)}$, 1 h, RT. Then, ice/water.

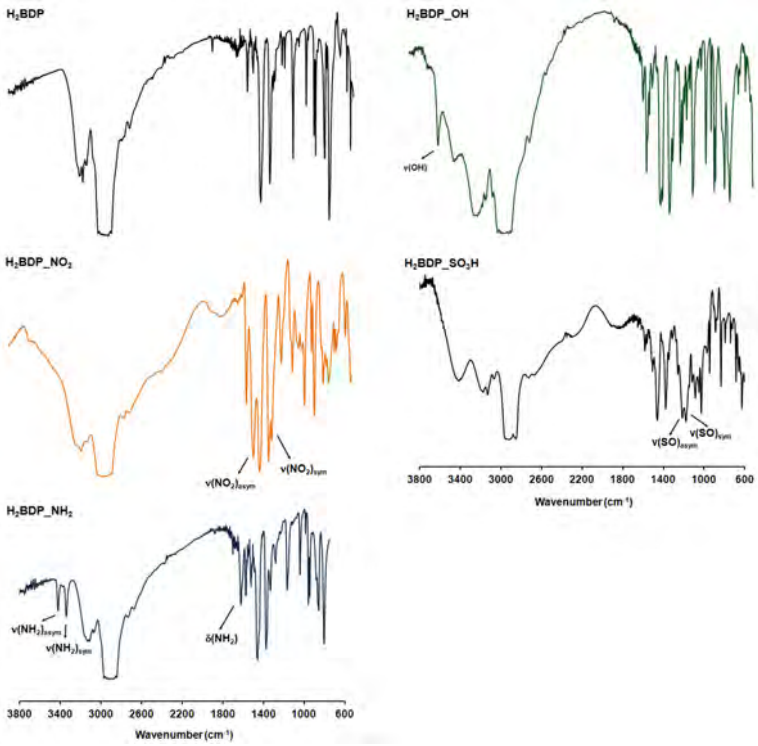

Figure 3.5. FTIR spectra of functionalized pyrazole-based ligands **H_2BDP_X** (X = NO_2, NH_2, OH, SO_3H)recorded as nujol mull and compared to the non-functionalized H_2BDP ligand. with highlighted the absorption bands attributed to each functional group.

In the IR spectrum of the **H_2BDP_OH** ligand, the region relevant for the OH-stretching modes of the hydroxyl group shows a broad signal centered at 3387 cm^{-1} (probably due to the presence of leftover water molecules from the synthesis process) with a sharpening at 3525 cm^{-1} assigned to the free -OH groups on the aromatic linker. Again, in the IR spectrum of the **H_2BDP_SO_3H** ligand, the presence of the introduced functional group can be confirmed by the strong IR absorption bands characteristic of sulfonic acid groups: the SO asymmetric

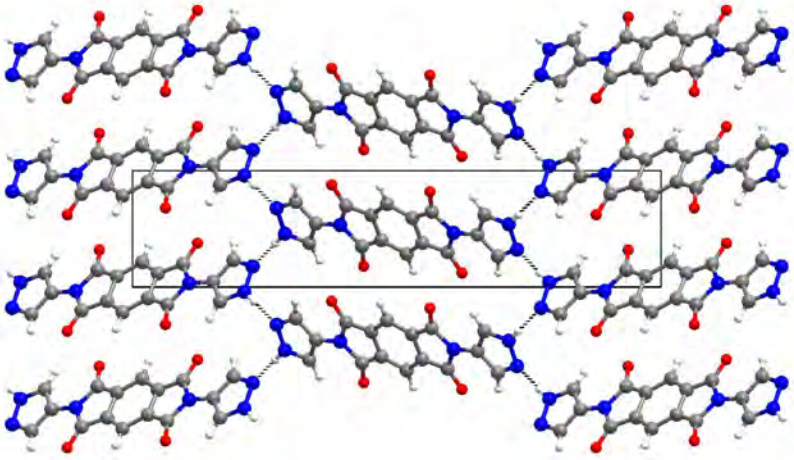

Figure 3.6. Crystal packing of **H_2TET**, viewed down [100]. Nitrogen, blue; oxygen, red; carbon, gray; hydrogen, white. Hydrogen bonds, depicted as fragmented lines, generate chains elongating along the [-104] direction; further hydrogen bond interactions along **b** connect the chains into corrugated 2D layers.

vibration, [**ν(**$SO)_{asym}$], is found at 1215 cm^{-1} as a medium band in the IR spectrum, while the symmetric stretching vibration, [**ν(**$SO)_{sym}$], appears around 1176 cm^{-1}. Unfortunately, the band assigned to the SOH bending, that should be found at ~ 1100 cm^{-1} is difficult to distinguish due to the presence of numerous bands in the lower frequencies. Moreover, the presence of a broad band at 2900 cm^{-1} it is probably attributable to the hydrate form of the sulfonic acid group (H_3O^+ stretching modes).[28]

Crystal structure solution of these ligands form powder diffraction data will be performed within the next future.

Pyrazolate Ligands with an aromatic bisimide core. Another class of polytopic pyrazolate-based ligands is characterized by a bisimide spacer linking the pyrazole rings, resulting from the use of an anhydride for their synthesis. The synthetic

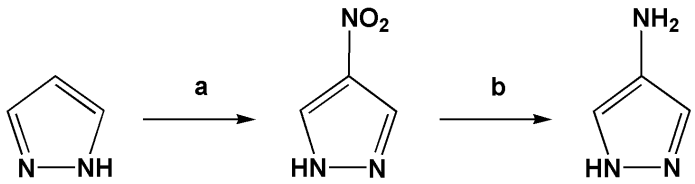

Scheme 3.8. Synthesis of the **4-amino-1*H*-pyrazole**. (a) H_2SO_4, HNO_3, 5 h, 55 °C. (b) H_2, Pd/C, ethanol.

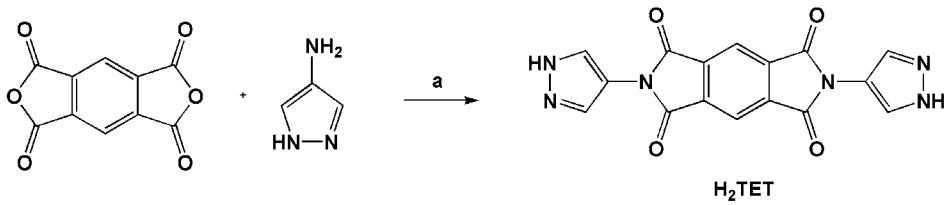

Scheme 3.9. Synthesis of the **2,6-bis(1*H*-pyrazol-4-yl)pyrrolo[3,4-*f*]isoindole-1,3,5,7(2*H*,6*H*)-tetrone (H_2TET)** ligand. (a) *N, N-dimethylacetamide*, reflux, 4 h.

strategy designed for this class of ligands is a really convenient and versatile one, due to the nature of the condensation reaction between an anhydride and an amino group. Once obtained the 4-amino pyrazole (prepared by nitration of the 1*H*-pyrazole followed by reduction of the nitro group, Scheme 3.8), the condensation with poly aromatic (di- or even tris-) anhydrides can be done in a one-pot reaction starting from soluble reagents, giving rise to a pure, insoluble product. Indeed, it is possible, in principle, to design and synthesize many types of ligands depending on the nature of the anhydride. However, in this thesis, only one example of ligand is presented, 2,6-bis(1*H*-pyrazol-4-yl)pyrrolo[3,4-*f*]isoindole-1,3,5,7(2*H*, 6*H*)-tetrone, **H_2TET**, prepared by reacting 4-aminopyrazole with pyromellitic anhydride in dimethylacetamide (DMA, Scheme 3.9). Worthy of note, this ligand shows a length comparable to that of the **H_2PBP** ligand (13.7 *vs* 14.2 Å) but the nature of

its bisimide core gives rise to a higher rigidity compared to the biphenyl-derivative, where a certain degree of flexibility about the exocyclic C-C links is expected.

As for the **H_2PBP**, **H_2TET** could be recovered only as a polycrystalline material and its structure was thus retrieved by XRPD. Probably due to the high similarity in geometry and length of the bisimide core with the parent biphenyl, this ligand is found to be isostructural with the **H_2PBP** one (Figure 3.6). However, the this ligand is even more thermally stable and decomposes at higher temperature (490 °C).

Hetero-functional ligands. In addition to purely azolate-based ligands, the vast repertoire of organic chemistry also allows the synthesis of organic molecules that include more than one type of potential coordination functional groups into their structure (*e.g.*, O-donor and N-donor). This combination of donor types, into a singular entity, allows the formation of a greater diversity of clusters and structures. For example, hetero-functional azolate-based ligands such as pyridine-tetrazolates,[29] carboxylate-tetrazolates,[30] imidazole-tetrazolates,[31] or pyridine-carboxylates,[32] have already been reported in the synthesis of metal-organic frameworks. However, the majority of structures are still synthesized serendipitously.

In this thesis, the potential of polytopic heterofunctional ligands to construct MOFs with topologies of interest is also explored with the use of a very simple pyrazole-carboxylate ligand: 4-carboxypyrazole (**H_2CPZ**, Figure 3.1). The reasons behind this choice are multiple: first, to the best of our knowledge, no examples of hetero-functional ligands based on pyrazoles are known in the literature. Moreover, an sp^3 oxygen atom, such as those in carboxylate ligands, usually coordinates in a variety of modes (typically up to three metal ions) compared to the coordination ability of the N-donors, that generally coordinate to only one transition-metal ion in the same direction as its lone electron pair. This could led to a number

of new structures featuring the main coordinative characteristics of the two different donors. Again, the ability of the pyrazolate anion in generating polymers of highly stable (chemically and thermally) nature is an important concept for a metal-organic framework: the pyrazolate branch in the heterofunctional ligand can thus impart a higher stability compared to the fully O-based polymers. Interestingly, it is worthy of note that the use of short ligands could also give rise to the formation of small pores into the metal-organic framework (that may be defined by the length of the linker) for useful applications in molecular sieving, adsorption of small gas molecules, as well as separation of isomers by size and shape selective mechanisms.[33]

The carboxypyrazolate ligand (**H_2CPZ**) was thus obtained according to the literature method originally proposed by C. Foces-Foces *et al.*[34] Notably, even though the synthesis was published already in 2001, no examples of porous coordination polymers exploiting this ligand have been found in the literature.

Conclusions

An important key feature of porous materials is their chemical and thermal inertness. Unfortunately, in most cases, these materials do not approach a robustness such that the development of their application in industrial processes can become a reality. In this regards, a number of new pyrazolate-based ligands as building-blocks for the synthesis of porous metal-organic frameworks have been here presented. The choice of this class of ligands has been done on the basis of the fact that the strength of the N-M bond in pyrazolate-based complexes, compared to the O-M bonds of those based on carboxylates, can afford polymers featuring higher stabilities (in terms of chemical and thermal robustness). Such advancements could extend the utility of metal-organic frameworks towards a variety of applications where zeolites have been widespread utilized. Moreover, pyrazolate-based ligands have not been widely

explored in the chemistry of metal-organic frameworks, thus leaving plenty of room for the discovery of new coordination compounds or even porous polymers containing polytopic pyrazolate-based ligands bridged by the metal clusters typically found in the chemistry of simple 1*H*-pyrazoles.

Acknowledgements

This work was supported by the Italian MIUR (PRIN2006: "Materiali Ibridi Metallo-Organici Multifunzionali con Leganti Poliazotati"), Fondazione Cariplo (Project 2007-5117), FP7-EU (nanoMOF), Spanish MCINN (CTQ2008-00037/PPQ) and Junta de Andalucía. For the **H_3BTP** ligand, the research was supported in the US by the Department of Energy under Contract No. DE-AC02-05CH11231.

References and Notes

1 (a) Matsuda, R.; Kitaura, R.; Kitagawa, S.; Kubota, Y.; Belosludov, R. V.; Kobayashi, T. C.; Sakamoto, H.; Chiba, T.; Takata, M.; Kawazoe, Y.; Mita, Y. *Nature* **2005**, *436*, 238. (b) Millward, A. R.; Yaghi, O. M. *J. Am. Chem. Soc.* **2005**, *127*, 17998. (c) Furukawa, H.;Miller,M. A.;Yaghi,O.M. *J.Mater. Chem.* **2007**, *17*, 3197. (d) Ma, S.; Sun, D.; Simmons, J.M.; Collier, C. D.; Yuan, D.; Zhou, H. C. *J. Am. Chem. Soc.* **2008**, *130*, 1012. (e) Morris, R. E.;Wheatley, P. S. *Angew. Chem., Int. Ed.* **2008**, *47*, 4966. (f) Llewellyn, P. L.; Bourrelly, S.; Serre, C.; Vimont, A.; Daturi, M.; Hamon, L.; De Weireld, G.; Chang, J.-S.; Hong, D.-Y.; Hwang, Y. K.; Jhung, S. H.; Férey, G. *Langmuir* **2008**, *24*, 7245. (g) Furukawa, H.; Ko, N.; Go, Y. B.; Aratani, N.; Choi, S. B.; Choi, E.; Yazaydin, A. Ö.; Snurr, R. Q.;O'Keeffe, M.;Kim, J.; Yaghi, O.M. *Science* **2010**, *329*, 424.

2 (a) Natarajan, S.; Mahata, P. *Curr. Opin. Solid State Mater. Sci.* **2009**, *13*, 46. (b) Almeida Paz, F. A.; Klinowski, J.; Vilela, S. M. F.; Tomé , J. P. C.; Cavaleiroc, J. A. S. and Rocha, J. *Chem. Soc. Rev.* **2011**, DOI: 10.1039/c1cs15055c. (c) Zhao, D.; Timmons, D. J.; Yuan, D.; Zhou, H.-C. *Acc. Chem. Res.* **2011**, *44*, 123.

3 (a) Dincă, M.; Yu, A. F.; Long, J. R. *J. Am. Chem. Soc.* **2006**, *128*, 8904. (b) Dincă, M.; Dailly, A.; Liu, Y.; Brown, C. M.; Neumann, D. A.; Long, J. R. *J. Am. Chem. Soc.* **2006**, *128*, 16876. (c) Dincă, M.; Han, W. S.; Liu, Y.; Dailly, A.; Brown, C. M.; Long, J. R. *Angew. Chem. Int. Ed.* **2007**, *46*, 1419. (d) Dincă, M.; Long, J. R. *J. Am. Chem. Soc.* **2007**, *129*, 11172. (e) Dincă, M.; Dailly, A.; Tsay, C.; Long, J. R. *Inorg. Chem.* **2008**, *47*, 11. (f) Sumida, K.; Horike, S.; Kaye, S. S.; Herm, Z. R.; Queen, W. L.; Brown, C. M.; Grandjean, F.; Long, G. J.; Dailly, A.; Long, J. R. *Chem. Sci.* **2010**, *1*, 184. (g) Sumida, K.; Horike, S.; Bloch, E. D.; Foo, M. L.; Murray, L. J.; Long, J. R. *unpublished results*. (h) Horike, S.; Dincă, M.; Tamaki, K.; Long, J. R. *J. Am. Chem. Soc.* **2008**, *130*, 5854. (i) Demessence, A.; D'Alessandro, D. M.; Foo, M. L.; Long, J. R. *J. Am. Chem. Soc.* **2009**, *131*, 8784.

4 (a) Masciocchi, N.; Ardizzoia, G. A.; LaMonica, G.; Maspero, A.; Sironi, A. *Eur. J. Inorg. Chem.* **2000**, 2507. (b) Barea, E.; Navarro, J. A. R.; Salas, J. M.; Masciocchi, N.; Galli,

S.; Sironi, A. *Inorg. Chem.* **2004**, *43*, 473. (c) Park, K. S.; Ni, Z.; Côté, A. P.; Choi, J. Y.; Huang, R.; Uribe-Romo, F. J.; Chae, H. K.; O'Keeffe, M.; Yaghi, O. M. *Proc. Natl. Acad. Sci. USA* **2006**, *103*, 10186.

5 Bordwell, F. G. *Acc. Chem. Res.* **1988**, *21*, 456. Given value for non-substituted tetrazole (pK_a = 4.9); 1,2,3-triazole (pK_a = 13.9); imidazole (pK_a = 18.6) and pyrazole (pK_a = 19.8). Note that these values are referenced to DMSO.

6 (a) Hayashi, H.; Côté, A.P.; Furukawa, H.; O'Keeffe, M.; Yaghi, O.M., *Nature Materials* **2007**, *6*, 501. (b) Banerjee, R.; Phan, A.; Wang, B.; Knobler, C.; Furukawa, H.; O'Keeffe, M.; Yaghi, O. M. *Science* **2008**, *319*, 939.

7 Phan, A.; Doonan, C. J.; Uribe-Romo, F. J.; Knobler, C. B.; O'Keeffe, M.; Yaghi, O. M. *Acc. Chem. Res.* **2010**, *43*, 58.

8 Arnold, Z. *Coll. Czech. Chem. Commun*. **1985**, *30*, 2783

9 M.p. = 182-185 °C in Addison, A. W.; Dalai, N. S.; Hoyano, Y.; Huizinga, S.; Weiler, L. *Can. J. Chem.* **1977**, 4191.

10 M.p. = 282-284 °C in Schwenk, E.; Papa, D. *J. Org. Chem.* **1946**, *11*, 798.

11 (a) M. S. Newmann and H. S. Lowrie, *J. Am. Chem. Soc.,* 1954, **76**, 6196. (b) R. Gompper, Gompper, C. Harfmann and K. Polborn, *J. Prakt. Chem*., 1998, **340**, 381.

12 Version 3.0, Bruker AXS, 2005, Karlsruhe, Germany.

13 Cheary, R.W.; Coelho, A. *J. Appl. Cryst.*, **1998**, *31*, 851-861; *ibid.* 862-868.

14 For reviews on the chemistry of vinamidinium salts, see: (a) Lloyd, D.; McNab, H. *Angew. Chem., Int. Ed. Engl.* **1976**, *15*, 459. (b) Gompper, R.; Harfmann, C.; Polborn, K. *J. Prakt. Chem.* **1998**, *340*, 381. (c) Gompper, R.; Müller, T. J. J.; Polborn, K. *J. Mater. Chem.* **1998**, *8*, 2011.

15 (a) Marson, C. M. *Tetrahedron* **1992**, *48*, 3659. (b) Jutz, C. in *Advances in Organic Chemistry*, (Eds. E. C. Taylor), John Wiley & Sons, N. Y., **1976**, *9*, 252. (c) Reichardt, C. *J. Prakt. Chem.* **1999**, *341*, 609.

16 Lozan, V.; Solntsev, P. Y.; Leibeling, G.; Domasevitch, K. V.; Kersting, B. *Eur. J. Inorg. Chem.* **2007**, 3217.

17 Maspero, A.; Galli, S.; Masciocchi, N.; Palmisano, G. *Chemistry Letters* **2008**, *37*, 956.

18 Masciocchi, N.; Galli, S.; Colombo,V.; Maspero, A.; Palmisano, G.; Seyyedi, B.; Lamberti, C.; Bordiga, S. *J. Am. Chem. Soc.* **2010**, *132*, 7902.

19 Newmann, M. S.; Lowrie, H. S. *J. Am. Chem. Soc.* **1954**, *76*, 6196.

20 Colombo, V.; Galli, S.; Choi, H. J.; Han, G. D.; Maspero, A.; Palmisano, G.; Masciocchi, N.; Long, J. R. *Chem. Sci*. **2011**, *2*, 1311.

21 (a) Gascon, J.; Aktay, U.; Hernandez-Alonso, M. D.; van Klink, G. P. M.; Kapteijn, F. *J. Catal.* **2009**, *261*, 75. (b) Couck, S.; Denayer, J. F. M.; Baron, G. V.; Remy, T.; Gascon, J.; Kapteijn, F. *J. Am. Chem. Soc.* **2009**, *131*, 6326. (c) Bauer, S.; Serre, C.; Devic, T.; Horcajada, P.; Marrot, J.; Ferey, G.; Stock, N. *Inorg. Chem.* **2008**, *47*, 7568. (d) Savonnet, M.; Bazer-Bachi, D.; Bats, N.; Perez-Pellitero, J.; Jeanneau, E.; Lecocq, V.; Pinel, C.; Farrusseng, D. *J. Am. Chem. Soc.* **2010**, *132*, 4518. (e) Ahnfeldt, T.; Guillou, N.; Gunzelmann, D.; Margiolaki, I.; Loiseau, T.; Ferey, G.; Senker, J.; Stock, N. *Angew. Chem., Int. Ed.* **2009**, *48*, 5163.

22 Gross, R. S.; Guo, Z.; Dyck, B.; Coon, T.; Huang, C. Q.; Lowe, R. F.; Marinkovic, D.; Moorjani, M.; Nelson, J.; Zamani-Kord, S.; Grigoriadis, D. E.; Hoare, S. R. J.; Crowe, P. D.; Bu, J. H.; Haddach, M.; McCarthy, J.; Saunders, J.; Sullivan, R.; Chen, T.-K; Williams J. P. *J. Med. Chem.* **2005**, *48*, 5780.

23 Jagtap, P. G.; Baloglu, E.; Southan, G. J.; Mabley, J. G.; Li, H.; Zhou, J.; van Duzer, J.; Salzman, A. L.; Szabo, C. *J. Med. Chem.* **2005,** *48,* 5100.

24 See *e.g.*: (a) Li, N-.H.; Frechet, J. M. J. *J. Chem. Soc., Chem. Comm.* **1985**, *16*, 1100. (b) Kumbhar, P. S.; Sanchez-Valente, J.; Figueras, F. *Tetrahedron Letters* **1998**, *39*, 2573.

25 See, *e.g.*: Raiford; C. *J. Am. Chem. Soc.* **1925**, *47*, 1456.

26 Colthup, N. B.; Daly, L. H.; Wiberly, S.E. *Introduction to IR and Raman spectroscopy*. Academic Press, New York, **1975**.

27 Zecchina, A.; Cerruti, L.; Coluccia, S.; Borello, E. *J. Chem Soc. B* **1967**, 1363.

28 Larkin, P. *Infrared and Raman Spectroscopy; Principles and Spectral Interpretation*, Elsevier **2011**, ISBN 978-0-12-386984-5.

29 (a) Jiang, C.; Yu, Z.; Wang, S.; Jiao, C.; Li, J.; Wang, Z.; Cui, Y *Eur. J. Inorg. Chem.* **2004**, 3662. (b) Luo, T.; Tsai, H.; Yang, S.; Liu, Y.; Yadav, R. D.; Su, C.; Ueng, C.; Lin, L.; Lu, K. *Angew. Chem. Int. Ed.* **2005**, *44*, 6063. (c) Xiong, R.; Xue, X.; Zhao, H.; You, X.; Abrahams, B. F.; Xue, Z. *Angew. Chem. Int. Ed.* **2002**, *41*, 3800. (d) Xue, X.; Wang, X.; Wang, L.; Xiong, R.; Abrahams, B. F.; You, X.; Xue, Z.; Che, C-M. *Inorg. Chem.* **2002**, *41*, 6544.

30 (a) Li, J.; Tao, J.; Huanga, R.; Zhang, L. *Acta Crystallogr.* **2005**, *E61*, m984. (b) Qu, Z. -R.; Zhao, H.; Wang, X. -S.; Li, Y. -H.; Song, Y. -M.; Liu, Y. -J.; Ye, Q.; Xiong, R. -G.; Abrahams, B. F.; Xue, Z. -L.; You, X. -Z. *Inorg. Chem.* **2003**, *42*, 7710.

31 Zhao, H.; Ye, Q.; Wu, Q.; Song, Y.; Liu, Y.; Xiong, R. *Z. Anorg. Allg. Chem.* **2004**, *630*, 1367.

32 (a) Kondo, M.; Okubo, T.; Asami, A.; Noro, S. -I.; Yoshitomi, T.; Kitagawa, S.; Ishii, T.; Matsuzaka, H.; Seki, K. *Angew. Chem. Int. Ed.* **1999**, *38*, 140. (b) Evans, O. R.; Lin, W. *Acc. Chem. Res.* **2002**, *35*, 511.

33 D. Farruseng (Ed.) *Metal-Organic Frameworks: Applications from Catalysis to Gas Storage* Wiley-VCH, **2011**.

34 Foces-Foces, C.; Echevarría, A.; Jagerovic, N.; Alkorta, I.; Elguero, J.; Langer, U.; Klein, O.; Minguet-Bonvehí, M.; Limbach, H.-H. *J. Am. Chem. Soc.* **2001**, *123,* 7898.

Chapter 4
Adsorption of Harmful Organic Vapors by Flexible Hydrophobic Bis-pyrazolate based MOFs

Introduction

The last years have witnessed a blooming of research interest on the preparation, characterization and optimization of porous functional materials based on metal ions linked by long organic spacers in three dimensional networks, with the aim of obtaining outperforming adsorbents.[1,2]

The pioneering work of Yaghi's,[3] Kitagawa's,[4] and Férey's,[5] groups has been mainly based on porous metal polycarboxylates possessing remarkable functional properties. Several, chemically and thermally stable, porous metal polycarboxylates have been isolated; yet, the easy hydrolyzability of the metal-carboxylate bonds,[6] or the high affinity for water of coordinatively unsaturated metal centers, are main drawbacks for their practical applications, if they have to compete with classical hydrophobic adsorbents like activated carbons.[7] In this thesis it has been widely discussed that polyazolate systems, such as tetrazolate, triazolate, imidazolate and pyrazolate, offer a closely related stereochemistry to carboxylates and, at the same time, a higher basicity, possibly guaranteeing more robust coordinative bonds.[8]

More recent reports have further substantiated the viability of the polyazolate approach to functional porous systems,[9] like MOF-5 analogues exhibiting sensing[10] and catalytic activity.[11]

In the last decade, release of harmful chemicals into our environment became a worldwide growing concern and the effective capture of these chemicals is of great importance for both the protection of the environment and of those who are exposed to such species.[12] Within this issue, there is a demand to reduce the content of sulfur-containing compounds, such as thiophene or benzothiophene, from natural gas and petroleum products both to reduce SO_2 emissions from fuel combustion and to avoid poisoning the precious metals catalysts used to upgrade the oil octane rating. So far, various methods have been investigated for sulfur removal: the main industrial process is hydrodesulfurization (HDS) in which sulfur compounds are hydrogenated to hydrocarbons and H_2S over, tipically, CoMo catalysts.[13] Adsorption is another attractive alternative for removal of these contaminants. Well-studied classes of porous materials such as activated carbons and zeolites have been shown to adsorb S-containing compound.[14] However, the current applications of activated carbons, and their performances, are largely limited by the lack of control over the dimensions and functionality of the pores due to the highly amorphous nature of its carbon network.

Very recently, the MOFs-type materials have also been investigated for the removal of S-compounds[15] or harmful organic vapors, like, *e.g.* benzene and cyclohexane.[16] For an efficient adsorption, some factors seems to be important like the presence of open metal sites,[17] or the pore functionality.[7] However, the effect of the presence of moisture in the vapor adsorption performances, currently a main drawback of MOF's practical applications, have never been deeply evaluated.

In Chapter 3 of this thesis the extensive work done in tailoring high-yield and cheap syntheses of the 1,4-bis(*1H*-pyrazol-4-yl)benzene ligand, H_2BDP,[18] is de-

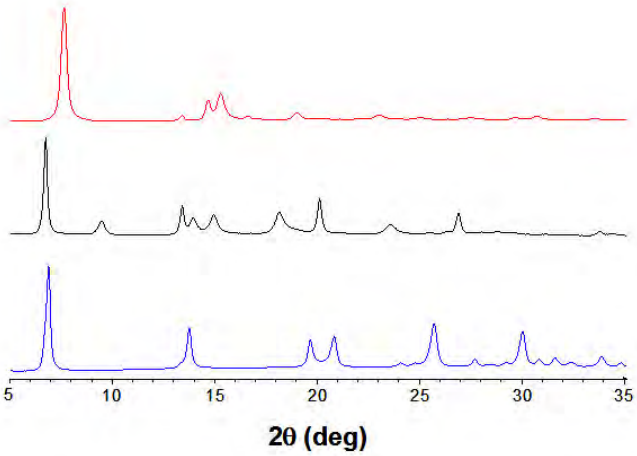

Figure 4.1. Plot of the low-angle portion (5 < 2θ < 30°) of the XRPD patterns of **Ni(BDP)**, **Zn(BDP)•2PhCN** and **Cu_2(BDP)** phases (top to bottom), showing less-than-ideal traces with evident anisotropic peak broadening.

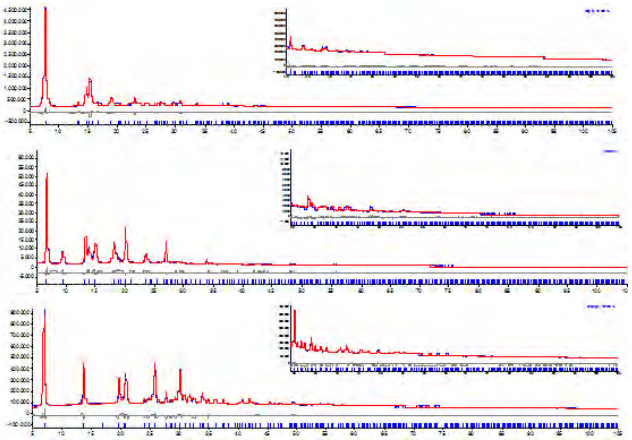

Figure 4.2. Rietveld refinement plots for species **Ni(BDP)**, **Zn(BDP)·2PhCN** and **Cu_2(BDP)** (top to bottom) with peak markers and difference plot at the bottom. The inserts show the high-angle regions at a magnified scale.

scribed and made it possible to investigate its coordination chemistry toward transition metal ions, in the search for homoleptic porous materials with high chemical and thermal stability, as well as selective adsorptive and catalytic properties.

Accordingly, in the following, the preparation and structural characterization by X-ray powder diffraction analysis of two new highly porous pyrazolate-based metal-organic frameworks, **NiBDP** and **ZnBDP** (see Figure 4.1-4.2), is presented. Worthy of note, these porous materials show an interesting framework flexibility and a high thermal stability. Moreover, their adsorptive and separation properties (in either static and dynamic conditions) towards gases (N_2, Ar, CH_4, CO_2) and harmful volatile organic compounds (thiophene, benzene, cyclohexane) have also been investigated, both in dry and humid conditions. Indeed, in the vapor adsorption performances, it has been demonstrated that even some of the best performing materials, as $Cu_3(btc)_2$ (H_3btc = 1,3,5-benzenetricarboxylic acid)[7] become inactive in the removal of organic vapor when moisture is present during the separation process.

Experimental Details

Chemicals. All chemicals were of reagent grade and used as commercially obtained. The starting materials 1,4-bis(4-pyrazolyl)-benzene (H_2BDP) was prepared as described in Chapter 2, while $Cu_3(btc)_2$ was prepared following a procedure previously reported.[19]

Synthesis of NiBDP. $Ni(CH_3COO)_2$ (0.084 g, 0.47 mmol) was added to a solution of acetonitrile (6 mL) and stirred at room temperature. Then, H_2BDP (0.100 g, 0.47 mmol) was added to the solution in one single portion. The mixture was then heated to 60 °C; after 2 min, triethylamine (1.5 mL) was added. The reaction was then kept at 80 °C for 8 h. The dark orange precipitate was filtered off, washed with acetonitrile, methanol and dried in vacuum. When necessary, the unreacted ligand was eliminated by washing the impure powder in dimethyl sulf-

oxide, DMSO, (4 mL, at 60 °C for 15 min). Depending on the experimental conditions, the material may contain variable amounts of solvent molecules within the framework cavities. As proved by XRPD, the presence of solvent affects the actual values of the unit cell parameters, yet not the main structural features, with full retention of the space group symmetry. Thus, for sake of simplicity, most of the characterization (elemental analysis, IR spectroscopy and structure determination) was carried out on a thoroughly evacuated batch, prepared by drying the pure precipitate in vacuum at 150 °C for 4 h. Yield: 70%. IR (nujol): 1581 (s), 1270 (w), 1178 (w), 1144 (m), 1060 (s), 957 (m), 817 (vs), 723 (w) cm^{-1}. Anal. Calcd. for $C_{12}H_8NiN_4$ (266.7 g mol^{-1}): C, 54.00; H, 3.02; N, 20.99. Found: C, 53.70; H, 3.58; N, 20.87.

An alternative procedure for the production of **NiBDP** in a pure form was later on discovered (see Chapter 7): H_2BDP (0.5 mmol) was dissolved in DMF (10 mL) in a 50 mL schlenk flask and heated to 60 °C. $Ni(CH_3COO)_2 \cdot 4H_2O$ (0.5 mmol) was then added to the solution under stirring. The mixture was allowed to react for 5 h at reflux. After cooling at room temperature, the orange solid was collected by filtration, washed with methanol (3 × 10 mL) and dried under vacuum. The solid was found to be pure from any trace of unreacted ligand. Anal. Calcd. for $C_{18}H_{27}N_5NiO_4$ (436.13 g mol^{-1}): C, 49.57; H, 6.24; N, 16.06. Found: C, 49.02; H, 6.02; N, 16.20.

Benzene loaded samples to be employed in thermodiffractometric analyses (see below) were prepared according to the following procedure: a **NiBDP** batch prepared following the synthetic procedure in acetonitrile was evacuated under mild heating (140 °C) and 10^{-3} mmHg pressure for about 3 h, then suspended in benzene, and stirred for about 1/2 h. After this treatment, it was filtered and immediately sent to the powder diffractometer for evaluation of its desorption kinetics.

Synthesis of ZnBDP·2PhCN. Solid H_2BDP (0.100 g, 0.47 mmol) was added to a solution of $Zn(ClO_4)_2 \cdot 6H_2O$ (0.177 g, 0.47 mmol) in benzonitrile (6 mL). The

mixture was heated at 70 °C; after 2 min, triethylamine (1.5 mL) was added. The reaction was then kept at 150 °C for 4 h. After cooling the reaction vessel down to RT, the white precipitate was filtered off, washed with benzonitrile, methanol and dried in vacuum at RT to afford the final product. Yield: 90%. IR (nujol): 1584 (s), 1350 (s), 1286 (m), 1174 (m), 1133 (s), 1056 (vs), 956 (s), 826 (vs), 723 (w) cm^{-1}. Anal. Calcd. for $C_{26}H_{18}N_6Zn$ (479.86 g mol^{-1}): C, 65.08; H, 3.78; N, 17.51. Found: C, 65.13; H, 3.90; N, 17.47. Depending on the experimental conditions, the polycrystalline material is recovered with variable amounts of solvent molecules hosted in the crystal lattice. For the sake of coherence, most of the characterization (elemental analysis, IR spectroscopy and structure determination) was carried out on the batch showing the highest degree of crystallinity – incidentally, the one possessing two molecules of PhCN per formula unit. A thoroughly evacuated batch can be prepared by drying the washed precipitate in vacuum at 150 °C for 4 h.

As in the case reported above, another synthetic procedure, employing N,N-dimethylformamide as solvent, can be performed: H_2BDP (0.5 mmol) was dissolved in DMF (10 mL) in a 50 mL schlenk flask and heated to 60 °C. $Zn(CH_3COO)_2{\cdot}2H_2O$ (0.5 mmol) was then added to the solution under stirring. The mixture was allowed to react for 5 h at reflux. After cooling at room temperature, the white solid was collected by filtration, washed with methanol (3 × 10 mL) and dried under vacuum. Anal. Calcd. for $C_{20}H_{30}N_6ZnO_4$ (483.88 g mol^{-1}): C, 49.64; H, 6.25; N, 17.37. Found: C, 49.23; H, 5.98; N, 17.42.

Synthesis of Cu_2BDP. To a solution of $Cu(NO_3)_2{\cdot}3H_2O$ (0.115 g, 0.47 mmol) in benzonitrile (6 mL) solid H_2BDP (0.100 g, 0.47 mmol) was added in one single portion under stirring. The mixture was heated to 60 °C and after 2 min tributylamine (1.5 mL) was added. The reaction was then kept at 140 °C for 8 h. After cooling the reaction vessel down to RT, the light brown precipitate was filtered off, washed with benzonitrile, methanol and dried in vacuum at RT. Another

washing in DMSO (4 mL) was necessary at 60 °C (15 min) to eliminate unreacted H_2BDP. The precipitate was dried in vacuum at 140 °C for 4 h to afford the final product, resulting from an unexpected *in situ* reduction of the Cu(II) ions. Notably, preparation of Cu_2BDP directly from different Cu(I) precursors as $[Cu(CH_3CN)_4]BF_4$ or CuCl, in a variety of solvents (DMSO, acetonitrile, benzonitrile or *n*-butanol) and in presence of triethylamine, never afforded the desired species. Yield: 70%. IR (nujol): 1575 (s), 1252 (w), 1180 (w), 1147 (m), 826 (s), 643 (w) cm^{-1}. Anal. Calcd. for $C_{12}H_8Cu_2N_4$ (335.31 g mol-1): C, 42.97; H, 2.39; N, 16.71. Found: C, 42.23; H, 3.08; N, 17.27.

Gas Adsorption Measurements. Conventional adsorption isotherms were measured using a Micromeritics Tristar 3000 volumetric instrument under continuous adsorption conditions. Brunauer-Emmet-Teller (BET) and Langmuir analyses were used to determine the total specific surface areas for the N_2 and Ar isotherms at 77 K. High pressure adsorption isotherms for CO_2 and CH_4 at 273 K were measured with a homemade volumetric adsorption instrument (University of Granada) equipped with two Baratron absolute pressure transducers (MKS type 627B). Their pressure ranges are 0-133.33 kPa and 0-3333.25 kPa, and the reading accuracy is 0.05% of the usable measurement range. Prior to measurement, powdered samples were heated at 403 K for 12 h and outgassed to 10^{-6} Torr.

Static Vapor Adsorption Studies. The vapor adsorption isotherms for benzene and cyclohexane were acquired at 303 K. All samples were kept for 24 h at each pressure value in order to guarantee that equilibrium was achieved. The amount of vapor adsorbed was measured gravimetrically in a calibrated spring.

Breakthrough Curve Tests. Thiophene removal ability of **ZnBDP**, **NiBDP** and $Cu_3(btc)_2$ (btc = benzene-1,3,5-tricarboxylate)[20] from a He:CO_2:CH_4 gas mixture (about 1:1:2.25 v/v) was examined by a breakthrough experiment using a flow of He:CO_2:CH_4 containing *ca.* 30 ppm of thiophene. The porous materials (*ca.* 0.25 g in the form of pellets)[21] were packed into a glass column (0.3 cm inner diameter × 5 cm

length). Helium gas was initially purged into the sample column. The column was maintained at 298 K. The gas mixture (100 kPa) was dosed into the column at a flow rate of 30 mL min^{-1}. The presence of humidity after adsorbent activation and the concomitant effect on thiophene removal was also investigated. The relative amounts of the gases passing through the column were monitored on a mass spectrometer gas analysis system (Pfeiffer vacoon) detecting ion peaks at *m/z* 4 (He), 16 (CH_4), 18 (H_2O), 44 (CO_2) and 84 (thiophene).

X-ray Powder Diffraction Analysis. Powdered, microcrystalline samples of **M_nBDP** (n = 1, M = Ni, Zn; n = 2, M = Cu) were gently ground in an agate mortar, then deposited in the hollow of an aluminum sample holder (equipped with a zero-background plate). Diffraction data were collected with overnight scans in the 5-105° 2ϑ range on a Bruker AXS D8 Advance diffractometer, equipped with a linear position-sensitive Lynxeye detector, primary beam Soller slits, and Ni-filtered Cu-Kα radiation (λ = 1.5418 Å). Generator setting: 40 kV, 40 mA. Figure 4.1 contains the low-angle portion of the collected diffraction data, highlighting the relative differences and the less-than-ideal crystallinity of these samples, all showing anisotropic peak broadening. Standard peak search, followed by indexing with TOPAS,[22] allowed the detection of the approximate unit cell parameters: orthorhombic *I*, *a* = 6.75 Å, *b* = 22.78 Å, *c* = 13.45 Å, *V* = 2069.4 $Å^3$ and GOF = 35.5 for **NiBDP**; tetragonal *P*, *a* = 13.28 Å, *c* = 7.26 Å, *V* = 1280 $Å^3$ and GOF = 12.4 for **ZnBDP**; (apparently) orthorhombic *P*, *a* = 12.85 Å, *b* = 5.79 Å, *c* = 7.18 Å, *V* = 534.2 $Å^3$ and GOF = 25.4 for **Cu_2BDP**. The space groups *Imma*, for **NiBDP**, and *P42/mmc*, for **ZnBDP**, were assigned on the basis of the systematic absences conditions and later confirmed by Le Bail refinements. Structure solutions were performed by the simulated annealing technique, as implemented in TOPAS, using for BDP a rigid, idealized model, and, for **ZnBDP**, adding a rigid (and disordered) PhCN molecule. The final refinements were carried out by the Rietveld method, maintaining the rigid bodies described above and, in the **Cu_2BDP** case,

allowing the refinement of the torsion angles of the C_{ipso} ring junctions. The determination of the structural model for **Cu_2BDP** proved to be rather difficult; systematic absences indicated *Pmcb* or *P2cb* as possible space groups, but all efforts in finding the correct structure were vanished by what was later found a wrong assumption: *mmm* Laue symmetry. On lowering the space group symmetry, eventually down to *Pc*, a chemically plausible structural model was easily found, well matching the observed data; a deeper analysis of the atomic coordinates allowed the detection of further symmetry elements, addressing the more familiar *P21/c* space group. In all three cases, the background was modeled by a polynomial function; and anisotropic broadening, in the form of spherical harmonics, was used to define the peak widths. Peak shapes were described by the fundamental parameters approach. One, refinable isotropic thermal parameter was assigned to the metal atoms, augmented by 2.0 Å^2 for lighter atoms. The final Rietveld refinement plots are shown in Figure 4.2.

Crystal data for NiBDP. $C_{12}H_8N_4Ni$, fw = 266.92 g mol^{-1}; orthorhombic, *Imma*, *a* = 6.7655(15) Å, *b* = 22.7353(3) Å, *c* = 13.4648(1) Å; *V* = 2071.1(4) Å^3; *Z* = 4; ρ_{calc} = 0.856 g cm^{-3}; *F*(000) = 544; μ(CuKα) = 12.6 cm^{-1}. R_p, R_{wp} and R_{Bragg} 0.034, 0.058 and 0.026, respectively, for 28 parameters.

Crystal data for ZnBDP 2PhCN. $C_{26}H_{18}N_6Zn$, fw = 479.86 g mol^{-1}; tetragonal, *P42/mmc*, *a* = 13.2657(7) Å, *c* = 7.2474(11) Å; *V* = 1275.4(3) Å^3; *Z* = 2; ρ_{calc} = 1.250 g cm^{-3}; *F*(000) = 492; μ(CuKα) = 15.2 cm^{-1}. R_p, R_{wp} and R_{Bragg} 0.059, 0.074 and 0.015, respectively, for 33 parameters.

Crystal data for Cu_2BDP. $C_{12}H_8Cu_2N_4$, fw = 335.31 g mol^{-1}; monoclinic, *P21/c*, *a* = 12.866(1) Å, *b* = 5.7898(4) Å, *c* = 7.1815(7) Å; β = 90.24(2)°; *V* = 534.94(7) Å^3; *Z* = 2; ρ_{calc} = 2.082 g cm^{-3}; *F*(000) = 332; μ(CuKα) = 47.6 cm^{-1}. R_p, R_{wp} and R_{Bragg} 0.027, 0.040 and 0.014, respectively, for 33 parameters.

Thermodiffractometric Studies. Thermodiffractometric experiments were performed on solvated **MBDP** materials, to highlight the response of the two

frameworks to desolvation. The experiments were carried out in air,[23] from 298 K up to the loss of crystallinity using a custom-made sample heater, assembled by Officina Elettrotecnica di Tenno, Ponte Arche, Italy. Powdered microcrystalline samples of **MBDP** (M = Ni, Zn) were deposited in the hollow of an aluminum sample holder; diffractograms at different temperatures (with steps of 20 K) were recorded in a significant low-angle 2*q* range. Le Bail refinements were used to derive the lattice constants, later employed in the determination of the thermal properties. By means of the same apparatus, another set of experiments was performed on benzene-loaded **NiBDP**: consecutive diffractograms were acquired in isothermal conditions at 298, 323 and 348 K to characterize the evolution of the system. The data were treated by the Le Bail refinement method to derive the corresponding unit cell parameters. Furthermore, estimation of the integrated area by single peak modeling of the low angle section, allowed the estimation of the kinetic parameters by applying the Avrami model.[24]

Other Physical Measurements. Infrared spectra were recorded on a Shimadzu Prestige-21 instrument. Elemental analyses were carried out on a Perkin Elmer CHN Analyzer 2400 Series II. Simultaneous TG and DSC analyses were performed in a N_2 stream on a Netzsch STA 409 PC Luxx (heating rate: 10 K min^{-1}).

Results and discussion

Syntheses. These materials have been prepared by the solvothermal technique. The **NiBDP** polymer is obtained in the form of a dark orange precipitate when a solution of $Ni(CH_3COO)_2$ is refluxed with H_2BDP in acetonitrile in the presence of triethylamine. However, the isolated product is often contaminated by the extremely insoluble H_2BDP ligand, either as ancillary phase, or trapped in the crystal cavities, much alike terephthalic acid in $Ga(OH)(O_2C\text{-}C_6H_4\text{-}CO_2)$ and related species of the MIL-53 topology.[25] A washing procedure with dimethyl sulfoxide was thus performed to obtain a pure phase of **NiBDP** by exploiting the

rather high solubility of the unreacted ligand in this solvent. **ZnBDP** is isolated as a white product by reacting $Zn(ClO_4)_2$ with H_2BDP in benzonitrile and, again, in the presence of triethylamine. This framework is always obtained as a pure phase, compared to the **NiBDP** one.

In both cases, analytical, spectroscopic and, above all, XRPD evidences suggested that samples obtained in different syntheses had slightly distinct stoichiometries and lattice metrics (*vide infra*), as if a variable amount of solvent had remained trapped in these highly porous coordination polymers.

Rather surprisingly, Cu(II) salts did not lead to the expected homoleptic CuBDP material: by reaction of $Cu(NO_3)_2$ and H_2BDP in the presence of tributylamine the cuprous species **Cu_2BDP** was obtained. This *in situ* reduction of Cu(II)-pyrazolate complexes, promoted by heating, is not new,[26] and has already been attributed to the partial oxidation of pyrazole.[27]

Crystal Structures. NiBDP crystallizes in the orthorhombic *Imma* space group. The asymmetric unit contains one Ni(II) ion (*2/m* symmetry positions, Wyckoff site *c*) and one BDP ligand located about an inversion centre. The metal centers are coordinated, in square-planar stereochemistry, by four nitrogen atoms of four distinct BDP moieties [Ni-N 1.973(1) Å; N-Ni-N 84.6(3) and 95.4(3)°]. This feature has already been found in simpler analogues, such as the nickel imidazolate,[28] and, more pertinently, pyrazolate species,[29] of which detailed descriptions are reported in Chapter 2. With each pyrazolic end, the BDP ligands bridge, in the common exo-bidentate mode, Ni···Ni contacts of 3.37 Å, (*a*/2), generating linear and parallel chains of Ni(II) ions. Intetestingly, the intermetallic distance in the two $Ni(pz)_2$ (Hpz = 1*H*-pyrazole) polymorphs is *ca.* 3.48 Å.[29] The chains, further connected, and maintained nearly 13.2 Å apart, by the BDP moieties, eventually generate a 3-D network, in which large cavities of rhomboic shape (see Figure 4.3) represent about the 57% of the crystal volume (as calculated by Platon)[30]. Not surprisingly, the estimated bulk density of **NiBDP** is only 0.86 g cm^{-3}.

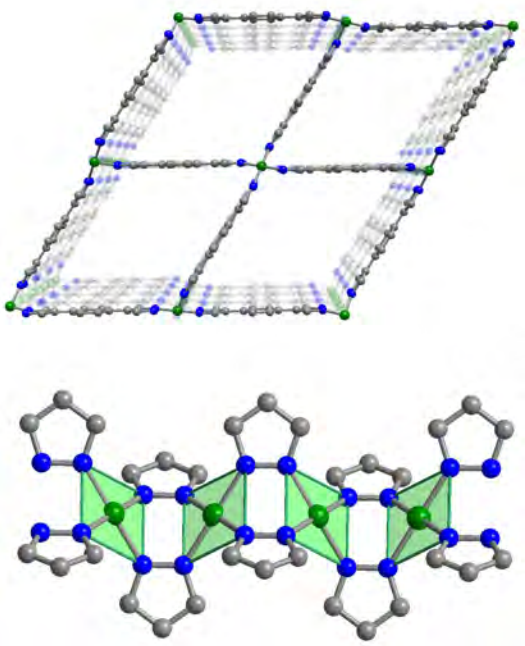

Figure 4.3. Schematic drawing of the crystal structure of **NiBDP** viewed approximately down **a** (upper). Carbon, grey; nitrogen, blue; nickel, green. In this view the large voids (accounting for nearly 57% of the total volume), generated by the rhomboic disposition of the bridging ligands can be appreciated. The enlargement at the bottom shows the square planar stereochemistry at the nickel(II) ions. Hydrogen atoms have been omitted for clarity.

As already pointed out in the experimental section, depending on the thermal history and on the actual reaction conditions, this porous structure may host variable amounts of solvent molecules, with significant deformation of the overall lattice metrics, but neither of the symmetry nor of the topology. Similar versatility and flexibility properties have been recently observed in some metal hydroxo-terephthalates, such as the Al/Cr/Fe/Ga-based MIL-53 or Fe-based MIL-88 frameworks, showing occasional symmetry changes upon guest adsorption or release.[31,32]

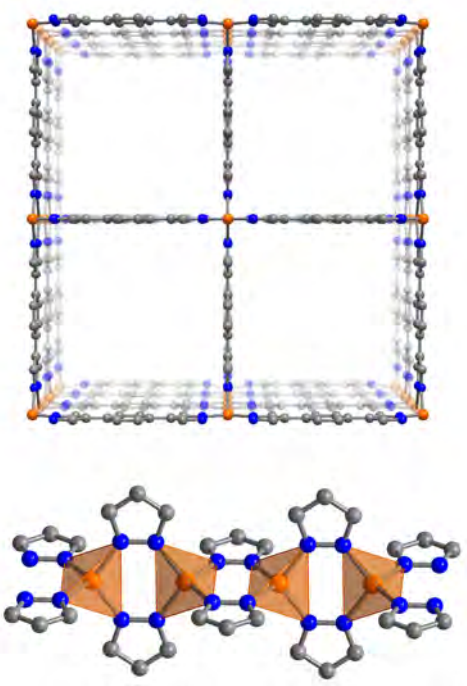

Figure 4.4. Schematic drawing of the crystal structure of **ZnBDP** viewed approximately down **c** (upper). Carbon, grey; nitrogen, blue; zinc, orange. While details of the metal center stereochemistry are lost in this view, the large voids (accounting for nearly 65% of the total volume), generated by the square disposition of the bridging ligands, can be appreciated. The view at the bottom shows the tetrahedral stereochemistry at the zinc(II) ions. Hydrogen atoms have been omitted for clarity.

ZnBDP crystallizes in the tetragonal space group $P4_2/mmc$; the asymmetric unit contains one crystallographically independent Zn(II) ion (*-4m2* position, Wyckoff site *e*) and one BDP molecule (*mmm* symmetry position, Wyckoff site *d*). The metal centers are tetrahedrally coordinated (Zn-N 2.04 Å; N-Zn-N 108-112°) and are kept 3.62 Å (*c/2*) apart by the BDP moieties along linear chains parallel to c. Once again, this geometrical motif has been already observed in simpler $Zn(pz)_2$ (Hpz = 1*H*-pyrazole) analogues where the intermetallic distance is 3.69 Å.[33] In **ZnBDP**, the mono-dimensional chains are further connected into a 3-D

framework by the BDP spacers, decorating the walls of the unit cell and generating square channels with 13.2 Å edges, running parallel to **c** (Figure 4.4). Notably, in this structure, the dimension of the pores is determined by the length of the ligand. Therefore, apart from the symmetry lowering induced by the partial organization of the trapped solvent molecules observed in Long's CoBDP,[9b] the zinc and cobalt species are isostructural, as expected for transition metal ions favoring tetrahedral stereochemistry. *In the freshly prepared samples*, analytical and structural data coherently suggest the presence of variable amounts of benzonitrile (PhCN), ranging from a **ZnBDP·2PhCN** formulation, down to a pure **ZnBDP** phase, once evacuation is achieved upon heating the solvated phase. Upon desolvation, the large cavities account for about 65%,[30] of the crystal volume, with a calculated density of only 0.71 g cm^{-3}, and can host infinitely long cylinders nearly 6.6 Å wide. The density value, and the slightly higher one observed for **NiBDP**, are in agreement with the exceptionally high surface area and gas and vapor adsorption performances found for these two frameworks (see below).

Cu_2BDP crystallizes in the monoclinic $P2_1/c$ space group, with one crystallographically independent Cu(I) ion in a general position and one BDP ligand sitting on an inversion center. Each metal ion is linearly coordinated by two nitrogen atoms of two distinct exo-bidentate BDP residues [Cu-N 1.926(8)-1.967(3) Å, N-Cu-N 172.6(5)°], which bridge adjacent Cu(I) ions 3.028(3) Å apart along 1-D wavy chains elongating along **b**. These features, as well as the wavy disposition of the Cu_n sequence (Cu···Cu···Cu *ca.* 146°), closely match those of the archaetipic copper pyrazolate α-phase,[34] described in Chapter 2. In **Cu_2BDP**, the parallel chains are further connected, and kept at about 12.9 Å (the **a** axis length), by the BDP ligands, thus generating an idealized 2-D centered rectangular lattice, well separated, approximately along [106] (slightly off from the **c** axis direction), from symmetry equivalent ones (Figure 4.5). Worthy of note, although sharing the same space group symmetry, the **Cu_2BDP** species is not isomorphous with the

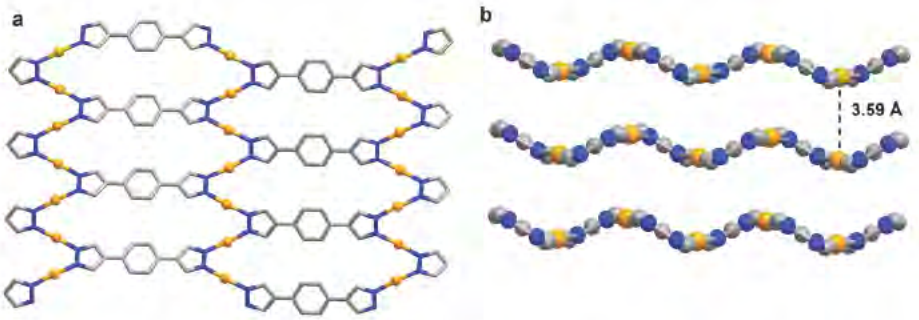

Figure 4.5. (a) Schematic drawing of the crystal structure of **Cu_2BDP** viewed approximately down **b**. Carbon, grey; nitrogen, blue; copper, orange in which can appreciated, in a) the linear coordinate Cu(I) atoms while in b) the 1D-wavy chains. Hydrogen atoms have been omitted for clarity.

Species	Metal Geometry	Color	M···M, Å	Chain packing (idealized)	Ref.
$Co(pz)_2$	Tetrahedral	Violet	3.72	Hexagonal	29
CoBDP	Tetrahedral	Violet	3.54	Square	9b
α-$Ni(pz)_2$	Square planar	Yellow	3.47	Hexagonal	29
β-$Ni(pz)_2$	Square planar	Yellow	3.49	Rectangular	29
NiBDP	Square planar	Orange	3.37	Rhombic	This work
α-Cu(pz)	Digonal	Colorless	3.17	Rectangular	34
β-Cu(pz)	Digonal	Colorless	3.40	Hexagonal (dimers)	34
Cu_2BDP	Digonal	Beige	3.03	Oblique	This work
$Zn(pz)_2$	Tetrahedral	Colorless	3.69	Hexagonal	29
ZnBDP	Tetrahedral	Colorless	3.62	Square	This work

Table 4.1. Synoptic collection of the main structural features of **MBDP** species and of their $M(pz)_2$ analogues.

parent H_2BDP derivative,[18] as it would be expected for the simple replacement of the NH···N hydrogen bond interaction in H_2BDP by a digonal N-Cu- N fragment in **Cu_2BDP**.

Chapter 2 widely describes a collection of metal pyrazolates of simple $M(pz)_2$ formulation. These complexes were found to belong to four different structural types: *i)* chain polymers with square-planar stereochemistry at the metal centers [M = Ni (α and β polymorphs) and Cu (β-phase)]; *ii)* chain polymers with tetrahedral metal stereochemistry [M = Fe, Co, Zn and Cd, as well as Cu (α-phase)]; *iii)* cyclic oligomers containing square-planar metal ions (as for M = Pd and Pt), and *iv)* mononuclear species with digonal N-M-N coordination, mutually linked by weak, ancillary M···N contacts (M = Hg).[35] The structural features of classes *i)* and *ii)*, synoptically collected in Table 4.1, are maintained in the BDP derivatives, with the high added value of keeping the collinear metal chains far away, thanks to the size and geometry of the longer organic spacer. Thus, **ZnBDP** and CoBDP,[9b] featuring the tetrahedral stereochemistry found in $Zn(pz)_2$ and $Co(pz)_2$, give rise to square lattices, while **NiBDP** chooses a rhomboic disposition, governed by the square-planar geometry, already found in both $Ni(pz)_2$ polymorphs. Apparently, *P42/mmc* and *Imma* are the unique space groups allowed for an *undistorted* framework.[36] More importantly, only the *Imma* (and *Pnma*, a proper subgroup) phases manifest a large breathing effect (extensively discussed in a number of papers, including vast experimental work as well as computational aspects)[37] and, following Kitagawa's classification, are representative examples of third-generation coordination polymers,[38] where flexibility is ensured by the length of the organic spacer, at the expenses of a limited variation of the (square-planar, or nearly so) metal stereochemistry. For simple mechanical reasons, ZnBDP containing (stiffly hinged) tetrahedrally coordinated ions, cannot "breathe" to this large extent. However, Long's CoBDP, has been found to be flexible, although its isostructural nature with **ZnBDP**, by showing a multistep breathing behavior in its nitrogen adsorption isotherm.[39]

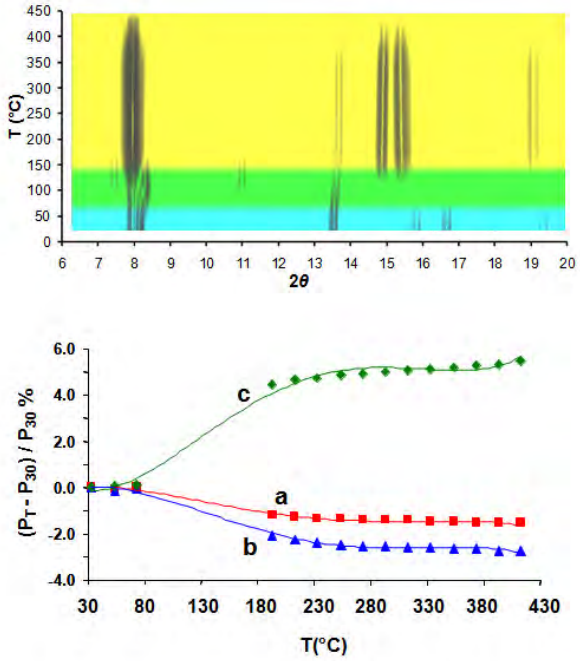

Figure 4.6. a) Variable temperature X-ray diffractograms acquired on solvated **NiBDP** in the 303-723 K temperature range. The cyan and yellow intervals denote, respectively, the solvated and the empty phase; the light green region indicates the transition between the two phases. b) Variation of the unit cell parameters of **NiBDP** (p_T) normalized to the correspondent 303 K values (p_{303}) as a function of the temperature. *a*, red squares; *b*, blue triangles; *c*, green rhombi. The reported lines have the only scope of guiding the eye. The Le Bail refinement of the temperature range drawn in green in the upper part was not possible, as no lattice periodicity values could be derived for this transient phase.

Thermal Behavior of the NiBDP and ZnBDP species. The thermal behavior of compounds **M_nBDP** (n = 1, M = Ni, Zn; n = 2, M = Cu) was investigated by coupling simultaneous thermal analyses (STA, simultaneous TG and DSC) to *in situ* variable temperature X-ray powder diffraction (TXRPD).

Simultaneous thermal analysis (STA) and Powder X-Ray Diffraction analysis in temperature (TXRPD) were carried out on the same batch. The STA performed

on a DMSO solvated batch of **NiBDP** showed a smooth and continuous mass loss, interpreted as the evolution of the clathrated solvent, in the range 323-733 K, temperature at which decomposition starts. The TXRPD experiments (Figure 4.6) carried out in air further substantiated the STA observations: up to 323 K, only the fully solvated (A) phase is present. Then, further heating in the 363-443 K temperature range induces a smooth and continuous solvent loss, during which a still unindexed material (with broad diffraction peaks) is found; after that, a single new phase (B) is formed, keeping losing the residual solvent molecules till decomposition. While preserving the unit cell metrics, the A→B process brings about definite changes in the positions and intensities of the XRPD peaks. A structureless Le Bail refinement of these data was carried out in the temperature ranges in which only pure A or B phases were present. The results show that, on passing from the A (303 K) to the B species (463 K), the cell axis less affected by the thermal treatment is the **a** one (Figure 4.6b). Actually, this result is expected, as **a** is associated with the chains propagation direction, where collinear metal atoms are kept at a nearly constant separation by the bridging pyrazolate rings. On the contrary, **b** and **c**, defining the rhomboic disposition of the 1-D chains, undergo higher, and inversely correlated, variations. Specifically, while **b** decreases, **c** increases, the two events globally resulting in a breathing of the 3-D framework promoted by guest release, with a concomitant unit cell volume increment of about 1.0%. Further heating of the B phase brings about moderate cell parameters variations in the same direction as those just described, with a modest cell volume shrinking (0.5%). Interestingly, different preparations typically afforded materials with different XRPD traces, all of them referring to the same *Imma* structure, but lying on intermediate points in the (solvent promoted) deformation path. RT measurements of **NiBDP** batches with different degree of solvation allowed to observe unit cell axes variations up to about 20% of their (lowest) values. For the same reasons as above, **a** is only marginally af-

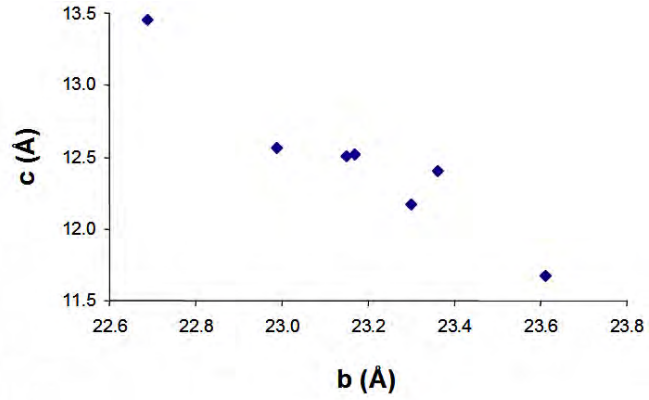

Figure 4.7. Variability of the **b** and **c** axes of *as prepared* different batches of **NiBDP** containing different amounts of solvent. A rough inverse relation of the **c** = k/**b** type can be envisaged, granting a near constancy of the massive density.

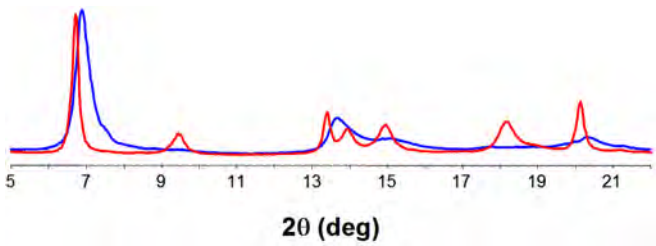

Figure 4.8. Comparison of the raw XRPD traces for two batches of the **ZnBDP** material, which shows a significantly variability in peaks position, intensity and width, attributed to distinct degrees of crystallinity and to the presence of different, unpredictable, amounts of trapped solvent molecules.

fected by the different work-up conditions, while **b** and **c** show significant, and inversely correlated variations, from which an *inverse* correlation can be (again) derived (Figure 4.7).

Also **ZnBDP** in its diffraction traces at room temperature differ among each other, although to a lesser extent. In Figure 4.8 are shown two powder diffraction

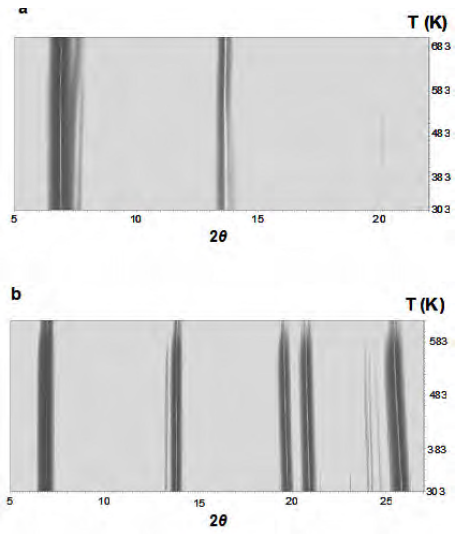

Figure 4.9. Thermodiffractometric plots for (a) **ZnBDP** and (b) **Cu_2BDP** showing limited flexibility and substantial framework rigidity.

pattern of samples in which the highest, even less than ideal, crystallinity (whose related structural details have been discussed above) is compared to a second batch in which a even lower degree of crystallinity is observed, as witnessed by the definitely broadened peaks. **ZnBDP** behavior in temperature shows that this material is rather stiff during desolvation and does not show the extreme flexibility of the Ni(II) analogue (Figure 4.9a). This behavior can be easily interpreted by looking closer to the structural features of **ZnBDP** in which the ZnN_4 tetrahedron and the tetragonal lattice as a whole are characterized by a high stereochemical rigidity. This observation is in contrast with what shown by the isostructural (orthorhombic and monoclinic) CoBDP materials: in both cases, thermal treatment[9b,40] or catalytic tests[40] induce, profound structural changes.[39]

By thermal treatment (Figure 4.9b), the layered **Cu_2(BDP)** species shows the maximum axis change for the **b** parameter (nearly coinciding with the pyrazolate-bridged Cu_n chains), with a thermal expansion coefficient $1/b\ \partial b/\partial T = 66 \times 10^{-6}\ K^{-1}$. This large value suggests that, upon heating, the slightly corrugated 2-D sheets flatten, rigorously maintaining, at the same time, the same distance among parallel Cu_n chains, about 12.9 Å apart (maximum deviation: 0.07%, with $1/a\ \partial a/\partial T = 2.6 \times 10^{-6}\ K^{-1}$, *i.e.* nearly 25 times less than for the **b** axis).

Gas Adsorption Properties. In order to evaluate their potential use for gas separation and storage of small gaseous molecules, the gas adsorption proper-

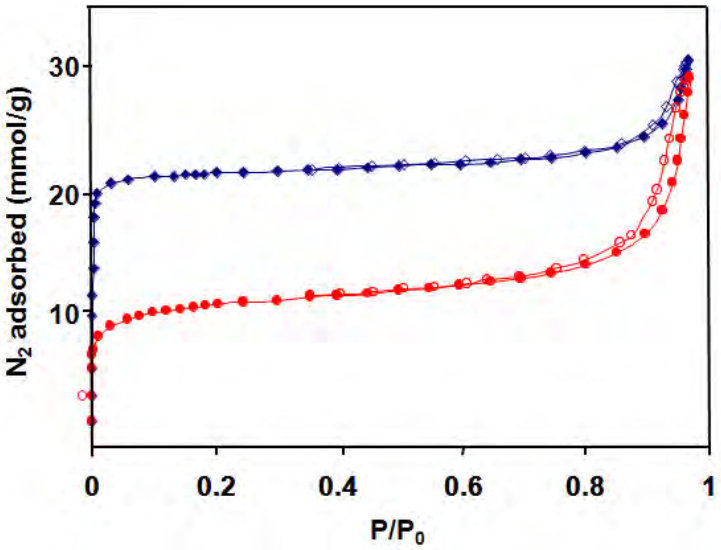

Figure 4.10. NiBDP (red circles) **ZnBDP** (blue diamonds) N_2 adsorption isotherms at 77 K. Open symbols denote desorption.

ties of the activated **NiBDP** and **ZnBDP** solids have been essayed towards Ar, N_2 at 77 K and CH_4, CO_2 at 273 K. Figure 4.10 shows the adsorption isotherms of Ar and N_2 at 77 K for the two materials. Both derivatives display the typical behavior of highly porous crystalline MOFs, exhibiting a type I adsorption isotherms with a sharp knee at low relative pressures (p/p_0 ~ 0.01, corresponding to the filling of the porous structure), followed by a *plateau*, suggesting that the permanent porosity of the samples is mainly composed of micropores, of rather uniform size. Additionally, the presence of a (type H1) hysteresis loop in the N_2 isotherms at relative pressures above 0.8 is indicative of textural mesoporosity arising from interparticle mesopores (voids).[41] This is indeed in line with the apparent average particle sizes (approximated by the coherent scattering domains) determined by diffraction methods, typically lying in the 50-200 nm range. These

materials thus posses large specific surface areas, with values of *ca.* 1600 and 2200 m^2 g^{-1} for **NiBDP** and **ZnBDP**, respectively, as obtained by fitting the BET equations (Table 4.2). The **ZnBDP** system exhibits a large gas storage capacity amounting to 22.5 mmol g^{-1} of N_2 and Ar at 77 K, which is indicative of a very high accessibility of its microporous structure (0.71 cm^3 g^{-1}, as calculated from the t-plot method, closely matching the value obtained from the structural model) (Table 4.2). It should be noted that, in contrast to the CoBDP species,[9b] the closely related **ZnBDP** material does not exhibit steps in the low pressure region. As anticipated, CoBDP and **ZnBDP** are isomorphous species (apart from negligible symmetry lowering due to the organization of the clathrated solvent molecules in the former); thus, we tentatively attribute the absence of detectable steps in the gas sorption curves of **ZnBDP** to its *extreme* rigidity (as witnessed by our TXRPD analysis), *i.e.* to the difficulty of distorting the T_d geometry of Zn(II) ions (but not that of Co(II) ones) toward D_{2d}. In the case of **NiBDP**, the storage capacity (12 mmol g^{-1} of N_2; 13.7 mmol g^{-1} of Ar) significantly diminishes. In this regard, it should be noted that pore volume (0.38 cm^3 g^{-1}), as calculated from the t-plot, is significantly lower than the crystallographic pore volume; it is possible that, due to its remarkable flexibility, a narrow pore form of this material is present at low temperatures, which we cannot trap.

The high pressure adsorption isotherms of CO_2 and CH_4 at 273 K for the **ZnBDP** and **NiBDP** materials (Figure 4.11) show, in the low pressure range, a smooth increase in the adsorbed amount and the appearance of a sigmodial shape at high pressures, which indicates a relatively weak interaction of these guest molecules within the cavities of the adsorbent. This is a consequence of the large size of the pore channels which lead to a behaviour that closely resembles that of the bulk fluid, as already found in highly porous MOFs, *e.g.* MOF-177 and IRMOF-1.[42] In contrast to the adsorption isotherms of N_2 and Ar at 77 K, the **NiBDP** material outperforms, by a factor of two, the adsorption capacity

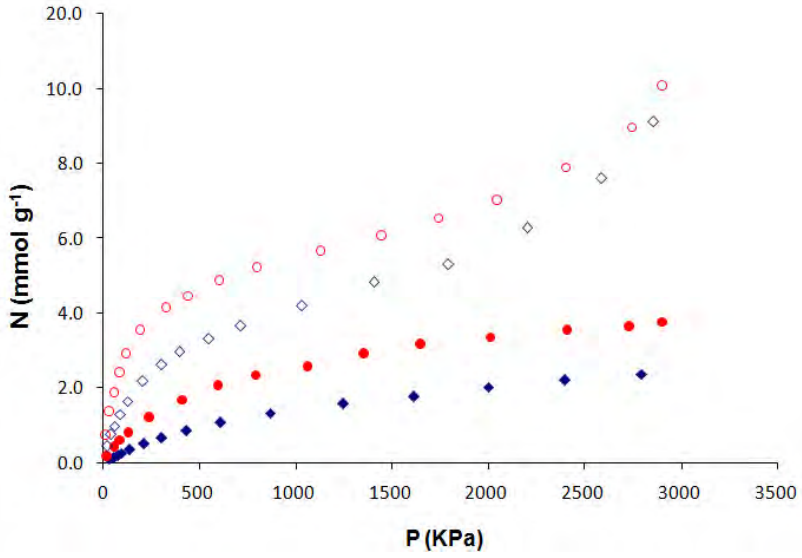

Figure 4.11. High pressure CO_2 (open symbols) and CH_4 (full symbols) adsorption isotherms at 273 K for **NiBDP** (red circles) and **ZnBDP** (blue diamonds).

Compound	BET ($m^2 g^{-1}$)	N_2 (mmol g^{-1})	Ar (mmol g^{-1})	CO_2 (mmol g^{-1})	CH_4 (mmol g^{-1})	Benzene (mmol g^{-1})	Cyclohexane (mmol g^{-1})	Pore V (ads)[a] ($cm^3 g^{-1}$)	Pore V (cryst)[b] ($cm^3 g^{-1}$)
NiBDP	1600	12.0	13.7	10.0	3.7	5.8	6.5	0.38	0.67
ZnBDP	2200	22.5	22.7	9.1	2.4	3.8	4.7	0.71	0.92

a: accessible pore volume obtained from N_2 adsorption isotherms (t-plot). b: pore volume calculated from crystal structures. c: These values were obtained from the adsorption isotherms of N_2 and Ar (77 K); CO_2 and CH_4 (273 K) and Benzene and cyclohexane (303 K). N_2 adsorption capacities corresponds to a relative pressure of 0.3, CO_2 and CH_4 capacities were taken at 3000 kPa and benzene and cyclohexane values correspond to relative pressure 1.

Table 4.2. Summary of gas and vapor adsorption capacities of **NiBDP** and **ZnBDP** materials.

of **ZnBDP** in the whole pressure range (up to 2850 kPa), thus suggesting that the narrower size and adaptive nature of the pores of the Ni(II) derivative is a fundamental issue.[43] For both materials, the adsorption capacity for CO_2, peaking up to 10 mmol g^{-1} at 2850 kPa for **NiBDP** (Table 4.2), closely approaches that exhibited by best performing MOF materials MIL-53,[43] IRMOFs-1,-3,-6 and -11[42] and might be of interest for the storage of this greenhouse gas. The storage capacities of CH_4 at 273 K are much smaller, with a maximum value of 3.75 mmol g^{-1} for **NiBDP** (Table 4.2). The lower adsorption capacity of CH_4 compared to CO_2 can be attributed to the fact that methane adsorption is carried out in super-critical conditions, with concomitant weaker adsorbate-adsorbate and adsorbate-adsorbent interactions for CH_4 in comparison to CO_2. All together, these results suggest that the interaction of small gaseous molecules like CO_2 and CH_4 is weak, thus requiring, in spite of the large surface areas exhibited by these materials, high pressures in order to achieve significant storage capacities at temperatures close to ambient conditions.

Organic Vapor Adsorption. Aiming at determining the suitability of **NiBDP** and **ZnBDP** for the separation and removal of harmful vapors, the adsorption of organic vapors in static (benzene, cyclohexane) or dynamic (thiophene) conditions (in both dry and humid environments) have been studied.

The interaction of the **NiBDP** and **ZnBDP** systems with organic vapors (benzene, cyclohexane, thiophene) appears to be very strong in both static and dynamic conditions, at variance with the results reported above for small gaseous molecules. Figure 4.12 shows the adsorption isotherms of the two materials towards benzene and cyclohexane at 303 K. In the case of cyclohexane, it can be appreciated the formation of quasireversible type I isotherms exhibiting high storage capacities of 6.5 and 4.7 mmol g^{-1} for **NiBDP** and **ZnBDP**, respectively (Table 4.2). These values are comparable to those exhibited by $[Zn(bdc)(ted)_{0.5}]$, which possesses a similar pore volume and similar adsorption capacity towards

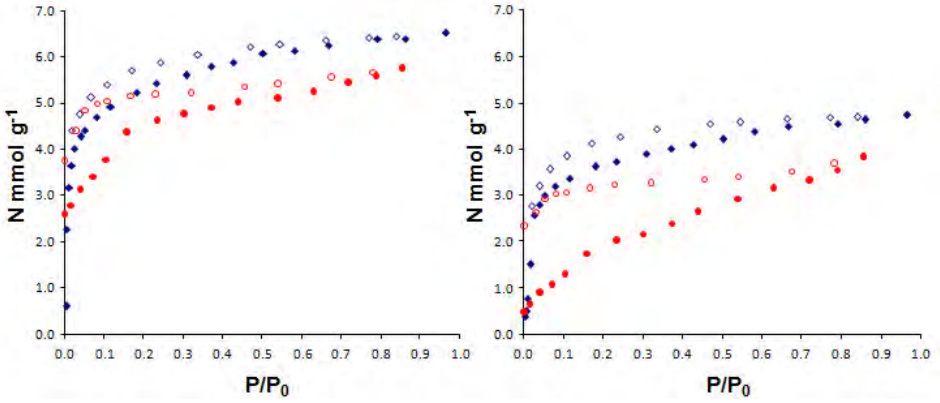

Figure 4.12. Vapor adsorption-desorption isotherms of benzene (red circles) and cyclohexane (blue diamonds) at 303 K for **NiBDP** (left) and **ZnBDP** (right). Open symbols denote the desorption branch.

organic vapors at 298 K, namely 6.2 mmol g^{-1} of benzene and 5 mmol g^{-1} of cyclohexane.[44] In the case of benzene, adsorption proceeds in a stepwise fashion, with an abrupt rise in the adsorption capacity in the low pressure range, particularly evident in the case of **NiBDP**. These observations possibly indicate strong interactions of the guest molecules with primary binding sites and, for **NiBDP**, a stepwise behavior, in which guest incorporation or release is responsible for a significant breathing effect of the porous flexible structure (see below).[43] By contrast, the desorption branch follows a type I isotherm. A significant part of the adsorbed benzene (3.8 mmol g^{-1} for **NiBDP** and 2.3 mmol g^{-1} for **ZnBDP**) (Table 4.2) is irreversibly captured inside the porous network giving rise to the formation of an irreversible adsorption isotherm with a pronounced hysteretic loop. This parallels our observations on the presence of residual solvents (DMSO or PhCN) after the isolation of the raw materials. On the other hand, in the case of **NiBDP**, the volume of adsorbed benzene (0.5 mL g^{-1}) and cyclohexane (0.7 mL g^{-1}) fits well with the calculated crystallographic pore volume (0.67 mL g^{-1}), which

implies the complete filling of the pores during the adsorption process and confirms the optimal interactions among these adsorbates and the pore walls. In contrast, in **ZnBDP**, the pore filling is lower than expected from crystallographic data (pore volume, 0.92 mL g^{-1}) as adsorbed benzene and cyclohexane account only for 0.3 ml g^{-1} and 0.5 ml g^{-1}, respectively. These results are probably indicative that, in this case, slightly weaker interactions of the organic molecules with the framework walls are taking place as a consequence of the stiffer nature of the coordination network and the larger size of the pores.

In view of the affinity of these systems for aromatic vapors, we realized that these systems might be of interest for the selective removal of harmful organic vapors from natural gas or air purification purposes. In this regard, it should be noted that although the well known $Cu_3(btc)_2$,[7] material has been shown to behave as an excellent adsorbent of tetrahydrothiophene, it is ineffective in the presence of humidity as a consequence of irreversible water coordination to the open metal sites. This feature of MOFs with open metal sites is a main drawback for their application if they have to compete with classical hydrophobic adsorbents like activated carbons. With the aim of studying the behavior of our pyrazolate based systems, we have evaluated their performance in the removal of thiophene (*ca.* 30 ppm) from a He:CH_4:CO_2 1:2.25:1 (*v*:*v*) flow in both dry and humid conditions. The dynamic adsorption process of thiophene in the absence of moisture has been studied by measurement of a breakthrough curve at 298 K. The results show that these systems are suited for the selective incorporation of thiophene in dynamic conditions (Figure 4.13a).

The maximum adsorbed vapor amounts reach 0.30 and 0.34 g thiophene g^{-1} for **NiBDP** and **ZnBDP**, respectively, and are fully comparable with those of the best performing MOF-type material known to date for thiophene adsorption, namely $Cu_3(btc)_2$.[7] Remarkably, exposition for 72 h to open air (298 K, 60% humidity) of the **NiBDP**, **ZnBDP** and $Cu_3(btc)_2$ materials prior to the breakthrough tests,

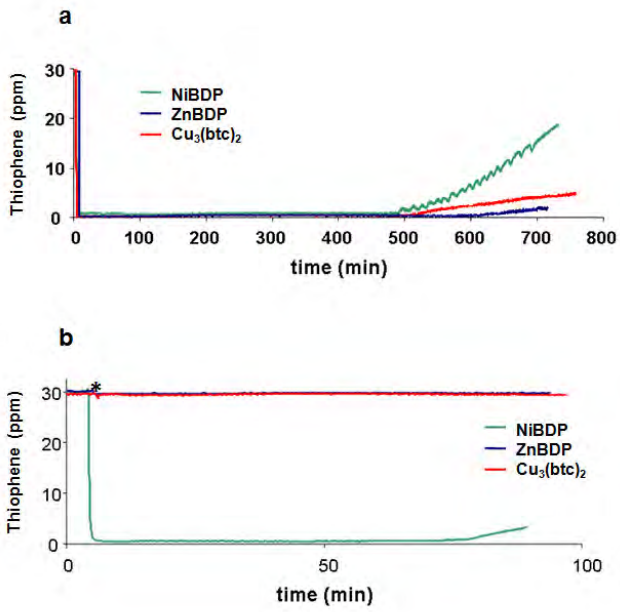

Figure 4.13. (a) Breakthrough curves for a He:CH_4:CO_2 1:2.25:1 (v/v) gas mixture containing 30 ppm of thiophene flowed through a column packed with activated **NiBDP** (green), **ZnBDP** (blue) or $Cu_3(btc)_2$ (red). (b) Effect of the presence of humidity on the performance of thiophene removal: **NiBDP**, **ZnBDP** or $Cu_3(btc)_2$ have been exposed to open air for 72 h prior to usage and the flowed gas mixture used contained 60% humidity. The asterisk indicates time in which the gas mixture is flowed through the MOF bed.

as well as incorporation of humidity (60%) in the gas flow stream still permits the incorporation of thiophene by the non-activated **NiBDP** (0.060 g thiophene g^{-1}, Figure 13b). By contrast, **ZnBDP** and $Cu_3(btc)_2$ materials are totally inefficient for this purpose in humid conditions (Figure 4.13b). Thus, thanks to the synergic effects of different structural, stereochemical and energetic features (the flexibility of its framework, the hydrophobic nature of the 1-D channels, the probable interactions of the thiophene *S*-donor atoms with the Ni centers and the insensitive nature of the metal coordination sphere to moisture and hydrolysis), **NiBDP**

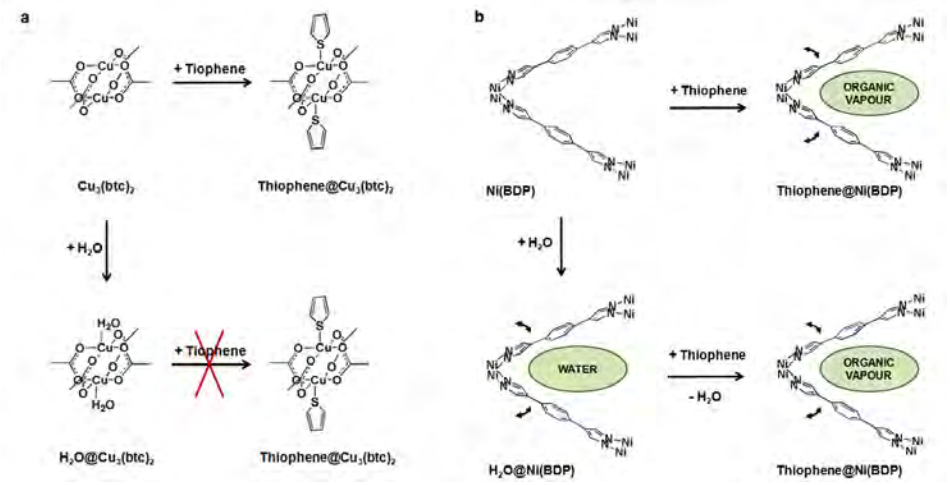

Scheme 4.1. Schematic drawing of thiophene interaction with the $Cu_3(btc)_2$ (left) and **NiBDP** (right) host frameworks in both dry and humid conditions. In the case of $Cu_3(btc)_2$, the blocking effect of coordinated water molecules on thiophene uptake is highlighted.

Compound	Space Group	*a*, Å	*b*, Å	*c*, Å	*V*, Å^3	*b* / *c*
NiBDP	*Imma*	6.76	22.73	13.46	2071	1.69
DMSO@NiBDP	*Imma*	6.84	23.24	12.95	2060	1.79
Benzene@NiBDP	*Imma*	6.67	22.58	13.29	2004	1.70

The effective uncertainty values of the lattice parameters of the solvated phases, measured at room temperature and upon heating (in air) on transient (unstable) materials, are expected to be larger than the e.s.d.'s determined by least squares methods and Le Bail refinements (a few thousands of Å), and estimated to be in the 0.01-0.02 Å range.

Table 4.3: Unit cell parameters of the **NiBDP** material loaded with different guest molecules at 298 K.

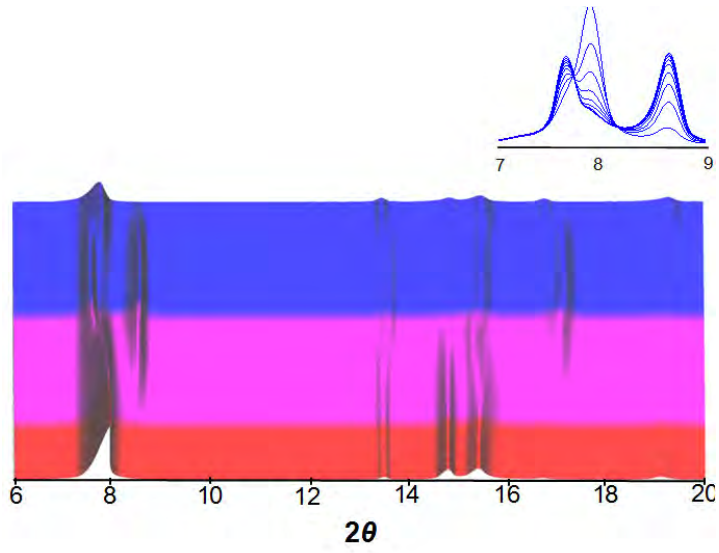

Figure 4.14. Evolution of the XRPD trace for **NiBDP** loaded with benzene during desorption under isothermal conditions, at 298, 323 and 348 K.. Blue, lilac and red traces represent isothermal measurements at 298, 323 and 348 K, respectively. Each full set of data took about 3 h (approximately 5 min per single pattern). The inserts show the low-angle regions from which clear isosbestic-like points can be observed, requiring the absence of intermediate phases during transformation.

appears to be very promising for the incorporation of a MOF in a gas purification device (Scheme 4.1). By contrast, the activity for thiophene removal under humid conditions is dramatically lowered in the case of **ZnBDP** and $Cu_3(btc)_2$: this can be attributed to framework rigidity in **ZnBDP**, and to the loss of the coordinatively unsaturated metal centers in $Cu_3(btc)_2$, which does not permit the direct interaction of the thiophene *S*-donor atoms with the M(II) ions.

Structural deformations upon vapor adsorption and removal. XRPD studies of the **NiBDP** material loaded with benzene have been performed in order to further highlight the structural changes that take place upon incorporation and

release of guest molecules. XRPD measurements on the **benzene@NiBDP** material performed at 298 K are indicative that the freshly loaded material shows the same space group and related cell metrics as the pristine **NiBDP** (Table 4.3). XRPD traces acquired at 298 K, under strictly isothermal conditions, are indicative of a dynamic desorption process which is accompanied with remarkable changes of the rhomboic channels dimensions (Figure 4.14), much alike Férey's MIL-53 species,[45] and its congeners. The evolution of benzene stops approximately after 40 min of air exposure: the XRPD traces asymptotically reach an equilibrium state with some benzene still occluded in the pores, as confirmed by the benzene adsorption experiments described above. This transformation *is not mediated by any intermediate phase,* since isosbestic-like points can be easily seen for overlapping (some increasing and some decreasing) peaks.

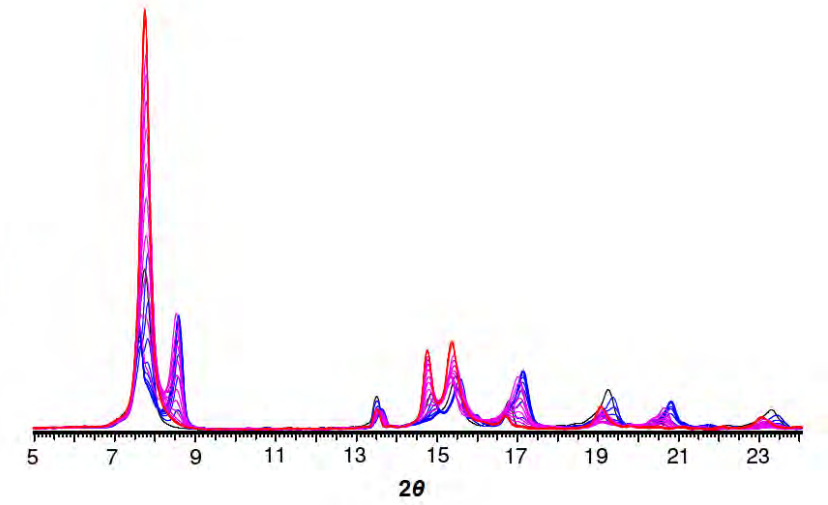

Figure 4.15. Thermodiffractometric plot for **NiBDP** loaded with benzene, showing remarkable framework flexibility. Blue, lilac and red colors indicate heating at 298, 323 and 348 K, respectively.

Using these data, the Avrami model,[24] for solid-state reaction kinetics has been applied, giving a phenomenological time-exponent of 1.5, thus discarding the occurrence of 3-D random nucleation. Progressive exposure of the material to higher temperatures, namely 323 K and, eventually, at 348 K overnight, fully restores the dimensions of the channels as in the empty **NiBDP** material (Figure 4.15), which is maintained also upon cooling the sample back to room temperature. These results are also in agreement with previous ones obtained by TXRPD on the DMSO loaded **NiBDP** samples (see above). However, it seems that DMSO induces larger distortions compared to benzene (Table 4.3) which might be related to the non-planar nature of the former guest.[46]

Conclusions

The recent reports on the structure and porosity of a few metal bis-tetrazolate and bis-pyrazolate 3-D networks,[9] and the availability of these ligands by the new efficient syntheses, reported in Chapter 3 of this thesis,[18] stimulated the investigation of pyrazolate-based ligands in the synthesis of novel coordination polymers with late transition metals. Here have been presented the synthesis and full characterization of the Ni(II) and Zn(II) species with the long 1,4-bis(1*H*-pyrazol-4-yl-benzene) as organic spacer, which show permanent porosity and a certain degree of flexibility. In this regard, the (thermo)diffractometric measurements have quantitatively addressed the nature and the extent of the lattice flexibility featured by the isostructural frameworks crystallizing in the *Imma* and closely related space groups, as discussed in a very recent contribution to this field.[31]

More importantly, these adsorption studies confirmed the formation of porous systems with highly accessible channels, particularly adequate for the selective incorporation of organic vapors. In this regard, the moisture insensitive nature of **NiBDP**, coupled to its framework flexibility and to its very high thermal stability, was shown to be highly suitable for thiophene removal from CO_2/CH_4

mixtures *even in the presence of humidity*, thus overcoming the still unsolved problems raised by classical carboxylate-based MOF's in real practical applications, such their incorporation in filters for air and gas purification processes.

Work can be anticipated in extending the isoreticular approach to other polyazolate systems with longer aromatic spacers, or with a different number of donor sites, aiming at the formation of porous networks with high flexibility and possessing high chemical inertness and thermal stability.

Acknowledgements

This work was supported by the Italian MIUR (PRIN2006: "Materiali Ibridi Metallo-Organici Multifunzionali con Leganti Poliazotati"), Fondazione CARIPLO (Project 2007-5117), FP7-EU (nanoMOF), Spanish MCINN (CTQ2008-00037/PPQ) and Junta de Andalucía.

References and Notes

1 Long, J.R., Yaghi, O.M. *Chem. Soc. Rev*. **2009**, *38*, 1213.

2 (a) Batten, S.R.; Neville, S.M.; Turner, D.R. *Coordination Polymers. Design, Analysis and Application* RSC Publishing, Cambridge, **2009**. (b) Wright, P.A. *Microporous Framework Solids* RSC Publishing, Cambridge, **2008**.

3 Banerjee, R.; Furukawa, H.; Britt, D.; Knobler, C.; O'Keeffe, M.; Yaghi, O.M. *J. Am. Chem. Soc.* **2009**, *131,* 3875 and references therein.

4 Noro, S.; Kitagawa, S.; Akutagawa, T.; Nakamura, T. *Prog. Polym. Sci.* **2009,** *34***, 240 and references therein.**

5 Férey, G. *Chem. Soc. Rev.* **2008**, *37*, 191 and references therein.

6 Proch, S.; Herrmannsdorfer, J.; Kempe, R.; Kern, C.; Jess, A.; Seyfarth, L.; Senker, J. *Chem. Eur. J.* **2008**, *14*, 8204.

7 Britt, D.; Tranchemontagne, D.; Yaghi, O.M. *Proc. Nat. Acad. Sci.* **2008**, *105*, 11623.

8 See e.g.: Park, K.S.; Ni, Z.; Coté, A.P.; Choi,.J.Y.; Huang, R.; Uribe-Romo, F.J.; Chae, H.K.; O'Keeffe, M.; Yaghi, O.M.; *Proc. Nat. Acad. Sci.* **2006**, *103*, 10186; Biswas, S.; Grzywa, M.; Nayek, H.P.; Dehnen, S.; Senkovska, I.; Kaskel, S.; Volkmer, D. *Dalton Trans.*, **2009**, 6487.

9 (a) Dincă, M.; Yu, A.F.; Long, J.R. *J. Am. Chem. Soc.* **2006**, *128*, 8904-8913. (b) Choi, H.J.; Dincă, M.; Long, J.R. *J. Am. Chem. Soc.* **2008**, *130*, 7848.

10 Hou, L.; Lin, Y.-Y.; Chen X.-M. *Inorg. Chem.,* **2008***, 47, 1346.*

11 Lu, Y., Tonigold, M.; Brendenkötter, B.; Volkmer, D.; Hitzbleck, J.; Langstein, G *Z. Anorg. Allg. Chem*. **2008**, *634*, 2411-2417; Tonigold, M.; Lu, Y.; Brendenkötter, B.; Rieger, B.; Bahnműller, S.; Hitzbleck, J.; Langstein, G.; Volkmer, D. *Angew. Chem. Int. Ed.* **2009**, *48*, 7546.

12 (a) Achmann, S.; Hagen, G.; Hammerle, M.; Malkowsky, I.; Kiener, C.; Moos, R. *Chem. Eng. Technol.* **2010**, *33*, 275. (b) *Kirk-Othmer Encyclopedia of Chemical Technology* **2008**, Whiley, New York. (c)

13 (a) Varga, Z.; Hancsok, J. *Pet. Coal* **2003**, *45*, 135; (b) Bej, S.; Maity, S.; Turaga, U. *Energy Fuels* **2004**, *18*, 1227; (c) Sarode, P.; Sankar, G.; Srinivasen, A.; Vasudevan, S.; Rao, C.; Thomas, J. *Angew. Chem.* **1984**, *96*, 288; *Angew. Chem. Int. Ed. Engl.* **1984**, *23*, 323; Kerby, M.; Degnan, T.; Marler, D.; Beck, J. *Catal. Today* **2005**, *104*, 55.

14 See, *e.g.*: (a) Zhang, Z. Y. et al. *Appl. Catal., B* **2008**, *82*, 1. (b) Lee, D. et al. *J. Phys. Chem. C* **2008**, *112*, 18955. (c) Yang, F. H.; Hernández-Maldonado, A. J.; Yang, R. T. *Sep. Sci. Technol.* **2005**, *39*, 1717. (d) Hernández-Maldonado, A. J.; Yang, R. T. *Catal. Rev. Sci. Eng.* **2004**; *46*, 111. (e) Yang, R. T.; Hernández-Maldonado, A. J.; Yang, F. H.

Science **2003**, 301, 79; (f) Deliyanni, E.; Seredych, M.; Bandosz, T. J. *Langmuir* **2009**, *25*, 9302.

15 (a) Cychosz, K. A.; Wong-Foy, A. G.; Matzger, A. J. *J. Am. Chem. Soc.* **2008**, *130*, 6938. (b) Khan, N. A.; Jun, J. W.; Jeong, J. H.; Jhung, S. H. *Chem. Comm.* **2011**, *47*, 1306. (c) Achmann, S.; Hagen, G.; Hämmerle, M.; Malkowsky, I.; Kiener, C.; Moos, R. *Chem. Eng. Technol.* **2010**, *33*, 275.

16 Li, J.- Rong.; Sculley, J.; Zhou, H.- C. *Chem. Rev.* **2012** doi: 10.1021/cr200190s.

17 Cychosz, K. A.; Wong-Foy, A. G.; Matzger, A. J. *J. Am. Chem. Soc.* **2009**, *131*, 14538.

18 (a) *Maspero*, A.; *Galli*, S.; *Masciocchi, N.; Palmisano*, G. *Chem. Lett*. **2008**, *37*, 956. (b) Maspero, A.; Galli, S.; Colombo, V.; Peli, G.; Masciocchi, N.; Stagni, S.; Barea, E.; Navarro, J. A. R. *Inorg. Chim. Acta* **2009**, *362*, 4340.

19 Schlichte, K.; Kratzke, T.; Kaskel, S. *Microporous Mesoporous Mater.* **2004**, *73*, 81.

20 Chui, S.S.; Lo, S.M.; Charmant, J.P.; Orpen, A.G.; Williams, I.D. *Science* **1999**, *283*, 1148.

21 The pellets were obtained by pressing the original powder up to 7 tons cm^{-2}. The resulting disks were ground over a 1 mm sieve. The adsorptive properties and XRPD patterns were checked indicating that they are not modified after the pellets formation.

22 Version 3.0, Bruker AXS 2005, Karlsruhe, Germany.

23 Thermal treatments of our materials have been performed in air (TXRPD) and in N_2 atmosphere, using the standard equipment available in our laboratories. While these difference must be considered important when O_2 can induce side reactions, decomposition, etc., in our cases the thermal analyses were performed to study the desorption of solvent (DMSO, PhCN and water) molecules, which are not affected by the presence of a pure gas, or of a mixture of gases, as long as their inert behaviour is guaranteed. Obviously, decomposition of the framework under oxidizing conditions may occur at lower temperatures than under N_2.

24 Avrami, M. *J. Chem. Phys.* **1941***, 9*, 177 and references therein.

25 Volkringer, C.; Loiseau, T.; Guillou, N.; Férey, G.; Elkaïm, E.; Vimont, A. *Dalton Trans.* **2009**, 2241and references therein.

26 Ehlert, M.K.; Retting, S.J.; Storr, A.; Thompson, R.C.; Trotter, J. *Can. J. Chem.* **1990**, *68*, 1444.

27 Schofield, K.; Grimmet, M.R.; Keene, B.R.T. *Heteroaromatic nitrogen compounds: the azoles*. Cambridge University Press, Cambridge. **1976**.

28 Masciocchi, N.; Castelli, F.; Forster, P.M.; Tafoya, M.M.; Cheetham, A. K. *Inorg. Chem.* **2003**, *42*, 6147.

29 Masciocchi, N.; Ardizzoia, G.A.; Brenna, S.; LaMonica G.; Maspero A.; Galli S.; Sironi A. *Inorg. Chem.* **2002**, *41*, 6080.

30 Spek, A.L. *J. Appl. Cryst.* **2003**, *36*, 7.

31 Chaplais, G.; Simon-Masseron, A.; Porcher, F.; Lecomte, C.; Bazer-Bachi, D.; Bats, N.; Patarin, J. *Phys. Chem. Chem. Phys.* **2009**, *11*, 5241. (b) Horcajada, P.; Salles, F.; Wuttke, S.; Devic, T.; Heurtaux, D.; Maurin, G.; Vimont, A.; Daturi, M.; David, O.;Magnier, E.; Stock, N.; Filinchuk, Y.; Popov, D.; Riekel, C.; Férey, G.; Serre, C. *J. Am. Chem. Soc.* **2011**, *133*, 17839. (c) Biswas, S.; Ahnfeldt, T.; Stock, N. *Inorg. Chem.* **2011**, *50*, 9518.

32 (a) Ferey, G.; Serre, C. *Chem. Soc. Rev.* **2009**, *38*, 1380 and references therein. (b) Horcajada, P.; Salles, F.; Wuttke, S.; Devic, T.; Heurtaux, D.; Maurin, G.; Vimont, A.; Daturi, M.; David, O.;Magnier, E.; Stock, N.; Filinchuk, Y.; Popov, D.; Riekel, C.; Férey, G.; Serre, C. J. Am. Chem. Soc. **2011**, *133*, 17839.

33 Masciocchi, N.; Ardizzoia, G.A.; Maspero, A.; LaMonica, G.; Sironi, A. *Inorg. Chem.* **1999**, *38*, 3657.

34 Masciocchi, N.; Moret, M.; Cairati, P.; Sironi, A.; Ardizzoia, G.A.; La Monica, G. *J. Am. Chem. Soc.* **1994**, *116*, 7668.

35 For a collection of references see Chapter 2.

36 Worthy of note, if *D2d* (and not *Td*) metal ions are present [as in the α-Cu$(pz)_2$ phase], a *C*-centered orthorhombic space group symmetry (*Cmca*) can be also achieved. Thus, it is not surprising that a number of porous networks recently prepared by

employing terephthalate (bdc) anions (or similar tetradentate ligands of *D2h* symmetry), with four- or even six-connected metal ions, fall within these structural classes: as representative examples, M(OH)(bdc) (M = Al, Ga, Cr, V), Cu(btb), Co(BDP), collectively quoted, among others, in: Murray, L.J.; Dincă, M.; Long, J.R. *Chem. Soc. Rev.* **2009**, *38*, 1294-1314 and in Ref. 25.

37 (a) Llewellyn, P.; Maurin, G.; Devic, T.; Loera-Serna, S.; Rosenbach, N.; Serre, C.; Bourrelly, S.; Horcajada, P.; Filinchuk, Y.; Férey, G. *J. Am. Chem. Soc.* **2008**, *130*, 12808-12814; (b) Salles, F.; Ghoufi, A.; Maurin, G.; Bell, R.G.; Mellot-Draznieks, C.; Férey, G. *Angew. Chem. Int. Ed.* **2008**, *47*, 8487-8491.

38 (a) Uemura, K.; Matsuda, R.; Kitagawa, S. *J. Solid State Chem.* **2005**, *178*, 2420-2428. (b) Horike, S.; Shimomura, S.; Kitagawa, S. *Nat. Chem.* **2009**, *1*, 695.

39 Salles, F.; Maurin, G.; Serre, C.; Llewellyn, P. L.; Knofel, C.; Choi, H. J.; Filinchuk, Y.; Oliviero, L.; Vimont, A.; Long, J. R.; Ferey, G. *J. Am. Chem. Soc.* **2010**, *132*, 13782.

40 Lu, Y.; Tonigold, M.; Bredenkötter, B.; Volkmer, D.; Hitzbleck, J.; Langstein, G.; *Z. Anorg. Allg. Chem.* **2008**, 2411.

41 Rouquerol, F.; Rouquerol, J.; Singh, K.S.S.; *Adsorption by powders and porous solids*, Academic Press, **1999**.

42 Millward, A.R.; Yaghi, O.M. *J. Am. Chem. Soc.* **2005**, *127*, 17998.

43 Llewellyn, P.L.; Bourrelly, S.; Serre, C.; Filinchuk, Y.; Férey, G. *Angew. Chem. Int. Ed*. **2006**, *45*, 7751.

44 Lee, J.Y.; Olson, D. H.; Pan, L.; Emge, T.J.; Li, J. *Adv. Funct. Mater.* **2007**, *17*, 1255.

45 Llewellyn, P.L, Bourrelli, S.; Serre, C.; Filinckuk, Y., Férey, G. *Angew. Chem.* **2006***, 45*, 7751 and references therein.

46 Whether the coordination of DMSO to Ni(II) ions occurs either through the oxygen or through the sulfur atoms could not be experimentally assessed. A search in the Cambridge Structural Database (v. September 2009) demonstrates that, for first row transition metal ions, O-linkage isomers are preferred, though S-linkage ones are also known.

Chapter 5
Cubic Octanuclear Ni(II) Clusters in Highly Porous Polypyrazolyl-based Materials

Introduction

Over the last two decades, many efforts have been devoted to devise hybrid three-dimensional porous systems, in which metallic nodes are linked by long organic spacers,[1] aiming at the formation of thermally stable and chemically inert materials[2] for gas storage, gas separation and catalytic purposes. To this goal, polycarboxylates,[3] and, later, polyazolates,[4] have been largely employed, reaching significant scientific and technological achievements, with some of the best performing materials being marketed by leading chemical companies.[5]

The versatility of these systems can be traced back to the variety of the metallic nodes (either simple ions or polymetallic oxo-clusters), of the organic linkers, of the different synthetic techniques, and to the possibility of generating polymorphic species depending on the reaction or on the environmental conditions. All together, thousands of species of this kind have appeared in the literature:[6] while some have been serendipitously isolated, several highly performing materials were engineered using (poly)metallic nodes with specific geometric requirements,[7] ligands of tailored coordination capacity, and,

particularly, the highly fruitful isoreticular approach.[8] In this respect, the polycarboxylate species of Yaghi,[9] and Férey,[10] as well as the polyazolate materials reported by Long,[11] are widely considered renowned cornerstones of this field.

To understand the structural aspects governing or influencing PCPs functionality, with the final aim of their optimization, a thorough investigation of their structural features is mandatory. In particular, when suitable single crystals are not available, state-of-the-art powder diffraction methods allow to unravel otherwise not accessible key structural aspects.[12] In some cases, this information may be fruitfully complemented by fundamental local-level details, typically concerning the inorganic nodes, retrieved through X-ray (absorption and emission) spectroscopy.[13]

Juxtaposing, to this piece of information, complementary observations retrieved by means of other solid state techniques,[14] such as UV-Vis and variable-temperature IR spectroscopy (in the presence, or not, of probe molecules), may give a more complete understanding of the influence of the chemicophysical and structural features of a PCP on its functional properties.

During the last years, the coordination chemistry of homoleptic metal pyrazolates, imidazolates, and pyrimidinolates, have been deeply explored and demonstrated an extreme structural versatility, witnessed by the existence of cyclic oligomeric species,[15] stretched[16] and helical[17] 1D polymers, layered compounds and dense, as well as porous, 3D frameworks (see Chapter 2 and 4).[18] Moreover, in Chapter 3, an extensive work done for the optimization of the synthesis of new polytopic nitrogen ligands containing several donor sites, made it possible the preparation of the two new bis-pyrazolyl species, 4,4'-bis(1*H*-pyrazol-4-yl)biphenyl, H_2PBP, and 2,6-bis(1*H*-pyrazol-4-yl)pyrrolo[3,4-*f*]isoindole-1,3,5,7(2*H*, 6*H*)-tetrone, H_2TET, in which the heterocycles are separated by long rigid spacers (Scheme 5.1).

In this Chapter, these new organic linkers have been successfully reacted with nickel(II) metal ions giving rise to two isomorphous and highly porous

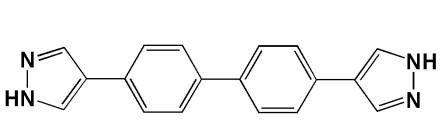

H_2PBP

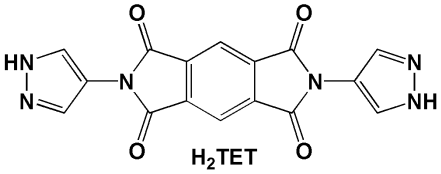

H_2TET

Scheme 5.1. Depiction of the polytopic pyrazole-based ligands 4,4'-bis(1H-pyrazol-4-yl) biphenyl, H_2PBP, and 2,6-bis(1H-pyrazol-4-yl)pyrrolo[3,4-f]isoindole-1,3,5,7(2H, 6H)-tetrone, H_2TET.

metal-organic frameworks of formula $[Ni_8(OH)_4(OH_2)_2(L)_6]$ (L = PBP or TET) in which the octanuclear secondary building units (SBUs) are structurally similar to the discrete complex $[Ni_8(\mu_4\text{-}OH)(pz)_{12}]^{2-}$, described in Chapter 2.[19] A deep structural investigation by coupling state-of-the-art *structural* powder diffraction techniques with X-ray absorption techniques and spectroscopic measurements, allow the detection and confirmation of relevant stereochemical features and of the complex formulation reported above. Moreover, preliminary studies on the adsorption properties of these two frameworks are here reported.

The large amount of different techniques employed in this work are the consequence of a fruitful collaboration with the Physical Chemistry groups of Professors Silvia Bordiga and Carlo Lamberti, from the University of Torino, Italy, that I sincerely thank. Indeed, the reader should be aware that some spectroscopic data are here reported only for the sake of completeness.

Experimental Details

Materials and Methods. Elemental analyses were done on a Perkin Elmer 2400 Series II. IR spectra (nujol mull) were recorded on a Shimadzu IRPrestige-21. DSC/TG were obtained on a Netzsch STA 409 PC under a nitrogen purge at 10 °C min^{-1}.

$Ni_8(OH_2)_2(OH)_4(PBP)_6$·10$H_2$O. To a solution of $Ni(OAc)_2$·4H_2O (0.087 g, 0.35 mmol) in DMF (7 mL), 4,4'-bis(1*H*-pyrazol-4-yl)biphenyl (0.100 g, 0.35 mmol) was added, at room temperature, under stirring. The mixture was heated to 60 °C; triethylamine (1.5 mL) was subsequently added dropwise over 1 min to the mixture. The reaction was then kept at reflux for 6 h. The green precipitate was filtered off, washed with successive aliquots of methanol (2 × 10 mL) and dried in vacuum at 130 °C for 1 h to afford the polycrystalline greenish product. IR 3565 (w), 3388 (br), 1651 (s), 1219 (w), 1102 (vs), 1056 (w), 830 (s), 723 (s), 631 (s) cm^{-1}. Anal. Calcd. for $C_{108}H_{100}N_{24}Ni_8O_{16}$ (2460 g mol^{-1}): C, 52.74 H, 4.10; N, 13.67. Found: C, 52.45; H, 4.21; N, 13.77 %.

$Ni_8(OH_2)_2(OH)_4(TET)_6$·8$H_2$O. To a suspension of $Ni(OAc)_2$·4H_2O (0.071 g, 0.287 mmol) in 1-methyl-2-pyrrolidinone (7 mL), 2,6-bis(1*H*-pyrazol-4-yl) pyrrolo[3,4-*f*]isoindole-1,3,5,7(2*H*,6*H*)-tetrone (0.100 g, 0.287 mmol) was added, at room temperature, under stirring. The mixture was then heated to 150 °C and kept in these conditions for 7 h. The brown precipitate was filtered off, washed with successive aliquots of methanol (2 × 10 mL) and dried under vacuum at 140 °C for 4 h to afford the polycrystalline product. IR 3571 (w), 3376 (br), 1720 (vs), 1658 (s), 1555 (s), 1242 (w), 1097 (br), 1051 (w), 657 (w), 817 (s), 722 (w) cm^{-1}. Anal., Calcd. For $Ni_8(OH_2)_2(OH)_4(TET)_6$·8$H_2O$, $C_{96}H_{60}N_{36}Ni_8O_{38}$ (2795.3 g mol^{-1}): C, 41.25; H, 2.16; N, 18.04. Found: C, 40.64; H, 2.99; N, 17.21 %. Note that, in distinct preparations, this species crystallizes with distinct amounts of chlatrated water molecules. Hence the difference between the number of water molecules obtained from the elemental analysis and that modelled *via* XRPD.

With the aim of identifying possible extraframework cations, attempts were carried out, without success (as checked by X-ray fluorescence), to exchange them with Cd(II) and uranyl ions: no new (poly)crystalline materials, from which to derive the position of the heavy atoms, were isolated.

$NiCl_2(H_2TET)$. A suspension of 2,6-bis(1*H*-pyrazol-4-yl)pyrrolo[3,4-*f*]isoindole-1,3,5,7(2*H*,6*H*)-tetrone (0.100 g, 0.287 mmol) in 1-methyl-2-pyrrolidinone (6 ml) was heated to 110 °C and then $NiCl_2 \cdot 6H_2O$ (0.069 g, 0.287 mmol) was added. The mixture was heated to 150 °C under vigorous stirring, and kept in these conditions for 6 hours. Then the suspension was slowly cooled to room temperature, the intense red solid was collected by filtration, washed with MeOH (2 × 10 mL) and dried in vacuum at 150 °C to give the desired product (0.100 g, 72%). IR 3275 (s), 1725 (vs), 1577 (w), 1491 (s), 1283 (w), 1225 (w), 1149 (s), 1100 (vs), 1063 (vs), 998 (s), 960 (w), 934 (w), 862 (s), 835 (vs), 715 (vs), 688 (s) cm^{-1}. Anal. Calcd. for $C_{16}H_8N_6Cl_2O_4Ni$ (477.8 g mol^{-1}): C, 40.21; H, 1.69; N, 1759. Found: C, 41.10; H, 1.25; N, 17.69 %.

X-Ray Powder Diffraction Structure Analysis. Powdered, microcrystalline samples of species 1-5 were gently ground in an agate mortar, then deposited in the hollow of an aluminum sample holder equipped with a zero-background plate. Diffraction data were collected with overnight scans, typically in the 5-105° 2θ range, on a Bruker AXS D8 Advance diffractometer, equipped with a linear position-sensitive Lynxeye detector, primary beam Soller slits, and Ni-filtered Cu-Kα radiation (λ = 1.5418 Å). The generator was set at 40 kV, 40 mA. Standard peak search, followed by indexing with TOPAS,[20] allowed the detection of the approximate unit cell parameters. The space groups were assigned on the basis of the systematic absences, checked by Le Bail refinements and later confirmed by successful structure solutions and refinements.

Structure solutions were performed by the simulated annealing technique, as implemented in TOPAS, using for the corresponding anions of H_2PBP and H_2TET ligands a rigid, idealized model, flexible at the arene-pyrazole torsion. The final refinements were carried out by the Rietveld method, maintaining the rigid bodies introduced at the structure solution stage. In all cases, the background

was modeled by a polynomial function. Peak shapes were determined by the Fundamental Parameters Approach.[21] Anisotropic peak broadening was modeled using spherical harmonics to define the peak widths in the case of species 5. One, refinable isotropic thermal parameter was assigned to the metal atoms, augmented by 2.0 $Å^2$ for lighter atoms. The final Rietveld refinement plots are shown in Figure 5.11.

Crystal data $[Ni_8(OH)_4(OH_2)_2(\mu_4\text{-PBP})_6]$. $C_{108}H_{80}N_{24}Ni_8O_6$, fw = 2279.53 g mol^{-1}, cubic, *Fm-3m*, a = 31.358(3) Å, V = 30836(9) $Å^3$, Z = 4, ρ = 0.49 g cm-3, μ (Cu-Kα) = 69.8 mm^{-1}, R_p, R_{wp} and R_{Bragg} = 0.007, 0.012, 0.008, respectively, for 3626 data collected in the 7.5-80.0° 2θ range.

Crystal data for $[Ni_8(OH)_4(OH_2)_2(\mu_4\text{-TET})_6]\cdot 6H_2O$. $C_{96}H_{56}N_{36}Ni_8O_{36}$, fw = 2759.27 g mol_{-1}, cubic, *Fm-3m*, a = 30.5845(2) Å, V = 28610(6) $Å^3$, Z = 4, ρ = 0.64 g cm^{-3}, μ (Cu-Kα) = 89.4 mm^{-1}, R_p, R_{wp} and R_{Bragg} = 0.030, 0.054, 0.054, respectively, for 4876 data collected in the 7.5-105.0° 2θ range.

Crystal data for $NiCl_2(H_2TET)$. $C_{16}H_8Cl_2N_6NiO_4$, fw = 477.88 g mol^{-1}, triclinic, *P-1*, a = 6.315(1), b = 3.620(1), c = 18.443(3) Å, α = 94.85(3), β = 109.93(1), γ = 89.25(3)°, V = 394.5(2) $Å^3$, Z = 1, ρ = 2.012 g cm^{-3}, μ (Cu-Kα) = 531.9 mm^{-1}, R_p, R_{wp} and R_{Bragg} = 0.025, 0.036, 0.023, respectively, for 3525 data collected in the 4.5-75.0° 2θ range.

Thermodiffractometric Studies. Thermodiffractometric experiments were performed on the hydrated species $Ni_8(OH_2)_2(OH)_4(TET)_6$, to highlight its "structural" response. The experiments were carried out in air from 298 K up to the loss of crystallinity, using a custom-made sample heater, assembled by Officina Elettrotecnica di Tenno, Ponte Arche, Italy. A powdered microcrystalline batch of 4 was deposited in the hollow of an aluminum sample holder; diffractograms at different temperatures (with steps of 20 K) were recorded, up to decomposition, in a significant low-angle 2θ range.

Infrared Spectroscopy. IR spectroscopy measurements were carried out by taking advantage of a cryogenic cell obtained by properly modifying a closed-cir-

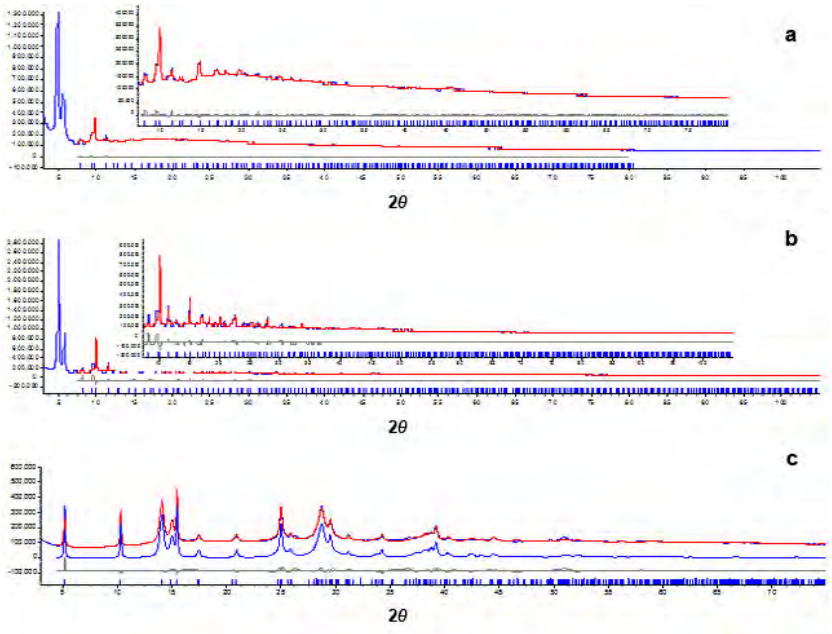

Figure 5.11. Rietveld Refinement Plots for a) **$Ni_8(OH_2)_2(OH)_4(PBP)_6$**; b) **$Ni_8(OH)_4(OH_2)_2(\mu_4\text{-}TET)_6(H_2O)_6$**; and c) **$NiCl_2(H_2TET)$**. Horizontal axis, 2θ, deg; vertical axis, counts. Peak markers and difference plots are reported at the bottom. The inserts show the pertinent plots at a magnified scale.

cuit liquid helium Oxford CCC 1204 cryostat, which allows the infrared monitoring of the adsorbed probes under controlled temperature (between 300 and 14 K) and pressure conditions. Thin self-supported wafers of **NiPBP** and **NiTET** were prepared in the cryogenic cell and outgassed under high vacuum (residual pressure < 10^{-4} mbar) at 453 K for 2 h. The spectra were recorded on a Bruker Equinox 55 FTIR spectrometer (equipped with an MCT cryogenic detector) mounting a sample compartment modified to accommodate the cryogenic head; 128 interferograms (recorded at 1 cm^{-1} resolution) were typically averaged for each spectrum. A typical IR experiment consisted of three steps: (i) 40 mbar of the gas probe (H_2 or CO) were initially dosed on the sample at 300 K. (ii) A set of IR spec-

tra was then recorded *in situ* while lowering the temperature down to 14 K for H_2 or to 60 K for CO. The samples were then left at the lowest temperature reached for one night, allowing the system to reach the equilibrium conditions. (iii) A set of IR spectra was finally recorded while stepwise outgassing the material. The spectrum obtained in the FIR region was acquired with a solid state beamsplitter based on silicon plate and FIR DLATGS detector (PE window).

DRS-UV-Vis Spectroscopy. Diffuse reflectance UV-Visible spectra were recorded on a Cary 5000 Varian spectrophotometer equipped with a reflectance sphere. A thick self-supported wafer of **NiPBP** and **NiTET**, inserted in a homemade quartz cell equipped with an optical window, was preliminary measured and then heated and outgassed under high vacuum (residual pressure < 10^{-4} mbar) at 453 K for 2 h, to acquire the spectrum of the activated sample.

X-ray absorption experiments. X-ray absorption experiments at the Ni K-edge (22117 eV), were performed in transmission mode at the BM26A of the ESRF facility (Grenoble, France).[22] The white beam was monochromatized using a Si(111) double crystal; harmonic rejection was achieved by using Pt-coated Si mirrors. The XANES part of the spectra was acquired with an energy step of 0.3 eV, while the EXAFS part was collected with a variable sampling step in energy, resulting in $\Delta k = 0.05$ Å^{-1}, up to 18 Å^{-1}. Integration time was 2 s/point in the pre-edge region, 5 s/point in the XANES region and a linearly variable interval from 5 to 30 s/point in the EXAFS region. The following experimental geometry was adopted: 1) I_0 (10% efficiency); 2) MOF sample; 3) I_1 (50% efficiency); 4) reference Ni foil; 5) I_2 (80% efficiency). This set-up allows a direct energy/angle calibration for each spectrum avoiding any problem related to little energy shifts due to small thermal instability of the monochromator crystals.[23] Samples of species 4 in form of self supported pellets of optimized thickness were measured in air.

The extraction of the χ(k) function was performed using the Athena code.[23] Three consecutive EXAFS spectra were collected and the corresponding χ(k) functions were averaged before data analysis.[25] EXAFS data analysis was performed using the Arthemis software.[24] Phase and amplitudes were calculated by the FEFF6 code[26] using as input the structure solved by powder X-ray diffraction (*see above*). Ni-O phase and amplitudes were successfully checked with NiO model compounds.[27,28] For each sample, the averaged k^3 χ(k) function was Fourier transformed in the Δk = 2.00-16.00 $Å^{-1}$ interval. The fits were performed in R-space in the ΔR = 1.00-4.50 Å range ($2\Delta k \Delta R/\pi > 31$).

Low Pressure Gas Sorption Measurements. Glass sample-tubes of a known weight were loaded with approximately 100 mg of sample, in the form of loose powder, and sealed using a TranSeal. The sample was degassed at 393 K overnight and, subsequently, at 453 K for 2 h on a Micromeritics ASAP2020 analyzer (Micrometrics Instruments Corp., Norcross, GA) until the outgas rate was less than 2 mTorr/min. The sample tube containing the degassed sample was weighed again and then transferred back to the analyzer. The outgas rate was again confirmed to be less than 2 mTorr/min. N_2 isotherms were measured at 77 K in a liquid nitrogen bath using UHP-grade gas sources.

High Pressure Gas Sorption Measurements. Excess H_2 adsorption isotherms were collected by volumetric measurements carried out at 77 K, over the 0–80 bar pressure range, on a PCI instrument supplied by Advanced Materials Corporation (Pittsburgh PA) which is capable of collecting isotherms over a wide range of pressures (0.01-200 bar) and temperatures (77-773 K). Ultra pure 6.0 grade H_2 (99.9999%V; Rivoira) was used to the purpose. A modified version of the Benedict-Webb-Rubin equation of state was used to correctly take into account the non ideal behaviour of the H_2 gas in the measurement conditions. In a typical measurement, about 500 mg of **NiPBP**, in the form of loose powder, were activated under ultra high vacuum (residual pressure < 10-4 mbar) at 393 K overnight

and, subsequently, at 453 K for 2 h. The activated material was then transferred, under protected atmosphere, in the measurement cell. The skeletal sample density was retrieved from the helium isotherm measured on the sample at 293 K in the 0-20 bar range, by means of the intelligent gravimetric analyzer IGA-002, supplied by Hiden Analytical Ltd, UK.

The total adsorption, n_{abs}, was calculated using the following relationship:

$$n_{abs} = n_{exc} + V_{pores} \cdot \rho_{gas}$$

where n_{exc} is the excess uptake, V_{pores} is the pore volume of the sample and ρ_{gas} is the density of pure H_2 gas as retrieved through the Benedict-Webb-Rubin equation. V_{pores} is calculated from the experimental skeletal density of the sample, d_{sk}, and the crystallographically determined bulk density of the sample, d_{bulk}, using the following expression:

$$V_{pores} = \frac{d_{sk} - d_{bulk}}{d_{sk}\, d_{bulk}}$$

The total volumetric uptake, n_{vol}, was calculated by:

$$n_{vol} = Q_{ads} \cdot d_{bulk}$$

where Q_{ads} represents the total H_2 adsorbed (in mmol/g).

Results and Discussion

Synthesis and Structure. On reacting H_2PBP and H_2TET with $Ni(OAc)_2 \cdot 4H_2O$ in a variety of solvents, two polycrystalline derivatives, $[Ni_8(OH)_4(OH_2)_2(PBP)_6] \cdot nSolv$ and $[Ni_8(OH)_4(OH_2)_2(TET)_6] \cdot nSolv$ (**NiPBP** and **NiTET**, respectively) were isolated. If, instead, $NiCl_2 \cdot 6H_2O$ is reacted with H_2TET, a different species, $[NiCl_2(H_2TET)]$, is formed, structurally characterized by XRPD

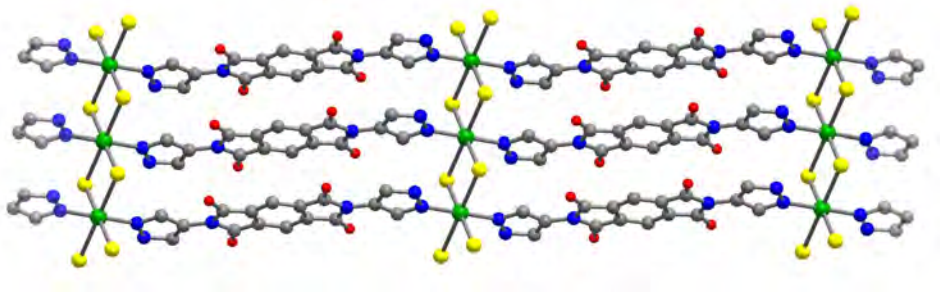

Figure 5.1. Schematic drawing of the crystal packing of **$NiCl_2(H_2TET)$**, viewed down [100]. Horizontal axis, **c**. Vertical axis, **b**. Carbon, gray; chlorine, yellow; nickel, green; nitrogen, blue; oxygen, red. Hydrogen atoms are omitted for clarity.

analysis as containing 2D layers built upon pseudooctahedral trans-NiCl4N2 chromophores linked in infinite $NiCl_2$ ribbons (Figure 5.1). The XRPD structural analysis of **NiPBP** and **NiTET** showed that these two isomorphous species are constituted by octanuclear Ni(II) hydroxo clusters linked by tetradentate μ_4-PBP and μ_4-TET ligands in a complex $Ni_8(\mu_4\text{-}X)_6(\mu_4\text{-}L)_6$ polyhedron of rigorous cubic symmetry (X = OH^- or H_2O; L = PBP or TET). Figure 5.2a shows the local stereochemistry of the octametallic node, which closely resembles that of the recently reported $[Ni_8(OH)_6(\mu_2\text{-pyrazolate})_{12}]^{2-}$ anion, described in Chapter 2. Similarly to the latter species, each Ni(II) ion in **NiPBP** and **NiTET** is hexacoordinated in a *fac*-NiN_3O_3 fashion and shows intermetallic non-bonding distances close to 3.0 Å (2.96-3.00 Å in ref. 19). In **NiPBP** and **NiTET**, the presence of long and rigid bis(exobidentate) spacers possessing pyrazolato moieties at both ends induces the formation of a *fcc* packing of the $[Ni_8(\mu_4\text{-}X)_6]^{12+}$ clusters, each linked to twelve symmetry-related nodes by the $\mu_4\text{-}L^{2-}$ ligands and kept more than 17 Å apart (see Figure 5.2b). As recently encountered in $Zr_6O_4(OH)_4(L^*)_6$ (L* = linear polyphenylendicarboxylates),[29] this favorable topology and coordination

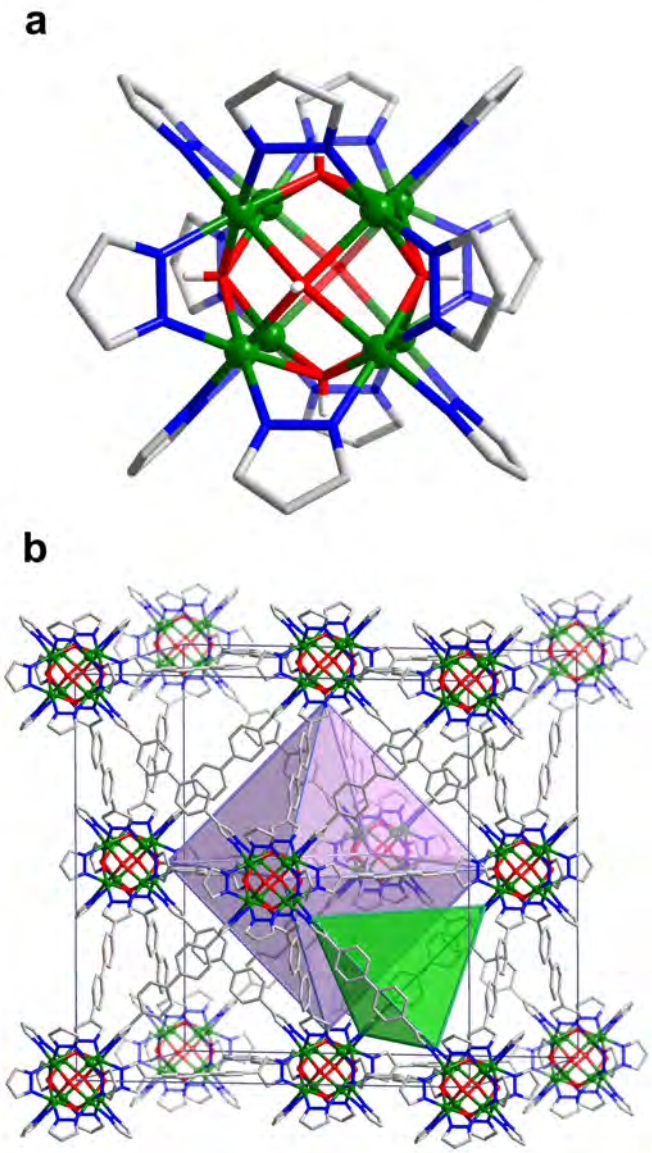

Figure 5.2. Representation of the crystal structure of **NiPBP**: a) the $Ni_8(OH)_4(OH_2)$ inorganic node; b) a portion of the overall 3-D packing, in which the octahedral cavity and one of the tetrahedral cavities have been highlighted. C, grey; H, white; Ni, green; N, blue; O, red. For the sake of clarity, the PBP has depicted according to an ideal ordered model.

geometry result in highly porous 3D frameworks: indeed, upon elimination of the residual solvents from the as-prepared samples, they possess accessible octahedral octahedral and tetrahedral cavities of about 1.8 nm and 1.0 nm inner size (*ca.* 72% void volume in **NiPBP**, *ca.* 70% in **NiTET**)[30] and, consequently, very low crystal density (down to less than 0.50 g cm^{-3}). Therefore, these materials are ideal candidates for gas sorption investigations (*vide infra*).

A special comment is deserved by the still ambiguous formulation set above for these new pyrazolate-based frameworks, due to structural disorder. While it is fairly obvious that solvent molecules can occupy the large voids of the structure (trapped either during direct precipitation, subsequent washing or from aerial moisture),[31] it proved much more difficult to assess the real nature of the X ligands, which has been model as a 2:1 ratio of OH^- and H_2O moieties. As a matter of fact, species **NiPBP** and **NiTET** contain octanuclear clusters similar to those found in $[Ni_8(OH)_4(H_2O)_2(C_5H_9O_2)_{12}]$,[32] where two of the six μ_4-O atoms were found to belong to water, rather than hydroxo, ligands, statistically distributed on the surface of the Ni_8 cube.

Spectroscopic Characterization. Aiming at the full comprehension of the nature of these interesting examples of highly porous frameworks, a number of complex spectroscopic analyses have been performed on the two isostructural MOFs.

Infrared Spectroscopy. The IR spectrum of the as-synthesized material is dominated by the bands due to the organic spacer - the major absorptions being present in the 3160-2850 and 1790-500 cm^{-1} ranges. The progressive elimination of water (Figure 5.3) brings about a sharpening of the absorption band at 3590 cm^{-1}, attributed to the bridging OH groups capping the faces of the Ni_8 polyhedra. Incidentally, this band lies at a significantly lower frequency than that observed for the hydroxyl groups in Ni-based phosphonates,[33] reasonably because of the unusual μ_4-bridging mode adopted by the hydroxyl moieties in **NiPBP** (*vs.* the

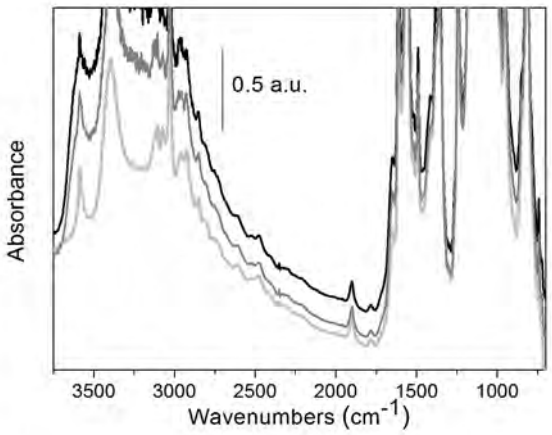

Figure 5.3. From black to light gray: effect of water removal on the FTIR spectrum of **NiPBP**.

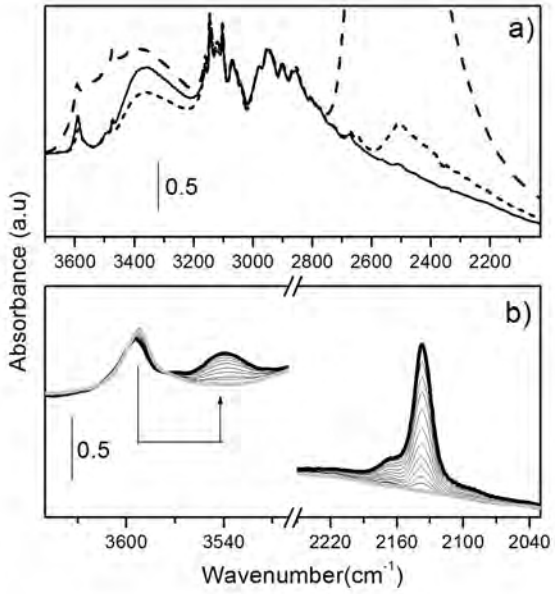

Figure 5.4. a) IR spectrum of sample **NiTET** collected after outgassing at 453 K (full line); dosage of D_2O (dashed line); sample outgassed at 453K 2 h (dotted line). b) effect of increasing dosages of CO at liquid nitrogen temperature. The grey curve corresponds to the sample outgassed 2 h at 453 K; the bold black curve corresponds to the highest coverage.

corresponding μ_4 mode observed in the phosphonates). *Notably, the persistence of a band centred at 3390 cm^{-1}, even after prolonged outgassing at 453 K, can only be explained by considering the presence of structural water molecules that cannot be removed without compromising the MOF structure.* According to the crystal structure, the persistence of the water capping molecules in the activated material is not compatible with the formation of exposed metal sites. These assignments are confirmed by IR spectroscopy, namely D_2O-induced proton exchange and (low temperature) framework interaction with CO.

Availability of hydroxyl groups and structural water molecules was thus tested through D_2O exchange. The results are reported in Figure 5.4. Upon equilibration with D_2O vapor pressure (dashed line), we observe the appearance of strong bands around 2500 cm^{-1} due to adsorbed species. Subsequent activation at 453 K causes a substantial decrease of the bands due to OH and H_2O and the appearance of a component at 2650 cm^{-1} ascribed to OD groups (short dashed line). The presence of residual absorption around 2500 cm^{-1} testifies the presence of structural D_2O. Unfortunately, we were not able to observe the eventual formation of DHO species.

To further strengthen this claim, the reactivity of an activated sample of **NiPBP** was investigated toward carbon monoxide, down to 60 K.[34] As evident in Figure 5.5a, upon CO adsorption, the band at 3590 cm^{-1}, ascribed to the stretching of the hydroxyl groups, is progressively eroded. Concomitantly, a broader component emerges and grows at a lower frequency ($\Delta\nu$ = -57 cm^{-1}), due to the formation of weak hydrogen bond interactions between the OH residues and the probe. At the same time, in the CO stretching frequency region, three distinct components can be appreciated: i) a very weak band growing at 2158 cm^{-1} and easily saturating, suggesting to be associated to defective sites; ii) a more relevant band developing at 2147 cm^{-1}, further confirming the formation of adducts between the hydroxyl groups and the CO molecules; iii) a band at 2134 cm^{-1},

associated to liquid-like CO liquefied inside the PCP cavities. The latter band becomes the major contribution upon progressive increase of the CO equilibrium pressure and, as expected, it is accompanied by the appearance of a band at 2094 cm^{-1}, due to the natural fraction of ^{13}C present in the CO gas. Finally, the absence of any components at higher frequencies excludes the presence of exposed Ni(II) ions, which should easily form Ni(II)···CO adducts, giving a strong band at 2178 cm^{-1}.[14b]

Moreover, hydrogen adsorption was monitored on an activated sample of **NiPBP** cooled down to 14 K (Figure 5.5b). At this point, it is worth recall that the H-H stretching of the H_2 molecule is IR inactive; nevertheless, upon adsorption, the interaction of H_2 with polarisable centres of the host disrupts its symmetry and activates its IR stretching mode, whose red-shift and intensity depend on the strength of the interaction.[35] Upon H_2 dosing, in the region of the OH stretching, the band at 3590 cm^{-1} is partially eroded in favor of the formation of a contribution at a lower frequency ($\Delta\nu$ = -9 cm^{-1}), due to extremely weak hydrogen bond interactions between the residual OH groups and the probe molecule. Concomitantly, the appearance of a band showing an initial shift of -53 cm^{-1} with respect to the Raman H-H stretching frequency of gaseous H_2 (4161 cm^{-1}), can be observed. Upon increasing coverage, this band progressively moves toward higher frequencies, till reaching a shift of just -25 cm^{-1}. The small value (-53 cm^{-1}) of the maximum observed shift at low coverage is in agreement with the results obtained using CO, confirming the absence of exposed Ni(II) ions. This is further corroborated by the low intensity of the H-H stretching band, which implies a weak interaction of H_2 with the material. Finally, the broad shape of the band, which does not show well defined features, is typical of H_2 weakly interacting with the walls of relatively large micropores, whereas materials with smaller pores exhibit more structured spectra.[36]

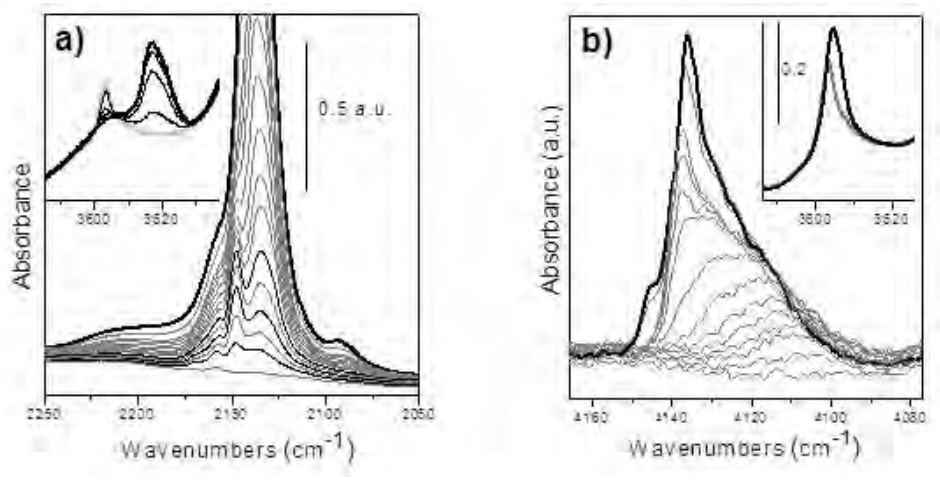

Figure 5.5. FTIR spectra of a) CO dosed at 60 K on an activated sample of **NiPBP** and its successive degassing. In the inset, the effect of CO dosing on the OH groups of the PCP is highlighted (the curves acquired at the same coverage in the CO stretching region are reported in black). b) H_2 dosed at 14 K on an activated sample of **NiPBP** and successive degassing. In the inset, the effect of H_2 dosing on the OH groups of the PCP is highlighted. In both cases, black bold curves represent the maximum coverage.

Electronic Transitions: UV-Vis, NIR, XANES. The material under study is characterized by a pale, not well defined color that does not change substantially upon outgassing in vacuum at 453 K. Figure 5.6a compares the DR-UV-Vis-NIR spectrum of an as prepared sample of **NiTET** with that obtained upon activation in vacuum at 453 K.

The spectra are similar, given by the combination of electronic transitions associated with the organic linker with those related to the presence of Ni(II) cations in a pseudo octahedral symmetry. Two strong bands associated with the ligand (maxima at 34500 and 29500 cm^{-1}) and at least three less intense components in the range of the *d-d* transitions (maxima at 22300, 15900. 10200 cm^{-1}) are present. With respect to a perfect octahedron, here we are in presence

of a more distorted structure, having Ni(II) sites with three oxygen and three nitrogen atoms in the first ccordination sphere. Upon activation, a change in the intensity ratio between the two components detected in the UV region is observed; the triplet at lower frequency becomes less defined and a new band centered at 7000 cm^{-1} appears, confirming that the local structure around the Ni(II) sites is significantly distorted upon outgassing. The phenomenon is completely reversible. Similar phenomena have been already obsered in the case of other MOFs,[14a] and microporous phosphonates.[33]

For sake of comparison, we report the spectrum of the as prepared Ni-CPO-27 MOF, characterized by *i*) a band at 9090 cm^{-1}, *ii*) a feature constituted by a double peak at 13333 and 15267 cm^{-1}, and *iii*) a component at about 20000 cm^{-1}. The last one is partially hidden by the intense absorption with an edge at 21740 cm^{-1}, associated with the lowest π-π* energy transition due to the organic linker. The other three main bands can be easily assigned by considering the UV-Vis-NIR spectrum of a Ni(II) aqueous solution as model, where Ni(II) has an O_h-like symmetry.

The XANES spectrum of species **NiTET** (dark blue curve in Figure 5.6b) is very similar to that observed for the Ni-CPO-27 MOF[14a,b,c] (green scattered curve in Figure 5.6b), indicating that we are dealing with a Ni(II) species in octahedral-like local symmetry. Moving from low to high photon energies, the XANES spectrum is characterized by three main features: *i*) a very weak 1*s* -- 3*d* dipole-forbidden electronic transition at 8333.3 eV (better appreciated in the inset); *ii*) a strong 1*s* -- 4*p* dipole-allowed electronic transition around 8343 eV (scarcely visible because too close to the edge jump; *iii*) a whiteline at 8349.5 eV (first resonance after the edge). The higher intensity of the 1*s* -- 3*d* transition observed for species **NiTET** with respect to that observed for the Ni-CPO-27 MOF reflects a higher distortion from a perfect local O_h symmetry: three oxygen and three nitrogen framework atoms form the first coordination

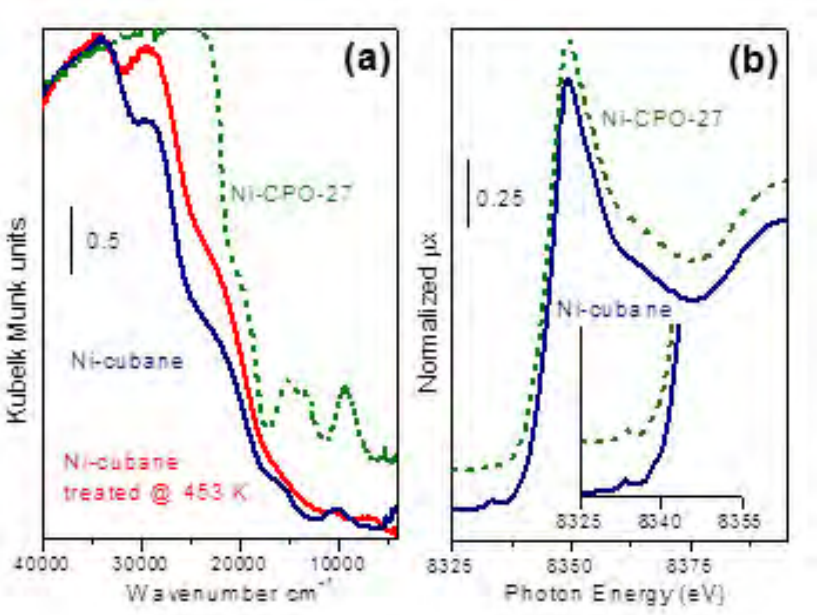

Figure 5.6. Comparison between the electronic features of species **NiTET** and those of the Ni-CPO-27 MOF. Part (a): DRS- UV-Vis spectra of *i*) sample as prepared (dark blue), ii) sample outgassed at 453 K (red), and *iii*) Ni-CPO-27 (scattered green). Part (b) Ni K-edge XANES spectrum of sample **NiTET** (dark blue) and of Ni-CPO-27 (scattered green). The inset reports a magnification of the 1*s* -- 3*d* dipole-forbidden electronic transition. In both part (a) and (b), the spectra of the Ni-CPO-27 MOF have been vertically translated for graphical reasons.

sphere in **NiTET**, *vs.* five framework oxygen atoms and a sixth oxygen atom from the adsorbed water molecules in Ni-CPO-27 MOF.

EXAFS Results. As was the case for other MOF systems,[2] notwithstanding the knowledge of the structure from XRPD, EXAFS data interpretation was not straightforward. Indeed, several single and multiple scattering (SS and MS) paths contribute to the overall amplitude. Contributions of the SS paths N1 (joint with O1), N2, Ni1 and Ni2, as can be singled out in Figure 5.7e, are highlighted as colored traces in Figure 5.7b-d, in k- (b) and R-space (c, d). The final results of

the structural refinement are shown in Table 5.1: the experimental geometrical parameters derived from our combined EXAFS and XRPD data analysis confirm the powder X-ray structure presented above, ruling out the presence of extraframework nickel-containing cations, balancing metallic nodes of a much simpler $[Ni_8(OH)_6(\mu_4\text{-}L)_6]^{2-}$ formulation. Other information of EXAFS data analysis are reported in the Supporting Information of *JACS* 2010, 132, 7902 and will not be discussed here in details.

The possible presence of other extraframework cationic moieties was thoroughly tested and coherently discarded, by coupling elemental analyses, chemical and unconventional spectroscopic evidences: the presence of protonated cations of the H_3L^+ type could be ruled out through vibrational spectroscopy, elemental analysis and in view of the basic environment in which the syntheses were performed. Thus, the final formulation of species **NiPBP** and **NiTET** is left formulated as $[Ni_8(OH)_4(OH_2)_2(\mu_4\text{-}L)_6]\cdot nH_2O$, eventually clearing out the ambiguity put forward in the previous pages.

Thermal Stability. The thermal stability of these coordination polymers has been investigated by DSC/TG and, particularly, by thermodiffractometric analyses. As shown in Figure 5.8, compound **NiTET** is stable from r.t. (blue trace) up to 410 °C, where decomposition begins. In this temperature range, variable temperature X-ray powder diffraction data indicate a substantial constancy of the crystal structure, with only marginal changes of some low-angle peaks intensity, due to water elimination. This process is reversible: in open air, moisture is readsorbed in a few hours.

Gas Adsorption Properties. The gas adsorption performances of **NiPBP** and **NiTET** were preliminary verified by collecting N_2 adsorption isotherms at 77 K (Figure 5.9). The optimally desolvated material was found to absorb significant amounts of N_2 at 77 K, displaying a Type I adsorption isotherm characteristic of materials possessing a microporous nature. Fitting the N_2 isotherm afforded

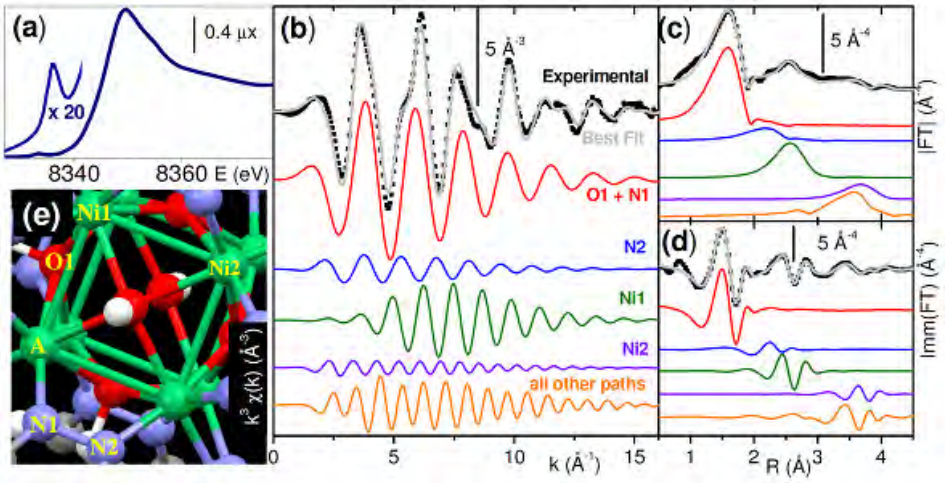

Figure 5.7. XANES spectrum for species **H_2TET** (a). Results of the EXAFS analysis for species **H_2TET** in k-space (b), and in R-space, both modulus (c) and imaginary part (d) reporting the most important SS contributions singled out from the cluster shown in (e), where A = adsorber.

Parameter	EXAFS (**4**)	XRPD (**3**)	XRPD (**4**)
R-factor	0.011	a	A
$\Delta E_{0,}$ eV	-4.1(5)	-	-
S_0^2	0.92(4)	-	-
$<R_{O1,N1}>$, Å	2.04(1)	2.09-2.15	2.01-2.08
σ^2(O1,N1), Å^2	0.0087(5)	-	-
R_{N2}, Å	2.77(2)	2.89	2.88
σ^2(N2), Å^2	0.010(2)	-	-
R_{Ni1}, Å	2.96(1)	2.92	2.83
σ^2(Ni1), Å^2	0.011(1)	-	-
R_{Ni2}, Å	4.12(3)	4.13	4.08
σ^2(Ni2), Å^2	0.010(3)	-	-
α (all other paths)	-0.03(3)	-	-
σ^2(all other paths), Å^2	0.007(1)	-	-

[a] see crystal data in Experimental Details.

Table 5.1. Summary of EXAFS and XRPD results. Esd's in parentheses.

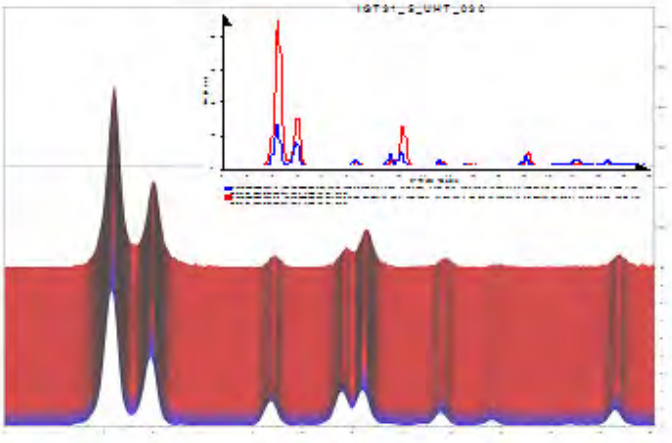

Figure 5.8. Thermodiffractogram of species **4**, highlighting the substantial constancy of its XRPD pattern, when heated, in air, from r.t. (blue trace) to 410 °C. The upper insert shows the relative changes of peak intensities due to extraframework water elimination.

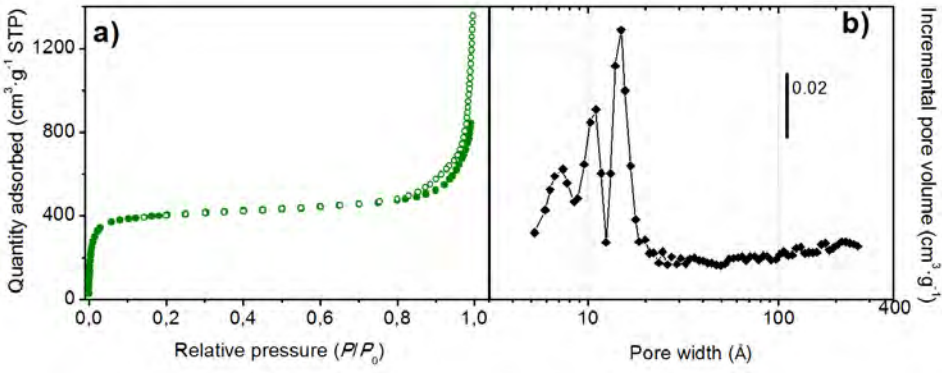

Figure 5.9. a) Volumetric N_2 adsorption isotherms acquired at 77 K on **NiPBP**. Filled and empty rhombi refer to the adsorption and desorption branches, respectively. b) Pore distribution obtained by applying the NLDFT method (Non-Local Density Functional Theory, cylindrical pore model, Tarazona) to the N_2 adsoption data in part (a). Note the logarithmic scale of the horizontal axis.

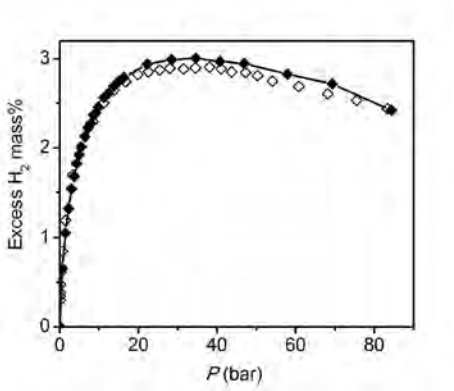

Figure 5.10. H_2 excess isotherm acquired at 77 K on **NiPBP**. Filled and empty rhombi refer to the adsorption and desorption branches, respectively.

Langmuir specific surface area of 1824(3) m^2/g and 1700(6) $m^2 g^{-1}$ (for **NiPBP** and **NiTET**, respectively) and an impressively high pore volume of 0.80 cm^3g^{-1}. For a complete study on the adsorption properties, **NiPBP** was chosen as a representative example. The contribution of the micropores only can be estimated as 0.56 cm^3g^{-1} which is in good agreement with the value of 0.63 cm^3g^{-1} retrieved by the crystal structure, thus highlighting that, after proper activation, most of the internal void volume is accessible to the gas probe. The microporous nature of the sample is confirmed also by both the t-plot and the DFT analysis. In particular, the pore size distribution, as obtained by the DFT approach (Figure 5.9b), highlights the presence of three distinct ranges of micropore sizes, peaking at 1.5, 1.1 and 0.7 nm. Notably, these dimensions roughly correspond to the diameters of the tetrahedral and octahedral cages of the material, and of their entrance windows, respectively (1.8, 1.0 and 0.5 nm, respectively).

The high pressure H_2 adsorption isotherm collected for **NiPBP**, recorded at 77 K, is shown in Figure 5.10. The coincidence of the adsorption and desorption branches indicates the full reversibility of the process, which is characterized by a fast kinetics, the equilibrium being reached in less than 5 minutes for each pressure point. This evidence perfectly matches the results emerged from the IR measurements, which exclude the presence of exposed metal sites

as possible preferential centers for interactions between the H_2 molecules and the framework. According to the high pressure H_2 adsorption isotherm, at 77 K **NiPBP** exhibits a maximum excess adsorption of 3.0 wt% at 34.5 bar. This uptake, although noteworthy, is sensitively lower than those reported for MIL-101, IRMOF-20 and MOF-177 in the same pressure and temperature conditions (6.1, 6.2 and 7.0 wt%, respectively).[37] The total adsorption, calculated using the experimental pore volume of 0.8 cm^3g^{-1} retrieved from the porosimetry measurements, reaches values of 3.9 and 4.4 wt% at 34.5 and 84.5 bar, respectively. Notably, an uptake of 4.4 wt% well agrees with the value theoretically expected assuming the formation of a complete monolayer of H_2 having a close packed *fcc* structure in the close packing limit (4.5 wt%), indicating that, at 77 K and 84.5 bar, the monolayer is completely filled.

Conclusions

Summarizing, state-of-the-art structural powder diffraction techniques (which have recently increased the basket of structural tools in the structural chemist's hands[38] - well beyond the traditional methods of qualitative and quantitative analyses), were coupled with X-ray absorption techniques and spectroscopic measurements, allowing the detection and confirmation of relevant stereochemical features, and, above all, the determination of the correct, but *elusive*, stoichiometry of these $[Ni_8(OH)_4(OH_2)_2(\mu_4\text{-}L)_6]\cdot nH_2O$ porous coordination polymers. Moreover, the foregoing results afford a coherent picture of the gas adsorption properties of **NiPBP**, as probed by low and high pressure adsorption measurements of N_2 and H_2, respectively, at 77 K. The adsorptive performances of **NiPBP** have been also interpreted through the information emerged from variable temperature IR spectroscopy. Thus, the absence of exposed metal sites, suggested by the not-so-exciting H_2 uptake, could be further corroborated by the response of the material toward CO and H_2, as monitored by IR.

Acknowledgments

Fondazione CARIPLO (Project No. 2007-5117) is heartily acknowledged for funding. XANES and EXAFS spectra were collected at BM26A at ESRF.

References and Notes

1 Batten, S.; Neville, S. N.; Rurner, D. R. *Coordination Polymers: Design, Analysis and Application*; RSC Publishing: **2009**, Cambridge, UK.

2 Cavka, J. H.; Jakobsen, S.; Olsbye, U.; Guillou, N.; Lamberti, C.; Bordiga, S.; Lillerud, K. P. *J. Am. Chem. Soc.* **2008**, *130*, 13850.

3 Britt, D.; Tranchemontagne, D. J.; Yaghi, O. M. *Proc. Nat. Acad. Sci. USA* **2008**, *105*, 11623, and references therein.

4 Galli, S.; Masciocchi, N.; Colombo, V.; Maspero, A.; Palmisano, G.; Lopez-Garzon, F. J.; Domingo-García, M.; Fernandez-Morales, I.; Barea, E.; Navarro, J. A. R. *Chem. Mater.* **2010**, *22*, 1664, and references therein.

5 Czaja, A. U.; Trukhan, N.; Müller, U. *Chem. Soc. Rev.* **2009**, *38*, 1284.

6 Long, J. R.; Yaghi, O. M. *Chem. Soc. Rev.* **2009**, *38*, 1213.

7 Tranchemontagne, D. J.; Mendoza-Cortés, J. L.; O'Keeffe, M.; Yaghi, O. M. *Chem. Soc. Rev.* **2009**, *38*, 1257.

8 Eddaoudi, M.;. Kim, J.; Rosi, N.; Vodak, D.; Wachter, J.; O'Keeffe, M.; Yaghi, O. M. *Science* **2002**, *295*, 469.

9 Eddaoudi, M.; Moler, D.; Li, H.; Reineke, T. M.; O'Keeffe, M.; Yaghi, O. M. *Acc. Chem. Res.* **2001**, *34*, 319, and references therein.

10 Férey, G.; Serre, C. *Chem. Soc. Rev.* **2009**, *38*, 1380, and references therein.

11 Choi, H. J.; Dinca, M.; Long, J. R. *J. Am. Chem. Soc.* **2008**, *130*, 7848.

12 Masciocchi, N.; Galli S.; Sironi A. *Comm. Inorg Chem.* **2005**, 26, 1.

13 Bordiga, S.; Bonino, F.; Lillerud, K. P., Lamberti, C. *Chem. Soc. Rev.*, **2010**, *39*, 4885.

14 (a) Bonino, F.; Chavan, S.; Vitillo, J. G.; Groppo, E.; Agostini, G.; Lamberti, C.; Dietzel, P. D. C.; Prestipino, C.; Bordiga, S. *Chem. Mater.* **2008**, *20*, 4957. (b) Chavan, S.; Vitillo, J. G.; Groppo, E.; Bonino, F.; Lamberti, C.; Dietzel, P. D. C.; Bordiga, S. *J. Phys. Chem. C* **2009**, *113*, 3292. (c) Chavan, S.; Bonino, F.; Vitillo, J. G.; Groppo, E.; Lamberti, C.; Dietzel, P. D. C.; Zecchina, A.; Bordiga, S. *Phys. Chem. Chem. Phys.* **2009**, *11*, 9811. (d) C. Lamberti, A. Zecchina, E. Groppo and S. Bordiga, *Chem. Soc. Rev.*, 2010, **39**, 4951.

15 Masciocchi, N.; Corradi, E.; Moret, M.; Ardizzoia, G. A.; Maspero, A.; La Monica, G.; Sironi, A. *Inorg. Chem.* **1997**, *36*, 5648.

16 See for example: Masciocchi, N.; Moret, M.; Cairati, P.; Sironi, A.; Ardizzoia, G. A.; La Monica, G. *J. Am. Chem. Soc.* **1994**, *116*, 7668.

17 Ardizzoia, G. A.; La Monica, G.; Masciocchi, N.; Maspero, A.; Sironi, A. *Angew. Chem. Int. Ed. Engl.* **1998**, *37*, 3366.

18 Galli, S.; Masciocchi, N.; Tagliabue, G; Sironi, A.; Navarro, J. A. R.; Salas, J. M.; Mendez-Liñan, L.; Domingo, M.; Perez-Mendoza, M.; Barea, E. *Chem. Eur. J.* **2008**, *14*, 9890, and references therein.

19 Xu, J.-Y.; Qiao, X.; Song, H.-B.; Yan, S. P.; Liao, D.-Z.; Gao, S.; Journaux, Y.; Cano, J. *Chem. Commun.* **2008**, 6414.

20 Version 3.0, Bruker AXS, **2005**, Karlsruhe, Germany.

21 Cheary, R.W.; Coelho, A. *J. Appl. Cryst.* **1998**, *31*, 851; ibid. 862-868.

22 Nikitenko, S.; Beale, A. M.; van der Eerden, A. M. J.; Jacques, S. D. M.; Leynaud, O.; O'Brien, M. G.; Detollenaere, D.; Kaptein, R.; Weckhuysen, B. M.; Bras, W. *J. Synchrotron Rad.* **2008**, *15*, 632.

23 Lamberti, C.; Bordiga, S.; Bonino, F.; Prestipino, C.; Berlier, G.; Capello, L.; D'Acapito, F.; Xamena, F. X. L. I.; Zecchina, A. *Phys. Chem. Chem. Phys.* **2003**, *5*, 4502.

24 Ravel, B.; Newville, M. *J. Synchrot. Radiat.* **2005**, *12*, 537.

25 Lamberti, C.; Bordiga, S.; Arduino, D.; Zecchina, A.; Geobaldo, F.; Spanò, G.; Genoni, F.; Petrini, G.; Carati, A.; Villain, F.; Vlaic, G. *J. Phys. Chem. B* **1998**, *102*, 6382.

26 Zabinsky, S. I.; Rehr, J. J.; Ankudinov, A.; Albers, R. C.; Eller, M. *J. Phys. Rev. B* **1995**, *52*, 2995.

27 Lamberti, C.; Groppo, E.; Prestipino, C.; Casassa, S.; Ferrari, A. M.; Pisani, C.; Giovanardi, C.; Luches, P.; Valeri, S.; Boscherini, F. *Phys. Rev. Lett.* **2003**, *91*, Paper n. 046101.

28 Groppo, E.; Prestipino, C.; Lamberti, C.; Luches, P.; Giovanardi, C.; Boscherini, F. *J. Phys. Chem. B* **2003**, *107*, 4597.

29 Cavka, J. H.; Jacobsen, S.; Olsebye, U.; Guillou, N.; Lamberti, C.; Bordiga, S.; Lillerud, K. P. *J. Am. Chem. Soc.* **2008**, *130*, 13850.

30 The inner size of the cavity has been estimated as twice the distance between the centre of the cavity and the nearest atom, A, decorating its walls. The proper correction for the vdW radius of A has been applied

31 The presence of (disordered) solvent is witnessed by the fact that framework atoms alone did not model the whole X-ray scattered intensity. The less-than-ideal quality of the XRPD traces hampered solvent modeling.

32 Ovcharenko, V.; Fursova, E.; Romanenko, G.; Eremenko, I.; Tretyakov, E.; Ikorskii, V. *Inorg. Chem.* **2006**, *45*, 5338.

33 Miller, S. R.; Pearce, G. M.; Wright, P. A.; Bonino, F.; Chavan, S.; Bordiga, S.; Margiolaki, I.; Guillou, N.; Férey, G.; Bourrelly, S.; Llewellyn, P. L. *J. Am. Chem. Soc*. **2008**, *130*, 15967.

34 Zecchina, A.; Scarano, D.; Bordiga, S.; Spoto, G.; Lamberti, C. *Adv. Catal*., **2001**, *46*, 265.

35 Vitillo, J. G.; Regli, L.; Chavan, S.; Ricchiardi, G.; Spoto, G.; Dietzel, P. D. C.; Bordiga, S.; Zecchina, A. *J. Am. Chem. Soc.* **2008**, *130*, 8386.

36 Figueroa-Gerstenmaier, S.; Daniel, C.; Milano, G.; Vitillo, J. G.; Zavorotynska, O.; Spoto, G.; Guerra, G. *Macromolecules*, **2010**, *43*, 8594.

37 (*a*) Wong-Foy, A. G.; Matzger, A. J.; Yaghi, O. M. *J. Am. Chem. Soc.* **2006**, *128*, 3494. (*b*) Long, J. R.; Dinca, M. *Angew. Chem. Int. Ed.* **2008**, *47*, 6766.

38 David, W. I. F.; Shankland, K.; Mc Cusker, L.B.; Bärlocher, Ch. Eds. Structure determination from powder diffraction data; Oxford University Press: **2006**, Oxford, UK.

Chapter 6
Towards new insights of high thermal and chemical stability in metal-organic frameworks

Introduction

A large segment of the global economy is based on the use of natural and synthetic zeolites in chemical industries as detergents, adsorbents/desiccants, and heterogeneous catalysts.[1] Consequently, worldwide consumption of these materials is estimated at about 4-4.5 million metric tons per year.[1c,d] As purely inorganic materials, zeolites are extraordinarily robust and provide moderately high surface areas, which together facilitate catalytic activity. Nevertheless, their performances can be limited by the stiffness of the framework, whose features, above all pore size and surface functionalization, are not readily modified using self-assembly approaches. As widely discussed in this thesis, metal-organic frameworks have begun to emerge as possible alternatives for such applications. Compared to zeolites, this new class of materials typically display a considerable degree of tunability, achievable by judicious selections of inorganic and organic components, or *via* post-synthetic modification of the surface.[2] Related to their stability, although metal-organic frameworks have in rare instances displayed thermal stability up to 500 °C,[3] none yet approach the robustness of zeolites, a disadvantage further worsened by problems generally related to their low

chemical stability. This is particularly true for those systems based on divalent metal cations combined with organocarboxylate bridging ligands,[4] which can be subject to hydrolysis and thermal decomposition in the presence of moisture.[5] In this regard, it is clearly beneficial to discover new high-surface area metal-organic frameworks that are stable toward diverse environments such as air, water, acidic and basic media, and even extreme temperatures and pressures. Such advancements will extend the utility of metal-organic frameworks towards a variety of applications where zeolites have been playing a major role.

Along this line, the research strategy of this project has involved the use of polyazolate-bridging ligands,[6] that can lead to frameworks with strong metal-nitrogen bonds, providing a greater chemical and thermal stability compared to their carboxylate-based counterparts. Employing polyazolate heterocycles, the strength of the resulting M-N bonds can be predicted to be closely related to the pK_a values for the deprotonation of the N-H bond. Indeed, increased stability has been observed for frameworks generated from organic ligands functionalized with 1,2,3-triazole (pK_a = 13.9)[7] than for analogues based upon tetrazole (pK_a = 4.9).[7,8] Imidazole, with an even higher pK_a of 18.6,[7] has been shown to afford frameworks of still greater thermal stability (T_{dec} up to 390 °C) and some chemical resistance to alkalinity and boiling solvents like water, methanol and benzene.[3a] In particular, however, organic ligands functionalized with pyrazole (pK_a = 19.8),[7] are of interest for the synthesis of robust pyrazolate-bridged frameworks.

A number of pyrazolate-based metal-organic frameworks exhibiting exceptional stability have already been realized,[9] the majority of which are part of this PhD research. Worthy of note, however, none of these high-stability pyrazolate-based frameworks possess internal surfaces bearing open metal coordination sites. Exposed metal cations within metal-organic frameworks have been demonstrated to lead to outstanding properties for hydrogen storage,[10] gas separations,[4c-f,11,11] and catalysis.[12] Among the azolate-based metal-organic

frameworks of this type, Mn-BTT, as already been described in Chapter 1, is a rigid high-surface area framework with an expanded sodalite-like structure and exposed Mn^{2+} sites of formula $Mn_3[(Mn_4Cl)_3(BTT)_8]_2 \cdot 20MeOH$ (H_3BTT = 1,3,5-tris(2*H*-tetrazol-5-yl)benzene). This framework exhibited a high H_2 binding affinity[14a] and Lewis acid catalytic activity.[11b] Unfortunately, the relatively low thermal stability (T_{dec} ~ 200 °C) and water-sensitivity of this tetrazolate-bridged framework limits its utility. Attempts to synthesize analogous triazolate-based structures afforded the more stable framework $H_3[(Cu_4Cl)_3(BTTri)_8]$ (Cu-BTTri, H_3BTTri = 1,3,5-tris(1*H*-1,2,3-triazol-5-yl)benzene).[8] With improved thermal stability (T_{dec} = 270 °C), this compound exhibits substantial chemical resistance, retaining its porous structure in a diluted HCl solution (pH 3) at room temperature or in boiling water for 3 days. Moreover, its stability in basic media enabled grafting of ethylenediamine on the open Cu^{2+} sites, leading to a record heat of CO_2 adsorption for a metal-organic framework.

In order to achieve a still greater level of stability, approaching that of zeolites, pyrazolate-bridged analogues of this important structure type were sought. Herein, the new linker 1,3,5-tris(1*H*-pyrazol-4-yl)benzene (H_3BTP), described in **Chapter 3**, have been successfully reacted with Co(II), Ni(II), Cu(II) and Zn(II) salts generating a series of exceptionally robust metal-organic frameworks, two of which adopt the Mn-BTT structure and feature exposed metal cation sites.

Experimental Details

All the reagents were obtained from commercial vendors, and were used without further purification. H_3BTP was synthesized according the procedure reported in **Chapter 3**.

$Ni_3(BTP)_2 \cdot 3DMF \cdot 5CH_3OH \cdot 17H_2O$ (1). Solid H_3BTP (500 mg, 1.81 mmol) was dissolved in DMF (50 mL) in a round-bottomed flask and $Ni(CH_3COO)_2 \cdot 4H_2O$ (676 mg, 2.72 mmol) was added to the stirred solution. The mixture was heated at

reflux for 16 h, with formation of a yellow precipitate observed in the first 4 h. Upon cooling, the yellow solid was collected by filtration, washed with methanol (3 x 10 mL) and dried under reduced pressure to yield 1.02 g (80%) of product. Anal. Calcd. for $C_{44}H_{93}N_{15}Ni_3O_{25}$ (Mw = 1408.37 g/mol): C, 37.52; H, 6.66; N, 14.92. Found: C, 37.66; H, 5.75; N, 14.35. IR (neat): 3370(br), 1655(s), 1609(vs), 1557(w), 1406(w), 1385(w), 1361(w), 1329(w), 1257(s), 1196(w), 1135(w), 1078(vs), 1015(s), 854(w), 761(vs), 685(w), 640(s), 461(w) cm^{-1}.

$Ni_3(BTP)_2 \cdot 3CH_3OH \cdot 10H_2O$ (1m). A methanol-exchanged form of **1** was obtained by heating the solid immersed in methanol (10 mL) at 180 °C in a PTFE sealed pressure vessel for three days. Upon cooling, the precipitate was collected by filtration, washed with methanol (3 x 5 mL) and dried under reduced pressure for 12 h. Anal. Calcd. for $C_{33}H_{50}N_{12}Ni_3O_{13}$ (Mw = 998.90 g/mol): C, 39.68; H, 5.05; N, 16.83. Found: C, 39.53; H, 4.32; N, 16.60. IR (neat): 3365(br), 1609(vs), 1556(w), 1407(w), 1329(w), 1257(s), 1196(w), 1135(w), 1078(s), 1014(vs), 852(w), 761(vs), 686(w), 640(s), 462(w) cm^{-1}. The desolvated form of the compound (**1d**) was generated by heating **1m** under dynamic vacuum at 250 °C, as described below.

$Cu_3(BTP)_2 \cdot 8CH_3OH \cdot 10H_2O$ (2). A solution of H_3BTP (200 mg, 0.725 mmol) in 25 mL of DMF was added to a round-bottomed flask, together with $Cu(CH_3COO)_2 \cdot H_2O$ (186 mg, 0.930 mmol). The mixture was stirred and heated at 150 °C for 16 h, during which time a brown solid precipitated. Upon cooling, the solid was collected by filtration and suspended in 5 mL of methanol for 2 h. The brown solid was then collected by filtration, washed with methanol (3 x 10 mL) and dried under reduced pressure for 12 h to yield 320 mg (75%) of product. Anal. Calcd. for $C_{38}H_{70}Cu_3N_{12}O_{18}$ (Mw = 1173.70 g/mol): C, 38.89; H, 6.01; N, 14.32. Found: C, 38.56; H, 5.23; N, 14.66. IR (neat): 3370(br), 1608(vs), 1557(w), 1426(w), 1385(w), 1354(w), 1322(w), 1243(w), 1180(w), 1126(s), 1061(vs), 1012(vs), 946(w), 832(s), 758(vs), 681(w), 637(w), 460(w) cm^{-1}. The desolvated form of the compound (**2d**) was generated by heating **2** under dynamic vacuum at 250 °C, as described below.

$Cu_3(BTP)_2 \cdot 6H_2O$ (2¢). Compound **2** (100 mg) was suspended in an aqueous HCl solution (10 mL, pH 3). The mixture was heated at 100 °C for one day in a 25-mL Teflon-capped scintillation vial. The dark brown suspension was then collected by filtration and washed with successive aliquots of water (3 x 10 mL) and methanol (3 x 5 mL). The same compound can be obtained by heating **2** in aqueous NaOH solution (10 mL, pH 14). Anal. Calcd. for $C_{30}H_{30}Cu_3N_{12}O_6$ (Mw = 845.27 g/mol): C, 42.63; H, 3.58; N, 19.88. Found: C, 42.69; H, 2.28; N, 19.23. IR (neat): 3130(br), 1679(w), 1610(s), 1593(vs), 1544(w), 1378(w), 1346(w), 1324(s), 1249(w), 1183(w), 1122(s), 1060(vs), 1043(w), 998(s), 942(w), 839(vs), 753(vs), 684(w), 643(s), 533(br), 456(w) cm^{-1}.

$Zn_3(BTP)_2 \cdot 4CH_3OH \cdot 2H_2O$ (3). H_3BTP (250 mg, 0.906 mmol) and $Zn(CF_3SO_3)_2$ (500 mg, 1.38 mmol) were dissolved in 30 mL of DMF in a round-bottomed flask, and the yellow solution was heated to 60 °C. Triethylamine (500 mL) was then added dropwise to the solution under vigorous stirring. Formation of a white precipitate was immediately observed. The mixture was then heated at reflux for 16 h. Upon cooling, the white solid was collected by filtration, washed with methanol (4 x 10 mL), and dried under vacuum to yield 320 mg (78%) of product. Anal. Calcd. for $C_{34}H_{38}N_{12}O_6Zn_3$ (Mw = 906.91 g/mol): C, 44.03; H, 4.22; N, 18.53. Found: C, 44.56; H, 3.98; N, 17.92. IR (neat): 3270(br), 1679(w), 1616(s), 1557(w), 1378(w), 1352(w), 1318(s), 1258(w), 1244(w), 1177(w), 1158(w), 1123(w), 1061(vs), 1009(s), 877(w), 845(s), 759(vs), 700(w), 677(w), 653(w) cm^{-1}.

$Zn_{12}[Zn_2(H_2O)_2]_6(BTP)_{16}$ (3¢). Compound **3** (100 mg, 0.1103 mol) was suspended in an aqueous NaOH solution (10 mL, pH 14) in a 25-mL Teflon-capped scintillation vial and stirred at room temperature for 1 h. The white solid was then collected by filtration, and washed with water (3 x 10 mL) and methanol (3 x 5 mL). Anal. Calcd. For $C_{240}H_{168}N_{96}O_{12}Zn_{24}$ (Mw = 6157.90 g/mol): C, 46.81; H, 2.75; N, 21.84. Found: C, 45.91; H, 3.05; N, 19.95. IR (neat): 3603(w), 3300(br), 3112(w),

1604(s), 1550(w), 1376(w), 1312(s), 1260(w), 1241(w), 1165(w), 1060(vs), 1004(s), 933(w), 847(vs), 753(vs), 695(w), 671(w), 656(w), 581(w), 544(br) cm^{-1}.

$Co_3(BTP)_2 \cdot 8CH_3OH \cdot 10H_2O$ (4). Under an N_2 atmosphere, H_3BTP (100 mg, 0.362 mmol) and $Co(CF_3SO_3)_2$ (194 mg, 0.543 mmol) were dissolved in 10 mL of DMF in a two-neck round-bottomed flask equipped with condenser and nitrogen inlet. The resulting purple solution was heated to 60 °C and triethylamine (250 µL) was added while hot. A deposit of dark purple solid immediately appeared. The mixture was then allowed to react for 16 h at reflux. Upon cooling, the solid was collected by filtration under nitrogen, washed with methanol (4 x 10 mL), and dried under vacuum to afford 150 mg (72%) of product as a purple powder. Anal. Calcd. For $C_{38}H_{70}Co_3N_{12}O_{18}$ (Mw = 1159.83 g/mol): C, 39.35; H, 6.08; N, 14.49. Found: C, 38.56; H, 5.98; N, 14.66. IR (neat): 3280(br), 1678(w), 1610(s), 1558(w), 1373(w), 1350(w), 1314(s), 1236(w), 1172(w), 1154(s), 1119(w), 1056(vs), 1042(s), 1007(s), 877(w), 843(s), 760(vs), 700(w), 675(w), 654(w) cm^{-1}.

Chemical Stability Tests. Compounds **1-3** (100 mg) were suspended in water in a 25-mL Teflon-capped scintillation vial and stirred at 100 °C for two weeks. At different time intervals (1 hour, 1 day, 3 days, 1 week, 2 weeks) an aliquot of each sample was collected by filtration, washed with successive aliquots of water (3 x 10 mL) and methanol (3 x 5 mL), dried under vacuum, and analyzed by X-ray powder diffraction. The same procedure was applied to the stability tests in acidic (aqueous HCl or HNO_3, pH 2) and basic media (aqueous NaOH, pH 14).

Gas Sorption Measurements. Gas sorption isotherms for pressures in the range of 0-1.2 bar were measured by the volumetric method using an ASAP2020 analyzer (Micrometrics Instruments Corp., Norcross, GA) and the following procedure. A sample of ca. 100 mg of as-synthesized compound was transferred to a pre-weighed analysis tube (0.5-inch diameter, 10 cm^3 bulb), which was capped with a gas-tight transeal to prevent intrusion of oxygen and atmosphere moisture during transfer and weighing. The samples were evacuated under dynamic

vacuum at 250 °C until an outgas rate of less than 2 mTorr/min (0.27 Pa/min) was achieved (2 days). The analysis tube containing the desolvated sample was then carefully transferred to an electronic balance and weighed again to determine the mass of the sample. It was then transferred back to the analysis port of the gas sorption instrument. The outgas rate was again confirmed to be less than 2 mTorr/min. For all isotherms, warm and cold free space correction measurements were performed using ultra high purity He gas (UHP grade 5.0, 99.999% purity); N_2 isotherms at 77 K were measured in a liquid nitrogen bath using UHP-grade gas sources.

Powder X-Ray Diffraction Structure Analysis. Microcrystalline samples were gently ground using an agate mortar and pestle, and were deposited in the hollow of an aluminum sample holder equipped with a zero-background plate. Diffraction data were collected by means of overnight scans in the 2θ range of 5-105° with 0.02° steps using a Bruker AXS D8 Advance diffractometer equipped with Ni-filtered Cu-Kα radiation (λ= 1.5418 Å), a Lynxeye linear position-sensitive detector, and mounting the following optics: primary beam Soller slits (2.3°), fixed divergence slit (0.3°), receiving slit (8 mm). The nominal resolution for the present set-up is 0.08° of 2θ (FWHM of the α_1 component) for the LaB_6 peak at about 2θ = 21.3°. The generator was set at 40 kV and 40 mA. A visual inspection of the acquired diffractograms revealed isomorphism between **1**, **1m**, **2**, and Mn-BTT,[10a] as well as between **3** and **4**.

As a representative example of the nickel compounds, **1m** was chosen for a complete structural study. A standard peak search, followed by indexing through the Single Value Decomposition approach,[13] as implemented in TOPAS-R,[14] allowed the determination of approximate unit cell parameters. Space groups were assigned on the basis of the systematic absences, taking into consideration, when sensible, the purported isomorphism. Unit cells and space groups were checked by Le Bail refinements and later confirmed by successful structure

solutions and refinements. For **1m**, **3**, and **3¢**, structure solutions were performed by the simulated annealing technique, as implemented in TOPAS, employing a rigid, idealized model for the crystallographic independent portion of the BTP^{3-} ligand;[15] when sensible, the arene-pyrazole torsion was allowed to refine. It is worth noting that **1m** (as well as **1** and **2**) are *isomorphous*, but not *isostructural*, to Mn-BTT,[10a] thus requiring an independent structure solution process to retrieve their structural features. For **2** and **4**, a Rietveld refinement process was directly carried out starting from the structural models of their isostructural counterparts **1m** and **3**, respectively.

In both **1m** and **2**, the difference Fourier map calculated with the F_cs of the framework alone revealed that the solvent is highly disordered, either as guest molecules within the octahedral cavities or one-dimensional channels (see below), or covalently bound to the metal ions. Thus, its electronic density was modeled by allocating: (i) two dummy atoms at the centre of the cavities (site [½, ½, ½]) and of the channels (site [½, 0, 0]) and (ii) one dummy atom occupying, at a restrained distance, the apical position of the square pyramidal stereochemistry of the metal ions. The presence of disorder was taken into account by assigning to the three dummy atoms a high isotropic thermal parameter. Their site occupancy factors were allowed to refine up to the total electron density of the solvent, as estimated from the elemental analysis. In the cases of **3** and **4**, it was also not possible to locate the solvent in a definite position. Thus, the same approach as for **1m** and **2** was adopted, allocating one dummy atom within the cavities. The final refinements were carried out by the Rietveld method, maintaining the rigid bodies introduced at the structure solution stage. The background was modeled by a polynomial function. Peak shapes were described by the Fundamental Parameters Approach.[16] Anisotropic peak broadening was modeled using spherical harmonics to define the peak widths in the case of compounds **3** and **4**. A single, refined isotropic thermal parameter was assigned to each metal atom,

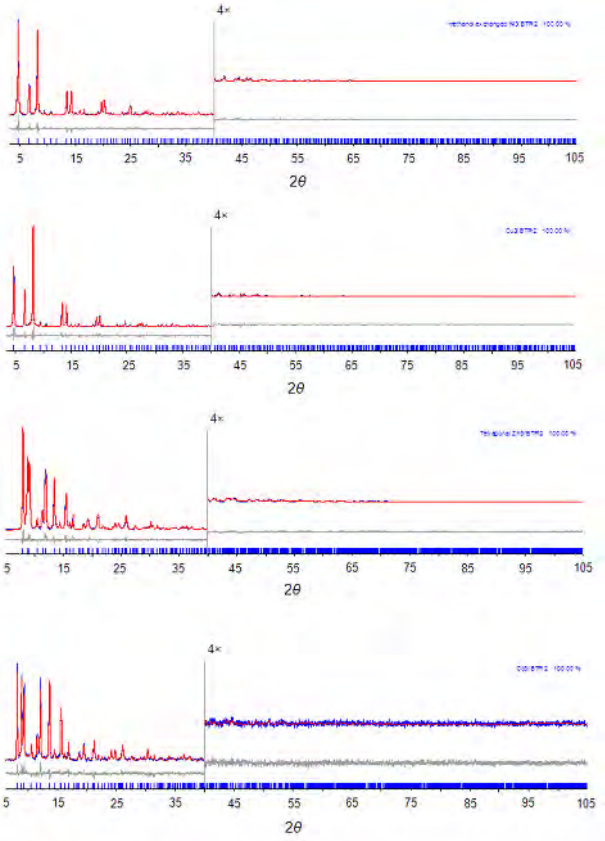

Figure 6.1a. Rietveld refinement results for compounds (upper to bottom) **1m**, **2, 3** and **4** in terms of experimental (blue), calculated (red) and difference (grey) diffraction traces. The peaks markers are shown at the bottom. The portion above 40 deg has been magnified (4×).

and this was augmented by 2.0 Å^2 for the atoms of the BTP^{3-} ligand. Preferred orientation was modeled by using the March-Dollase approach along the [111] direction for compounds **1m** and **2**, and along the [001] direction for **3** and **4**. The final Rietveld refinement plots are shown in Figures 6.1a-b. It is worth noting that the still imperfect agreement between the experimental and the calculated traces in the case of **3¢** is reasonably due to the fact that the positional

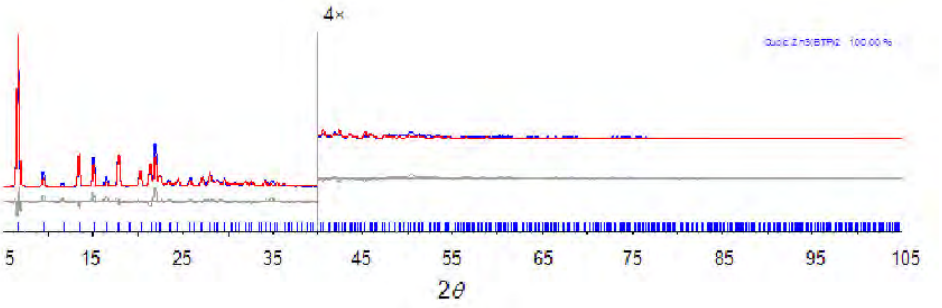

Figure 6.1b. Rietveld refinement results for compounds **3¢** of experimental (blue), calculated (red) and difference (grey) diffraction traces. The peaks markers are shown at the bottom. The portion above 40 deg has been magnified (4×). Please note that the limited agreement between the experimental and the calculated trace is reasonably due to the fact that the positional disorder affecting the Zn2/O couple (see Scheme 6.1 and the crystal structure description) may induce disorder of the pyrazolate moieties, which we cannot easily model. Indeed, according to the atom (Zn2 *vs* O) present, the pyrazolate rings reasonably adopt two distinct orientations with respect to the central benzene ring.

disorder affecting the Zn2/O atoms (see Scheme 6.1 and the crystal structure description) intrinsically induces disorder of the pyrazolate moieties, which cannot easily be modelled. Indeed, according to the atom present (Zn2 vs. O) and to its specific geometrical requirements (different for the Zn2-N and O-H···N bond distances) the pyrazolate rings may adopt two distinct orientations with respect to the central benzene ring, possibly forcing (locally) the whole ligand out from the crystallographic threefold axis. In spite of its high degree of crystallinity, we were unable to solve the structure of compound **2¢**; hence, only the unit cell parameters and space group are available. X-ray crystallographic data of **1m**, **2**, **3**, **3¢** and **4** CIF format have been deposited with the Cambridge Crystallographic Data Center as supplementary publications no.s 804989 - 804993. Copies of the data can be obtained free of charge on application to the Director, CCDC, 12 Union Road, Cambridge, CB2 1EZ, UK (Fax: +44-1223-335033; e-mail: deposit@ccdc.cam.ac.uk or http://www.ccdc.cam.ac.uk).

Thermodiffractometric Studies. Variable-temperature powder X-ray diffraction experiments were performed on the solvated compounds **1m**, **2**, **3**, and **3¢** to probe their structural response to temperature increases. The experiments were carried out in air using a custom-made sample heater, assembled by Officina Elettrotecnica di Tenno, Ponte Arche, Italy. Powdered microcrystalline samples of the compounds were pulverized using an agate mortar and pestle, and were deposited in the hollow of an aluminum sample holder. Typically, the thermodiffractometric experiments were planned on the basis of the thermogravimetric analyses. The diffractograms were recorded in a significant low-angle 2θ range, heating *in situ* by increments of 30 °C, starting from 30 °C, until significant loss of crystallinity was observed. Parametric treatment (using the Le Bail method) of the data acquired before loss of crystallinity revealed the unit cell parameter variations as a function of the temperature in the cases of **1m**, **2**, **3**, and **3¢**. When comparing the thermogravimetric and thermodiffractometric results, the reader should be aware that the thermocouple of the latter set up was *not* in direct contact with the sample, potentially leading to slight difference in the temperature at which the same event is detected by the two techniques. The temperatures obtained by thermogravimetric analysis should be considered more reliable.

Other Physical Measurements. ^{1}H-NMR spectra (in DMSO-d_6) were recorded at 298 K on a Bruker Avance 400 instrument (400 MHz) in the NMR Facility of the University of California, Berkeley. Elemental analyses were obtained from the Microanalytical Laboratory of the University of California, Berkeley. Infrared spectra were recorded on a Perkin Elmer Spectrum 100 Optica FTIR spectrometer. Thermogravimetric analyses were carried out at a ramp rate of 3 °C/min under nitrogen flow with a TA Instruments TGA Q5000. X-ray fluorescence analyses were performed with a Panalytical Minipal 2 instrument, equipped with a Cr source, on a powdered batch of **1**.

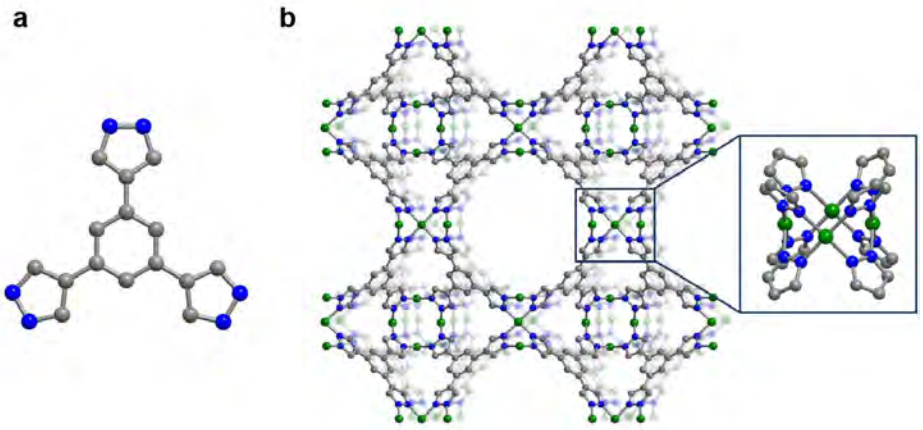

Figure 6.2. Scheme of the pyrazole-based ligand 1,3,5-tris(1*H*-pyrazol-4-yl)benzene, H_3BTP (a) and portions of the structure of $Ni_3(BTP)_2{\cdot}3CH_3OH{\cdot}10H_2O$ (**1m**), as determined from powder X-ray diffraction data (b). Green, blue, and gray spheres represent Ni, N, and C atoms, respectively; H atoms and solvent molecules are omitted for clarity. The inset shows the square-planar Ni_4 cluster bridged by eight pyrazolate rings. The compound $Cu_3(BTP)_2{\cdot}8CH_3OH{\cdot}10H_2O$ (**2**) is isostructural. Selected bond distances (Å) and angles (deg) for the structures of **1** and **2**, respectively: M-N 2.0200(4) and 2.1225(6); M···M 3.118(6) and 3.013(7); N-M-N 77.4(2), 102.6(2), 178.9(3) and 73.7(2), 106.0(2), 174.4(3); M-N-N 64.2(1), 116.7(1) and 67.1(1), 117.3(1). Please note that in both cases, the crystallographically independent portion of the BTP^{3-} ligand has been modeled by means of a rigid body.[25]

Results and Discussion

Synthesis and Structure of Sodalite-Type $Ni_3(BTP)_2$ and $Cu_3(BTP)_2$ Phases. Reaction of H_3BTP with nickel(II) or copper(II) acetate in DMF at 160 °C afforded, upon washing with methanol and drying in air, $Ni_3(BTP)_2{\cdot}3DMF{\cdot}5CH_3OH{\cdot}17H_2O$ (**1**) and $Cu_3(BTP)_2{\cdot}8CH_3OH\cdot10H_2O$ (**2**) as yellow and brown microcrystalline powders, respectively. Preliminary powder X-ray diffraction acquisitions showed both compounds to be isomorphous with the sodalite-like structure of Mn-BTT.[10a] The latter compound consists of chloride-centered $[Mn_4(\mu_4\text{-}Cl)]^{7+}$ squares linked via triangu-

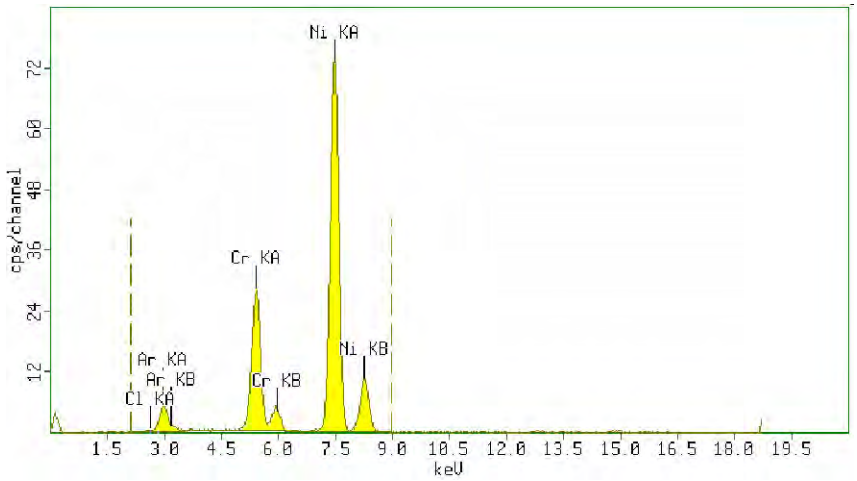

Figure 6.3. Qualitative X-Ray Fluorescence analysis of $Ni_3(BTP)_2 \cdot 3DMF \cdot 5CH_3OH \cdot 17H_2O$, **1**.

lar BTT^{3-} ligands to form a porous, three-dimensional framework in which each metal center further has a bound DMF molecule directed into the pores. Overall, the framework has an anionic charge, which is balanced by $[Mn(DMF)_6]^{2+}$ cations included in the pores. Despite the great similarity in size and shape between H_3BTT and H_3BTP, our attempts at synthesizing a Mn-BTT analogue using H_3BTP and various metal chlorides were unsuccessful. Instead, the use of metal acetates in DMF was found to promote the deprotonation of the pyrazole ligand to form M-N bonds and the extended sodalite-like framework structure of **1** and **2**. As assessed by X-ray powder structure analysis, **1** and **2** are isomorphous, but not isostructural with Mn-BTT. Specifically, the m_4 bridging chloride anion present in Mn-BTT, is absent in **1** and **2**, as evidenced by elemental analysis and X-ray fluorescence (see Figure 6.3) and consideration on their structural features (see below).

Compounds **1** and **2** crystallize (see Figure 6.2) in the cubic space group *Pm* $\bar{3}m$, with the metal ions lying on crystallographic two-fold axes and arranged in tetranuclear cores of rigorous, crystallographically-imposed square symmetry,

with M···M edges of 3.118(6) and 3.013(7) Å, for **1** and **2**, respectively. The chloro-centered Mn_4 squares in Mn-BTT showed Mn···Mn distances of 3.70(3) Å, in agreement with the presence of the inner m_4-Cl ion and leading to a larger accessible empty volume (as measured, *e.g.*, by the BET specific area, *vide infra*). In **1** and **2**, each M···M edge is bridged by pyrazolate groups from two distinct BTP^{3-} ligands, resulting in a square planar coordination geometry at each metal ion. Residing on a 3*m* crystallographic site, each BTP^{3-} ligand employs its three pyrazolate substituents to bridge M···M edges of three different M_4 squares. Each square is connected to eight adjacent squares, generating a rigid three-dimensional framework. Thus, the framework structure features octahedral cavities centered at [½, ½, ½], with BTP^{3-} ligands spanning each face and M_4 squares truncating each vertex to give an expanded sodalite cage unit. The sharing of squares between neighboring cage units along the three unit cell axes, results in one-dimensional channels running parallel to the cell axes. These channels have a wide diameter of nearly 10 Å (based upon van der Waals radii). Yet, only a very small entrance, possibly limiting the size and shape of adsorbable gases, allows access to the ca. 6-Å cavity within the octahedral, sodalite-like cage units. Based upon van der Waals radii, a total void volume of 66% and 69% is estimated from the structures of **1** and **2**, respectively.[17,18] The slight increase of unit cell and void volumes from **1** to **2** is consistent with the ionic radii of square planar Ni^{2+} and Cu^{2+} ions (0.63 and 0.71 Å, respectively), which result in longer Cu-N bonds and a slightly expanded framework for **2**. The electron density residues present in the Fourier difference maps, as resulting from the modelling of the frameworks alone, clearly indicate that: (i) both cavities and channels contain guest solvent molecules, and (ii) solvents such as DMF, CH_3OH, and water can bind to open metal coordination sites. As evidenced by the isolation and characterization of different solvated forms, coordinated solvent is indeed likely to be present at an apical position, protruding into the large channels and creating a

square pyramidal coordination at each metal center.[19]

In examining the chemical stability of **2**, some amount of the solid was refluxed in a concentrated basic (NaOH, pH 14) solution. A brown deposit isolated from the solution turned out to be a distinct new phase, $Cu_3(BTP)_2 \cdot 6H_2O$ (**2¢**), which could be also obtained by refluxing **2** in an acid solution (HCl, pH 3). This microcrystalline product appears, however, to be non-porous, as evidenced by a thermogravimetric analysis showing no weight loss up to decomposition (see Figure 6.4). Its powder diffraction trace could be easily be indexed to a *R*-centered trigonal unit cell, with the likely presence of *c*-type glide planes. Possible space groups candidates are therefore $R\bar{3}c$ and *R*3*c*, which share the same systematic extinction conditions. Indeed, a structureless Le Bail fit matched well with the observed diffraction pattern (see Table 1). Unfortunately, compound **2¢** has thus far resisted all attempts of structural resolution, although clear indications of a nearly layered disposition of the BTP^{3-} ligands (parallel to *ab*) and of trinuclear Cu_3 units were found. Work is in progress to assess the complete crystal structure, but the results, if any, will be postponed to a future contribution.

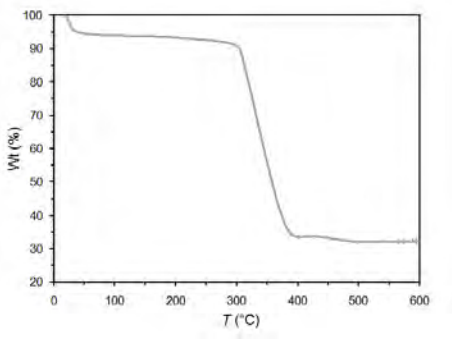

Figure 6.4. Thermal gravimetric analysis of as-synthesized $Cu_3(BTP)_2(H_2O)_6$, **2¢**.

Synthesis and Structure of Tetragonal $Zn_3(BTP)_2$ and $Co_3(BTP)_2$ Phases. Since the discovery of Mn-BTT, it has been established that isostructural tetrazolate-based frameworks can be synthesized with a variety of other transition metal ions, including Cr^{2+}, Fe^{2+}, Co^{2+}, Ni^{2+}, Cu^{2+}, and Cd^{2+}.[13,20] Similarly, we sought to obtain pyrazolate-bridged analogues of $Ni_3(BTP)_2$ and $Cu_3(BTP)_2$ incorporating other transition metal ions with a high affinity for nitrogen-based

	1m	**2**	**3**
Emp. Form.	$C_{33}H_{50}Ni_3N_{12}O_{13}$	$C_{38}H_{70}Cu_3N_{12}O_{18}$	$C_{34}H_{38}N_{12}O_6Zn_3$
Mw, g mol^{-1}	998.9	1173.7	906.9
Crystal system	Cubic	Cubic	Tetragonal
Space group, *Z*	$Pm\bar{3}m$, 4	$Pm\bar{3}m$, 4	$P4_2/ncm$, 4
a, Å	18.5490(8)	18.8070(8)	15.555(1)
b, Å			
c, Å			20.030(2)
V, Å^3	6382.0(8)	6652.1(8)	4846.5(7)
ρ_{calc}, g/cm^3	1.04	1.13	1.20
F(000)	2080	2452	1856
μ(CuKα) cm^{-1}	14.62	16.50	21.33
T, K	298(2)	298(2)	298(2)
2θ range, °	5-105	5-105	5-105
N_{data}	5001	5001	5001
R_{wp}, R_p	0.068, 0.042	0.103, 0.065	0.102, 0.072
R_{Bragg}	0.028	0.028	0.040

ligands.[21] After numerous attempts applying different reaction conditions, a white microcrystalline powder was obtained through addition of triethylamine to a solution of $Zn(CF_3SO_3)_2$ and H_3BTP in DMF. Due to the high pK_a of the pyrazole rings, either base or high temperature is essential to force the reaction to proceed.[22] Washing with wet methanol followed by drying *in vacuo* resulted in a compound of formulation $Zn_3(BTP)_2{\cdot}4CH_3OH{\cdot}2H_2O$ (**3**). As might be expected for transition metal ions favoring tetrahedral stereochemistry, such as zinc(II) and cobalt(II), $Co_3(BTP)_2{\cdot}8CH_3OH_8{\cdot}10H_2O$ (**4**) was synthesized following the same reaction procedure.

Table 6.1. Crystallographic data for species **1m**, **2**, **3**, **4**, **2¢** and **3¢**.

4	**2′**[a]	**3′**
$C_{38}H_{70}Co_3N_{12}O_{18}$	$C_{30}H_{30}Cu_3N_{12}O_6$	$C_{120}H_{84}N_{48}O_6Zn_{12}$
1159.8	845.3	3079.0
Tetragonal	Rhombohedral	Cubic, 2
$P4_2/ncm$, 4	$R3c$	$Pn\bar{3}n$
15.462(1)	23.794(6)	18.547(1)
20.047(2)	12.869(4)	
4793(1)	6309(4)	6380(1)
1.55	n.a.	3096
2428	n.a.	1.60
87.93	n.a.	30.2
298(2)	298(2)	298(2)
5-105	5-105	5-105
5001	5001	5001
0.119, 0.092	0.019, 0.013	0.156, 0.113
0.037	n.a.	0.094

Compounds **3** and **4** crystallize in the tetragonal space group $P4_2/ncm$. The local coordination geometry can be appreciated from the depiction at the left side of Figure 6.5, while the overall framework structure is shown at the right side. The structures contain tetrahedrally coordinated metal(II) centers arranged in collinear chains running along [110] (and equivalent directions), with pyrazolate-bridged intermetallic separations of 3.748(1)and 3.654(1) Å and for Co and Zn, respectively. The BTP^{3-} ligands are bisected by a crystallographic two-fold axis and possess one pyrazolate moiety in plane with the inner arene and the other two making a dihedral angle of about 64° to the benzene core.

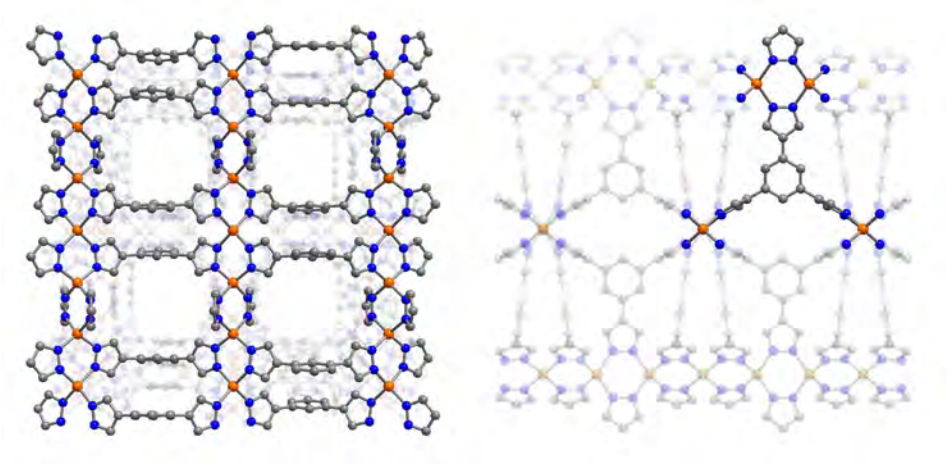

Figure 6.5. Portions of the structure of $Zn_3(BTP)_2 \cdot 4CH_3OH \cdot 2H_2O$ (**3**), determined by powder X-ray diffraction analysis, as viewed along the c (left) axis and [110] direction (right). Orange, blue, and gray spheres represent Zn, N, and C atoms, respectively; H atoms and solvent molecules are omitted for clarity. The compound $Co_3(BTP)_2 \cdot 8CH_3OH \cdot 10H_2O$ (**4**) is isostructural. Selected bond distances (Å) and angles (deg) for the structures of **3** and **4**, respectively: M-N 2.077(6), 2.053(6), 2.106(7) and 2.124(7), 2.035(8), 2.046(9); M···M 3.654(1) and 3.748(1); N-M-N 102.3(4)-127.3(4) and 97.7(4)-120.8(2); M-N-N 120.0(4), 121.3(2) 123.1(2) and 119.1(3), 119.7(3), 125.8(3). Please note that in both cases, the crystallographically independent portion of the BTP^{3-} ligand has been modeled by means of a rigid body.[25]

Each chain connects to three adjacent chains to afford a three-dimensional framework. Porosity is apparent in the structures, with one-dimensional channels of slightly less than 4 Å-diameter, running parallel to *c* and filled with guest solvent molecules. The surfaces exposed within these channels appear to be only π-rings, thus imparting a hydrophobic character. Overall, the accessible void volume reaches 46% and 50% for the structures of **3** and **4**, respectively.[21] Unlike **1** and **2**, these compounds do not feature metal-bound solvent molecules that could potentially be removed to generate coordinatively-unsaturated metal centers.

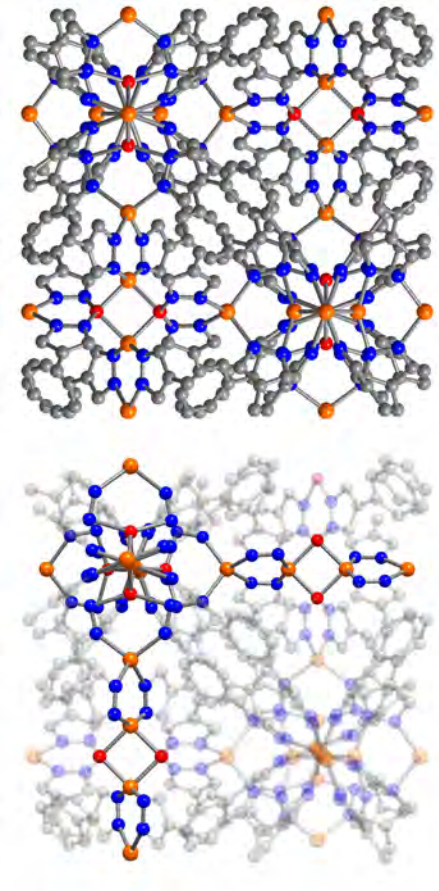

Figure 6.6. Portions of the molecular structure of $Zn_{12}[Zn_2(H_2O)_2]_6(BTP)_{16}$ (**3¢**) analyzed by powder X-ray diffraction as viewed along *a* axis. Orange, red, blue, and gray spheres represent Zn, O, N, and C atoms, respectively; H atoms are omitted for clarity. For a description of the local disorder affecting the Zn_2O_2 fragment see the Supporting Information. Selected bond distances (Å) and angles (deg) for the structure of **3¢**: Zn-N 2.07(2), 2.099(6); Zn-O 1.97(2); Zn···Zn 2.97(1), 3.13(5); N-Zn-N 106.7(2), 115.2(4), 140.8(2); N-Zn-O 85.3(2); O-Zn-O 82(2); Zn-N-N 101(1), 129.0(3); Zn-O-N 84(1), 129(2). Please note that in both cases, the crystallographically independent portion of the BTP^{3-} ligand has been modeled by means of a rigid body.25

When compound **3** was heated in boiling water, a new crystalline phase $Zn_{12}[Zn_2(H_2O)_2]_6(BTP)_{16}$ (**3¢**) was obtained, as identified by X-ray powder diffraction. The same phase was also isolated through the reaction of **3** in a concentrated basic solution (NaOH, pH 14) for 30 min. Although **3** is highly resistant to high temperatures (up to 510 °C), the solid state transformation in basic pH conditions occurs at room temperature in a very short time, indicating that the presence of water is critical to its instability. Compound **3¢** crystallizes in the cubic space group $Pn\bar{3}n$. The best structural model derived from our X-ray powder diffraction analysis was found to contain

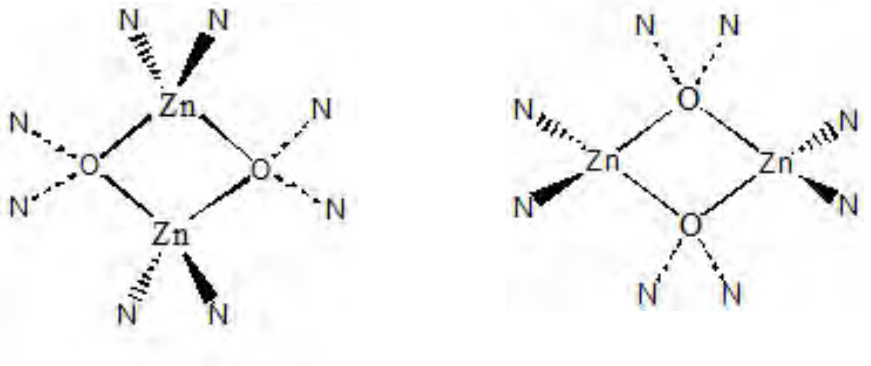

Scheme 6.1. Schematic description of the local disorder affecting the $[Zn_2(H_2O)]_2$ fragment in **3¢**. The H atoms of the N---HO hydrogen bonds are omitted for clarity.

one-dimensional chains running along the three crystallographic axes. Two crystallographically distinct zinc(II) centers, referred to as Zn1 and Zn2, alternate along the chains (see Figure 6.6). Site Zn1 possesses a tetrahedral stereochemistry, with coordination by four nitrogen atoms belonging to the pyrazolate moieties of four distinct BTP^{3-} ligands. Situated at the vertices of a $[Zn_2(H_2O)_2]^{4+}$ rhombic unit, Zn2 shows a *cis*-ZnN_2O_2 tetrahedral stereochemistry, where the nitrogen atoms belong to pyrazolate groups from two distinct BTP^{3-} ligands. Due to the orientational disorder affecting the rhombic units (which reside on a crystallographic four-fold axis), along each chain, Zn1 may be bridged, by the BTP^{3-} ligands, either to Zn2, *via* a Zn-N bond, or to a water molecule, *via* a N···HO hydrogen bond (see Scheme 6.1). Given the overall coordination mode of the BTP^{3-} ligands, which employ all of their nitrogen atoms to form bonds, the chains are mutually connected to give a dense, three-dimensional framework with no voids or channels for hosting solvent. As expected in the absence of guest solvent molecules, thermogravimetric analysis shows no weight loss for the compound up to decomposition, which occurs at a rather high temperature of above 400 °C.

Gas Adsorption Properties.

Prompted by their porous structures, we evaluated the permanent porosity of compounds **1**-**4** by collecting N_2 adsorption isotherms at 77 K. Complete removal of coordinating solvents without collapsing the structure is not always trivial, however, due to an activation barrier which should be overcome by applying vacuum and high temperatures, often subsequent to solvent exchange using a volatile coordinating solvent such as methanol. To determine the optimal activation temperatures of the methanol-exchanged phases, the samples were heated under dynamic vacuum at gradually increasing temperatures, while N_2 adsorption was repeatedly measured at each stage. From the N_2 isotherm measurements, the best activation method for compounds **1** and **2** was determined to be application of dynamic vacuum at 250 °C for at least two days. With no bound solvent, **3** and **4** can be activated by heating under vacuum at the lower temperature of 160 °C for two days.

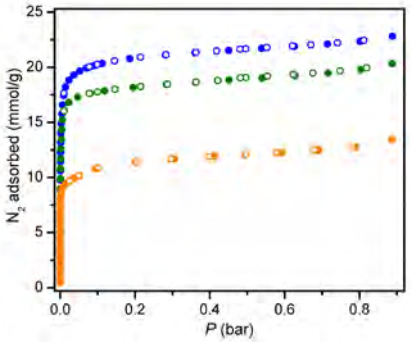

Figure 6.7. Nitrogen adsorption isotherms measured at 77 K for **1** (green), **2** (blue) **3** (orange) and **4** (purple). Filled and empty symbols represent adsorption and desorption, respectively.

The optimally desolvated materials were found to adsorb significant amounts of N_2 at 77 K, displaying Type I adsorption isotherms characteristic of microporous solids (see Figure 6.7). Fitting the N_2 isotherms afforded BET surface areas of 1650(20), 1860(10), 930(10) and 1027(3) m^2/g and Langmuir surface areas of 1900(13), 2159(10), 1242(11) and 1588(40) m^2/g for **1**, **2**, **3** and **4** respectively. Perhaps owing to a smaller unit cell dimension, the surface areas of **1** and **2** are slightly lower than observed for Mn-BTT, which, thanks to the (μ_4-Cl induced) inflation of the inner Mn_4 core (*vide supra*), displayed a BET surface area of 2100 m^2/g.[10a]

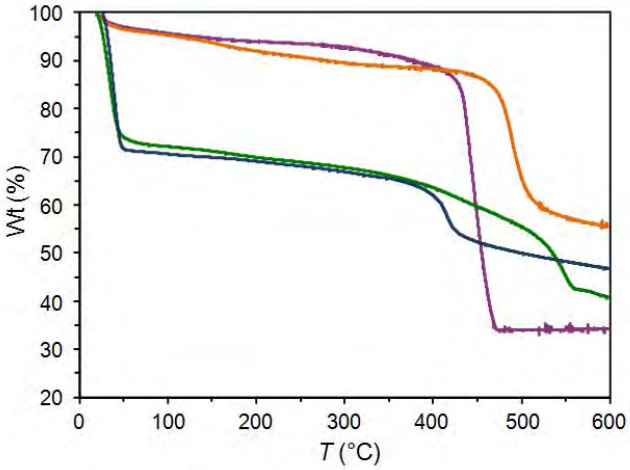

Figure 6.8. Thermal gravimetric analysis of as-synthesized $Ni_3(BTP)_2 \cdot 3DMF \cdot 5CH_3OH \cdot 17H_2O$ (**1**, green), $Cu_3(BTP)_2 \cdot 8CH_3OH \cdot 10H_2O$ (**2**, blue), $Zn_3(BTP)_2 \cdot 4CH_3OH \cdot 2H_2O$ (**3**, orange) and $Co_3(BTP)_2 \cdot 8CH_3OH \cdot 10H_2O$ (**4**, purple).

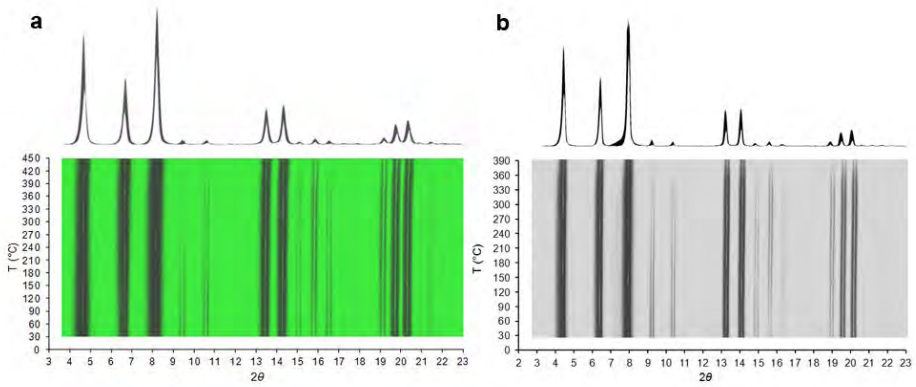

Figure 6.9. Overlaid powder X-ray diffraction patterns measured at elevating temperatures in the range 30-450 °C for **1** (left) and 30-390 °C for **2** (right), and their two-dimensional contour plots as a function of 2ϑ and temperature, both displaying their thermal stability. Notably, the diffraction patterns remained unaltered during the measurements except for minor changes in peak intensity occurring at above 400 °C.

Notably, the increase in surface area from **1** to **2** is consistent with their unit cell dimension and void volume, which is ultimately related to the ionic radii of the two metal ions (see above). The surface area of **3** and **4** are also consistent with that of Zn(1,3-BDP) and Co(1,3-BDP), which display much similarity in the framework connectivity and pore size.[3e]

Thermal Behavior. In order to probe the thermal stability of the new compounds, thermogravimetric analyses were performed, combined with *in situ* variable-temperature powder X-ray diffraction experiments. While the thermogravimetric analyses were carried out under N_2 for as-synthesized compounds **1-4**, complete and detailed characterization of the thermal behaviors of **1**-**3** were carried out *in air* by means of variable-temperature diffraction experiments.

As depicted in Figure 6.8 the thermogravimetric trace of **1** shows a weight loss of 30% between 30 and 150 °C, corresponding to the partial evolution of guest solvent (4 methanol and 16 water molecules corresponds to 30%). A gradual further weight loss of 15% occurs in the range 150-430 °C, consistent with the evolution of DMF solvent molecules coordinated to the metal sites (3 DMF molecules corresponds to 16%). Further heating prompts decomposition at 450 °C. In the TG trace of **2**, a 30% weight loss occurs below 50 °C, corresponding roughly to the evolution of 5 methanol and 10 water molecules (29%). A gradual weight loss of 8% then follows up to 410 °C, consistent with the loss of 3 metal-coordinated methanol molecules, and further heating induces decomposition.

The foregoing observations are consistent with thermodiffractometric analyses (see Figure 6.9). These results confirm the high thermal stability of **1** and **2**, while also showing that their crystallinity is retained to afford permanent porosity. Indeed, solvent loss does not significantly affect the crystal structures, with the powder diffraction patterns remaining largely unchanged up to 450 °C for **1** and 390 °C for **2**. Notably, parametric Le Bail refinements against the data show that the two compounds respond to heat with a distinct framework flexibility.

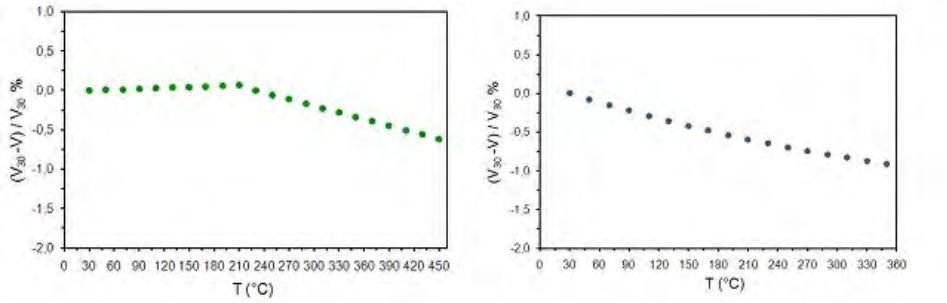

Figure 6.10. Variation of the unit cell volume (V) of **1** (left) and **2** (right) normalized to the corresponding 30 °C values (V_{30}) as a function of the temperature.

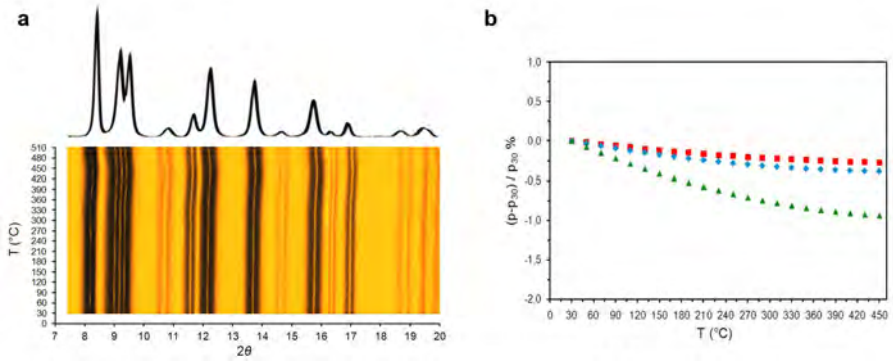

Figure 6.11. a) Overlaid powder X-ray diffraction patterns measured at elevating temperatures in the range 30-510 °C for **3** (left) and its two-dimensional contour plots as a function of 2ϑ and temperature, both displaying their thermal stability. Notably, the diffraction patterns remained unaltered during the measurements except for minor changes in peak intensity occurring at above 400 °C. b) Variation of the unit cell parameters of **3** (p) normalized to the corresponding 30 °C values (p_{30}) as a function of the temperature. *a*, red squares; *c*, blue rhombi; *V*, green triangles.

In the case of **1**, the unit cell volume remains almost constant up to ca. 200 °C, while above this temperature, a modest contraction, reaching 0.5%, is observed. In comparison, the unit cell volume of **2** experiences a modest, yet continuous, decrease in the temperature range 30-350 °C, reaching 0.8% (see Figure 6.10).

As evidenced by their thermal behavior, compounds **3** and **4** provide further examples of robust metal-organic frameworks. The thermogravimetric traces show less weight loss than expected on the basis of the pore solvent contents. For example, an 18% weight loss is expected for **3**, corresponding to 4 methanol and 2 water molecules, but only a 12% loss is observed for both **3** and **4** in the temperature range 30-500 °C (see Figure 6.8). This discrepancy is reasonably due to solvent evolution during weighing and transferring the sample, particularly in view of the hydrophobic nature of the pore surfaces within these compounds. After solvent removal, decomposition begins at 510 and 450 °C for **3** and **4**, respectively. The remarkably high thermal stability of **3** was confirmed by diffraction measurements, which also revealed retention of the structure upon heating in air (see Figure 6.11a). A parametric Le Bail refinement of the data revealed this compound to be an extremely rigid material, showing a very limited volume changes upon heating. At lower temperatures, this suggests that the partial, and very limited, desolvation overcomes thermal expansion effects (see Figure 6.11b). Notably, among all the members of the $M_3(BTP)_2$ family, the tetragonal zinc(II) derivative shows the greatest thermal stability. Indeed, in this regard, zinc(II) compounds have proven superior to other metal(II) analogues for all of the pyrazolate-bridged metal-organic frameworks reported so far. In the cases of $M(2\text{-pymo})_2$ and $M(4\text{-pymo})_2$ compounds (*n*-pymo$^-$ = pyrimidin-*n*-olate), the highest tolerances to elevated temperatures have also been found for M = Zn.[23]

Chemical Stability. The chemical resistance of **1**-**3** was examined by suspending samples of the compounds in boiling water, boiling aqueous HCl or HNO_3 solutions at pH 2, and a boiling aqueous NaOH solution at pH 14, conditions that

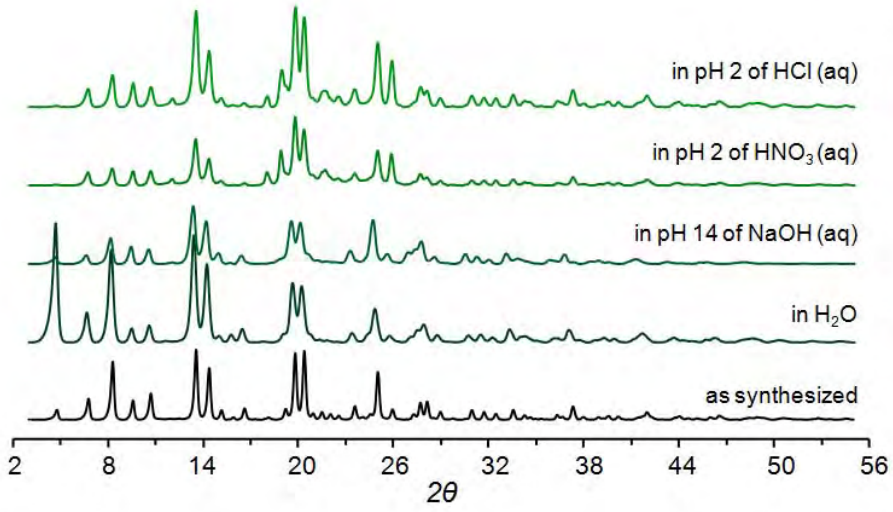

Figure 6.12. X-ray diffraction patterns for **1** after treatment in water, acids or base for two weeks at 100 °C.

reflect extreme operational parameters in industry. Each sample (ca. 100 mg) was soaked in the applicable test solution, which was subsequently heated at 100 °C for two weeks. During this period of time, a portion of each sample was periodically removed, filtered, dried at room temperature and checked by X-ray powder diffraction analysis. For compound **1**, after each two-week treatment, the sample was desolvated by heating at 250 °C and N_2 adsorption isotherms were collected at 77 K to test retention of surface area.

Remarkably, the $Ni_3(BTP)_2$ framework of **1** is stable to all of the environments tested and maintained both its crystallinity and porous nature after 14 days of uninterrupted test reactions. Powder X-ray diffraction data collected before and after each test confirm its structural chemical integrity (see Figure 6.12). No change in crystallinity was observed, but only in the intensities of the peaks, which is reasonably due to the difference in solvent contents. The accessibility of the pores within

Table 2. Langmuir Surface Areas for Compound **1** As-Synthesized and After Treatment with Boiling Water, $HCl_{(aq)}$ at pH 2, $HNO_{3(aq)}$ at pH 2, and $NaOH_{(aq)}$ at pH 14.[a]

	as-synthesized	H_2O	$HCl_{(aq)}$	$HNO_{3(aq)}$	$NaOH_{(aq)}$
$SA_{Langmuir}$ (m^2/g)	1900(13)	1830(10)	1791(14)	1774(11)	1925(15)

[a]Values were obtained from N_2 adsorption measurements performed at 77 K on samples subjected to the conditions specified for two weeks and then desolvated by heating at 250 °C under dynamic vacuum.

the retained structure was unequivocally demonstrated by measuring the surface areas of the solid after each chemical stability test (see Table 2). Significantly, **1** retains its surface area after two weeks under all of the aforementioned extreme conditions. To our knowledge, this is the most extensive range of chemical stability yet demonstrated for a metal-organic framework. Although some frameworks are chemically resistant in a basic solution, none have been known to be stable in a pH 2 acid solution at 100 °C. Some imidazolate-based frameworks are known to be substantially retained in boiling solvents (water, methanol, benzene) for 7 days, yet only for 24 h in aqueous NaOH solution, with a poor stability in acidic solutions reported. The zirconium-based framework UIO-66,[3b] has been shown to display thermal stability up to 540 °C, but its chemical stability in water and common organic solvents was verified only for no longer than 24 h at room temperature. Other stability studies on tetrazolate-,[6b] triazolate-,[8] and pyrazolate-based[3e,11] frameworks have been performed but, despite their sometimes good water tolerance, the chemical stability in acidic and basic media is either inferior to **1** or not reported. Combined with its exceptional stability, the presence of exposed metal cation sites in **1**, typically the preferred binding sites for adsorbates (including non-polar species like H_2), should raise its potential for a variety of applications.

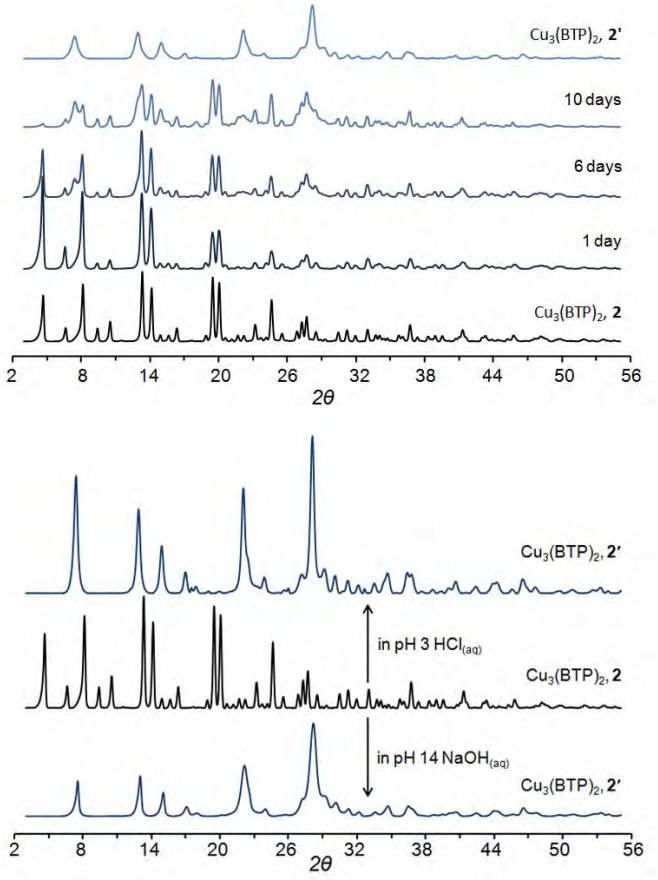

Figure 6.13. Powder X-ray diffraction patterns of **2** during treatment in water for 14 days at 100 °C (top), and transformation of **2** in **2¢** after treatment in an acidic or a basic solution (bottom).

In contrast, the copper- and zinc-based frameworks of **2** and **3**, undergo transformation to non-porous crystalline solids upon extreme chemical treatment, as rather commonly observed for metal-organic frameworks. As depicted in Figure 6.13, compound **2** shows a progressive phase transition in boiling water, converting to **2¢**. This transformation occurs upon refluxing **2** in aqueous

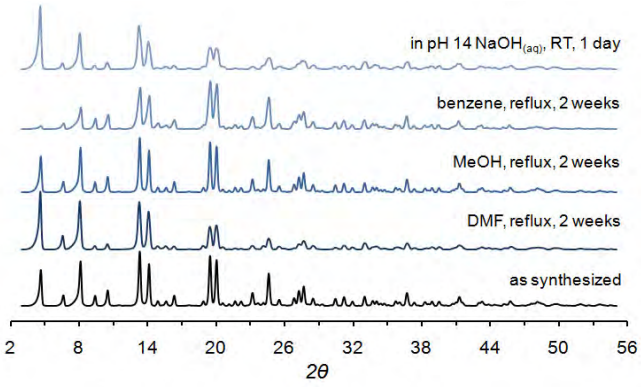

Figure 6.14. X-ray powder diffraction patterns of (bottom to top) $Cu_3(BTP)_2$ as-synthesized, **2**; after two weeks in DMF, MeOH and benzene at reflux and in a pH 14 of aqueous NaOH solution for 1 day at room temperature.

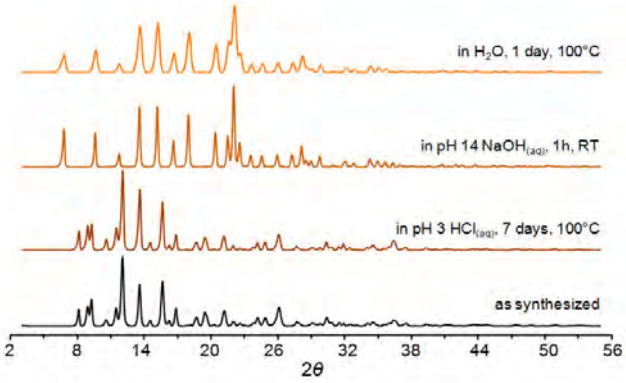

Figure 6.15. Powder X-ray diffraction patterns of **3** after treatment in water, acid or base for various durations at various temperatures.

NaOH (pH 14) or HCl (pH 3) solutions for one day. The longest resistance of **2** to pH 14 solution at room temperature was found to be one day, and it was further found to be stable for one day in benzene, DMF, and methanol heated at reflux (see Figure 6.14). Despite its extremely high thermal stability, compound **3** displays a resistance to hot acidic media that is somewhat inferior to that of **1**.

While its structure is maintained upon heating at 100 °C in pH 3 aqueous HCl for 7 days, as shown in Figure 6.15, it is not stable to a similar treatment at pH 2. In addition, **3** reacts in water and especially in basic solutions, transforming into the cubic phase **3¢**.

Conclusions

The foregoing results demonstrate the use of the new triangular trispyrazole molecule H_3BTP in construction of microporous frameworks of the type $M_3(BTP)_2$ (M = Co, Ni, Cu, Zn) exhibiting exceptional thermal and chemical stability. In particular, $Ni_3(BTP)_2$ retains its integrity in the face of an unprecedented range of extreme conditions, including heating in air to 430 °C and treatment with boiling aqueous solutions of pH 2 to 14 for two weeks. Thus, this stability parallels, or even overcome, that of zeolites, where the presence of selectively removable Al sites makes their frameworks unstable in highly acidic and basic conditions.[24] Moreover, $Ni_3(BTP)_2$ represents the first high-stability metal-organic framework with accessible metal sites lining the pore surfaces. Such a remarkable combination of properties may open the way for testing metal-organic frameworks in a variety of applications that currently employ zeolites under extreme conditions. Indeed, future efforts will focus on exploring the performance of these new high-surface area materials in various high-temperature catalytic processes, as well as on the synthesis of other pyrazolate-based metal-organic frameworks featuring exposed metal sites.

Acknowledgements

This research was supported in the US by the Department of Energy under Contract No. DE-AC02-05CH11231 and in Italy by Fondazione Cariplo (Project 2007-5117). We thank Dr. Leslie J. Murray, and Mr. Eric D. Bloch for helpful discussions.

References and Notes

1 (a) Corma, A. *Chem. Rev.* **1997**, *97*, 2373. (b) Maesen, T.; Marcus, B. *Introduction to Zeolite Science and Practice* **2001**, eds. Van Bekkum, H.; Flanigen, E. M.; Jacobs, P. A. & Jansen, J. C.; Elsiever, Amsterdam. 1-9. (c) Lauriente, D. H.; Inoguchi, Y. *The Chemical Economics Handbook* **2005**, SRI Consulting, 599.1000 F, *14*, 6. (d) Yilmaz, B.; Muller, U. *Top. Catal.* **2009**, *52*, 888.

2 (a) Tanabe, K. K.; Cohen, S. M. *Chem. Soc. Rev.* **2011**, Advance Article, DOI: 10.1039/C0CS00031K. (b) Cohen, S. M. *Chem. Sci.* **2010**, *1*, 32. (c) Wang, Z.; Cohen, S. M. *Chem. Soc. Rev.* **2009**, *38*,1315. (d) Ahnfeldt, T.; Gunzelmann, D.; Loiseau, T.; Hirsemann, D.; Senker, J.; Férey, G.; Stock, N. *Inorg. Chem.* **2009**, *48*, 3057. (e) Hwang, Y. K.; Hong, D.-Y.; Chang, J.-S.; Jhung, S. H.; Seo, Y.-K.; Kim, J.; Vimont, A.; Daturi, M.; Serre, C.; Férey, G. *Angew. Chem. Int. Ed.* **2008**, *47*, 4144. (f) Farha, O. K.; Mulfort, K. L.; Hupp, J. T. *Inorg. Chem.* **2008**, *47*, 10223. (g) Mulfort, K. L.; Farha, O. K.; Stern, C. L.; Sarjeant, A. A.; Hupp, J. T. *J. Am. Chem. Soc.* **2009**, *131*, 3866. (h) Bae, Y.-S.; Farha, O. K.; Hupp, J. T.; Snurr, R. Q. *J. Mater. Chem.* **2009**, *19*, 2131. (i) Ingleson, M. J.; Barrio, J. P.; Guilbaud, J.-B; Khimyak, Y. Z.; Rosseinsky, M. J. *Chem. Comm.* **2008**, 2680. (l) Ingleson, M. J.; Heck, R.; Gould, J. A.; Rosseinsky, M. J. *Inorg. Chem.* **2009**, *48*, 9986. (m) Britt, D.; Lee, C.; Uribe-Romo, F. J.; Furukawa, H.; Yaghi, O. M. *Inorg. Chem.* **2010**, *49*, 6387. (n) Oisaki, K.; Li, Q.; Furukawa, H.; Czaja, A. C.; Yaghi, O. M. *J. Am. Chem. Soc.* **2010**, *132*, 9262. (o) Meilikow, M.; Yusenko, K.; Fischer, R. A. *J. Am. Chem. Soc.* **2009**, *131*, 9644.

3 (a) Park, K. S.; Ni, Z.; Côté, A. P.; Choi, J. Y.; Huang, R.; Uribe-Romo, F. J.; Chae, H. K.; O'Keeffe, M.; Yaghi, O. M. *Proc. Natl. Acad. Sci. USA* **2006**, *103*, 10186. (b) Hafizovic Cavka, J.; Jacobsen, S.; Olsbye, U.; Guillou, N.; Lamberti, C.; Bordiga, S.; Lillerud, K. P. *J. Am. Chem. Soc.* **2008**, *130*, 13850. (c) Loiseau, T.; Huguenard, C.; Fink, G.; Taulelle, F.; Henry, M.; Bataille, T.; Férey, G. *Chem. Eur. J.* **2004**, *10*, 1373. (d) Galli, S.; Masciocchi, N.; Colombo, V.; Maspero, A.; Palmisano, G.; Lopez-Garzon, F. J.; Domingo-

García, M.; Fernandez-Morales, I.; Barea, E.; Navarro, J. A. R. *Chem. Mater.* **2010**, *22*, 1664. (e) Choi, H. J.; Dincă, M.; Dailly, A.; Long, J. R. *Energy Environ. Sci.* **2010**, *3*, 117. (f) Masciocchi, N.; Galli, S.; Colombo, V.; Maspero, A.; Palmisano, G.; Seyyedi, B.; Lamberti, C.; Bordiga, S. *J. Am. Chem. Soc.* **2010**, *132*, 7902. (g) O. K. Farha, A. M. Spokoyny, K. L. Mulfort, M. F. Hawthorne, C. A. Mirkin and J. T. Hupp, *J. Am. Chem. Soc.*, 2007, **129**, 12680. (h) J.-P. Zhang and S. Kitagawa, *J. Am. Chem. Soc.*, 2008, **130**, 907. (i) hoi, H. J.; Dincă, M.; Long, J. R. *J. Am. Chem. Soc.* **2008**, *130*, 7848.

4 (a) Kaye, S. S.; Dailly, A.; Yaghi, O. M.; Long, J. R. *J. Am. Chem. Soc.* **2007**, *129*, 14176. (b) Eddaudi, M.; Moler, D. B.; Li, H.; Chen, B.; Reineke, T. M.; O'Keeffe, M.; Yaghi, O. M. *Acc. Chem. Res.* **2001**, *34*, 319.

5 a) Greathouse, J. A.; Allendorf, M. D. *J. Am. Chem. Soc.* **2006**, *128*, 10678. (b) Low, J. J.; Benin, A. I.; Jakubczak, P.; Abrahamian, J. F.; Faheem, S. A.; Willis, R. R. *J. Am. Chem. Soc.* **2009**, *131*, 15834.

6 (a) Cingolani, A.; Galli, S.; Masciocchi, N.; Pandolfo, L.; Pettinari, C.; Sironi, A. *J. Am. Chem. Soc.* **2005**, 127, 6144. (b) Dincă, M.; Yu, A. F.; Long, J. R. *J. Am. Chem. Soc.* **2006**, *128*, 8904. (c) Maspero, A.; Galli, S.; Colombo, V.; Peli, G.; Masciocchi, N.; Stagni, S.; Barea E.; Navarro, J. A. R. *Inorg. Chim. Acta* **2009**, *362*, 4340. (d) Demessence, A.; Long, J. R. *Chem. Eur. J.* **2010**, *16*, 5902.

7 Bordwell, F. G. *Acc. Chem. Res.* **1988**, *21*, 456. Note that the values given are for the non-substituted azoles, and are referenced to DMSO.

8 Demessence, A.; D'Alessandro, D. M.; Foo, M. L.; Long, J. R. *J. Am. Chem. Soc.* **2009**, *131*, 8784.

9 To quickly summarize them, 1,4-bis(1*H*-pyrazol-4-yl)benzene (1,4-H_2BDP) was found to react with salts of cobalt(II), nickel(II), or zinc(II) (see **Chapter 4** and ref 3i) to afford frameworks exhibiting good thermal stability (T_{dec} = 420-460 °C). Employing instead the bent molecule, 1,3-bis(1*H*-pyrazol-4-yl)benzene (1,3-H_2BDP), the Long group have synthesized a double-walled zinc-based framework of even greater thermal stability (T_{dec} = 500 °C), which further shows chemical stability in a hot acidic solution

(pH 3).[3e] The thermal stability of pyrazolate-based materials was again observed for the cubic frameworks $Ni_8L_6(OH)_4(H_2O)_2$ with L = 4,4¢-bis(1*H*-pyrazol-4-yl)biphenyl, (T_{dec} = 420 °C) or 2,6-bis(1*H*-pyrazol-4-yl)pyrrolo[3,4-*f*]isoindole-1,3,5,7(2*H*, 6*H*)-tetrone, (T_{dec} = 410 °C) described in **Chaper 5**. Furthermore, a Cu(I) framework based on the 3,3',5,5'-tetramethyl-4,4'-bipyrazolate (H_2Me_4bpz) was found stable up to 500 °C in nitrogen atmosphere but also in air atmosphere with a decomposition temperature of above 400 °C.[3h]

10 (a) Dincă, M.; Dailly, A.; Liu, Y.; Brown, C. M.; Neumann, D. A.; Long, J. R. *J. Am. Chem. Soc.* **2006**, *128*, 16876. (b) Dincă, M.; Han, W. S.; Liu, Y.; Dailly, A.; Brown, C. M.; Long, J. R. *Angew. Chem., Int. Ed.* **2007**, *46*, 1419. (c) Dincă, M.; Long, J. R. *Angew. Chem., Int Ed.* **2008**, *47*, 6766.

11 (a) Quartapelle-Procopio, E.; Liñares, F.; Montoro, C.; Colombo, V.; Maspero, A.; Barea, E.; Navarro, J. A. R. *Angew. Chem., Int. Ed.* **2010**, *49*, 7308. (b) Horike, S.; Dincă, M.; Tamaki, K.; Long, J. R. *J. Am. Chem. Soc.* **2008**, *130*, 5854.

12 (a) Seo, J. S.; Whang, D.; Lee, H.; Jun, S. I.; Oh, J.; Jeon, Y. J.; Kim, K. *Nature* **2000**, *404*, 982. (b) Wu, C.-D.; Hu, A.; Zhang, L.; Lin, W. *J. Am. Chem. Soc.* **2005**, *127*, 8940. (c) Horike, S.; Dincă, M.; Tamaki, K.; Long, J. R. *J. Am. Chem. Soc.* **2008**, *130*, 5854. (d) Ma, L.; Abney, C.; Lin, W. *Chem. Soc. Rev.* **2009**, *38*, 1248. (e) Lee, J.; Farha, O. K.; Roberts, J.; Scheidt, K. A.; Nguyen, S. T.; Hupp, J. T. *Chem. Soc. Rev.* **2009**, *38*, 1450.

13 Coelho, A. *J. Appl. Cryst.* **2003**, *36*, 86.

14 Version 3.0, Bruker AXS **2005**, Karlsruhe, Germany.

15 To build the rigid model describing the ligand, the followind bond distances and angles have been adopted a) for the benzene ring: C-C = 1.39 Å; C-H = 0.95 Å; C-C-C, C-C-H = 120°; b) for the pyrazole ring: C-C, C-N, N-N = 1.36 Å; C-H = 0.95 Å; internal ring angles = 108°; C-C-H = 126°. $C_{benzene}$-$C_{pyrazole}$ = 1.45 Å.

16 Cheary, R. W.; Coelho, A. *J. Appl. Cryst.* **1998**, *31*, 85; *ibid.* 862.

17 PLATON, Spek, A. L. *J. Appl. Cryst.* **2003**, *36*, 7-13.

18 Due to the extreme rigidity of the frameworks, the values quoted are representative of the void volume of the outgassed counterparts.

19 It is worth emphasizing again that, due to the heavy disorder affecting the solvent molecules in the structure, both clathrated and coordinated, their electron density has been described by a very simplified model (see Experimental Section).

20 (a) Sumida, K.; Horike, S.; Kaye, S. S.; Herm, Z. R.; Queen, W. L.; Brown, C. M.; Grandjean, F.; Long, G. J.; Dailly, A.; Long, J. R. *Chem. Sci.* **2010**, *1*, 184. (b) Sumida, K.; Horike, S.; Bloch, E. D.; Foo, M. L.; Murray, L. J.; Long, J. R. unpublished results.

21 (a) Masciocchi, N.; Ardizzoia, G. A.; Maspero, A.; LaMonica, G.; Sironi, A. *Inorg. Chem.* **1999**, *38*, 3657. (b) Sadimenko, A. P.; Basson, S. S. *Coord. Chem. Rev.* **1996**, *147*, 247.

22 (a) Evans, W. *J. Chem. Educ.* **2004**, *81*, 1191. (b) Vos, J. G.; Groeneveld, W. L. *Trans. Met. Chem.* **1979**, *4*, 137.

23 (a) Masciocchi, N.; Ardizzoia, G. A.; LaMonica, G.; Maspero, A.; Sironi, A. *Eur. J. Inorg. Chem.* **2000**, 2507. (b) Barea, E.; Navarro, J. A. R.; Salas, J. M.; Masciocchi, N.; Galli, S.; Sironi, A. *Inorg. Chem.* **2004**, *43*, 473.

24 (a) Cizmek, A.; Komunjer, L.; Subotic, B.; Siroki, M.; Roncevic, S. *Zeolites* **1991**, *11*, 258. (b) Cizmek, A.; Komunjer, L.; Subotic, B.; Siroki, M.; Roncevic, S. *Zeolites* **1991**, *11*, 810. (c) Cizmek, A.; Komunjer, L.; Subotic, B.; Siroki, M.; Roncevic, S. *Zeolites* **1992**, *12*, 190. (d) Petushkov, A.; Freeman, J.; Larsen, S. C. *Langmuir* **2010**, *26*, 6695. (e) Hartman, R. L.; Fogler, H. S.; *Langmuir* **2007**, *23*, 5477. (f) Murata, K. J. *J. Am. Mineral.* **1943**, *28*, 545.

25 To build the rigid model describing the ligand, the following bond distances and angles have been adopted a) for the benzene ring: C-C = 1.39 Å; C-H = 0.95 Å; C-C-C, C-C-H = 120°; b) for the pyrazole ring: C-C, C-N, N-N = 1.36 Å; C-H = 0.95 Å; internal ring angles = 108°; C-C-H = 126°. $C_{benzene}$-$C_{pyrazole}$ = 1.45 Å.

Chapter 7
Tuning Adsorption Properties in Highly Stable Pyrazolate-based MOFs through Ligand Modification

Introduction

Metal-organic frameworks (MOFs) are a fascinating class of materials in which the combination of inorganic sub-unit and organic ligands are linked each other by strong bonds generating robust and often porous polymers featuring extended network architectures. The extraordinary peace of the research in this field has resulted in an increasing number of new structures and frameworks compositions with many different potential applications.[1]

In the field of coordination polymers, structure predictability is an important requirement for the synthesis of functional materials with tailored properties, and now has become possible. The concept of rational design was developed by O'Keeffe *et al*.[2] and, as brilliantly described by Ferey in his review,[3] was rooted in the fact that topochemically-selected reactions govern the construction process of the metal-organic framework in solvothermal conditions. This suggest that, with adequate synthetic conditions, the targeted inorganic sub-unit may be obtained in a systematic way for the construction of a framework. Therefore, as soon as the chemical conditions associated to the existence of a parent structure are known, the possible modulation of the

pore size and walls decoration can be directly achieved through a modification of the length of the ligand or introduction of different functionalities on the organic spacer. This means that is possible, in principle, to tune and study, in a single class of materials, those properties that are exclusively dependent on the modification introduced on the organic bridge (*i.e.* pore size and shape, surface selectivity, uptake capacity, *etc.*). However, the number of possibilities of combining inorganic and organic moieties is immense, and the infinite variation on the nature of the linkers can either provide a series of isostructural compounds or, without neglecting the unexpected results of serendipity, even new structures.[4]

Among the numerous ligands used in MOFs chemistry, terephtalate ligands are a highly studied family that can be easily functionalized with groups of different nature such as basic, acidic or with different polarities.[5] Within many examples reported in the literature, an exceptional one is the isoreticular synthesis of the IRMOFs 1-16 series, derived from the prototypic MOF-5 structure.[6] Yaghi *et al.* demonstrate that the organic spacer of MOF-5 can be functionalized with many different substituents (such as -Br, -NH_2, -OC_3H_7, etc.) and the pore size of the framework can be expanded with longer molecular struts as, *e.g.*, biphenyl or tetrahydropyrene, with no changes in the underlying topology.

Porous metal organic frameworks have been also explored as a new kind of zeolite-analogous materials because are expected to be more designable in pore size and shape, as well as exhibiting wide structural diversity. However, in Chapter 6, one of the main weakness of MOFs, has been widely described, that is the lack of stability in temperature, moisture, acid or basic media and, sometimes, even in air, that limits their utility in industrial applications. In this PhD research, a new generation of pyrazolate-based metal organic frameworks have been presented,[7] and the ability of pyrazoles in generating metal-organic frameworks of

highly robust nature have now been demonstrated. For example, the extended sodalite-type Ni_3BTP_2 [H_3BTP = 1,3,5-tris(1*H*-pyrazol-4-yl)benzene] framework,[7d] described in Chapter 6, represents the first example of metal-organic framework exhibiting high surface area and exposed metal sites coupled to a high thermal stability (up to 430 °C) and an exceptional resistance to hydrolysis and decomposition during treatment with water, acidic and basic solutions.

A new, important, challenge in the field of porous polymers is the development of stable structures including functional organic sites, with the aim of tuning their pore properties (pore size and shape, pore volume and decoration) to enhance uptake capacity and selectivity toward a targeted guest. Indeed, our present goal is to study how functionalization of the organic linker can affect the chemical and physical properties of those pyrazolate-based materials. Particularly, for extracting the trends of stability and adsorption properties versus the nature of the substituents in pyrazolate-based frameworks, the synthesis and characterization of two large series of porous framework based on the skeleton of the two **NiBDP** and **ZnBDP** materials [H_2BDP = 1,4-bis(1*H*-pyrazol-4-yl)benzene, Figure 7.1] built by four new tagged organic linkers (Scheme 7.1) bearing a nitro, amino, hydroxyl and sulfonic acid functionalities (-NO_2, -NH_2, -OH, -SO_3H), is presented. Although this work is still underway, in the following, synthetic strategies and structural investigation by means X-ray powder diffraction analysis (XRPD), are discussed. Thermal stability of the tagged MBDP_X materials has been evaluated by simultaneous TG/DSC analyses, while the effective presence of the functional sites in the resulting MOFs was probed by FTIR. Moreover, the potential application of these new frameworks in selective adsorptive properties for gas separation and purification purposes has been investigated by conventional single component adsorption isotherms, as well as, advanced experiments of pulse gas chromatography and breakthrough curve measurements.

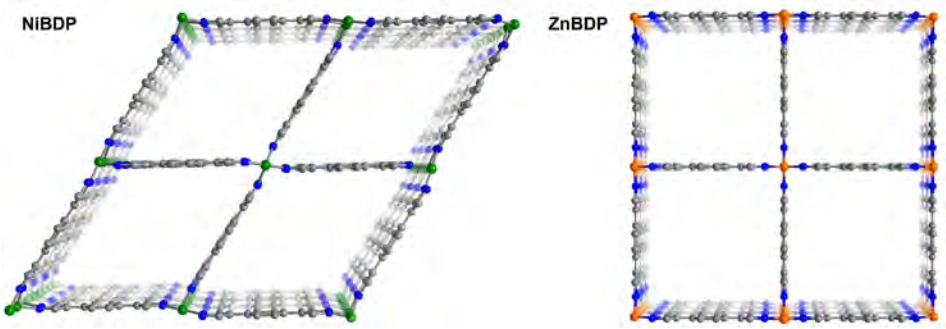

Figure 7.1. Depiction of the primitive structures of **NiBDP** and **ZnBDP** [H_2BDP = 1,4-bis(*1H*-pyrazol-4-yl)benzene] highlighting romboic and square lettices fror NiBDP and ZnBDP, respectively.

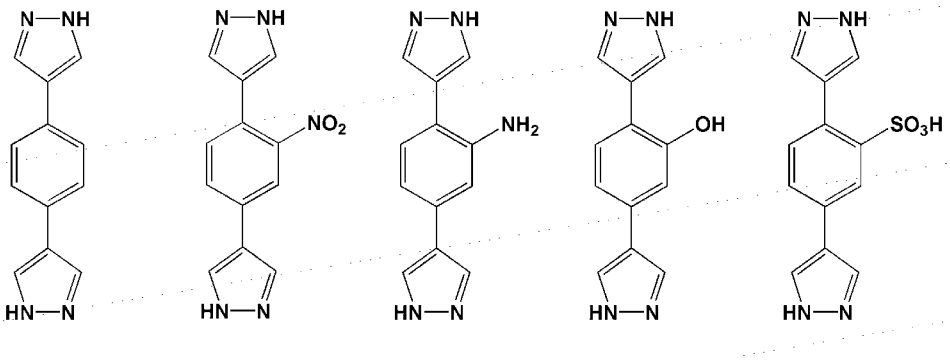

Scheme 7.1. Organic ligands used in this work for the construction of tagged metal-organic frameworks with the corresponding abbreviations.

Experimental Details

Synthesis and Characterization. All chemicals were obtained commercially and used without further purification. The 1,4-bis(1*H*-pyrazol-4-yl)benzene (H_2BDP) was prepared as described in Chaper 3,[8] and the tagged organic ligands were prepared according to the procedure reported in Chapter 3.

General procedure for NiBDP_X (X = H, NO_2, NH_2, OH) preparation. H_2BDP_X (0.5 mmol) was dissolved in DMF (10 mL) in a 50 mL schlenk flask and heated to 60 °C. $Ni(CH_3COO)_2 \cdot 4H_2O$ (0.5 mmol) was then added to the solution under stirring. The mixture was allowed to react for 5 h at reflux. After cooling at room temperature, the orange solid was collected by filtration, washed with methanol (3 × 10 mL) and dried under vacuum.

Anal. Calcd. for **$Ni(C_{12}H_7N_5O_2)(C_3H_7NO)_2(CH_3OH)_2$, (NiBDP_$NO_2$)** (Mw = 522 g/mol): C, 46.00; H, 5.60; N, 18.78. Found: C, 45.96; H, 5.45; N, 19.28. IR (nujol): 1676(vs), 1649(vs), 1571(s), 1523(s), 1256(vs), 1179(w), 1136(w), 1107(w), 1062 (s), 1006(w), 982(w), 955(w), 869(w), 837(w), 762(w, 738(w), 673(w) cm^{-1}.

Anal. Calcd. for **$Ni(C_{12}H_9N_5)(C_3H_7NO)(H_2O)(CH_3OH)$, (NiBDP_$NH_2$)** (Mw = 405 g/mol): C, 47.44; H, 5.47; N, 20.75. Found: C, 47.80; H, 5.95; N, 21.05. IR (nujol): 3437(s), 3355(s), 1654(s), 1620(w), 1573(s), 1346(w), 1262(w), 1169(w), 1134(w), 1064(s), 954(s), 855(w), 810(w), 722(w) cm^{-1}.

Anal. Calcd. for **$Ni(C_{12}H_8N_4O)(H_2O)_3(CH_3OH)$, (NiBDP_OH)** (Mw = 369 g/mol): C, 42.31; H, 4.92; N, 15.18. Found: C, 41.99; H, 4.81; N, 15.39. IR (nujol): 3579(s), 1619(w), 1577(s), 1269(w), 1222(w), 1175(w), 1147(w), 1064(s), 955(s), 866(w), 843(w), 813(w), 722(w) cm^{-1}.

General procedure for ZnBDP_X (X = H, NO_2, NH_2, OH) preparation. H_2BDP_X (0.5 mmol) was dissolved in DMF (10 mL) in a 50 mL schlenk flask and heated to 60 °C. $Zn(CH_3COO)_2 \cdot 2H_2O$ (0.5 mmol) was then added to the solution under stirring. The mixture was allowed to react for 5 h at reflux. After cooling at room temperature, the white solid was collected by filtration, washed with methanol (3 × 10 mL) and dried under vacuum.

Anal. Calcd. for **$Zn(C_{12}H_7N_5O_2)(C_3H_7NO)_2(CH_3OH)_2(H_2O)_5$, (ZnBDP_$NO_2$)** (Mw = 619 g/mol): C, 38.81; H, 6.35; N, 15.84. Found: C, 38.63; H, 6.03; N, 16.06. IR (nujol): 3350(br), 1670(vs), 1578(s), 1527(s), 1532(w), 1257(vs), 1134(w), 1092(w),

1064(s), 1012(w), 982(w), 954(w), 869(w), 847(w), 764(w), 739 (w), 722(w), 659(w), 623(w) cm^{-1}.

Anal. Calcd. For **$Zn(C_{12}H_9N_5)(C_3H_7NO)_2(CH_3OH)(H_2O)$, (ZnBDP_NH$_2$)** (Mw = 484.8 g/mol): C, 47.07; H, 6.03; N, 20.22. Found: C, 47.33; H, 5.74; N, 20.07. IR (nujol): 3409(w), 3341(w), 1675(vs), 1629(w), 1571(s), 1402(w), 1344(w), 1256(s), 1177(w), 1131(s), 1091(w), 1060(s), 1012(w), 995(w), 951(s), 856(w), 810(w), 724(w), 662(w) cm^{-1}.

Anal. Calcd. for **$Zn(C_{12}H_8N_4O)(C_3H_7NO)_2(CH_3OH)$, (ZnBDP_OH)** (Mw = 467.8 g/mol): C, 48.78; H, 5.60; N, 17.96. Found: C, 48.63; H, 5.98; N, 18.29. IR (nujol): 3470(br), 1675(vs), 1575(s), 1354(w), 1254(s), 1223(w), 1170(w), 1141(w), 1125(w), 1102(w), 1058(s), 1013(w), 955(w), 867(w), 840(w), 814(w), 720(w), 663(w), 603(w) cm^{-1}.

Synthesis of $Ni(C_{12}H_9N_4SO_3)(C_3H_7NO)(H_2O)_3$, (NiHBDP_SO$_3$) H_2BDP_SO_3H (0.050 g, 0.172 mmol) was dissolved in DMSO (3 mL) in a 50 mL schlenk flask and DMF (3 mL) was added to this solution. The mixture was heated to 60 °C and $Ni(CH_3COO)_2{\cdot}4H_2O$ (0.085 g, 0.5 mmol) was added under stirring. The mixture was then allowed to react for 5 h at 160°C. After cooling at room temperature, the yellowish solid was collected by filtration, washed with DMF (3 × 10 mL) and dried under vacuum. Anal. Calcd. for $Ni(C_{12}H_9N_4SO_3)(C_3H_7NO)(H_2O)_3$ (Mw = 475.1 g/mol): C, 37.92; H, 4.67; N, 14.74. Found: C, 37.54; H, 4.85; N, 14.55. IR (nujol): 3442(s), 3159(w), 1666(s), 1590(w), 1572(w), 1251(s), 1158(s), 1080(w), 1053(w), 1022(s), 961(w), 854(w), 790(w), 721(w), 691(w). 823(w) cm^{-1}.

Crystal data for Ni(HBDP_SO$_3$). $NiC_{12}H_9N_4SO_3$, fw, 347.98 g mol^{-1}, monoclinic, *P2$_1$/c*, a = 7.4138(4), b = 15.466(1), c = 17.173(2) Å, β = 91.958(5)°, V = 1968.3 $Å^3$, Z = 2, R_p, R_{wp} and R_{Bragg} = 0.019, 0.030, 0.019, respectively, for 53 parameters.

X-Ray Powder Diffraction Analysis (XRPD). Powdered, microcrystalline sample of **NiHBDP_SO$_3$** was deposited in the hollow of an aluminum sample holder (equipped with a zero-background plate). Diffraction data were collected

at ambient atmosphere and temperature with scans in the 5-105° 2θ range on a Bruker AXS D8 Advance diffractometer, equipped with a linear position-sensitive Lynxeye detector, primary beam Soller slits, and Ni-filtered Cu-Kα radiation (λ = 1.5418 Å). Generator setting: 40 kV, 40 mA. Standard peak search, followed by indexing with TOPAS,[9] allowed the detection of the approximate unit cell parameters. The space group $P2_1/c$ was assigned on the basis of the systematic absences conditions and later confirmed by Le Bail refinements. Structure solutions were performed by the simulated annealing technique, as implemented in TOPAS, using for the ligand a rigid, idealized model. The final refinement was carried out by the Rietveld method. The background was modeled by a polynomial function; and anisotropic broadening, in the form of spherical harmonics, was used to define the peak widths. Peak shapes were described by the fundamental parameters approach. One, refinable isotropic thermal parameter was assigned to the metal atoms, augmented by 2.0 $Å^2$ for lighter atoms.

For the whole series of NiBDP_X and ZnBDP_X (X = NO_2, NH_2, OH) standard peak search, followed by indexing with TOPAS, allowed the detection of the approximate unit cell parameters on diffraction data collected at room temperature with scans in the 5-35° 2θ range.

X-Ray Powder Diffraction in Temperature. Thermodiffractometric experiments were performed on the as-synthesized samples, to highlight their "structural" response. The experiments were carried out in air from 298 K up to the loss of crystallinity, using a custom-made sample heater, assembled by Officina Elettrotecnica di Tenno, Ponte Arche, Italy. A powdered microcrystalline batch of each sample was deposited in the hollow of an aluminum sample holder; diffractograms at different temperatures (with steps of 20 K) were recorded, up to decomposition, in a significant low-angle 2θ range.

IR Spectroscopy Analysis. The infrared (IR) spectra were performed on transmission mode on a FTIR Shimadzu Prestige-21 spectrometer. The materials

under study were mixed with nujol to form a mull and recorded with KBr plates in the spectral range 4000-600cm^{-1}.

Thermal Analysis. Simultaneous TG and DSC analyses were performed in a N_2 stream on a Netzsch STA 409 PC Luxx with an heating rate of 10 K min^{1} up to 900 °C.

Elemental Analysis. Elemental analyses were carried out on a Perkin Elmer CHN Analyzer 2400 Series II at the facility of the Università dell'Insubria in Como.

Gas Adsorption Measurements. Conventional adsorption isotherms were measured using a Micromeritics Tristar 3000 volumetric instrument under continuous adsorption conditions. Brunauer-Emmet-Teller (BET) and Langmuir analyses were used to determine the total specific surface areas for the N_2 isotherms at 77 K. In addition, CO_2 isotherms at 273 K were measured in order to evaluate the micropore region by means of the Dubinin-Radushkevich equation (Table 7.3).-Prior to measurement, powdered samples were heated at 453 K for 12 h and outgassed to 10^{-6} Torr.

Variable Temperature Pulse Gas Chromatography. Gas-phase adsorption at zero coverage surface was studied using the pulse chromatographic technique,[10] employing a Gas Chromatograph (Varian 450-GC) with a 15 cm-column (0.4 cm internal diameter) packed with *ca.* 1 g of pelletized sample (particle size 0.5 mm *ca.*) (See Scheme 7.2). In order to avoid pressure drops in the chromatographic column the microcrystalline particles of the materials were aggregated by emulsifying them in a water suspension (1 mL) of starch (0.1 g) at 343 K for 1 minute. The solvent was then removed under reduced pressure and the resulting solid was grounded through a 0.5 mm sieve to give the pelletized samples. For the activation of the material, a He flow (30 mL min^{-1}) was passed through the column at 453 K for 7 h. Later on, 1 mL of an equimolecular gas mixture (C_2H_2, H_2, CH_4, CO_2) was injected at 1 bar on an He flow (15 mL min^{-1}) and the separation performance of the chromatographic column was examined at different temperatures (273 K - 323 K) by means of a mass Spectrometer Gas Analysis System (Pfeiffer vacoon) detecting ion peaks

	$SA_{BET}/m^2 g^{-1}$	$SA_{Langmuir}/m^2 g^{-1}$	$SA_{DR}/m^2 g^{-1}$
NiBDP	1066 (18)	1350 (9)	1480
NiBDP_NO_2	1131 (17)	1423 (9)	2350
NiBDP_NH_2	1305 (22)	1645 (8)	990
NiBDP_OH	1103 (18)	1394 (10)	1980
NiHBDP_SO_3	819 (16)	1044 (6)	1220
ZnBDP	2288 (41)	2857 (2)	1220
ZnBDP_NO_2	1875 (52)	2358(5)	730
ZnBDP_NH_2	1345(21)	1788(78)	600
ZnBDP_OH	1170 (22)	1484 (7)	1420

Table 7.3. Langmuir, BET (N_2, 77K) and Dubinin-Radushkevich (CO_2, 273 K) surface areas for the two series of **NiBDP_X** and **ZnBDP_X** (X = H, NO_2, NH_2, OH, SO_3H) as-synthesized and desolvated under reduced pressure at 180 °C for 12 hours.

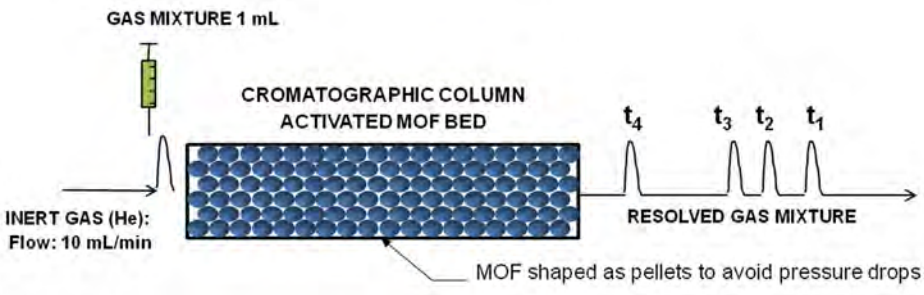

Scheme 7.2. Scheme of experimental set up for pulse gas chromatographic measurements.

at m/z 44 (CO_2), 26 (C_2H_2), 16 (CH_4), 4 (He) and 2 (H_2). The dead volume of the system was calculated using the retention time of hydrogen as a reference.

On the other hand, the retention time of H_2O was determined by using a thermal conductivity detector (TCD) of the Gas Chromatograph Equipment

configured for this determination using an on-column injector (0.2 mL) at variable temperature (363 K - 473K).

Breakthrough Experiments for Gas Separation. The as above prepared 15-cm chromatographic column was activated under a pure He flow (30 mL min^{-1}) at 453 K for 7 h and used for evaluating the CO_2/N_2, CO_2/CH_4 and C_2H_2/CH_4 separation performances of the materials. The desired gas mixture (10 mL min^{-1}) was prepared via mass flow controllers (see Scheme 7.3). For instance CO_2/N_2 (0.14:0.86) mixtures were prepared in order to simulate a emission flue gas from a power plant employing a 1.4 mL min^{-1} of CO_2 and 8.6 mL min^{-1} of N_2 flows and the breakthrough experiments were carried out by step changes from He to CO_2/N_2 flow mixtures. These experiments were performed at 273 K, 303 K and 323 K. The relative amounts of gases passing through the column were monitored on a Mass Spectrometer Gas Analysis System (Pfeiffer Vacoon) detecting ion peaks at m/z 44 (CO_2), 28 (N_2) and 4 (He).

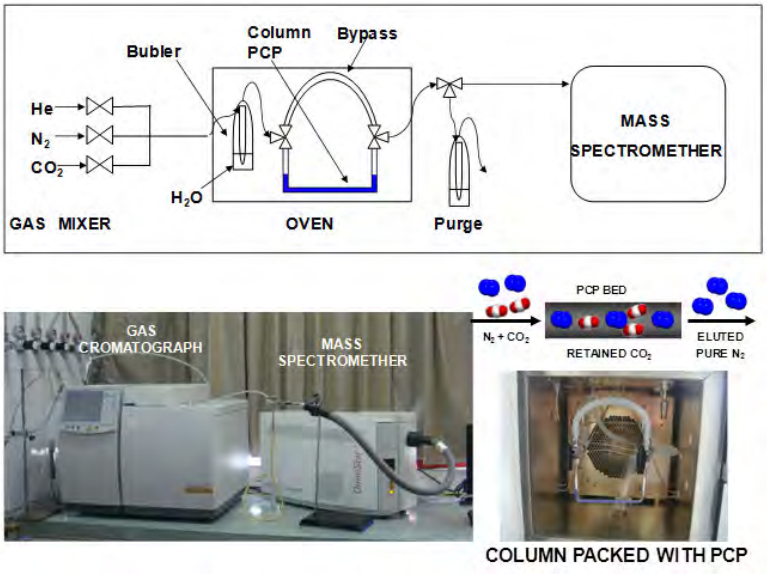

Scheme 7.3. Experimental setup used for breakthrough measurements showing a view of instruments and packed chromatographic column inside the gas chromatograph oven.

Results and Discussion

Syntheses. The 1,4-Bis(pyrazol-4-yl)benzene, H_2BDP ligand has been chosen as parent ligand for the preparation of new series of functionalized linkers due to its easy availability from synthesis, in good yields and in a grams scale (see Chapter 3). Later on, for the preparation of the isostructural series of porous metal-organic frameworks, we focused our attention on nickel(II) and zinc(II) salts, that generally result in stable frameworks of easy handling in air. In a previous study, discussed in Chapter 4,[11] **NiBDP** was obtained by reacting the H_2BDP ligand with Ni(II) acetate in acetonitrile at 80 °C in the presence of triethylamine. The isolated product was found to be contaminated by unreacted H_2BDP ligand, that is extremely insoluble in the reaction solvent, implying the necessity of an additional washing procedure in dimenthyl sulfoxide at 60°C. On the other hand, **ZnBDP** was isolated as a pure product, by reacting $Zn(ClO_4)_2$ with H_2BDP in benzonitrile and triethylamine.[12] However, in this work, the preparation that have been found to afford the whole series of MBDP_X (M = Ni^{2+}, Zn^{2+}; X = NO_2, NH_2, OH) frameworks, in a crystalline and pure form, differs with respect to the latter. Indeed, acetates salts were reacted in boiling N, N-dimethylformamide and the organic linkers, with no extra base, such as triethylamine, in the reaction system. Interestingly, the very same procedure, has been adopted also for the parent frameworks **NiBDP** and **ZnBDP**, providing crystalline and pure materials of DMF solvates. A special comment is deserved for this reaction where deprotonation of the ligand is promoted by the acetate anion as an internal base, allowing a slow precipitation of a highly insoluble and crystalline powders. Moreover, this synthetic procedure is fully reproducible and could be scaled up making these MOFs available on a large scale.

Unfortunately, any attempt to produce an isostructural MOF containing the ligand bearing the sulfonic acid functionality (H_2BDP_SO_3H, see Scheme 7.1), have failed. However, by employing different synthetic conditions, another

isomer of the parent **NiBDP** structure, **NiHBDP_SO$_3$**, was obtained (*vide infra*). Repeated attempts at obtaining a pure phase with Zn(II) metal ions, by varying the synthesis parameters, such as time, temperature program, stoichiometry, solvents and pH, were unsuccessful.

Structures. The bulk crystallinity of each tagged MOF was then evaluated by X-Ray Powder Diffraction Analysis (XRPD) and their diffraction patterns are reported in Figure 7.2 and 7.3 revealing that the material are all crystalline. The comparison between the diffraction patterns of the parent structures and the ones obtained with the new linkers demonstrated the formation of pure, topologically equivalent, phases for each NiBDP_X and ZnBDP_X (X = NO_2, NH_2, OH) series. The parent structure resulted in two porous framewroks where, in **NiBDP**, the chains are arranged in a rhombic disposition, governed by the square-planar geometry of the Ni(II) ions, and, in **ZnBDP**, linear chains of tetrahedral coordinated Zn(II) metal ions are arranged to form a square lattice (See Figure 7.1) in orthorhombic *Imma* and tetragonal *P4$_2$/mmc* space groups, for **NiBDP** and **ZnBDP** respectively. Indexing process on the diffraction data collected for each tagged MBDP_X species, followed by Le Bail refinement, allowed us to retrieve the unit cells parameters for each framework, which results are reported in Table 7.1 and 7.2.

Regarding the ZnBDP_X series, as evidenced by an independent indexing process followed by a Le Bail refinement (Table 7.2), the new synthesis, carried out in DMF as the solvent, leads, for **ZnBDP** and **ZnBDP_NH$_2$**, to an orthorhombic deformation of the expected tetragonal square-grid framework, possibly due to the actual nature and 'distribution' of the solvent within the network pores. Indeed, the original synthesis for the parent **ZnBDP** framework, was carried out in benzonitrile.[7] This observation is not surprising, while Long's CoBDP, a *N,N*-diethylformamide solvate, was found to belong to the orthorhombic *P222$_1$* space group.[14a] Worthy of note, the XRPD traces of the new DMF solvates of **ZnBDP**

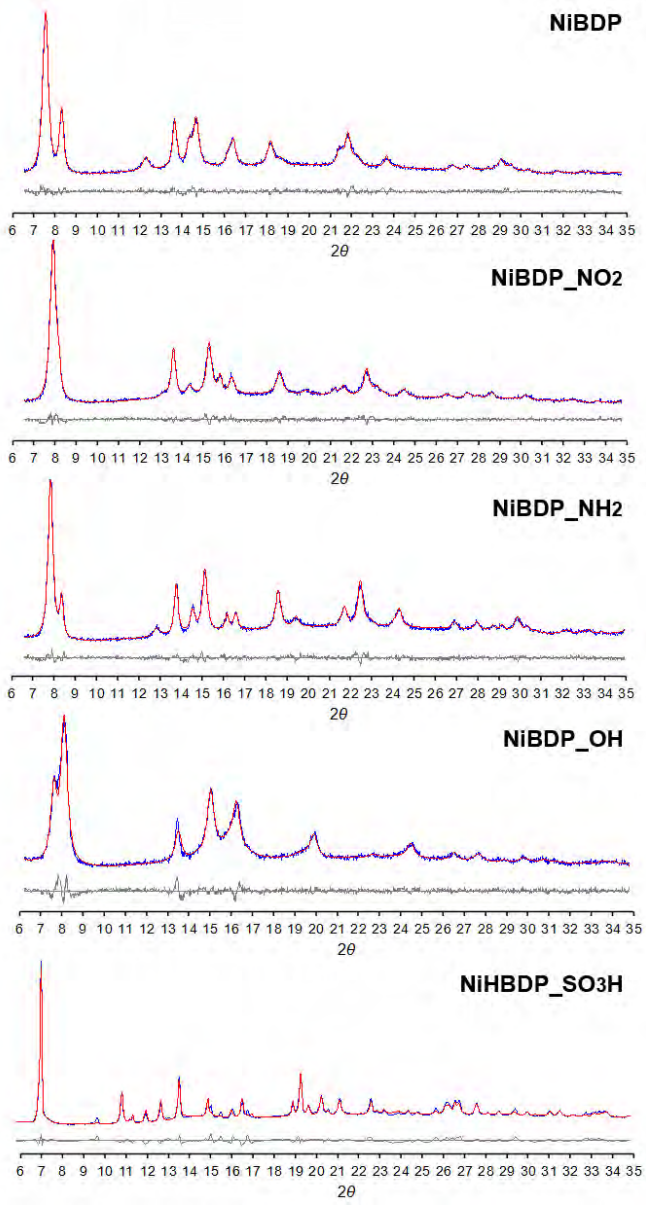

Figure 7.2. Le Bail refinements plots for (up to bottom) species **NiBDP**, **NiBDP_NO$_2$**, **NiBDP_NH$_2$**, **NiBDP_OH** and **NiHBDP_SO$_3$**. Horizontal axis, 2θ, deg. Difference plots are reported at the bottom (gray curve).

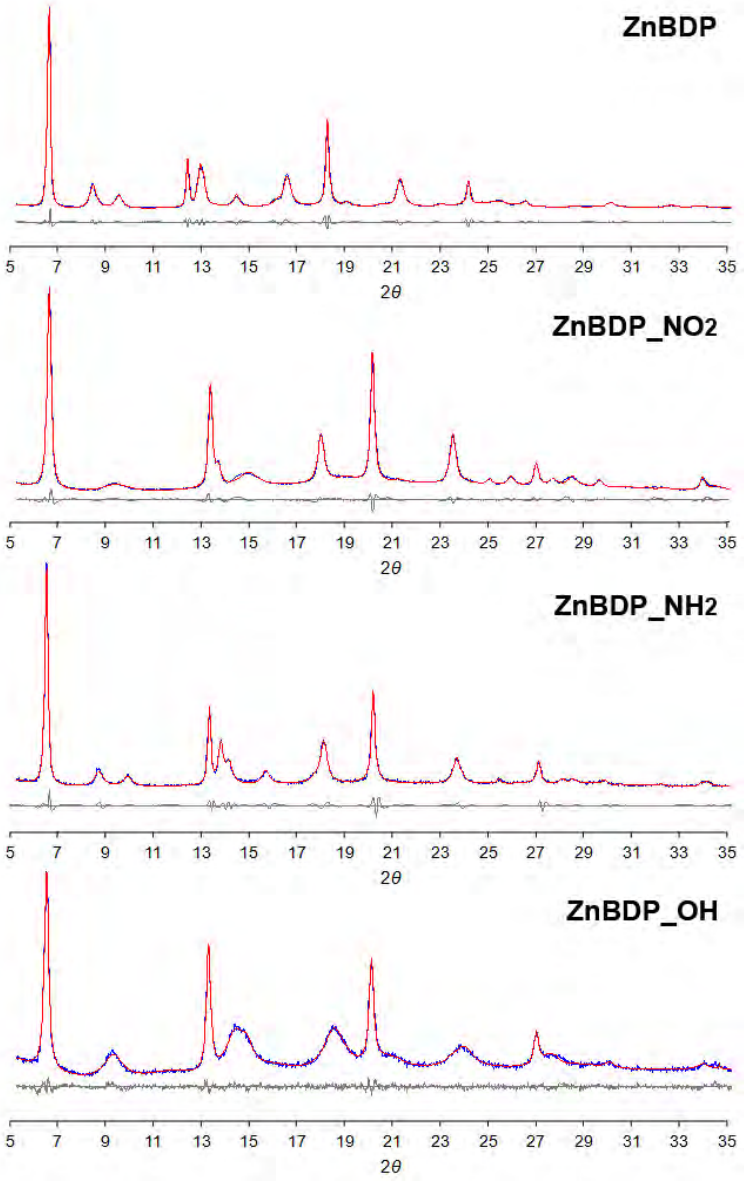

Figure 7.3. Le Bail refinements plots for (up to bottom) species **ZnBDP**, **ZnBDP_NO$_2$**, **ZnBDP_NH$_2$**, and **ZnBDP_OH**. Horizontal axis, 2θ, deg. Difference plots are reported at the bottom (gray curve).

MOFs	Space Group	a, Å	b, Å	c, Å	V, Å^3	β
NiBDP	Imma	6.924	22.108	14.692	2249.1	90
NiBDP-NH_2	Imma	6.939	22.356	14.179	2199.5	90
NiBDP-NO_2	Imma	7.040	22.762	13.758	2204.7	90
NiBDP-OH	Imma	6.658	23.037	12.271	1882.3	90
NiHBDP_SO_3	$P2_1/c$	7.413	15.463	17.16	1966.4	91.576

Table 7.1. NiBDP_X as synthesized samples, unit cells parameters.

MOFs	Space Group	a, Å	b, Å	c, Å	V, Å^3
ZnBDP	Cccm	17.518	19.986	7.187	2516.3
ZnBDP-NH_2	Cccm	17.566	19.913	7.267	2542.2
ZnBDP-NO_2	$P4_2/mmc$	13.241	13.241	7.404	1298.2
ZnBDP-OH	$P4_2/mmc$	13.280	13.280	6.985	1231.9

Table 7.2. ZnBDP_X as synthesized samples, unit cells parameters.

and **ZnBDP_NH_2** are affected by a non negligible anisotropic broadening of some classes of peaks: it appears that, while the [*h*00] peaks are sharp, those with *l* distinct from 0 are rather broad. The presence of broadening is the evidence of a distortion form the 'perfect' square-grid network. Moreover, the observation that specific classes of peaks are broadened, is a clear indication of the fact that the deformation is not random, yet proceeds in a concerted way. Further studies are in progress for a collecting new data toward a comprehensive and coherent picture of these observations.

In Figure 7.2, is reported the powder diffraction pattern of the nickel framework bearing a sulfonic acid functionality on the benzene ring. As visually evident, its diffraction data slightly differs in 2θ compared to the rest of the Ni(II)

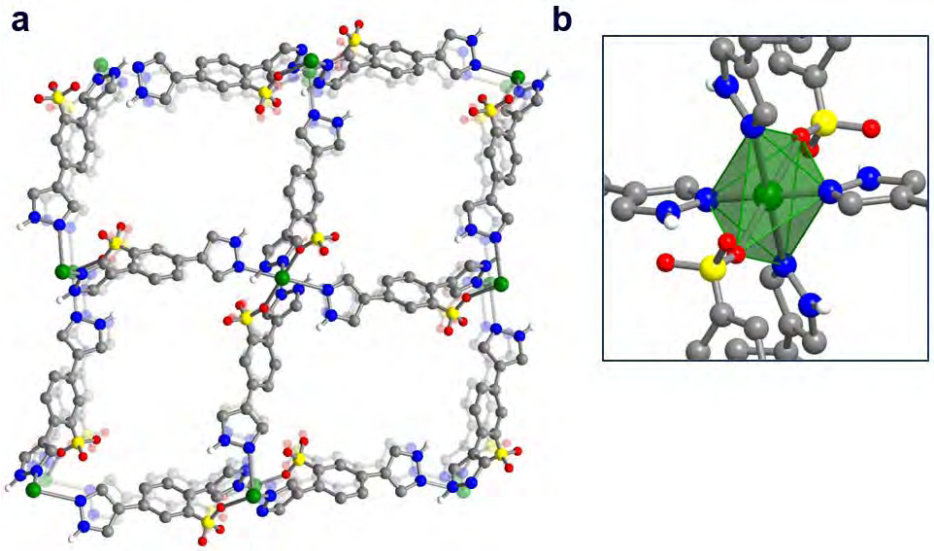

Figure 7.4. a) Depiction of the crystal structure of **NiHBDP_SO$_3$** viewed along the **a** direction and b) enlargement of the Ni(II) octahedral geometry.

series. Structure solution from powder diffraction allows to retrieve its crystal structure that has been found to be an isomer of the **NiBDP** parent framework of formula **Ni($C_{12}H_9N_4SO_3$)**·3H_2**O**, in the following **NiHBDP_SO$_3$**. The local coordination geometry of this heteroleptic framework can be appreciated in Figure 7.4a, while the overall structure is shown in Figure 7.4b. This framework crystallizes in the monoclinic *P2$_1$/c* space group. Each metal centre is esacoordinated, in a trans-NiNN_4O_2 octahedral sterochemistry by 4 nitrogen atoms of four distinct ligand moieties and two oxygen atoms of the -SO_3 groups of other two distinct ligands. This coordination geometry results in a 3D framework in which the acid proton is located on the nitrogen atom of the pyrazole ligand. This N-H group interact, through an hydrogen bond, with the oxygen of the adjacent -SO_3 functional group and the chlatrated solvent molecules. Dimension of the pores is about 7.5 x 5 Å.

IR Spectroscopy Characterization. Since each functional group introduced on the organic linkers shows a characteristic signal in the IR region, the all series of modified MOFs were studied by means IR spectroscopy experiments. The samples were first dried under vacuum and then quickly prepared as a nujol mull and collected. For the sake of simplicity the characterization description is here done for the **NiBDP_X** series. In Figure 7.5 is indeed shown the comparison between each tagged nickel MOFs and the parent **NiBDP**. As for the nickel(II) series, the **ZnBDP_X** infrared spectra are reported in Figure 7.7.

The FTIR spectrum of the **NiBDP_NO_2** framework is depicted in Figure 7.5b. Aromatic nitro groups shows a typical spectroscopy features due to absorption of asymmetric [$\nu(NO)_{asym}$] and symmetric [$\nu(NO)_{sym}$] stretching modes. The asymmetric mode typically result in a strong band in the 1550-1500 cm^{-1} region, while the symmetric mode absorb in the 1360-1290 cm^{-1}.[13] In the **NiBDP_NO_2** spectra the asymmetric stretching of the NO_2 group can be assigned to the strong band at 1530 cm^{-1}. Unfortunately, the symmetric mode is partially overshadowed by the strong band of the nujol mull (1377 cm^{-1}). For comparison, similar absorption mode are found also in the spectrum of the H_2BDP_NO_2 linker (see Chapter 3). The presence of numerous bands in the lower frequencies region of the IR spectrum complicates the assignment of the C-N stretching vibration that should be present in the 920-850 cm^{-1} region.

In the FTIR spectrum of the amino-tagged MOF, **NiBDP_NH_2**, the confirmation of the presence of amino groups can be obtained by observing the signals in the high frequency region where the primary aromatic amino group displays two absorptions, one at 3520-3420 cm^{-1} and the other one at 3420-3340 cm^{-1} assigned to the asymmetric and symmetric N-H stretching modes. In the **NiBDP_NH_2** spectrum these two absorptions bands are present at 3436 and 3355 cm^{-1} for the asymmetric and the symmetric modes respectively (see inset enlargement of Figure 7.5c). Is it also possible to distinguish another characteristic band at 1620

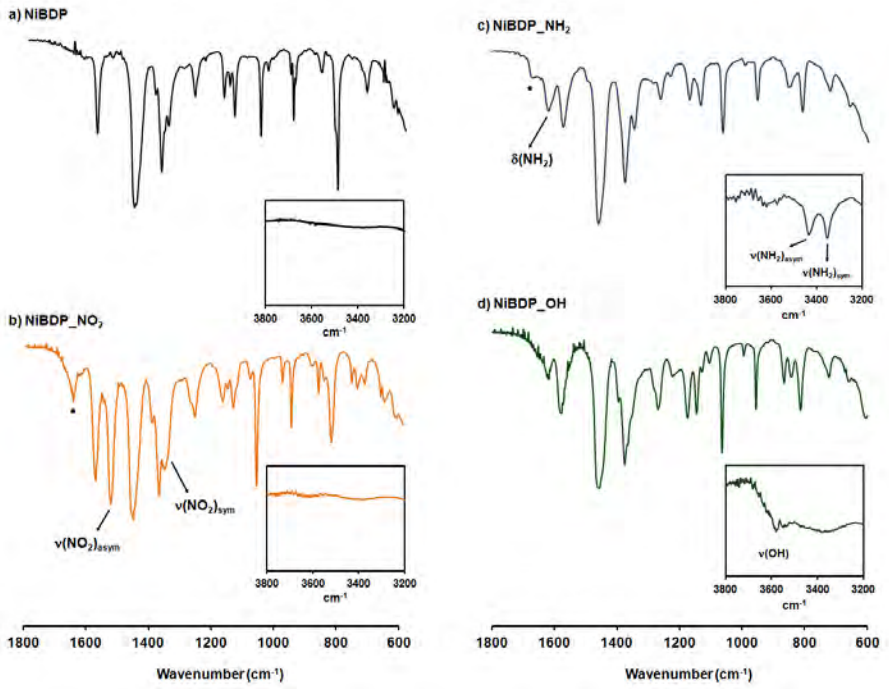

Figure 7.5. FTIR spectra of tagged NiBDP_X (X = H, NO_2, NH_2, OH) recorded as nujol mull. (a) NiBDP; (b) NiBDP_NO_2; (c) NiBDP_NH_2; (d) NiBDP_OH. • Denotes residual DMF.

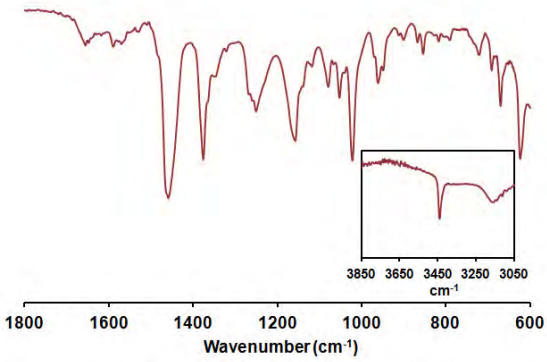

Figure 7.6. FTIR spectra of tagged **NiHBDP_SO_3** recorded as nujol mull. In the inset highlighted the IR region around 3500 cm^{-1} in which the two absorption bands of a partially desolvated material are visible.

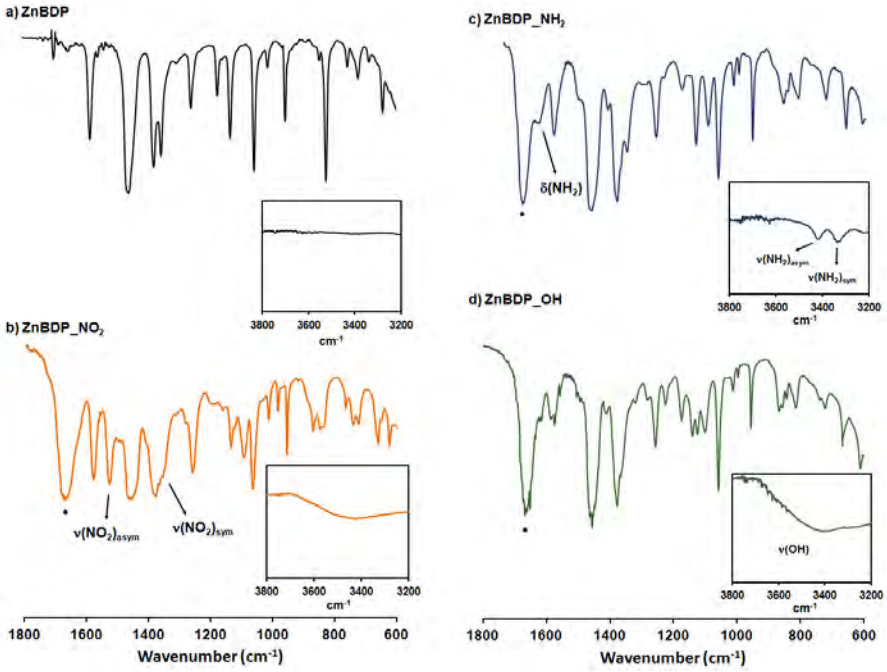

Figure 7.7. FTIR spectra of tagged ZnBDP_X (X = H, NO_2, NH_2, OH) recorded as nujol mull. (a) ZnBDP; (b) ZnBDP_NO_2; (c) ZnBDP_NH_2; (d) ZnBDP_OH. • Denotes residual DMF.

cm^{-1} related to the N-H bending vibration (scissoring) that is generally found at 1620-1518 cm^{-1}. Contrariwise, the strong C-N stretching absorption typical for aromatic amines is not found here due, again, to the presence of the nujol signals. These assignments were confirmed also by comparing them with the parent H_2BDP_NH_2 spectrum in which the N-H stretching modes are found at 3420 and 3340 cm^{-1} for asymmetric and symmetric stretching while the N-H vibration is found at 1624 cm^{-1} (see Chapter 3).

The IR spectrum of **NiBDP_OH** is also shown in Figure 7.5d. The region relevant for OH-stretching modes of hydroxyl groups shows a broad signal centered at 3400 cm^{-1} with a small sharpening at 3579 cm^{-1} assigned to the free

-OH groups on the aromatic linker. This broad band can be assigned to the formation of hydrogen bonding between the leftover chlatrated solvent molecules (either from moisture and synthesis process) and the hydroxyl groups. It is also very difficult to discriminate the CO stretching that should be found in the range 1200-1300 cm^{-1}.

Again, in the IR spectrum of the **NiHBDP_SO_3**, Figure 7.6, the presence of the introduced functional group can be confirmed by the strong IR absorption bands characteristic of sulfonic acid groups: the SO asymmetric stretching vibration, [**ν(**$SO)_{asym}$], is found at 1250 cm^{-1} as a medium band in the IR spectrum, while the symmetric stretching vibration, [**ν(**$SO)_{sym}$], appears around 1160 cm^{-1}. Moreover, the region relevant for N-H stretching modes shows two absorption bands, a sharp one at 3440 cm^{-1} and another one, of a broad shape, at 3150 cm^{-1}. This material is partially desolvated and this two absorption bands could be assigned to the presence of the N-H stretching vibration and the formation of hydrogen bonding between the proton of the N-H and the oxygen atom of the SO_3 group. To clarify and confirm, or not, the assignments of these two absorption bands, further structural studies on the desolvated material will be performed.

Thermal Stability. Thermogravimetric and differential scanning calorimetry analyses performed *simultaneously* on the two series of nickel(II) and zinc(II) framework demonstrated the high thermal stability of their pyrazolate bridged frameworks, even in the presence of substituents on the organic linkers (see Figure 7.8 and 7.9).

As reported by Lillerud et al. in his paper,[5g] the correlation between the thermal stability of tagged MOFs and both electronic and steric nature of the functional group introduced on the organic linkers, it is not of easy interpretation.

In pyrazolate-based tagged MOFs, the higher thermal stability has been observed for the amino-substituted ones, both in the case of nickel(II) and zinc(II)

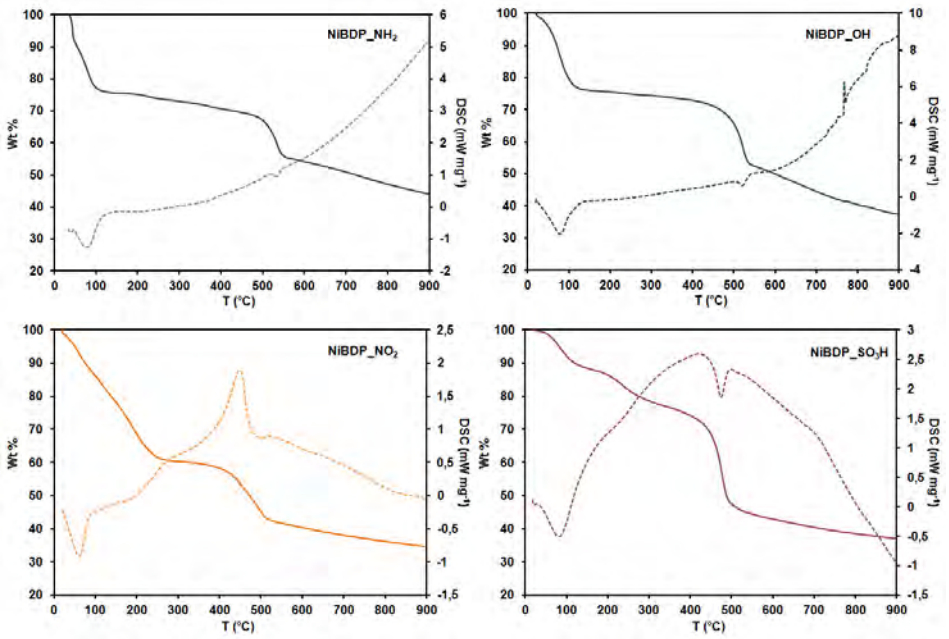

Figure 7.8. Simultaneous DSC (dotted line) and TGA (solid line) analyses for **NiBDP_NH_2** (blue); **NiBDP-NO_2** (orange); **NiBDP_OH** (green) and **NiBDP_SO_3H** (red).

frameworks (T_d *ca.* 470 °C). Moreover, while the rest of the ZnBDP_X series, undergo decomposition at rather similar temperature (T_d ca. 420 °C; similar to what observed for **ZnBDP**, see Chapter 4), the NiBDP_X series, displays decomposition temperatures in the NH_2 > H > OH > SO_3H > NO_2 order (T_d between 470 and 400 °C).

In the TG curves of the as-synthesized forms of all the MBDP_X (Figure 7.8 and 7.9), each weight loss step that occurs below the decomposition temperature of the frameworks can be assigned to the removal of the occluded guest molecules. The observed weight losses are indeed consistent with the calculated ones as well as the elemental analyses indicating phase purity of the compounds. Figure 7.8 shows a comparison between the DSC/TGA analysis performed on the nickel(II) species. In the **NiBDP_NO_2** TG curve, a solvent loss step (40 %, 2 methanol and two DMF molecules) from RT up

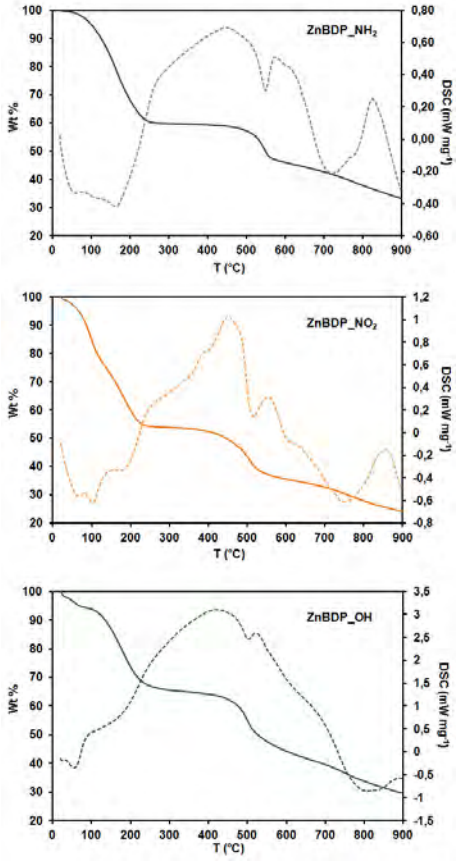

Figure 7.9. Simultaneous DSC (dotted line) and TGA (solid line) analyses for **ZnBDP_NH$_2$** (blue); **ZnBDP-NO$_2$** (orange) and **ZnBDP_OH** (green).

to 300 °C, is observed (with the corresponding DSC exothermic event), followed by a plateau of compositional stability up to 400 °C. Thermogravimetric traces of **NiBDP_NH$_2$** and **NiBDP_OH** show a weight loss of 28 % and 25 %, respectively, in the temperature range 30-200 °C, corresponding to evolution of guest solvent (1 methanol, 1 water and 1 DMF molecules corresponds to 30 % in **NiBDP_NH$_2$** while 1 methanol and 3 water molecules corresponds to 23 % in **NiBDP_OH**). Further heating prompts decomposition at 470 and 430 °C, for **NiBDP_NH$_2$** and **NiBDP_OH** respectively. In **NiBDP_SO$_3$H**, a gradual weight loss of 26 %, consistent with the evolution of 3 water and one DMF molecules from RT up to decomposition, is observed. These results are consistent with elemental analyses performed on the same batches (see Experimental Details).

The thermal behavior of the ZnBDP_X series is reported in Figure 7.9. The three frameworks show a similar behavior with a solvent loss step (**ZnBDP_NO$_2$**, 48 %, corresponds to 2 methanol, 5 water and 2 DMF molecules; **ZnBDP_NH$_2$**, 40 %, corresponds to 1methanol, 1 water and 2 DMF molecules; **ZnBDP_OH**, 38%, corresponds to 1 methanol and 2 DMF molecules) followed by a plateau up to decomposition

(T_d = 420 460, 420 °C, respectively), in agreement with the elemental analyses. Worthy of note, in the DSC curves only thermal events in correspondence with the evolution of solvents molecules or decomposition of the frameworks, are observed, as a further confirmation of the high stability of these frameworks.

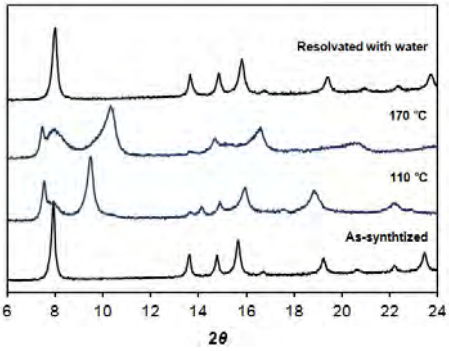

Figure 7.10. Powder X-ray diffraction patterns for (bottom to upper) as-synthesized **NiBDP_NH$_2$**, heated at 110 °C; heated at 170 °C and resolvated material obtained upon exposure to water.

Thermodiffractometric experiments (TXRPD) are still underway, but preliminary results are reported in the following. TXRPD analysis performed on on **NiBDP_NH$_2$** revealed that, upon fully desolvating the material by heating at 170 °C, the X-ray powder diffraction pattern indicated a complete and substantial change of structure (see Figure 7.10). Although the structure of the desolvated material could not be determined owing to the poor quality of the diffraction data, subsequent exposure to water regenerated the original **NiBDP_NH$_2$** framework. These observations are consistent with an accordion-type flexing behavior that closes and opens the channel pores, as previously observed in Long's CoBDP.[14] The thermodiffractometric measurement for **ZnBDP_OH** and **ZnBDP_NO$_2$** frameworks were performed in air on solvated derivatives of tetragonal symmetry. As expected, progressive heating causes a gradual peaks shift to higher 2θ angles, *i.e.* to smaller cell volumes, which is consistent with a progressive solvent loss promoted by the temperature raise (Figure 7.11). The materials are thermally robust: they starts losing crystallinity at 420 °C. Decomposition is basically complete at 510 °C.

Further studies are planned in order to investigate the thermal behavior of the remained materials of the MBDP-X series.

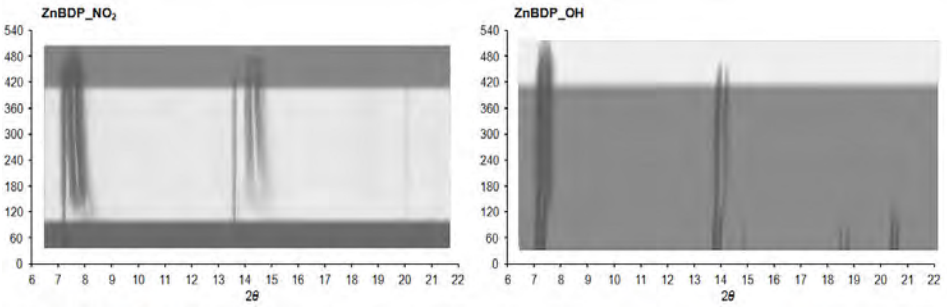

Figure 7.11. X-Ray Powder diffraction in temperature for ZnBDP_NO_2 (left) and ZnBDP_OH (right). Horizontal axis, 2θ deg.; vertical axis, temperature (°C). Highlighted the region up to 420 °C were the loss of crystallinity starts with decomposition.

Adsorption Properties. One of the areas of highest interest in the field of MOFs research is the potential application of their selective adsorptive properties for gas separation and purification purposes.[15] Particularly, the possible application of these systems in greenhouse gas capture processes is one of the most challenging research areas.[16] With this purpose and in order to examine the suitability of these materials for this application, we have carried out different studies for characterizing the porous features of the MBDP_X series. Thus, conventional single component adsorption isotherms, as well as, advanced experiments (pulse gas chromatography and breakthrough curve measurements) have been carried out.

Static adsorption experiments. To evaluate the porosity, N_2 adsorption/desorption isotherms at 77 K (see, Figure 7.12a and b) were collected and Langmuir surface areas were consequently calculated (Table 7.3). CO_2 isotherms at 273 K (Figure 7.13) were used to evaluate the micropore region by means of the Dubinin-Radushkevich equation (Table 7.3). All crystalline tagged MOF samples were found to retain porosity to both N_2 and CO_2 despite the presence of different functional groups on the linker.

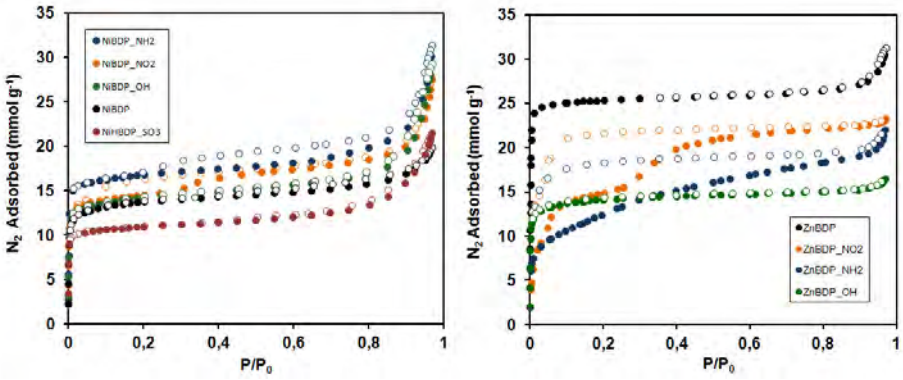

Figure 7.12. Left: N_2 adsorption isotherms measured at 77 K for **NiBDP_NH$_2$** (blue), **NiBDP_NO$_2$** (orange), **NiBDP_OH** (green), **NiBDP** (black) and **NiHBDP_SO$_3$** (red). Filled and empty symbols represent adsorption and desorption, respectively. Right: N_2 adsorption isotherms measured at 77 K for **ZnBDP_NH$_2$** (blue), **ZnBDP_NO$_2$** (orange), **ZnBDP_OH** (green) and **ZnBDP** (black). Filled and empty symbols represent adsorption and desorption, respectively.

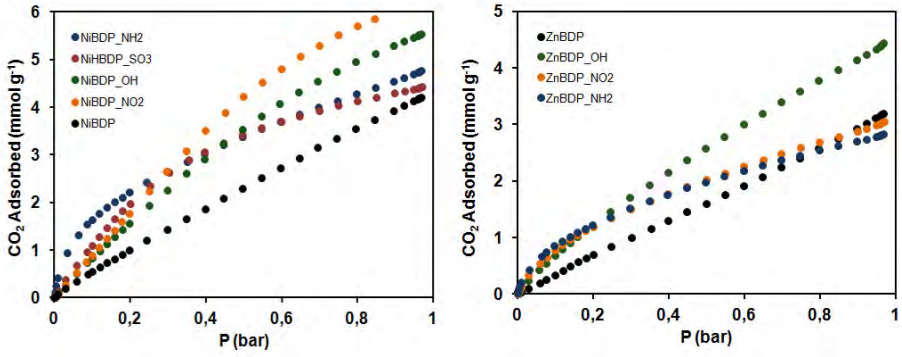

Figure 7.13. CO_2 adsorption isotherms measured at 273 K for MBDP_X (M= Ni, Zn, X= H, NH_2, NO_2, OH, SO_3H) systems. MBDP_NH_2 (blue), MBDP_NO_2 (orange), MBDP_OH (green), MBDP (black) and MHBDP_SO_3 (red).

	$SA_{BET}/m^2 g^{-1}$	$SA_{Langmuir}/m^2 g^{-1}$	$SA_{DR}/m^2 g^{-1}$
NiBDP	1066 (18)	1350 (9)	1480
NiBDP_NO_2	1131 (17)	1423 (9)	2350
NiBDP_NH_2	1305 (22)	1645 (8)	990
NiBDP_OH	1103 (18)	1394 (10)	1980
NiHBDP_SO_3	819 (16)	1044 (6)	1220
ZnBDP	2288 (41)	2857 (2)	1220
ZnBDP_NO_2	1875 (52)	2358(5)	730
ZnBDP_NH_2	1345(21)	1788(78)	600
ZnBDP_OH	1170 (22)	1484 (7)	1420

Table 7.3. Langmuir, BET (N_2, 77K) and Dubinin-Radushkevich (CO_2, 273 K) surface areas for the two series of **NiBDP_X** and **ZnBDP_X** (X = H, NO_2, NH_2, OH, SO_3H) as-synthesized and desolvated under reduced pressure at 180 °C for 12 hours.

For N_2 isotherms, the Langmuir surface areas data were found to range between 1044 to 1645 m^2/g and 1484 to 2860 for NiBDP_X and ZnBDP_X, respectively. The observed surface areas for the tagged nickel(II) materials follow the order NiBDP_NH_2 > NiBDP_NO_2 > NiBDP_OH > NiBDP > NiHBDP_SO_3 while, for the zinc(II) series, this order have been found to be different, and equal to ZnBDP > ZnBDP_NO_2 > ZnBDP_NH_2 > ZnBDP_OH. The decreases in surface areas for tagged zinc(II) frameworks, compared to the parent ZnBDP structure are largely attributed to both reduced free space available and increased overall weight of the new MOFs as a result of introducing the substituents on the organic linker. However, the **ZnBDP_NO_2** framework shows, within the tagged ones, the highest surface area, concomitant to the presence of an hysteretic loop. This is also observed in the isotherm of the amino-tagged MOF, although to a lesser extent. Indeed, the **ZnBDP_OH** framework shows the lowest N_2 uptake, with a classical type I isotherm. For flexible-type MOFs with hydroxyl groups decorating the pores walls, the formation of intraframework interactions, can be envisaged, to

explain the low uptake.[5e] Again, the N_2 isotherm with an hysteresis loop has been previously observed in Long's CoBDP.[14] As already pointed out, **ZnBDP** and CoBDP are isostructural species. Nevertheless, while the cobalt(II) derivative showed a certain degree of flexibility, the parent ZnBDP framework behaved only as a rigid framework (see Chapter 4). Indeed, further studies will be planned to investigate the possibility of a flexible-type behavior in the tagged ZnBDP_X frameworks.

CO_2 isotherms at 273 K were also collected in order to investigate the adsorption properties of each tagged framework with respect to this gas of environmental significance.[17] Indeed, the results show that the introduction of tags in the BDP linkers give rise to a general increase of the steep of the adsorption isotherm in the low pressure region, which can be attributed to a narrowing of the pore size with a concomitant increase of adsorbate-adsorbent interaction (Figure 7.13). This fact is particularly evident in the case of NH_2 substituents. However, in this case the formation of H-bonding interactions with quadrupolar CO_2 molecules should be claimed for the enhancement of adsorption energy.[18]

Pulse gas chromatographic studies

To assess the possible application of these materials on gas purification processes a chromatographic column has been constructed and packed with each tagged MOF. The samples were first pelletized in order to avoid pressure drops over the column. Afterward it has been studied the adsorption selectivity of the materials by injecting a complex gas mixture (1 mL), composed of equimolecular amounts of C_2H_2, H_2, CH_4, CO_2, on an inert He flow (15 mL min^{-1}) as carrier gas. In order to quantify the strength of the interaction of these guest molecules with the tagged materials, their zero-coverage adsorption heats (ΔH_{ads}) from the variation of the retention volumes (V_g) as a function of temperature, according to the Claisius-Clapeiron type equation $\Delta H_{ads} = -R\delta(\ln V_g)/\delta(1/T)$,[10] have been calculated. The direct relation between the retention volume (V_g) and Henry constants (K_H) also permits to calculate the Henry constant values at ambient condi-

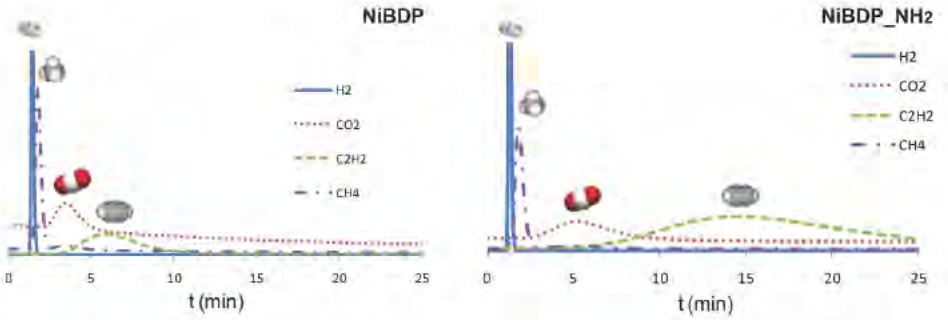

Figure 7.14. Pulse gas chromatograms for an equimolecular mixture of C_2H_2, H_2, CH_4, CO_2. For the sake of simplicity, these curves are reported only for NiBDP and NiBDP_NH_2.

Table 7.4a. Isosteric heat, Henry constant and adsorption selectivity for NiBDP_X systems obtained from pulse gas chromatographic studies.

Adsorbate (A)	Qst(KJmol^{-1})	K_H(cm^{3}m^{-2})*	Partition coefficient $\alpha_{/CH4/A}$*	Partition coefficient $\alpha_{CO2/A}$*	Partition coefficient $\alpha_{C2H2/A}$*	Partition coefficient $\alpha_{H2O/A}$*
NiBDP						
C_2H_2	-25	0.098	0.072	0.74	1	54
CO_2	-20	0.052	0.097	1	1.35	101
CH_4	-	0.005	1	10	13.8	1000
H_2O	-42.49	5.294	0.001	0.01	0.018	1
NiBDP_NH_2						
C_2H_2	-32.55	0.267	0,02	0,35	1	38
CO_2	-27.8	0.089	0,056	1	2.8	115
CH_4	-	0.005	1	17.85	50	2052
H_2O	-51	10.265	0.0005	0.009	0.026	1
NiBDP_NO_2						
C_2H_2	-23.32	0.062	0,09	0,81	1	-
CO_2	-24.74	0.122	0,12	1	1,23	-
CH_4	-	0.005	1	8,13	10	-
H_2O	-	-	-	-	-	-
NiBDP_OH						
C_2H_2	-26.16	0.194	0,26	0,77	1	-
CO_2	-21.30	0.068	0,33	1	1,29	-
CH_4	-	0.005	1	3,6	4,66	-
H_2O	-	-	-	-	-	-

*Calculated from the relation of KH at 298 K

Table 7.4b. Isosteric heat, Henry constant and adsorption selectivity for ZnBDP_X systems obtained from pulse gas chromatographic studies.

Adsorbate (A)	Qst(KJmol^{-1})	K_H(cm^{3}m^{-2})*	Partition coefficient $\alpha_{i/CH4/A}$*	Partition coefficient $\alpha_{CO2/A}$*	Partition coefficient $\alpha_{C2H2/A}$*	Partition coefficient $\alpha_{H2O/A}$*
ZnBDP						
C_2H_2	20.16	0.015	0,85	1,02	1	-
CO_2	19.66	0.009	0,84	1	0,98	-
CH_4	-	0.005	1	2,39	2,35	-
H_2O	-	-	-	-	-	-
ZnBDP_NH_2						
C_2H_2	20.16	0.015	0,11	0,89	1	-
CO_2	19.66	0.009	0,13	1	1,13	-
CH_4	-	0.005	1	16,6	18,7	-
H_2O	-	-	-	-	-	-
ZnBDP_NO_2						
C_2H_2	20.16	0.015	0,31	0,90	1	-
CO_2	19.66	0.009	0,35	1	1,11	-
CH_4	-	0.005	1	5,74	6,39	-
H_2O	-	-	-	-	-	-
ZnBDP_OH						
C_2H_2	20.16	0.015	0,18	0,34	1	-
CO_2	19.66	0.009	0,54	1	2,9	-
CH_4	-	0.005	1	12,1	35,7	-
H_2O	-	-	-	-	-	-

*Calculated from the relation of KH at 298 K

tions (298 K) (see Table 7.4). The results on the NiBDP series show that retention volumes follow the trend H_2O >> C_2H_2 > CO_2 >> CH_4 > H_2 (see Figure 7.14, water is not shown since it has been measured separately). The interaction of H_2 with the frameworks is almost negligible and consequently it has been taken as reference value for the column dead volume.

Noteworthy, the introduction of polar tags in the framework is responsible for an enhancement of the interaction with polar adsorbates (higher adsorption energies), and a concomitant increase in the partition coefficient between apolar (CH_4) and polar (CO_2, C_2H_2) adsorbates (Table 7.4). However, the adsorption selectivity (partition coefficients) between CO_2/C_2H_2 is not significantly increased

upon functionalization, which should be attributed to the closely related nature of these two types of adsorbates (quadrupole moments, similar size and similar physical properties).

From these results it can be concluded that the tagged materials are adequate for gas purification purposes; particularly for the removal of small impurities of polar gases and vapors (e.g. moisture, CO_2, C_2H_2)

N_2/CO_2 breakthrough experiments. In the case of bulk separation of gases, breakthrough experiments are the adequate experiments in order to assess the gas separation performances of the new materials. Thus, gas mixture adsorption breakthrough experiments were measured on columns packed with each tagged MOF. As for the above experiments, the samples were first pelletized to avoid pressure drops over the column and the desired gas mixture was flowed through the material.

On the non-functionalized NiBDP system, a preliminary breakthrough experiment with a complex gas mixture of $CH_4/CO_2/C_2H_2$, has been performed to assess, qualitatively, the interaction of the framework with these gases. As expected, the results show that CH_4 is not retained in the column in the essayed temperature range (273-323 K). The higher interaction of the materials takes place with quadrupolar CO_2 and C_2H_2 gases which are efficiently retained in the essayed experimental conditions (see Figure 7.15). For both gases the interaction is similarly strong and consequently in $CH_4/CO_2/C_2H_2$ mixtures both CO_2 and C_2H_2 are jointly retained, although there is a higher retention of C_2H_2.

Later on, a simpler experiment was carried out on the whole series of tagged MBDP_X in order to simulate an emission flue gas from a power plant employing a 1.4 mL min^{-1} of CO_2 and 8.6 mL min^{-1} of N_2 flows. Indeed, the breakthrough experiments were carried out by step changes from He to CO_2/N_2 flow mixtures. Again, the results show that N_2 is not retained in the column, while the higher interaction takes place with quadrupolar CO_2in the essayed temperature range (273-323 K). Framework functionalization also plays

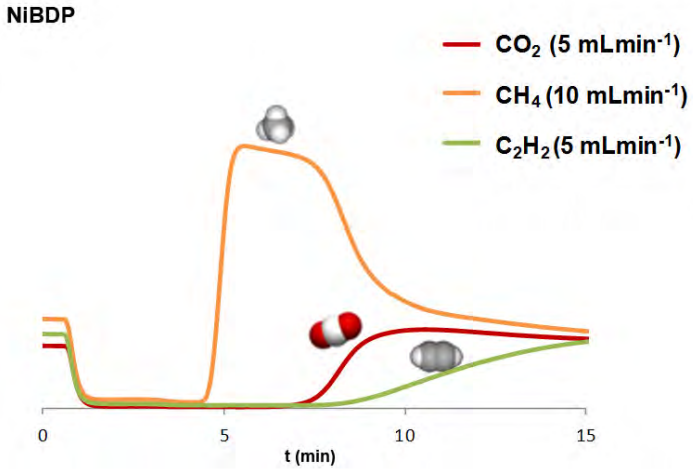

Figure 7.15. $CH_4/CO_2/C_2H_2$ separation breakthrough experiments performed on NiBDP at 273 K.

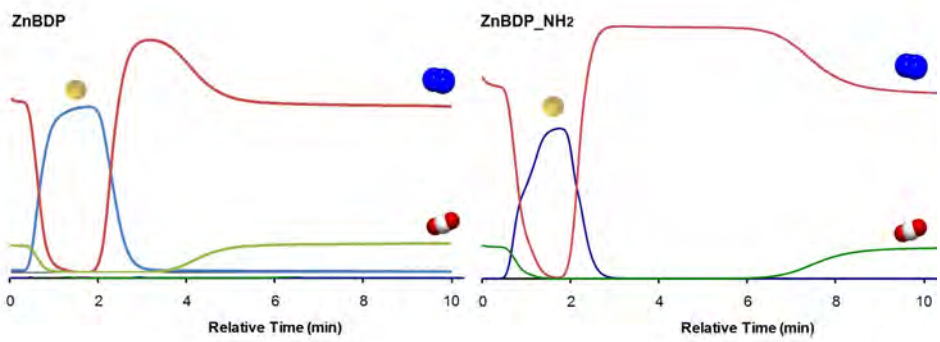

Figure 7.16. N_2/CO_2 separation breakthrough experiments at 273 K showing the effect of tag nature on the ZnBDP_X. Breakthrough curves for other tagged frameworks are reported in Appendix 1.

Table 7.5. Amount of CO_2 (mmol) retained in dynamic conditions from CO_2/N_2 breakthrough experiments at different temperatures in the MBDP_X systems.

MOFs	273 K	298 K	323 K
ZnBDP	0,34	-	-
ZnBDP_NO_2	0,63	0,27	0,16
ZnBDP_NH_2	1,02	0,57	0,28
ZnBDP_OH	0,50	0,20	0,15
NiBDP	0,69	0,32*	0,17
NiBDP_NO_2	1,07	0,38	0,24
NiBDP_NH_2	1,34	0,54	0,32
NiBDP_OH	0,89	0,35*	0,23
NiBDP_SO_3H	1,04	-	-

*Calculated at 303 K

an important role in this separation, thus, according to the CO_2 adsorption isotherms collected at 273K, the highest interaction has been achieved for the MBDP_NH_2 systems (See Table 7.5 and Figure 7.16). Noteworthy, the retention of CO_2 at 323 K, which is the typical conditions of flue gas emission from a fossil fuel power plant, are 0.28 mmol g^{-1} and 0.32 mmol g^{-1} for **ZnBDP_NH_2** and **NiBDP_NH_2**, respectively.

Conclusions

A systematic study, in oreder to investigate and understand the effect of (pre-synthesis) ligand functionalization in the gas adsorption and separation processes on two large series of isostructural metal-organic frameworks, has been carried out. Indeed, two large families of isoreticular MOFs, based on poly-pyrazolate ligands bearing NO_2, NH_2, OH and SO_3H functional groups, have been obtained. The results presented in this chapter are, however, preliminary, even though it has been demonstrated that the incorporation of func-

tional groups, in the parent NiBDP and ZnBDP frameworks, is possible without compromising their stability. Moreover, these studies demonstrate that the adsorption of quadrupolar gases, such as CO_2 and C_2H_2, is primary affected by the chemical properties of the framework. Indeed, upon functionalization, the modified compounds show greatly enhanced CO_2 and C_2H_2 uptakes compared to the non-functionalized ones, with the MBDP_NH_2 tagged MOFs as the best performing materials.

Ongoing experimental efforts as well as future efforts planned for a complete exploring of the properties of these MOFs, will hopefully shed some more light on their (possibly) flexible behavior as well as in respect to their future applications.

Acknowledgements

Support by the EU (NanoMOF-228604) is acknowledged.

References and Notes

1 (a) Themed issue on metal-organic frameworks: *Chem. Soc. Rev.* **2009**, *38*, 1201. (b) Kitagawa, S.; Kitaura, R.; Noro, S.-I. *Angew. Chem., Int. Ed.* **2004**, *43*, 2334. (c) Hamon, L.; Llewellyn, P. L.; Devic, T.; Ghoufi, A.; Clet, G.; Guillerm, V.; Pirngruber, G. D.; Maurin, G.; Serre, C.; Driver, G.; van Beek, W.; Jolimaitre, E.; Vimont, A.; Daturi, M.; Férey, G. *J. Am. Chem. Soc.* **2009**, *131*, 17490. (d) Taylor-Pashow, K. M. L.; Della Rocca, J.; Xie, Z. G.; Tran, S.; Lin, W. B. *J. Am. Chem. Soc.* **2009**, *131*, 14261. (e) Horcajada,

P.; Chalati, T.; Serre, C.; Gillet, B.; Sebrie, C.; Baati, T.; Eubank, J. F.; Heurtaux, D.; Clayette, P.; Kreuz, C.; Chang, J. S.; Hwang, Y. K.; Marsaud, V.; Bories, Y.-N.; Cynober, L.; Gil, S.; Férey, G.; Couvreur, P.; Gref, R. *Nat. Mater.* **2010**, *9*, 172. (f) Liu, Y.; Kravtsov, V. C.; Larsen, R.; Eddaoudi, M. *Chem. Commun.* **2006**, 1488. (g) Wiers, B. M.; Foo, M.-L.; Balsara, N. P.; Long, J. R. *J. Am. Chem. Soc.* **2011**, *133*, 14522 (h) Bloch, E. D.; Murray, L. M.; Queen, W. L.; Chavan, S.; Maximoff, S. N.; Bigi, J. P.; Krishna, R.; Peterson, V. K.; Grandjean, F.; Long, G. J.; Smit, B.; Bordiga, S.; Brown, C. M.; Long, J. R. *J. Am. Chem. Soc.* **2011**, *133*, 14814.

2 (a) O'Keeffe, M.; Eddaoudi, M.; Li, H.; Reineke, T. M.; Yaghi, O. M. *J. Solid State Chem.* **2000**, *152*, 3. (b) Yaghi, O. M.; O'Keeffe, M.; Ockwig, N. W.; Chae, H. K.; Eddaoudi, M.; Kim, J. *Nature* **2003**, *423*, 705. (c) Ohrstrom, L.; Larsson, K. *Molecular Based Materials: The Structural Network Approach*; Elsevier: Amsterdam, **2005**.

3 Férey, G. *Chem. Soc. Rev.* **2008**, *37*, 191.

4 (a) O'Keeffe, M. and Yaghi, O. M. Chem. Rev. **2012**, DOI: 10.1021/cr200205j and references therein.

5 (a) Braun, M. E.; Steffek, C. D.; Kim, J.; Rasmussen, P. G.; Yaghi, O. M. *Chem. Comm.* **2001**, 2532. (b) Akiyama, G.; Matsuda, R.; Sato, H.; Takata, M.; Kitagawa, S. *Adv. Mater.* **2011**, *23*, 3294. (c) Horike, S.; Bureekaew, S.; Kitagawa, S. *Chem. Comm.* **2008**, 471. (d) Zhao, Y.; Wu, H.; Emge, T. J.; Gong, Q.; Nijem, N.; Chabal, Y. J.; Kong, L.; Langreth, D. C.; Liu, H.; Zeng, H.; Li, J. *Chem. Eur. J.* **2011**, *17*, 5101. (e) Biswas, S.; Ahnfeldt, T.; Stock N. *Inorg. Chem.* **2011**, *50*, 9518. (f) Horcajada, P.; Salles, F.; Wuttke, S.; Devic, T.; Heurtaux, D.; Maurin, G.; Vimont, A.; Daturi, M.; David, O.; Magnier, E.; Stock, N.; Filinchuk, Y.; Popov, D.; Riekel, C.; Férey, G.; Serre, C. *J. Am. Chem. Soc.* **2011**, *133*, 17839. (g) Kandiah, M.; Nilsen, M. H.; Usseglio, S.; Jakobsen, S.; Olsbye, J.; Tilset, M.; Larabi, C.; Quadrelli, E. A.; Bonino, F.; Lillerud, K. P. *Chem. Mater.* **2010**, *22*, 6632.

6 (a) Li, H.; Eddaoudi, M.; O'Keeffe, M.; Yaghi, O. M. *Nature* **1999**, *402*, 276. (b) Eddaoudi, M.; Kim, J.; Rosi, N.; Vodak, D.; Wachter, J.; O'Keeffe, M.; Yaghi, O. M. *Science*

2002, *295*, 469. (c) Yaghi, O. M.; Eddaoudi, M.; Li, H.; Kim, J.; Rosi, N. U.S. *Patent Application* **2003**/ 0004364. (d) Rosi, N. L.; Eckert, J.; Eddaoudi, M.; Vodak, D. T.; Kim, J.; O'Keeffe, M.; Yaghi, O. M. *Science* **2003**, *300*, 1127.

7 (a) Galli, S.; Masciocchi, N.; Colombo, V.; Maspero, A.; Palmisano, G.; Lopez-Garzon, F. J.; Domingo-Garcia, M.; Fernandez-Morales, I.; Barea, E.; Navarro, J. A. R. *Chem. Mater.* **2010**, *22*, 1664. (b) Masciocchi, N.; Galli, S.; Colombo, V.; Maspero, A.; Palmisano, G.; Seyyedi, B.; Lamberti, C.; Bordiga, S. *J. Am. Chem. Soc.*, **2010**, *132*, 7902. (c) Quartapelle-Procopio, E.; Liñares, F.; Montoro, C.; Colombo, V.; Maspero, A.; Barea, E.; Navarro, J. A. R. *Angew. Chem., Int. Ed.* **2010**, *49*, 7308. (d) Colombo, V.; Galli, S.; Choi, H. J.; Han, G. D.; Maspero, A.; Palmisano, G.; Masciocchi, N.; Long, J. R. *Chem. Sci.* **2011**, *2*, 1311.

8 (a) Lozan, V.; Solntsev, P. Y.; Leibeling, G.; Domasevitch, K. V.; Kersting, B. *Eur. J. Inorg. Chem.* **2007**, *20*, 3217. (b) Maspero, A.; Galli, S.; Masciocchi, N.; Palmisano, G. *Chem. Lett.* **2008**, 37, 956.

9 Version 3.0, Bruker AXS, 2005, Karlsruhe, Germany.

10 Diaz, E.; Ordoñez, S.; Vega, A. *J. Colloid Interf. Sci*. **2007**, *305*, 7-16.

11 Galli, S.; Masciocchi, N.; Colombo, V.; Maspero, A.; Palmisano, G.; López-Garzón, F. J.; Domingo-García, M.; Fernández-Morales, I.; Barea, E.; Navarro, J. A. R. Chem. Mater. 2010, 22, 1664.

12 At the same time the Long's group published another synthetic procedure for the same material where they were reacting $Zn(CF_3SO_3)_2$ and the ligand in N-N,diethylformamide in a boron silicate tube for 5 days at 150 °C. See Choi, H. J.; Dincă, M.; Dailly, A.; Long, J. R. *Energy Environ. Sci.* **2010**, *3*, 117.

13 (a) Colthup, N. B.; Daly, L. H.; Wiberly, S. E. *Introduction to IR and Raman spectroscopy*, Academic Press, New York, **1975**. (b) Larkin, P. *Infrared and Raman Spectroscopy; Principles and Spectral Interpretation*, Elsevier **2011**, ISBN 978-0-12-386984-5.

14 (a) Choi, H. J.; Dincă, M.; Long, J. R. *J. Am. Chem. Soc.* **2008**, *130*, 7848. (b) Salles, F.; Maurin, G.; Serre, C.; Llewellyn, P. L.; Knofel, C.; Choi, H. J.; Filinchuk, Y.; Oliviero, L.; Vimont, A.; Long, J. R.; Ferey, G. *J. Am. Chem. Soc.* **2010**, *132*, 13782.

15 Barea, E.; Turra, F.; Navarro, J. A. R. *Gas separation and Purification by MOFs* (in Metal-Organic Frameworks: Applications from Catalysis to Gas Storage; D. Farruseng (Ed.)) Wiley-VCH, **2011**.

16 Li, J.-R.; Ma, Y.; McCarthy, M. C.; Sculley, J.; Yu, J.; Jeong, H.-K.; Balbuena, P. B.; Zhou, H.-C. *Coord. Chem. Rev.* **2011**, *255*, 1791.

17 D'Alessandro, D. M.; Smit, B.; Long, J. R. *Angew. Chem., Int. Ed.* **2010**, *49*, 6058.

18 Arstad, B.; Fjellvåg, H.; Kongshaug, K. O.; Swang, O.; Blom, R. *Adsorption*, **2008**, 14, 755.

Chapter 8
Cation exchange porosity tuning in anionic metal-organic frameworks

Introduction

The outperforming adsorptive properties of the so called open metal-organic frameworks rely on their fully accessible porous structure and the easy tuning of the shape, size and chemical nature of their pores.[1,2,3] The synthesis of MOFs has presently reached a stage were tunable organic functionalities are being introduced into large zeolite-like cavities having high structural robustness and high stability against moisture.[4] It has also been realized that these systems have, in some instances, the ability to mimic the structures and properties of zeolites.[5,6]

For example, by exploiting the well known similarity in coordination geometries between tetrahedral metal imidazolates and aluminosilicates, Yaghi *et al.* have produced the so called zeolitic-imidazolate frameworks (ZIFs) series, already described in Chapter 1. However, while the structural networks are comparable, ZIFs materials posses only neutral frameworks, in contrast with the anionic ones generally observed in zeolites.[7]

A newly introduced class of porous materials, called zeolite-like metal-organic frameworks (ZMOFs), is based on anionic frameworks. In these materials, the negatively charged frameworks are charge-compensated by extra-framework

cations inside the cavities, much alike zeolites materials. As an example, Eddaoudi *et al.* reported two novel porous anionic zeolite-like metal-organic frameworks based on the hetero-functional molecule 4,5-imidazoledicaboxylic acid as a bridging linker and indium(III) as a metal ion source, synthesized in the presence of a structure-directing agent.[8] This class of materials has the advantage of possessing these tunable extra-framework cations that are exploitable as strong sorption sites for a tagged guest. Moreover, these cationc sites are exchangeable through ion-exchange procedures by other ions source (as e.g. alkali metals), as generally done with zeolites-type materials.

As a matter of fact, zeolite-like metal-organic frameworks have been adopted for H_2 adsorption studies, by exploiting the exchangeable nature of the framework, *i.e.* the features of the cationic extraframework, *vs* the adsorption properties,[9] even though affording such type of materials is not of easy obtaining and only few examples are found in the literature.[10] Indeed, in contrast to the well known cation exchange features of zeolites, the zeomimetic coordination polymers generally possess neutral or cationic frameworks and consequently do not usually give rise to cation exchange processes.[11]

As already discussed along this thesis, there are unsolved problems related to the general lower thermal and chemical stability (hydrolysis sensitive nature) of MOF compared to their zeolite counterparts.[12] In this regard, the robustness of the metal-nitrogen(heterocycle) coordinative bonds gives rise to MOF materials with enhanced chemical and thermal stabilities.[4b-13] Here, by exploiting the reactivity of copper(II) metal ions towards the hetero-functional ligand 1,4-carboxypyrazole (H_2cpz, Figure 8.1a), a new zeolite-like metal organic framework of formula $NH_4[Cu_3(\mu_3\text{-}OH)(\mu_3\text{-}4\text{-carboxypyrazolato})_3]$ (**NH_4@1**, Figure 8.1), has been obtained. In this chapter, the synthesis, structural characterization, thermal/chemical stability, adsorptive and separation properties of this new anionic metal organic framework, are reported. In addition, the plausible modulation

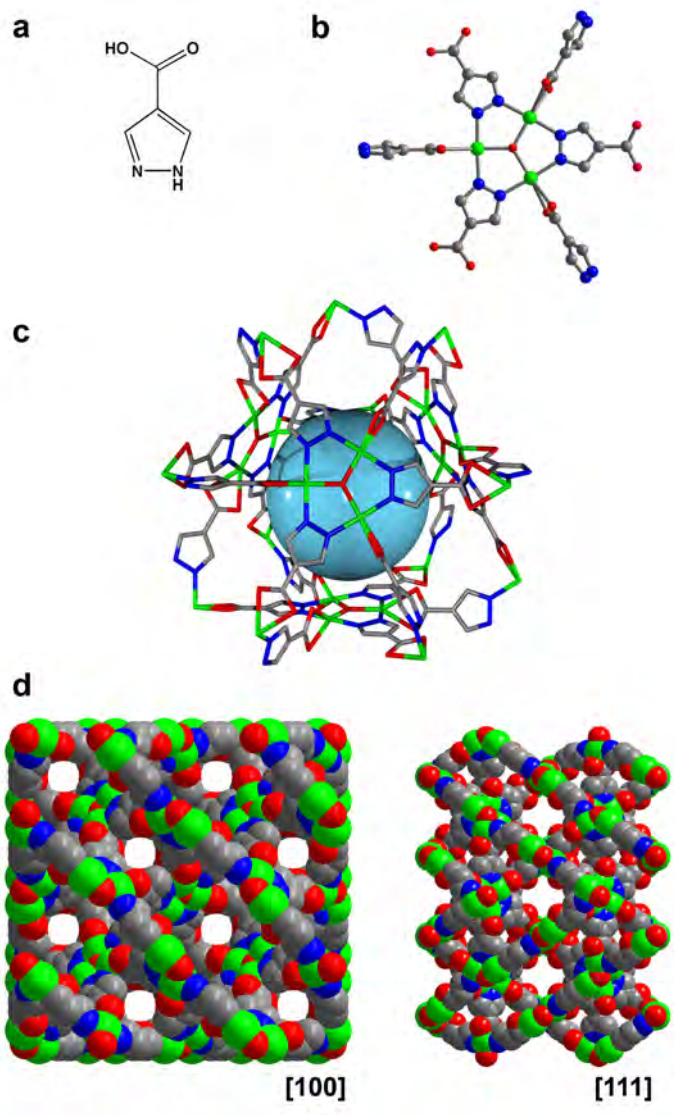

Figure 8.1. (a) The 1,4-carboxypyrazole, H_2cpz, linker. (b) Trinuclear Cu(μ_3-OH) clusters of formula $[Cu_3(\mu_3\text{-OH})(cpz)_6]^-$, (c) View of the tetrahedral cages found in the crystal structure of $NH_4[Cu_3(\mu_3\text{-OH})(\mu_3\text{-4-carboxypyrazolato})_3]$ (**NH_4@1**). The blue sphere indicates the size of the inner void. (d) Space filling view along the crystallographic [100] and [111] directions. Cu, green; N, blue, O, red; C, grey.

of its porous network by means of ion exchange processes of the extraframework cations, has been examined. Therefore, this new type of framework has been regarded as an excellent platform for systematic studies of the effect of various structural factors on targeted guests interaction (*vide infra*) with the porous metal-organic material. Indeed, the results show that the ion exchange processes on these systems lead to profound changes on the textural properties of their porous surface and on the adsorption selectivity on different separation processes of gases and vapors.

Experimental details

4-carboxypyrazole was obtained according to a previously reported method.[14] Other materials were obtained from commercial suppliers and used without further purification. IR absorption spectroscopy were done on a Midac FT-IR with KBr pellets. Thermogravimetric and differential calorimetric analyses were performed, under air atmosphere, on a Shimadzu-TGA-50H/DSC equipments, at heating rate of 20 °C min^{-1}. XRPD experiments were done on a Philips PW100 diffractometer using Cu-Kα radiation (λ = 1.5418 Å).

Synthesis of $NH_4[Cu_3(\mu_3\text{-}OH)(\mu_3\text{-}4\text{-carboxypyrazolate})_3]$. 4-carboxypyrazole (2 mmol) was added to a previously prepared aqueous ammonia solution (NH_3:H_2O 1:15, 30 mL). Later on, 2 mmol of $Cu(NO_3)_2$ were added to this solution, under stirring. A deep blue clear mixture is formed. After three days, dark blue crystals of **NH_4@1**, suitable for X-ray diffraction experiments, were obtained from this solution. Anal. calc. for $NH_4[Cu_3(OH)(C_4H_2N_2O_2)_3]\cdot 15\ H_2O$: C, 17.45; H, 5.00; N, 11.87. Found. C, 17.06; H, 4.51; N, 12.13.

Crystal data of NH_4@1. $NH_4[Cu_3(OH)(C_4H_2N_2O_2)_3]\cdot 8H_2O$, M = 700.02, cubic, space group *Fd-3c*, a = 30.1955(9) Å, V = 27531(1) $Å^3$, Z = 32, ρ = 1.351 g cm^{-3}, T = 293 K, λ Mo-Kα = 0.71073 Å, R_{int} = 0.0617, R(F, $F^2 > 2\sigma$) = 0.0841, $R_w(F^2$, all data) = 0.242 for 1429 unique reflections, goodness-of-fit = 1.099.

Thermodiffractometric Studies. Variable-temperature X-ray powder diffraction experiments were performed on **NH_4@1** to highlight its "structural" response. These experiments were carried out in air by employing a custom-made sample heater, mounted on a Philips PW100 diffractometer equipped with a Cu-Kα (λ = 1.5418 Å) radiation. The compounds were manually grounded in an agate mortar, then deposited in the hollow of an aluminum sample holder. The thermodiffractometric experiments were planned on the basis of the TGA/DSC results and a sequence of scans, in a significant low-angle 2ϑ range (4-15°), was performed at 10 °C *per* step, heating *in situ* from room temperature up to 200 °C and subsequently down to room temperature (Figure 8.2b).

Gas adsorption measurements. Gas sorption isotherms for pressures in the range of 0-1.2 bar were measured by the volumetric method using a Micromeritics Tristar 3000 analyzer (Micrometrics Instruments Corp., Norcross, GA) and the following procedure. A sample of ca. 100 mg of as-synthesized compound was transferred to a pre-weighed analysis tube (0.5-inch diameter, 10 cm^3 bulb), which was capped with a gas-tight transeal to prevent intrusion of oxygen and atmosphere moisture during transfer and weighing. The samples were evacuated under dynamic vacuum at 110 °C and outgassed to 10^{-6} mbar (7 h). In the case of **NH_4@1**, prior to activation, the single crystals obtained after synthesis were grounded for a few minutes in an agate mortar and subsequently suspended in a 3:1000 NH_3:H_20 solution and stirred for 8 hours. The analysis tube containing the desolvated sample was then carefully transferred to an electronic balance and weighed again to determine the mass of the sample. It was then transferred back to the analysis port of the gas sorption instrument. For all isotherms, warm and cold free space correction measurements were performed using ultra high purity He gas (UHP grade 5.0, 99.999% purity); N_2 isotherms at 77 K were measured in a liquid nitrogen bath using UHP-grade gas sources.

Ion exchange procedure. The procedure for performing ion exchange in **NH_4@1** is here described: 100 mg of the **NH_4@1** material were suspended in 12 mL of a 0.1 M aqueous solution of the corresponding inorganic salt: $LiNO_3$, KNO_3, $Ca(NO_3)_2$. Contrariwise, the **Me_3NH@1** and **Et_3NH@1** exchanged materials were obtained by suspending 100 mg of **NH_4@1** in a 0.5 M methanolic solution of the corresponding organic amine base. All the exchanged solids were subsequently filtered, washed with EtOH and Et_2O and suspended during 4 hours in distilled water in order to remove the eventual adsorbed ion pairs. Afterwards, the materials were filtered again and washed with EtOH. The effect of ion exchange on the materials was examined by means of elemental analysis, thermal analysis, infra-red spectroscopy (Figure 8.6), atomic absorption, N_2 adsorption (Figure 8.4) and X-ray powder diffraction experiments (Figure 8.5).

Anal. calc. for $[(CH_3)_3NH]_{0.5}(NH_4)_{0.5}[Cu_3(OH)(C_4H_2N_2O_2)_3][Cu(OH)_2]_{0.5}\cdot 6H_2O$: C, 21.56; H, 3.89; N, 13.04; Found. C, 21.50 H, 3.45 N, 12.60.

Anal. calc. for $[(CH_3CH_2)_3NH]_{0.5}(NH_4)_{0.5}[Cu_3(OH)(C_4H_2N_2O_2)_3][Cu(OH)_2]_{0.5}\cdot 7H_2O$: C, 23.31; H, 4.17; N, 12.67. Found. C, 23.10; H, 4.05; N, 12.80.

It should be noted that in the case of **Me_3NH@1** and **Et_3NH@1** materials a slight contamination with $Cu(OH)_2$ is appreciated on the elemental analysis.

Atomic absorption results for **A@1** materials: the following formulations have been obtained from atomic absorption analyses: $Li_{0.37}(NH_4)_{0.63}[Cu_3(\mu_3\text{-OH})(\mu_3\text{-4-carboxypyrazolato})_3]$, $K_{0.58}(NH_4)_{0.42}[Cu_3(\mu_3\text{-OH})(\mu_3\text{-4-carboxypyrazolato})_3]$ and $Ca_{0.5}[Cu_3(\mu_3\text{-OH})(\mu_3\text{-4-carboxypyrazolato})_3]$.

Effect of ion exchange on the adsorption selectivity of A@1 materials towards benzene/cyclohexane vapor mixtures. The **A@1** materials (50 mg) were activated at 110 °C under high vacuum for 7 h. Then, these activated samples were exposed to a saturated atmosphere of a 1:1 benzene/cyclohexane mixture in a schlenk tube during 24 h at 298 K. Afterwards, the increase of the weight

of the materials was measured and the composition of the adsorbed phase was checked by ^{1}H NMR (DMSO-d_6, 0.5 mL) (see Table 8.2).

Gas separation experiments: variable temperature pulse gas chromatography. Gas-phase adsorption at zero coverage surface was studied using the pulse chromatographic technique employing a Gas Chromatograph (Varian 450-GC) with a 10 cm-column (0.4 cm internal diameter) packed with *ca.* 0.75 g of the material in microcrystalline form. Prior to measurement, powder samples were heated at 110 °C for 7 h and outgassed to 10^{-6} mbar. Subsequently, the sample was conditioned in He flow (10 mL min^{-1}). Later on, 1 mL of an equimolecular gas mixture (C_2H_2, N_2, CH_4, CO_2) was injected at 1 bar and the separation performance of the chromatographic column was examined at different temperatures (273 K-363 K) by means of a mass spectrometer gas analysis system (Pfeiffer vacoon) detecting ion peaks at *m/z* 44 (CO_2), 28 (N_2), 26 (C_2H_2) and 16 (CH_4).

Gas separation experiments: breakthrough curves. The gas-separation properties of **NH_4@1** and **Et_3NH@1** were also examined by breakthrough experiments using CO_2:CH_4 gas mixtures (about 0.5:0.5 w/w; 0.27:0.73 v/v) flowed through the activated sample of **A@1** (~0.75 g) packed into a glass column (0.3 cm inner diameter ×10 cm length). Helium gas was initially purged into the sample column. The column was then cooled to 273 K using an ice bath and afterwards the gas mixture (100 kPa) was dosed into this column at a flow rate of 10 mL min^{-1}. The relative amounts of gases passing through the column were monitored on a mass spectrometer gas analysis system (Pfeiffer vacoon) detecting ion peaks at *m/z* 44 (CO_2) and 16 (CH_4).

Result and discussion

Synthesis and structure. The synthesis of $NH_4[Cu_3(\mu_3\text{-}OH)(\mu_3\text{-}4\text{-carboxypyrazolate})_3]$, **$NH_4$@1**, was performed in ammonia solution of $Cu(NO_3)_2$, allowing the deprotonation of the 4-carboxypyrazole ligand, at room temperature, with a concomitant slow precipitation of blue single crystals suitable for X-ray

diffraction analysis. Actually, the synthesis of MOFs are generally much simpler, with the solvent itself (in most cases DMF) acting as main template for the reaction. As described in Chapter 1, this synthetic strategy generates a neutral skeleton for most of the MOFs structures in the literature. Here, however, ammonia is an additional ingredient for this chemical reaction, besides the components of the MOF skeleton and the reaction solvent (H_2O). Thus, an anionic skeleton has been isolated where the negative charge is balanced by ammonium cations into the pores, similarly to what is generally observed in zeolite-types materials. The crystal structure of $NH_4[Cu_3(\mu_3\text{-}OH)(\mu_3\text{-}4\text{-carboxypyrazolato})_3]$ (**NH_4@1**) is indeed based on an anionic 3D porous framework built up by trinuclear $Cu(\mu_3\text{-}OH)$ clusters connected to another six ones through μ_3-4-carboxypyrazolato bridges (Figure 8.1b). In this way, tetrahedral cages with an inner diameter of *ca*. 13 Å are generated, which host two extraframework NH_4^+ cations and crystallization water molecules (Figure 8.1c). Calculations with Platon,[15] after removal of the hosted water molecules, give rise to a high potentially accessible empty volume, accounting to *ca*. 49 % of the unit cell volume. Moreover, these tetrahedral voids are connected each other through 4.5 Å and 8 Å wide windows along the [100] and [111] crystallographic directions, respectively, generating a 3D framework (Figure 8.1d).

In Chapter 2, the ability of the pyrazolate anion in generating, within many clusters of different nuclearity, trinuclear copper(II) complexes of general formula $[Cu_3(\mu_3\text{-}X)(R\text{-}pz)_3L_3]^{m+}$, has been extensively described.[16] These trinuclear complexes are generally synthesized starting from Cu(II) salts in the presence of a base, as in the case of the **NH_4@1** framework, and have been observed only with N-based organic ligands. In **NH_4@1**, the further connection between these trinuclear units, guaranteed by the polytopic nature of the organic bridges, generates a 3D framework with the high added value of having these trinuclear anionic complexes as secondary building units (SBUs). Moreover, the **NH_4@1**

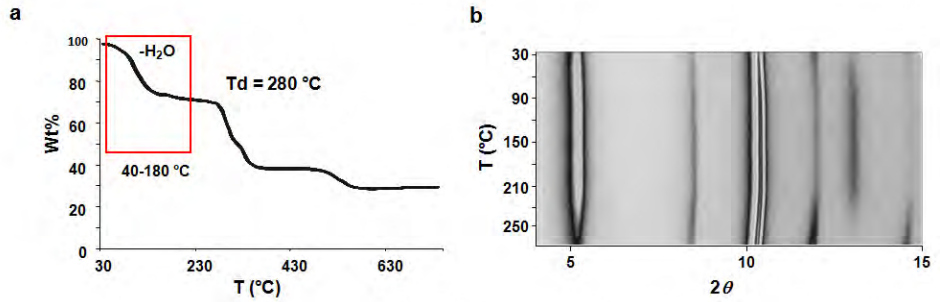

Figure 8.2. (a) Thermogravimetric experiment highlighting the initial loss of water molecules (in the temperature range 40-180 °C) and the decomposition temperature (T_d = 280 °C). (b) X-ray powder diffraction experiments in temperature collected in a 2D plot. Horizontal axis: 2θ; vertical axis, temperature. The black lines represents picks positions.

framework is also reminiscent to the one found in the $[Cu_3(\mu_3\text{-OH})(4\text{-pyridyltetrazolato})_3(OH)_2(DMF)_4]$ system reported by Zubieta et al.,[17] however, in this case the framework is neutral whereas in **NH_4@1** is anionic.

Thermal and Chemical Stability. In order to probe the thermal stability of **NH_4@1**, thermogravimetric analysis (TGA) was performed, combined with *in situ* variable-temperature X-ray powder diffraction experiments (XRPD). It should be emphatized that, in this study, both the TGA and the XRPD experiments are carried out *in air*.

As depicted in Figure 8.2a, the thermogravimetric analysis, TGA, is indicative of the sequential dehydration of this material in the 40-135 °C range (8 water molecules) and 150-180 °C (1 water molecule). Further heating prompts decomposition at 280 °C.

The foregoing observations are consistent with thermodiffractometric analyses, TXRPD (Figure 8.2b). The results confirm the good thermal stability of **NH_4@1**, while also showing that its crystallinity is retained to afford permanent porosity. Indeed, solvent loss does not significantly affect the crystal structure,

with the powder diffraction pattern remaining unchanged up to 280 °C. Thus, the framework does not undergo significant stress during heating with a δlnV/δT value of $-4.8 \cdot 10^{-5}$ K^{-1}, which suggests a slight cell contraction concomitant with the dehydration process. Interestingly, this process is fully reversible, indeed, upon lowering the temperature and exposing the material to open air at room temperature, the original hydrated material is formed in a few hours.

The robustness of **NH_4@1** in diverse chemical environments has also been tested by suspending samples in boiling organic solvents; in water at 80 °C and in diluted aqueous solution of HNO_3 and NaOH. 100 mg of this species were soaked in the applicable test solution and then removed, filtered, dried at room temperature and checked by X-ray powder diffraction analysis. The results are reported in Figure 8.3 which shows that **NH_4@1** remains unaltered in the tested boiling organic solvents (methanol, benzene, cyclohexane), in water (up to 80 °C, for 4 h) and at room temperature in dilute acidic (0.001 M HNO_3, for 4 h) or basic (0.001 M NaOH, for 4 h) aqueous solutions. Unfortunately, the chemical stability of **NH_4@1** is not so remarkable, compared to that found for the NiBTP framework, presented in Chapter 6, that remains one of the most stable porous metal-organic structure yet attained. However, the stability of **NH_4@1** could be yet considered as a good improvement, if comparing it with the typical stability displayed in carboxylate-based MOFs. This can certainly be ascribed to the presence of the N-donor fragment in the hetero-functional organic spacer, that can generate stronger M-N bonds when coupled with late-transition metal ions, thus leading to an increase in the overall stability of the formed framework.

Adsorption properties and ions exchange experiments. Prompted by the porous nature of **NH_4@1**, its permanent porosity has been evaluated by collecting N_2 adsorption isotherms at 77 K. The optimally desolvated material were found to adsorb a good amount of N_2 at 77 K, displaying Type I adsorption isotherm

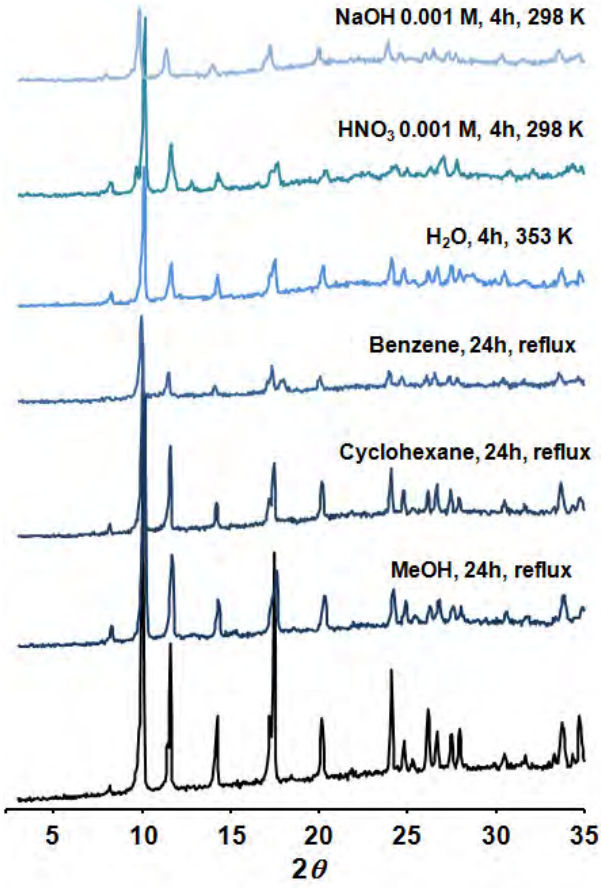

Figure 8.3. X-ray powder diffraction patterns of **NH_4@1** collected after each chemical stability test.

characteristic of microporous solids (see Figure 8.4). Fitting the N_2 isotherm afforded BET surface area of 680 m^2/g for **NH_4@1**.

The existence of an extraframework NH_4^+ cation in **NH_4@1** could be exploited for evaluating a possible modulation of its surface area by ion exchange experiments. Indeed, the exchangeable nature of the ammonium cations has been evaluated by suspending **NH_4@1** in 0.1-0.5 M aqueous solutions of nitrate

salts of different cations [$A(NO_3)_n$; n = 1, A= Li^+, Na^+, K^+; n= 2, A = Ca^{2+}] or in 0.5 M methanolic solutions of organic amines (Me_3N, Et_3N). This process has lead to the exchanged materials, formulated as $A_x(NH_4)_{1-x}[Cu_3(\mu_3\text{-}OH)(\mu_3\text{-}4\text{-carboxypyrazolato})_3]$ (**A@1**) ($x \geq 0.5$).

The new series of exchanged-frameworks have been characterized by XRPD analyses. In Figure 8.5 I reported a collection of the XRPD patterns of each exchanged framework, compared to the parent **NH_4@1**, showing unchanged peak positions for each **A@1**, according to the maintenance of the original topology. Moreover, the effect of the ion exchange on **NH_4@1**, with trimethyl and triethyl ammonium cations, was examined by IR spectroscopy (Figure 8.6). Unfortunately, the presence of large amount of solvent molecules within the framework overshadows the signals of the organic amines, that are visible only in as weak bands in the exchanged framework. However, elemental analyses on **Me_3NH@1** and **Et_3NH@1** (see experimental details) confirmed that the exchange procedure was performed with efficiency. Moreover, atomic absorption have been performed in order to confirm the formulations attributed to the exchanged MOFs by elemental analysis. The results are indicative that monovalent cations give rise to an exchange of the 50 % of ammonium cations, giving rise to materials of $A_{0.5}(NH_4)_{0.5}[Cu_3(OH)(4\text{-carboxypyrazolato})_3]$ (A= Et_3NH^+, Me_3NH^+, Li^+, K^+) formula. This means that only one of the two NH_4^+ cations *per* cavity could be exchanged (Figure 8.7). However, in the case of ions with higher charge (i.e. Ca^{2+}) a complete ion exchange takes place as in agreement with the common zeolite ion exchange behavior.

N_2 adsorption measurements performed on the exchanged systems show profound changes in the adsorption isotherms concomitant to the ion exchange processes, which are indicative of the effective modulation of the porosity of the parent **NH_4@1**framework (Figure 8.4). Indeed, on passing from NH_4^+ to Et_3NH^+ a lowering of the adsorption capacity and pore surface is observed (BET surface

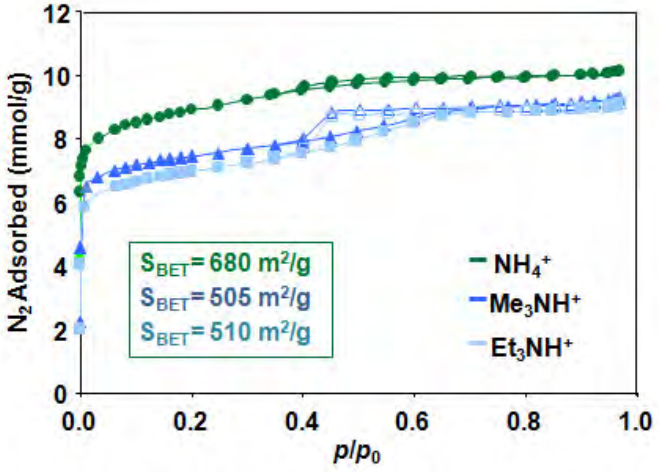

Figure 8.4. Cation exchange modulation of the porous network in **A@1** systems (A= NH_4^+, Me_3NH^+, Et_3NH^+) as shown by N_2 adsorption isotherms at 77 K. **NH_4@1** (diamonds), **Me_3NH@1** (triangles), **Et_3NH@1** (squares). Open symbols denote desorption.

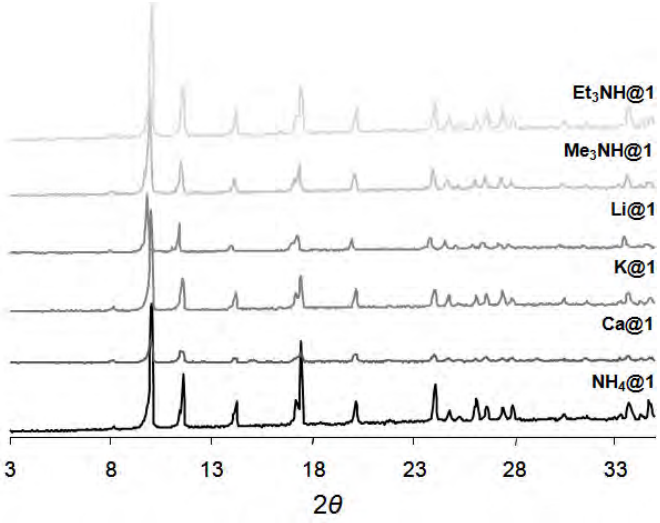

Figure 8.5. XRPD patterns for the exchanged **A@1** (A = Ca^{2+}, K^+, Li^+, Me_3NH^+, Et_3NH^+) materials compared to the as-synthesized **NH_4@1** framework.

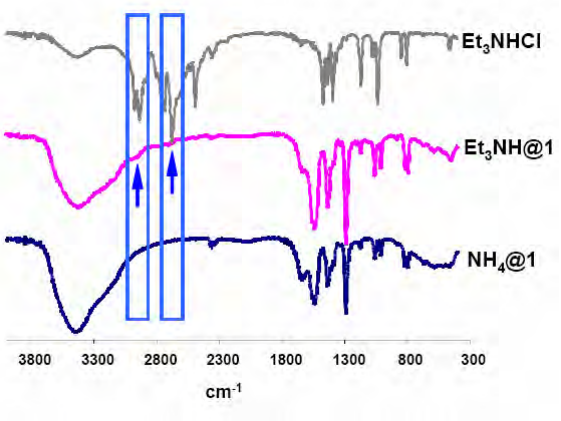

Figure 8.6. Comparison of IR spectrum of as-synthesized **NH_4@1, Et_3NH@1** and Et_3NHCl. The broad band around 3000 cm^{-1} is attributed to the water molecules into the pores of the framework.

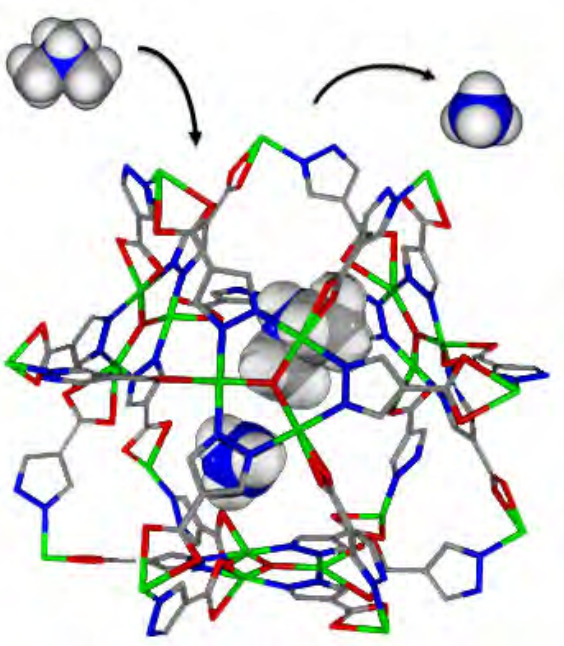

Figure 8.7. Depiction of the exchange process of one of the two NH_4^+ cations per each tetrahedral cavity of the framework by one Me_3NH^+ ion.

area of 680 $m^2 g^{-1}$ for **NH_4@1** diminishes to 505 and 510 $m^2 g^{-1}$ for **Me_3NH@1** and **Et_3NH@1**, respectively). These results are well in agreement with the decrease of the accessible pore volume of the framework as results of the bulkier nature of R_3NH^+ compared to NH_4^+ cations.

Gas separation experiments. Once obtained the whole series of **A@1** species, the effect of the ion exchange process has been exploited for evaluating how the modulation of both dimension and nature of the pores may affect the separation properties in the primitive, anionic, metal-organic framework. Thus, the separation selectivity of the **A@1** series has been investigated by means adsorption experiments of gases of environmental and industrial interest (N_2, CH_4, CO_2, C_2H_2). and harmful organic vapors (benzene, cyclohexane).[18]

Variable temperature pulse gas chromatography. These experiments have been carried out in the 273-363 K temperature range with a complex gas mixture (N_2, CH_4, CO_2, C_2H_2) in order to examine the possible utility of these systems for gas separation purposes.

The discovery of new adsorbents capable of storing acetylene (C_2H_2) has attracted a great attention due to the difficulties in storage and purification of this important gas.[19] Although many adsorbents have demonstrated to be able to achieve large uptake of the highly reactive C_2H_2, very few of them have demonstrated high selectivity over its counterpart carbon dioxide, despite the fact that the separation between these two gases is of great industrial interest.[20]

In this work, the separation process of CO_2/C_2H_2 mixtures has been studied on the **NH_4@1** and **Et_3NH@1** frameworks for the sake of simplicity. The results show that these two frameworks give rise to significant interactions with acetylene and carbon dioxide, whereas the interactions with nitrogen and methane are negligible. Noteworthy, at low temperatures ($T < 286$ K), acetylene is more tightly retained by **A@1** frameworks than carbon dioxide while, at higher temperatures ($T > 286$ K), the reverse situation is found, with C_2H_2 being eluted

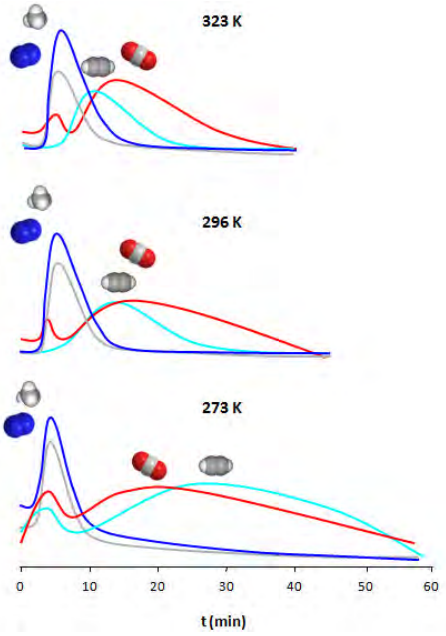

Figure 8.8. Variable-temperature pulse gas chromatography experiments of an equimolecular N_2 (blue), CH_4 (gray), CO_2 (red) and C_2H_2 (light blue) gas mixture passed through a chromatographic column packed with **NH_4@1** using a He flow of 10 mL min^{-1}.

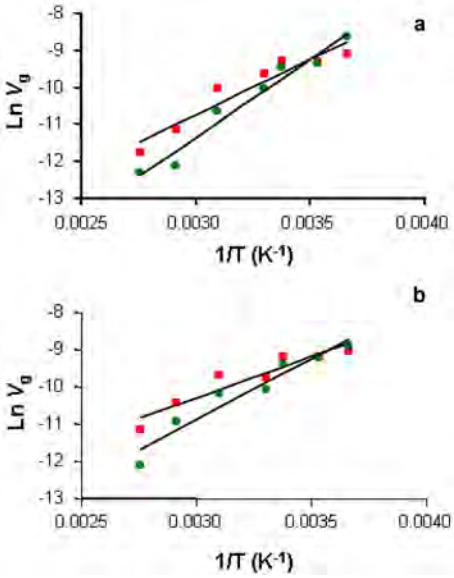

Figure 8.9. Variation of CO_2 (red squares) and C_2H_2 (green circles) retention volumes V_g [m^3 g^{-1}] on **NH_4@1** (a) and **Et_3NH@1** (b) as a function of adsorption temperature (273-363 K).

before than CO_2 (Figure 8.8). This behavior can be easily visualized by plotting the lnV_g (m^3g^{-1}, retention volume) *vs* 1/T (Figure 8.9). In this plot it can be observed that the tendency lines of CO_2 and C_2H_2 intersect at about 286 K. This means that, at this temperature, the CO_2/C_2H_2 separation become ineffective. The zero coverage adsorption heats (ΔH_{ads}) for CO_2 and C_2H_2 have been calculated from the slope of these plots according to $\Delta H_{ads} = -R\delta(\ln V_g)/\delta(1/T)$,[21] and the results are summarized in Table 8.1. These ΔH_{ads} values are similar to

the ones reported by Kitagawa *et al.* on metal-organic frameworks with narrow basic pores, obtained from monocomponent adsorption isotherms, applying the Clausius-Clapeyron equation.[20a-22] In this regard, these authors indicated the possible utility of this type of microporous networks for the separation of C_2H_2/CO_2 mixtures but no experiments on the gas mixture were performed to demonstrate it. Consequently, to the best of our knowledge, the utility of MOFs for this difficult separation process, highlighting the importance of the adsorption temperature on the efficiency of the separation, is here demonstrated for the first time.

	NH_4@1	**Et_3NH@1**
$-\Delta H_{ads}$ C_2H_2 (kJmol^{-1})	34.9	27.3
$-\Delta H_{ads}$ CO_2 (kJmol^{-1})	24.7	18.4
K_H C_2H_2 (cm^3 m^{-2})[a]	0.358	0.325
K_H CO_2 (cm^3 m^{-2})[a]	0.225	0.280
lnK_r [a]	4.51	3.92

[a] calculated values at 273K.

Table 8.1. Calculated adsorption heats DH_{ads}, Henry constants K_H and partition coefficients K_r for CO_2 and C_2H_2 from variable temperature zero coverage gas chromatography experiments on **NH_4@1** and **Et_3NH@1** materials.

Moreover, the discrimination of the **A@1** systems towards the C_2H_2/CO_2/CH_4 mixture might be of interest for acetylene purification obtained from partial burning of methane and oxygen. The efficiency of this separation is tentatively attributed to the presence of basic sites (carboxylates), coordination unsaturated metal ions, H-bonding and size of the cavities, but further experimental confirmation is required. In this regard, the separation coefficients (K_r) calculated for a binary mixture according to ln$K$r= ($\Delta Hads_1$-$\Delta Hads_2$)/(RT),[23] are large enough to ensure separation of C_2H_2/CO_2 (Table 8.1). Moreover, in the case of C_2H_2/CH_4 or CO_2/CH_4 mixtures the separation coefficients are expected to be nearly infinite.

Breakthrough Curves. Measurements of breakthrough curves of a 0.27:0.73 (v/v) mixture of CO_2/CH_4 flowed through a chromatographic column packed with **NH_4@1** at 273 K reveal the passage of CH_4 through this material and the selective

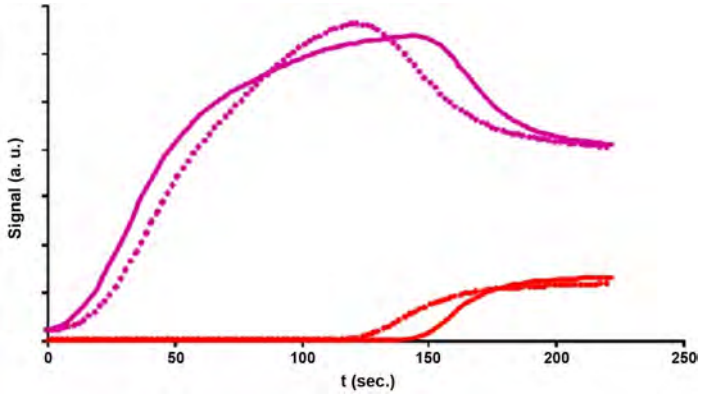

Figure 8.10. Breakthrough curves for the separation of a 0.27:0.67 (v/v) 10 mL min-1 flow of CO_2/CH_4 mixture (CO_2, red; CH_4, purple) at 273 K by NH@1 (solid line) and Et_3NH@1 (dotted line).

retention of CO_2 (Figure 8.10). The breakthrough takes place at ca. 150 s after dosing the gas mixture, which represents 0.42 mmol of CO_2 being retained per gram of **NH_4@1** under these dynamic conditions. This kind of behavior was expected in view of the differentiated interaction of these two gases with the **NH_4@1** framework. The same measurement performed on the **Et_3NH@1** framework showed a related behavior, with the breakthrough taking place at ca. 125 s, that however corresponds to a lower CO_2 removal capacity of 0.30 mmol/g.

Separation of harmful organic vapors. Distillation separation of benzene and cyclohexane is a highly demanding and energy-consuming process in the petrolchemical industry. This is due to the fact that C_6H_{12} is produced by hydrogenation of C_6H_6 in the C_6H_6-C_6H_{12} miscible system and the two substances have very similar boiling points (C_6H_6, 80.1 °C and C_6H_{12}, 80.7 °C). However, the chemical properties (C_6H_6 is an aromatic system whereas C_6H_{12} is a saturated one) and molecular geometry (C_6H_6, 3.3 x 6.6 x 7.3 Å; C_6H_{12}, 5.0 x 6.6 x 7.2 Å)[24] of these two molecules differentiate the one from the other and can be exploited for their

effective separation. Indeed, separation by shape selective adsorption could be an interesting alternative to what reported above. Therefore, the effect of ion exchange on the separation selectivity towards benzene/cyclohexane mixtures, has also been investigated in **A@1**. The results are collected in Table 8.2.

	benzene /cyclohexane
Li@1	11.76
Et_3NH@1	9.52
Me_3NH@1	10.52
Ca@1	7.41
K@1	6.06
NH_4@1	4.88

Table 8.2. Adsorption selectivity of **A@1** towards a 1:1 benzene:cyclohexane mixture at 298 K determined by ^{1}H-NMR.

Exposition of the **A@1** materials towards benzene:cyclohexene 1:1 mixtures show a significant enrichment of the adsorbate phase in the benzene component. In the case of the original **NH_4@1**, the composition of the adsorbed benzene:cyclohexane phase reaches a 5:1 ratio, showing a clear enrichment in the benzene component. This is further substantiated in the case of the **Et_3NH@1** and **Li@1** materials with benzene:cyclohexane ratios of 8:1 and 12:1, respectively. The increased selectivity for the **Et_3NH@1** and **Li@1** systems should be related to the increasing bulk of Et_3NH^+ and $Li(H_2O)_4^+$ ions within the pores.

Conclusions

Summarizing, in this chapter, have been shown the successfully formation of a anionic porous framework of formula $NH_4[Cu_3(\mu_3\text{-}OH)(\mu_3\text{-}4\text{-carboxypyrazolato})_3]$ (**NH_4@1**). This framework shows reasonably high thermal and chemical stabilities able to withstand the typical conditions found in practical applications. Moreover, it has been demonstrated that it is also possible to modulate its porous network, much alike zeolites, by means of cation exchange processes of the extraframework NH_4^+ cations leading to **A@1** (A= Li^+, Na^+, K^+; A = Ca^{2+}) materials. Indeed, the increasing bulk of the exchanged cations still permit the access of

molecules to their porous structure with a concomitant increased size exclusion selectivity. In this regard, the discrimination properties of **A@1** frameworks towards complex mixtures *i.e.* $CO_2/C_2H_2/CH_4$ and C_6H_6/C_6H_{12} is highlighted. Moreover, it has been demonstrated that in gas separation processes the temperature at which the separation is performed has a great importance on the efficiency of the separation of a binary gas mixture with metal-organic framework.

Acknowledgements

Support by the Spanish MCINN [grant CTQ2008-00037/PPQ], Junta de Andalucía, and EU (NanoMOF-228604) is acknowledged.

References and Notes

1 Batten, S. R.; Neville, S. M.; Turner, D. R. *Coordination Polymers. Design, Analysis and Applications* RSC Publishing, Cambridge, **2009**.

2 See, *e.g.*: (a) Ferey G. *Chem. Soc. Rev.* **2008**, *37*, 191.; (b) Farrusseng, D.; Aguado, S.; Pinel, C. *Angew. Chem.* **2009**, *121*, 7638.; *Angew. Chem. Int. Ed.* **2009**, *48*, 7502.

3 Wang, Z.; Cohen, S. M. *Chem. Soc. Rev.* **2009**, *38*, 1315.

4 (a) Phan, A.; Doonan, C. J.; Uribe-Romo, F. J.; Knobler, C. B.; O'Keeffe, M. Yaghi, O. M. *Acc. Chem. Res.* **2010**, *43*, 58. (b) Colombo, V.; Galli, S.; Choi, H. J.; Han, G. D.; Maspero, A.; Palmisano, G.; Masciocchi, N.; Long, J. R. *Chem. Sci.* **2011**, *2*, 1311.

5 Alkordi, M. H.; Brant, J. A.; Wojtas, L.; Kravtsov, V. C.; Cairns, A. J.; Eddaoudi, M. *J. Am. Chem. Soc.* **2009**, *131*, 17753.

6 Navarro, J. A. R.; Barea, E.; Rodríguez-Diéguez, A.; Salas, J. M.; Ania, C. O.; Parra, J. B.; Masciocchi, N.; Galli, S.; Sironi, A. *J. Am. Chem. Soc.* **2008**, *130*, 3978.

7 Park, K. S.; Ni, Z.; Côté, A. P.; Choi, J. Y.; Huang, R.; Uribe-Romo, F. J.; Chae, H. K.; O'Keeffe, M.; Yaghi, O. M. *Proc. Natl. Acad. Sci. USA* **2006**, *103*, 10186.

8 Liu, Y.; Kravtsov, V.C.; Larsena, R.; Eddaoudi, M. *Chem. Commun.* **2006**, 1488.

9 Nouar, F.; Eckert, J.; Eubank, J. F.; Forster, P.; Eddaoudi, M. *J. Am. Chem. Soc.* **2009**, *131*, 2864.

10 (a) Alkordi, M. H.; Liu, Y.; Larsen, R. W.; Eubank, J. F.; Eddaoudi, M. *J. Am. Chem. Soc.* **2008**, *130*, 12639. (b) Chen, C.; Kim, J.; Yang, D.-A.; Ahn, W.-S. *Chem. Eng. J.* **2011**, *168*, 1134.

11 Ockwig, N.W.; Delgado-Friedrichs, O.; O'Keeffe, M.; Yaghi, O. M. *Acc. Chem. Res.* **2005**, *38*, 176.

12 Greathouse, J. A.; Allendorf, M. D. *J. Am. Chem. Soc.* **2006**, *128*, 10678.

13 Galli, S.; Masciocchi, N.; Colombo, V.; Maspero, A.; Palmisano, G.; López-Garzón, F. J.; Domingo-García, M.; Fernández-Morales, I.; Barea, E.; Navarro, J. A. R. *Chem. Mater.* **2010**, *22*, 1664.

14 Foces-Foces, C. et al. *J. Am. Chem. Soc.* **2001**, *123*, 7898.

15 Spek; A. L. *J. Appl. Crystallogr.* **2003**, *36*, 7.

16 See: Pettinari, C.; Masciocchi, N.; Pandolfo, L.; Pucci, D. *Chem.—Eur. J.* **2010**, *16*, 1106 and Ref. 34 in Chapter 2 of this thesis.

17 Ouellette, W.; Liu, H.; O'Connor, C. J.; Zubieta, J. *Inorg. Chem.* **2009**, *48*, 4655.

18 Li, J.-R.; Kuppler, R. J.; Zhou, H.-C. *Chem. Soc. Rev.* **2009**, *38*, 1477.

19 Leeds, F. H.; Butterfield, W. J. A. *Acetylene, the principle of its generation and use*; Charles Griffin: London, **1910**.

20 (a) Matsuda, R.; Kitaura, R.; Kitagawa, S.; Kubota, Y.; Belosludov, R. V.; Kobayashi, T. C.; Sakamoto, H.; Chiba, T.; Takata, M.; Kawazoe, Y.; Mita, Y. *Nature* **2005**, *436*, 238. (b) Lim, S.; Kim, H.; Selvapalam, N.; Kim, K.-J.; Cho, S. J.; Seo, G.; Kim, K. *Angew. Chem., Int. Ed.* **2008**, *47*, 3352. (c) Tanaka, D.; Higuchi, M.; Horike, S.; Matsuda, R.; Kinoshita, Y.; Yanai, N.; Kitagawa, S. *Chem. Asian J.* **2008**, *3*, 1343.

21 Diaz, E.; Ordoñez, S.; Vega, A. *J. Colloid Interf. Sci.* **2007**, *305*, 7.

22 Zhang, J. P.; Chen, X. M. *J. Am. Chem. Soc.* **2009**, *131*, 5516.

23 Keltsev, N. V. *The Essential Principles of Adsorption Engineering*, Moscow, **1984**.

24 Webster, C. E.; Drago, R. S.; Zerner, M. C. *J. Am. Chem. Soc.* **1998**, *120*, 5509.

Chapter 9
Conclusions

An important key feature of porous materials is their chemical and thermal stability, toward which researchers are continuously striving. In this regard, in this thesis, it has been highlighted that is clearly beneficial to discover new porous metal–organic frameworks that are stable towards diverse environments such as air, water, acidic and basic media, and even extreme temperatures and pressures, to extend their utility toward a variety of applications where other porous materials, such as zeolites, have been playing a major role. Therefore, metal-organic frameworks based on a linkage between pyrazolate ligands and transition metal ions could be of great interest in the research field of hybrid porous frameworks due to the ability of the pyrazole ring in the construction of materials of high chemical and thermal stability.

In this regard, a number of new pyrazole-based ligands as building-blocks for the synthesis of porous metal-organic frameworks have been successfully synthesized and are described in Chapter 3.

In Chapter 4, the synthesis and characterization of the Ni(II) and Zn(II) species with the long 1,4-bis(1*H*-pyrazol-4-ylbenzene) as organic spacer, which show permanent porosity and a certain degree of flexibility, have been presented. More

importantly, the moisture insensitive nature of **NiBDP**, coupled to its framework flexibility and to its very high thermal stability, was shown to be highly suitable for thiophene removal from CO_2/CH_4 mixtures *even in the presence of humidity*, thus overcoming the still unsolved problems raised by classical carboxylate-based MOFs in real practical applications, such their incorporation in filters for air and gas purification processes.

Chapter 5 describes the synthesis and characterization of the first example of a porous metal organic framework based on octanuclear Ni(II) hydroxo clusters linked by tetradentate μ_4-polytopic pyrazolate ligands in a complex polyhedron of rigorous cubic symmetry. Here, it has been demonstrate the utility of *state-of-the-art* structural powder diffraction techniques that, coupled with X-ray absorption techniques and spectroscopic measurements, allowed the detection and confirmation of relevant stereochemical features, and, above all, the determination of the correct, but *elusive*, stoichiometry of the $[Ni_8(OH)_4(OH_2)_2(\mu_4\text{-}L)_6]\cdot nH_2O$ porous coordination polymer.

Afterwards, in Chapter 6, it has been demonstrated that with the use of polytopic pyrazole ligands it is even possible to synthesize pyrazolate-based frameworks featuring, upon activation, open metal sites. Indeed, $Ni_3(BTP)_2$ represents the first high-stability metal-organic framework with accessible metal sites lining the pore surfaces. Such a remarkable combination of properties may open the way for testing metal-organic frameworks in a variety of applications that currently employ zeolites under extreme conditions.

A new, important, challenge in the field of porous polymers is the development of stable structures including functional organic sites, with the aim of tuning their pore properties (pore size and shape, pore volume and decoration) to enhance uptake capacity and selectivity toward a targeted guest. Indeed, in chapter 7, a systematic study, in order to investigate and understand the effect of (pre-synthesis) ligand functionalization in the gas adsorption and separation

processes on two large series of isostructural pyrazolate-based metal-organic frameworks, has been carried out with success.

A newly introduced class of porous materials, called zeolite-like metal-organic frameworks (ZMOFs), is based on anionic frameworks. This class of materials has the advantage of possessing these tunable extra-framework cations that are exploitable as strong sorption sites for a targeted guest. Indeed, in Chapter 8, a new zeolite-like metal organic framework of formula $NH_4[Cu_3(\mu_3\text{-}OH)(\mu_3\text{-}4\text{-carboxypyrazolato})_3]$, has been synthesized. Moreover, its porous nature have been modulated, much alike zeolites, by means of cation exchange processes of the extraframework NH_4^+ cations leading to a series of exchanged materials. These exchanged materials have demonstrated to lead to an increased size exclusion selectivity with the increasing of the bulk of the exchanged cations. Therefore, the discrimination properties of these frameworks towards complex gases and vapor mixtures and the importance of the temperature on the efficiency in the separation of a binary gas mixture, have been highlighted.

Nearly all the results presented in this thesis have been published in scientific journals of international reputation and further manuscripts are under preparation. In the following, a list of publications is provided to the reader (that is gratefully acknowledged for the reading of this manuscript).

List of Publications

"High Thermal and Chemical Stability in Pyrazolate Bridged Metal-Organic Frameworks with Exposed Metal Site" **Colombo, V.**; Galli, S.; Choi, H. J.; Han, G. D.; Maspero, A.; Palmisano, G.; Masciocchi, N.; Long, J. R.; *Chem. Sci*. **2011**, *2*, 1311.

"Cation-Exchange Porosity Tuning in Anionic Metal–Organic Frameworks for the Selective Separation of Gases and Vapors and for Catalysis"; Quartapelle Procopio, E.; Linares, F.; Montoro, C.; **Colombo, V.**; Maspero, A.; Barea, E.; Navarro, J.A.R.; *Angew. Chem. Int. Ed.* **2010**, 49,7308.

"Cubic Octanuclear Ni(II) Clusters in Highly Porous Polypyrazolyl-Based Materials"; Masciocchi, N.; Galli, S.; **Colombo, V.**; Maspero, A.; Palmisano, G.; Seyyedi, B.; Lamberti, C.; Bordiga, S.; *J. Am. Chem. Soc.* **2010**, 132, 7902.

"Adsorption and Separation of Harmful Organic Vapors by Flexible Hydrophobic bis-Pyrazolate Based MOFs"; Galli, S.; Masciocchi, N.; **Colombo, V.**; Maspero, A.; Palmisano, G.; López-Garzón, F.J. ; Domingo-García, M.; Fernández-Morales, I.; Barea, E.; Navarro, J.A.R.; *Chemistry of Materials* **2010**, 22, 1664.

"The chemistry of thiazolo[5,4-d]thiazole-2,5-dicarboxylic acid, $C_6H_2N_2O_4S_2$, and its coordination polymers"; Aprea, A.; **Colombo, V.**; Galli, S.; Masciocchi, N.; Maspero, A.; Palmisano, G.; *Solid State Science* **2010**, *12*, 795.

"Metalorganic Frameworks based on the 1,4-bis(4-tetrazolyl) benzene ligand: the Ag and Cu derivatives"; Maspero, A.; Galli, S.; **Colombo, V.**; Peli, G.; Masciocchi, N.; Stagni, S.; Barea, E.; Navarro, J. A. R. *Inorg. Chim. ACTA* **2009**, 362, 4340.16

"A complete spectroscopic and adsorptive study of a thermally robust pyrazolato-based PCP"; Mino, L.; **Colombo, V.**; Vitillo, J. G.; Lamberti, C.; Bordiga, S.; Gallo, E.; Glatzel, P.; Maspero, A.; Galli, S. *Dalton Trans.* **2012**, *Accepted*.

"*Tuning Adsorption Properties in Highly Stable Pyrazolate-based MOFs through Ligand Modification*" Manuscript in preparation.